The role of debris in fretting: Investigation into the interrelated effects of displacement amplitude and frequency in fretting wear

ADAM KIRK, MEng

Thesis submitted to The University of Nottingham
for the degree of Doctor of Philosophy

FEBRUARY 2021

Abstract

This thesis concerns an investigation of the role of debris in fretting contacts, which has been highlighted in fretting literature over several decades to be critical in affecting the development of wear in fretting contacts; retained debris plays a significant role in fretting contacts due to a significant proportion of the wearing interface remains covered throughout the displacement cycle, thus restricting the transport into the contact of active species involved in the formation of wear debris (e.g. oxygen) and the transport out of the contact of debris once it is formed. The processes involved in the formation, flow and expulsion of oxide debris in fretting contacts are examined via the effects of frequency and displacement amplitude on fretting wear of a high strength steel, two parameters which are widely reported to influence critical processes of debris formation and ejection, but to have significantly different impacts on these processes. Examining these two parameters together therefore enables insight to be gained into processes of debris formation, retention in the form of compacted beds and the ejection of material from the contact (i.e. wear).

The fretting behaviour of a cylinder-on-flat configuration was examined over a range of fretting frequencies and displacement amplitudes, and the nature of wear debris generated in fretting tests investigated, both in the form of compacted beds retained in the contact and particles ejected during the wear process, as well as the conditions affecting the formation of debris beds. Extensive characterisation of the surface and subsurface regions of wear scars was conducted to gain insight into the mechanisms by which oxide debris beds form and the impact of their formation (or otherwise) on the development of the tribologically transformed structure.

At all conditions examined, debris ejected from the contact was found to consist predominantly of haematite, with a small (< 6%) fraction of metallic iron that exhibits a modest dependence on both frequency and displacement amplitude. Likewise, the overall range of particle sizes is largely independent of frequency and displacement amplitude, ranging from approximately 0.4 μm to 50 μm under all conditions tested, although some large pieces of the order of 100 μm are observed, proposed to be pieces of compacted debris beds formed in the contact which become detached and are subsequently ejected. Examining the morphology of ejected debris particles showed particles to consist of sub-micron crystallites of iron oxide, of the order of 0.1 μm in diameter, which sinter together to form larger coherent structures. The size of these crystallites is observed to be largely independent of displacement amplitude, and as such it is proposed that the impact of the examined parameters on the size of debris particles expelled from the contact is due to their influence upon the sintering of debris particles within the contact and their subsequent ejection, as opposed to the mechanism of detachment of particles from first body surfaces.

Two distinct wear regimes are identified, namely (i) at low frequencies and displacement amplitudes, an oxide debris bed covers most of the worn surface, preventing the development of subsurface damage and adhesive transfer but resulting in relatively high wear rates, and (ii) at high frequencies and displacement amplitudes oxide coverage of worn surfaces is relatively sparse, resulting in metal-to-metal contact and the development of significant subsurface damage and adhesive transfer. The significant change in the nature of debris retained within wear scars contrasts with the nature of debris ejected from the contact, which does not exhibit a strong dependence upon the examined parameters; as such it is proposed that wear occurs by the formation and removal of oxide debris in all of the cases examined, with any metallic debris formed being retained within the contact.

The effects of displacement amplitude and frequency in the mechanisms of fretting wear are found to exhibit a significant degree of interdependence, with the magnitude of either parameter having a significant impact upon the effect of the other on the wear rate and damage mechanism. It is proposed that the interacting effects of frequency and displacement amplitude arise from the impact of both parameters on three key processes, namely (i) ingress of oxygen to the contact; (ii) formation of oxide debris; (iii) expulsion of oxide debris from the contact. A model is outlined based on these processes to calculate wear rates and determine the operative wear mechanism under a given set of conditions; a key supposition of the model is that these three processes are in competition with one another, with the observed wear rate being governed by whichever of these rates is the smallest, accordingly termed the "rate-determining process". Equations relating these key processes to fretting parameters are derived based on current understanding of the physics of fretting wear, enabling wear rates and mechanisms (i.e. the operative processes that control the overall wear rate) to be predicted.

The model is implemented using a simple time-marching method, calibrated against experimental data for the set of frequencies and displacement amplitudes examined in the experimental investigation. The alignment of predicted wear rates and mechanisms with experimental data is assessed over a broad range of fretting parameters, including observations reported in the literature employing the same specimen configuration and material combination. Relatively good agreement is observed between the mechanisms predicted using this model and those observed in laboratory experiments, although the accuracy of wear rate predictions is seen to vary considerably. The alignment of the model with experimental data provides a promising indication of the capability of the proposed physical framework to model fretting based on the physical processes of wear, although significant errors in the predicted wear rates at some conditions highlight the need for further investigation of the effects of parameters on debris behaviour, in order to improve the accuracy and applicability of the model going forward.

Publications

A.M. Kirk, P.H. Shipway, W. Sun, C.J. Bennett - Debris development in fretting contacts – Debris particles and debris beds. *Tribology International* 149 (2020), 105592. https://doi.org/10.1016/j.triboint.2019.01.051
[Dowson Prize at the 45th Leeds-Lyon Symposium on Tribology]

A.M. Kirk, P.H. Shipway, W. Sun, C.J. Bennett - The effect of frequency on both the debris and the development of the tribologically transformed structure during fretting wear of a high strength steel. Wear 426–427(A) (2019) 694-703. https://doi.org/10.1016/j.wear.2018.12.035

A.M. Kirk, W. Sun, C.J. Bennett, P.H. Shipway - Interaction of displacement amplitude and frequency effects in fretting wear of a high strength steel: impact on debris bed formation and subsurface damage (Submitted)

A.M. Kirk, P.H. Shipway, C.J. Bennett - Rate-determining processes in fretting wear: reconsidering wear rate in predictive modelling applications (In preparation)

Acknowledgements

I would like to express my immense gratitude to my supervisors, Phil Shipway, Chris Bennett and Wei Sun, for the guidance they have given me throughout my PhD. Having the opportunity to work with and learn from them over the course of this journey has been a pleasure and a privilege, and the encouragement I received to pursue opportunities and their support in the more difficult moments has made a world of difference to me and I owe them my deepest thanks.

I am grateful to my friend and colleague Thomas Zhu, whom I have spent countless hours talking with about all things fretting wear, as well as the personal journey of pursuing this research. I would also like to thank my colleagues at the Gas Turbine and Transmissions Research Centre (G2TRC) for the supportive and collaborative atmosphere that I have had the good fortune to work in throughout my PhD.

I would also like to thank the technicians at the University of Nottingham who provided invaluable assistance in the experimental testing conducted during the course of my PhD, with special thanks to Tom Buss and Andrew Plummer. I am also very grateful to the Nanoscale and Microscale Research Centre (nmRC) for providing access to instrumentation that was critical in the work of this thesis, and the technicians who provided me with training and assistance that has greatly improved my abilities as a researcher.

I would like to thank Rolls-Royce plc for their support and funding of this research through the Transmissions University Technology Centre (UTC) at the University of Nottingham, UK, and to my colleagues at the UTCs at the University of Oxford and Imperial College London who have provided valuable feedback on my work along the way.

Finally, I would like to thank my parents, Neil and Gill, and my sister Nicky; we have stood together through everything, and I am forever grateful for their love and support. I know I could not have done this without them.

Contents

Chapter 1

Introduction

Fretting wear may occur between any loaded interface subject to vibration, often occurring at interfaces between components that are designed with the intention of being nominally static and hence not expected to experience significant degradation. The consequences of such unexpected wear can be severe, as build-up of debris can result in seizure of assemblies, components may no longer meet tolerances and fatigue life may be severely diminished. The prediction and mitigation of fretting wear are therefore necessary considerations in a wide range of engineering applications, including bearings, spline couplings, blade-disk interfaces, steel ropes, surgical implants, electrical contacts and components in nuclear reactors [1].

The oscillatory motion that causes fretting wear at a loaded interface is typically a result of system vibrations, which give rise to micro-displacements on the order of tens to hundreds of micrometres; the small amplitude of these oscillations is a key defining feature of fretting contacts, broadly defined as contacts in which a part of the interface remains hidden from the atmosphere for the whole duration of sliding. The closed nature of fretting contacts restricts the flow of active species into the contact, such as oxygen or lubricant, and the flow of wear debris out of the contact. The mechanism of fretting is therefore dependent upon both mechanical and chemical processes, with complex interactions between processes in turn being dependent upon aspects of contact configuration such as geometry and specimen material, in addition to the sliding conditions. As such, the response of contacts to fretting wear (as with other forms of sliding wear) can vary significantly between different experimental investigations, and while numerous empirical models have been proposed to predict the development of wear in fretting, agreement between models has generally been observed to be poor [2].

In fretting research for aeroengine applications, there are further challenges relating to the difficulty associated with establishing true service conditions (compounded by variation in contact geometry and materials), and with recreating these conditions in a laboratory setting; due to large number of factors that must be controlled and the significant interdependence of these factors, it is not feasible to simulate service conditions in the laboratory and as such, the effects of parameters must be investigated individually. Accordingly, there is much that may be gained from further investigation into the physical processes of fretting wear on a fundamental level, notably the role of debris, which is proposed to be critical in developing improved predictive models based on physics as opposed to empirical models reliant on data fitting.

This thesis seeks to improve understanding of the role of debris in fretting wear via an experimental investigation into the fretting response of steel pairs over a range of displacement amplitudes and fretting frequencies, two parameters which are widely reported to influence critical processes of debris formation and ejection, such as oxygen transport into the wearing interface and the flows of debris within and out of the contact. Frequency and displacement amplitude influence some of the same aspects of fretting contacts, for example sliding velocity, which directly influences the time over which processes take place and the temperature at which they occur, thereby affecting the rates of these processes. Examining the effects of these parameters, both together and individually, can therefore provide useful insight into the processes of debris formation, flow and ejection, and hence the role of debris in fretting more broadly.

The nature of fretting debris is examined, both in the form of particles expelled from the contact over the course of fretting tests as well as that retained in the contact in the form of coherent, compacted beds; together these are characterised to better understand the mechanisms of debris bed formation and how these depend upon fretting parameters. The impact of the formation (or otherwise) of debris beds on fretting response, such as the extent of wear and the development of subsurface damage are explored. Experimental observations are then used to outline a novel approach to modelling fretting wear via a comprehensive physical framework in which wear rate is controlled by competition between critical processes; a model is outlined based on the competition between physical processes controlling the overall wear rate (termed "rate-determining processes"), namely the transport of oxygen into the contact, the formation of oxide debris and the ejection of debris from the contact. This approach demonstrates the benefit of conducting extensive characterisation of debris and subsurface damage, namely for quantitative modelling of interacting effects of various parameters in fretting wear. Transport of oxygen into the contact is highlighted as a critical factor in the influence of parameters on the development of debris, and hence on the mechanisms and rates of fretting wear.

Chapter 2

Literature review

1.1 Introduction

Instances of degradation and wear at interfaces of nominally static contacting surfaces were first described in academic literature in 1911 by Eden et al. [3], who noted significant corrosion between test-pieces and specimen holders in fatigue experiments. While it was not described as such at the time, it has since been considered to be the first observation of the phenomenon initially called "fretting corrosion"; it was sixteen years after the observations of Eden et al. [3] that Tomlinson [4] would first use this term to describe such degradation associated with small-scale relative movement at a loaded interface. Since these earliest reported observations of such phenomena, the term "fretting corrosion" has become less prevalent in favour of more specific terms based on the dominant damage mechanism, namely "fretting wear" and "fretting fatigue"; however, the early description as a form of corrosion highlights the significant role of chemical processes in fretting wear, namely between substrate material and the atmosphere, which set up complex interactions between mechanical and chemical processes.

Differing definitions of fretting wear have been proposed since the phenomenon was first outlined, but is widely held to be distinct from reciprocating sliding wear due to the small displacements that characterise fretting. As such there are two critical displacements that serve to define the phenomenon of fretting, namely: (i) that which distinguishes fretting wear from fretting fatigue (at smaller displacements); (ii) that between fretting wear and reciprocating sliding wear (at larger displacements). Reports of these critical displacement amplitudes vary significantly between authors, with Vingsbo and Söderberg [5] comparing reports in the literature and estimating the critical displacements to be (i) approximately 15 μm, and (ii) between 150 – 300 μm, respectively. However, it was also noted that these boundaries may vary significantly depending on aspects of the contact configuration such as geometry and material combination, and as such there is no universally applicable displacement range that defines fretting wear.

The boundary between a partially stuck interface (typically associated with fretting fatigue) and one in which sliding occurs over the whole nominal area of contact (associated with fretting wear) can be readily calculated using the mechanical analysis first outlined by Mindlin [6] and separately by Cattaneo [7], which will be explored in further detail in Section 2.1. However, at larger displacement amplitudes, the boundary between fretting wear and reciprocating sliding wear is less clearly defined; Fouvry et al. [8] proposed that the critical feature distinguishing fretting wear from reciprocating sliding is that, in the former, part of the contact remains unexposed throughout the displacement cycle, while in the latter every part of the wear track is exposed at some stage of the cycle. Displacement amplitude is therefore critical in defining fretting wear, as is the applied normal load, which also directly influences the operative slip regime at the interface.

In addition to slip regimes, sliding conditions in fretting contacts (e.g. displacement amplitude, normal load, fretting frequency) influence numerous physical processes of wear that have significant impact on the development of damage and wear (i.e. material removal from the contact), including the processes by which wear particles form, their behaviour within the contact and their expulsion from the interface. As mentioned previously, the high sensitivity of fretting mechanisms to aspects of contact configuration that vary between experimental studies contributes to significant variation in reports in the literature regarding these mechanisms, compounded by the competing influences of sliding conditions on processes that are critical to the development of wear. For example, displacement amplitude has been noted by some observers as an important factor in the availability of oxygen at a fretting interface to form oxide debris [8–10], although the nature of this relationship is not well understood due to the competing influences of exposing a greater area of the contact to the atmosphere (acting to promote oxygen availability) and a faster rate of oxygen consumption (acting to restrict oxygen availability). Likewise, the impact of displacement amplitude on the flow of debris involves complex interacting processes, as larger displacement amplitudes are generally reported to promote the flow of debris within and out of the contact, while the faster rate of energy dissipation in the contact increases contact temperature, acting to promote cohesion and sintering of debris particles. The role of fretting frequency also involves competing processes, affecting the time over which processes can occur, while changes in the temperature affect the rate at which reactions take place, as well as diffusion-related processes such as debris sintering. Higher fretting frequencies are typically associated with more efficient oxygen exclusion from fretting contacts, with wear scars becoming more metallic (i.e. reduced coverage by oxide debris beds) and a smaller volume of material removed. Normal load is known from static contact mechanics to affect the real area of contact, which in the case of fretting wear plays a critical role in the number of asperity interactions and hence the rate of formation of wear particles. The impact of normal load on the flow of debris once formed, however, is less clearly understood, due to competing influences on processes related to debris bed formation such as oxygen availability, compaction and sintering of debris particles, and the rate at which debris beds are broken down. Moreover, several processes have competing influences upon them from changes in a single parameter, and as such the effect of a given parameter may in turn be dependent upon several other parameters, adding further complexity to the interpretation of observed effects of parameters in fretting literature.

Displacement amplitude and frequency, along with the coefficient of friction and the normal load, control the rate at which energy is dissipated in the contact (i.e. power dissipation), and hence the increase in local temperature generated during sliding. The extent of temperature rise in fretting contacts has been the subject of much investigation, although the inherently "closed" nature of fretting contacts presents a barrier to obtaining accurate experimental measurements, and therefore to validation of predictive models; this adds another layer of complexity to comprehensive modelling of fretting mechanisms. Investigation of fretting behaviour at elevated environmental temperatures has indicated that under suitable conditions, wear debris retained in the contact can sinter to form stable, protective beds capable of accommodating relative displacements between wearing bodies, and hence result in a sharp drop-off in wear rate. These "glaze layers", named for their smooth, glassy appearance highlight the importance role of retained debris in wear mechanisms in fretting, in particular the ability for debris particles to sinter to form protective beds.

While numerous empirical models of fretting have been outlined, due to the wide range of testing configurations employed and the complex interdependence of fretting processes, the output of such models have been found to vary considerably [2], and accordingly there is much that may be gained from further investigation into the physical processes of fretting wear on a fundamental level, which in turn may guide efforts towards improved predictive modelling.

This review seeks to clarify the state of knowledge of the physical processes that constitute fretting wear, with emphasis on how the rates of formation and retention of wear debris affect wear mechanisms; both the amplitude and frequency of fretting displacements are reviewed in detail due to their influence on the exposure of wearing contacts to the atmosphere and the entrapment of debris, which are shown to be important considerations in predictive models of fretting wear.

2.1 Analysis of fretting contacts

The response of a fretting contact to a given loading can have significant implications for the degree of slip at the interface, and hence the operative modes of damage, namely fretting wear or fretting fatigue. Analytical solutions have been developed to describe the mechanics of contact for geometries that may be considered representative of laboratory conditions, and therefore enable critical aspects of fretting contacts to be evaluated based on available inputs such as material properties and sliding conditions; in addition to the degree of slip at the interface, these include the coefficient of friction, the energy dissipated in a fretting cycle and stress distributions in both specimens of a pair. In this section, the principles of contact mechanics most relevant to the analysis of fretting contacts in laboratory conditions are discussed, in order to highlight the tools available to researchers investigating the processes of fretting wear, including the strengths and weaknesses of these particular tools.

2.1.1 Hertzian contact mechanics

Laboratory experiments of fretting wear typically employ simplified specimen geometries such as cylinder-on-flat and ball-on-flat contacts, for which analytical solutions can be readily derived to obtain relevant information such as stresses within the bodies and the nominal area of contact. The cylinder-on-flat configuration used in this thesis can be analysed using Hertz theory of elastic line contact between two cylinders, a diagram of which is shown in Figure 2.1; a flat body is simulated by taking the radius of a cylindrical body to be infinite. The method, as detailed by Johnson [11], is outlined below:

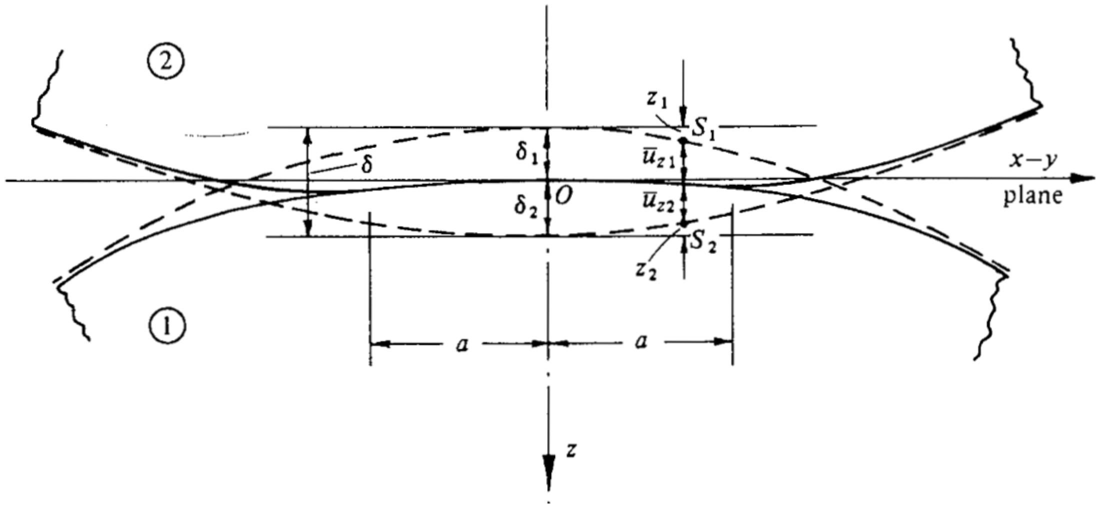

Figure 2.1. Schematic diagram of two elastic cylinders in contact [11]

The half-width, a, of the line contact generated when two parallel cylinders of radius R_1 and R_2, Youngs modulus E_1 and E_2 and Poisson's ratio ν_1 and ν_2 are brought into contact with an applied force, P, is calculated as:

$$a = \left(\frac{4PR^*}{\pi E^*}\right)^{\frac{1}{2}}$$ Equation 2.1

Where the radius of curvature, $1/R^*$, and composite modulus, E^*, are calculated by Equation 2.2 and Equation 2.3, respectively:

$$\frac{1}{R^*} = \frac{1}{R_1} + \frac{1}{R_2}$$ Equation 2.2

$$\frac{1}{E^*} = \frac{1-\nu_1^2}{E_1} + \frac{1-\nu_2^2}{E_2}$$ Equation 2.3

The normal pressure distribution, $p(x)$, is then calculated as:

$$p(x) = P_0\sqrt{1 - \frac{x^2}{a^2}}$$ Equation 2.4

The maximum contact pressure, p_0, given by Equation 2.5 occurs at the centre of the contact ($x = 0$), and the contact pressure falls to zero at the contact edges ($x = a$):

$$p_0 = \left(\frac{P'E^*}{\pi R}\right)^{\frac{1}{2}} \qquad \text{Equation 2.5}$$

The stresses within the two solids can then be calculated using equations for loading of an elastic half-space:

$$\sigma_x = -\frac{p_0}{a}\left\{(a^2 + 2z^2)(a^2 + z^2)^{-\frac{1}{2}} - 2z\right\} \qquad \text{Equation 2.6}$$

$$\sigma_z = -\frac{p_0}{a}(a^2 + z^2)^{-\frac{1}{2}} \qquad \text{Equation 2.7}$$

$$\tau_1 = -\frac{p_0}{a}\left\{z - z^2(a^2 + z^2)^{-\frac{1}{2}}\right\} \qquad \text{Equation 2.8}$$

Where σ_x and σ_z are the principal stresses in the x and z axes respectively, and τ_1 is the principal shear stress. From Equation 2.6 and Equation 2.8 it is found that $(\tau_1)_{max} = 0.30p_0$ at $z = 0.78a$. The distribution of subsurface stresses is shown in Figure 2.2.

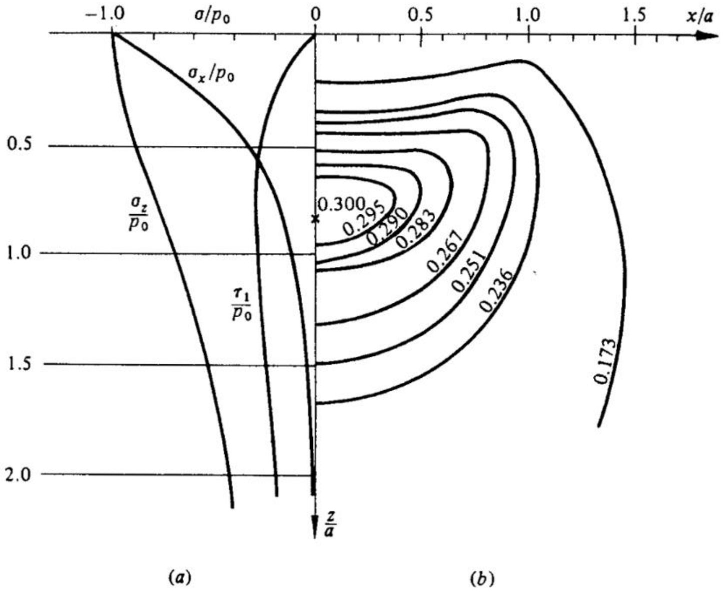

Figure 2.2. Variations of principal stresses resulting from line contact between two parallel elastic cylinders (a) subsurface stresses along the axis of symmetry; (b) contours of principal shear stress τ_1.

The above analysis demonstrates the value of simplified analysis of static elastic contacts in evaluating quantities relevant to fretting analysis, namely the *initial* nominal area of contact under an applied normal load, the pressure distribution at the interface and the subsurface stress distributions developed in the specimen. These may all be calculated based on readily available inputs, namely the geometry and material properties of the bodies in contact, and the applied loading conditions. It should be noted that for non-conforming configurations (e.g. cylinder-on-flat) the nominal area of contact increases significantly as wear progresses, resulting in a more-conforming interface, which will in turn have significant implications for the pressure and stress distributions [12], although the initial values derived analytically still provide an important basis for comparing the impact of different fretting loadings on initial parameters. Furthermore, the analysis may be implemented in numerical models to evaluate how pressure and stress distributions evolve as wear progresses over the duration of a fretting test, such as in the time-marching finite-element approach outlined by McColl et al. [12].

2.1.2 Slip regimes

The Hertz theory above describes the case of static contact, but can be expanded to include an applied tangential force; when tangential force (Q) is less than the static friction limit (μP), the distribution of tangential traction, $q(x)$, is given by Equation 2.9:

$$q(x) = \frac{Q}{\pi(a^2 - x^2)^{\frac{1}{2}}}$$ Equation 2.9

It can be seen from Equation 2.9 that from this solution, tractional force tends towards infinity at the contact edges ($x = a$); as infinite tractional force cannot occur in reality, there must be some limiting condition past which the force is relieved. Mindlin [6] proposed that tractional force must be limited by friction ($q(x) < \mu\, p(x)$), above which slip occurs at the interface; slip begins at the edges of the contact, where tractional force would otherwise tend to infinity, and grows inwards towards the centre of the contact until $x = \pm c$. The definition of c is given by Equation 2.10:

$$\frac{c}{a} = \left(1 - \frac{Q}{\mu P}\right)^{\frac{1}{2}}$$ Equation 2.10

The surface tractions within the central stuck region ($-c \leq x \leq c$) and surrounding slip regions ($c \leq |x| \leq a$) are calculated by:

$$q(x) = \mu p_0 \left(1 - \frac{x^2}{a^2}\right)^{\frac{1}{2}} \qquad \text{for } c \leq |x| \leq a \qquad \text{Equation 2.11}$$

$$q(x) = \mu p_0 \left(1 - \frac{x^2}{a^2}\right)^{\frac{1}{2}} - \frac{c}{a}\left(1 - \frac{x^2}{c^2}\right)^{\frac{1}{2}} \qquad \text{for } -c \leq x \leq c \qquad \text{Equation 2.12}$$

The width of the central stuck region decreases with increasing tangential force until eventually slip occurs over the whole interface. This relationship between normal and frictional forces at sliding interfaces is a vital foundation for the study of fretting contacts, where displacements are sufficiently small that a region of a contact may remain stuck; the dominant *slip regime* in a fretting contact can have significant implications for the dominant mode of damage which can be summarised as follows:

- When displacement amplitude is sufficiently low, and normal load is sufficiently high, a central region of the contact remains stuck and fretting occurs in the *partial slip regime*. This gives rise to crack growth at the slip-stick-boundary, and as such the dominant mode of damage is *fretting fatigue*.
- As displacement amplitude is increased (or normal load is decreased), the slip annulus grows until eventually slip occurs over the whole contact area, termed the *gross slip regime*. In this regime, material is removed from the surface at a rate sufficient that significant crack growth is limited, and the dominant mode of damage is *fretting wear*.

As displacement amplitude is increased further, another transition occurs from fretting wear to reciprocating sliding, with estimates of this threshold displacement amplitude varying significantly in the literature; Vingsbo and Söderberg [5] reported this threshold displacement amplitude to lie between 150 – 300 μm, based on an analysis of reports in literature, noting that the transition is likely to be highly dependent on aspects of contact configuration that vary between experimental configurations such as geometry, material combination, ambient temperature etc.

2.1.3 Fretting loops

Hysteresis loops of fretting contacts (i.e. fretting loops) are generated by plotting tangential force (Q) against displacement (Δ), and enable important physical quantities of the system to be derived, such as the energy dissipated per cycle (E_d), the stiffness of the contact and test rig (S), and to differentiate the slip displacement at the interface ($2\delta^*$) from the overall applied displacement ($2\Delta^*$) in a fretting cycle. In their work on fretting contacts, Mindlin and Deresiewicz [13] observed symmetrical hysteresis loops, which would go on to become an important tool in the study of fretting wear. A schematic diagram of an ideal fretting loop in the gross slip regime is shown in Figure 2.3.

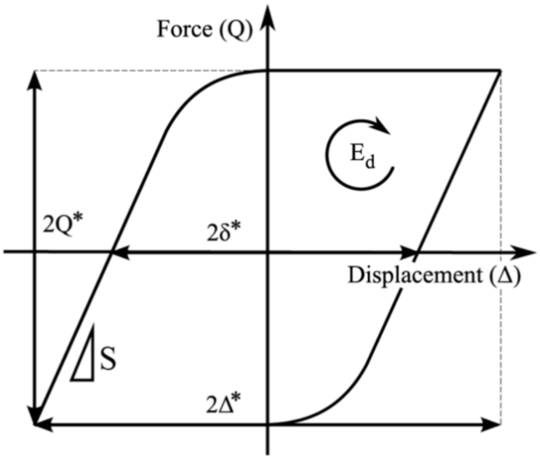

Figure 2.3. Example of a fretting loop exhibiting an idealised shape [14].

When a tangential force (Q) is applied to the interface, the specimen material and testing rig will deform elastically, and so there is a linear increase in displacement with applied tangential load; the slope of these regions is equal to the contact stiffness (S). When the applied tangential load is increased sufficiently that it can no longer be accommodated by elastic deformation, sliding occurs across the interface without any increase in load. The distance between the two points of intersection with the displacement axis (i.e. when tangential force is equal to zero) is equal to the distance slid over the course of the fretting cycle (2δ) taking into account the stiffness of the system, as opposed to the applied displacement amplitude ($2\Delta^*$).

The sliding regime can be readily identified from the shape of a fretting loop, for example the parallelogram shape of the fretting loop in Figure 2.3 indicates fretting in the gross slip regime, while an elliptical fretting loop (as shown in Figure 2.4) indicates fretting in the partial slip regime, as displacement remains dependent upon tangential load throughout the fretting cycle. A closed loop indicates that the contact is fully stuck, although the mechanics of interfacial slip (detailed in Section 2.1.2) indicate that such a regime cannot exist in practice when a tangential load is applied.

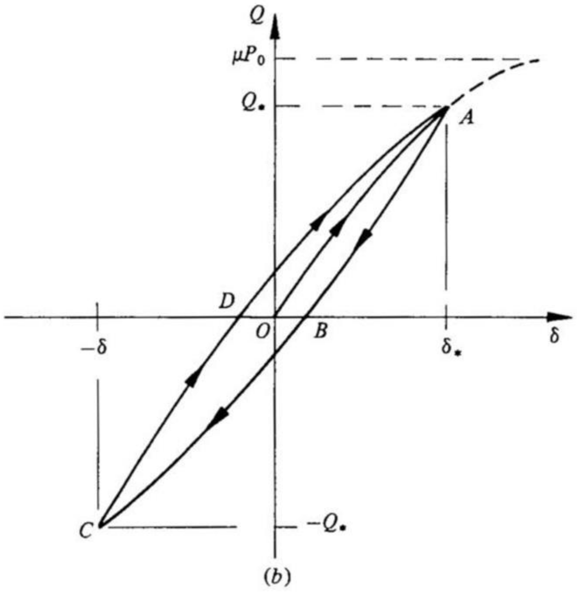

Figure 2.4. Example of an elliptical fretting loop, indicating that full sliding does not occur over the entire interface [11]

Fretting loops provide a useful visual representation of changes in tangential force throughout the displacement cycle, which can be used to interpret contact behaviour. Two types of behaviour commonly observed in fretting literature are (i) large force peaks at the ends of the fretting cycle; (ii) steadily increasing force throughout the cycle, resulting in an elongated, "hook-shaped" fretting loop. Examples of both types of fretting loop are illustrated in Figure 2.5.

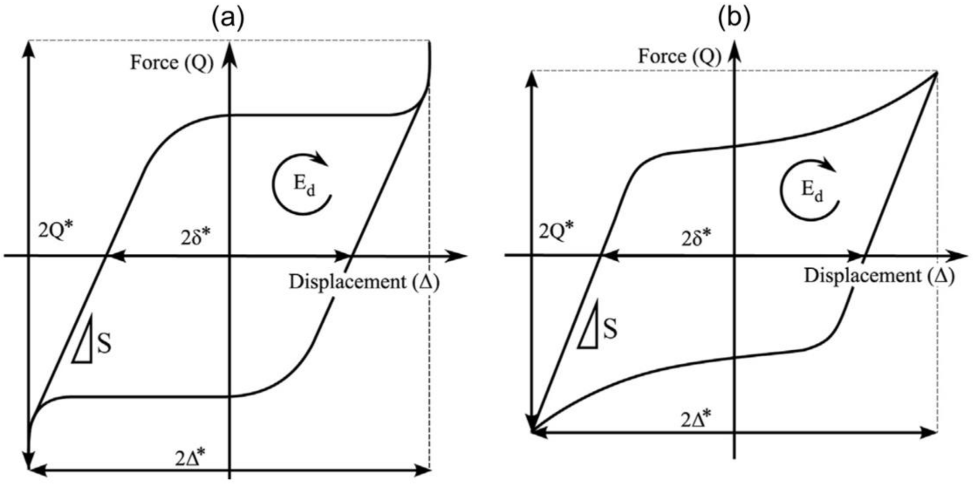

Figure 2.5. Examples of fretting loops exhibiting (a) tangential force peaks at ends of cycle; (b) steady increase in tangential force resulting in hook-shaped fretting loop [15].

Various explanations for these behaviours have been proposed; Fouvry et al. [16] proposed that end peaks in tangential force are the result of a *ploughing effect,* in which plastic deformation causes build-up of material at the edges of the scar, thereby increasing the force necessary to reach the required displacement. However, the ploughing effect does not explain hook shaped fretting loops, and as such it was proposed by Mulvihill et al. [17] that increases in tractional force occur due to the formation of local pit and peak features, the interaction of which increases the force necessary to reach the required displacement, thereby resulting in hook-shaped fretting loops. The diagrams in Figure 2.6 illustrate these effects (on an exaggerated scale).

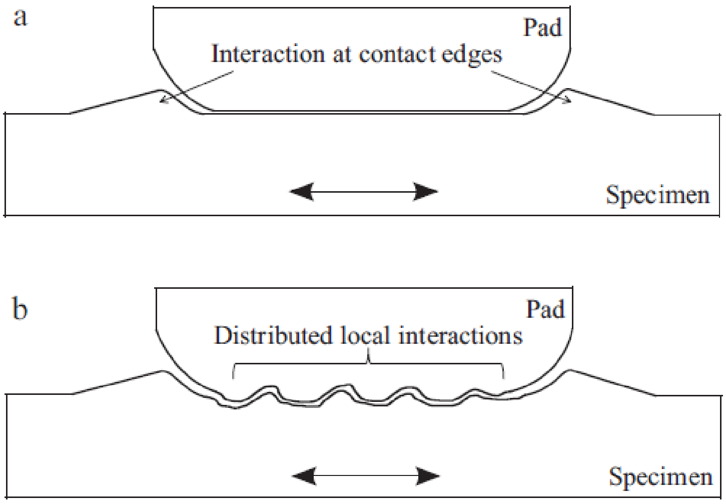

Figure 2.6. Diagram illustrating (on an exaggerated scale) the effect of (a) the ploughing effect; (b) local pit-peak features on friction as proposed by Mulvihill et al. [17].

Multiple fretting loops can be plotted together against a measure of test duration (e.g. number of cycles, elapsed time) to generate three-dimensional *fretting logs*, an example of which is shown in Figure 2.7, which can be used to assess the stability of a fretting test and identify the mixed fretting regime [18].

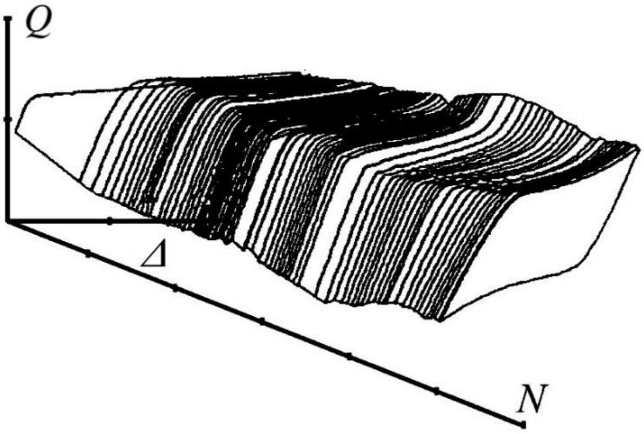

Figure 2.7. Example of a fretting log, a 3D plot of tangential force, displacement and number of cycles [19].

2.1.4 Coefficient of friction

Fretting loops enable the coefficient of friction in a laboratory test to be calculated, with several methods which may be used depending on the nature of the fretting cycle. When *Coulomb friction* dominates (i.e. no force peaks at the end of cycles and loop shape is similar to that in Figure 2.3), this is simply calculated as the ratio of the applied normal load and the tangential force at the ends of the cycle; alternatively the mean tangential force across the top edge of the loop may be used instead of that at the maximum displacement only. However, when non-Coulomb friction dominates (i.e. increases in tangential force result in end peaks or hook-shaped fretting loops as shown in Figure 2.5), the significant variation in tangential force across the cycle renders the conventional coefficient of friction unrepresentative of the true behaviour of the contact. Accordingly, alternative approaches to calculating coefficient of friction have been developed, such as the *energy coefficient of friction* proposed by Fouvry et al. [16], which is calculated as the ratio of the energy dissipated in the contact over one cycle (E_d) and the product of the applied load (P) and the distance slid over the cycle ($4\delta^*$) as follows:

$$\mu_E = \frac{E_d}{4\,\delta^*\,P} \qquad \text{Equation 2.13}$$

While the energy coefficient of friction is not impacted as significantly as the conventional coefficient of friction under conditions exhibiting non-Coulomb friction behaviour, it was observed by Hintikka et al. [20] that increases in tractional force (due either to ploughing or pit-peak interactions) may impact the overall energy dissipated in the system, and therefore both approaches are to some extent dependent upon the geometry of the wear scar. This was further demonstrated by Jin et al. [15], who also outlined a geometry-independent coefficient of friction (GICoF), in which coefficient of friction is taken to be equal to the ratio of tractional force and normal force at the point where the slope of the contact is equal to zero, described by $Q = S\Delta$, where Q is tractional force, S is contact stiffness and Δ is the applied displacement. The diagram in Figure 2.8 illustrates how this approach results in a coefficient that is independent of scar geometry (i.e. fretting loop shape), as the tangential force used to calculate the coefficient of friction (equal to the product of the stiffness and displacement in the middle of the displacement cycle) is the same regardless of whether the loop is an ideal parallelogram shape, or exhibits the variations in tangential force that are characteristic of non-Coulomb friction behaviour.

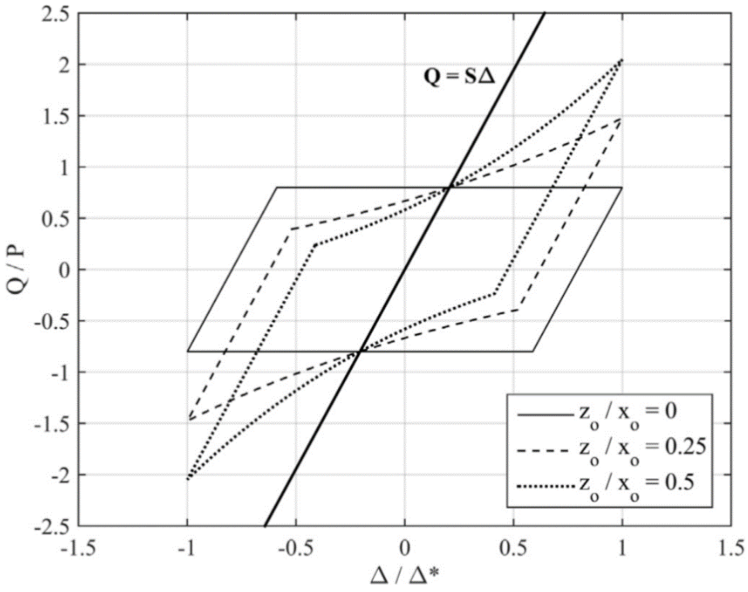

Figure 2.8. Comparison of fretting loops exhibiting varying degrees of tangential force increase as a result of scar geometry, from which the geometry-independent coefficient of friction can be derived [15].

Llavori et al. [21] reviewed approaches of quantifying friction, comparing four methods used in fretting literature by generating fretting loops using an applied "true" coefficient of friction of 0.8, and subsequently calculating coefficient of friction by each method; an example of this comparison is shown in Figure 2.9. It was observed that GICoF was the most accurate, followed by ECoF, with CoF (both mean and maximum tangential force methods) varying significantly from the "true" value of friction.

In the same work, an analysis of 163 recent papers was performed to identify the relative usage of the four techniques; of the 96 papers which specified the method used, it was observed that GICoF was used in the smallest proportion of papers (2%) compared to ECoF (21%) or the conventional CoF methods (30% maximum force; 7% mean force), with the authors attributing this to the relative novelty of GICoF compared to the other methods. However, the advantages of using GICoF as opposed to ECoF are difficult to determine from its current limited use in fretting literature, which also limits the possibility for comparing friction values reported in the literature.

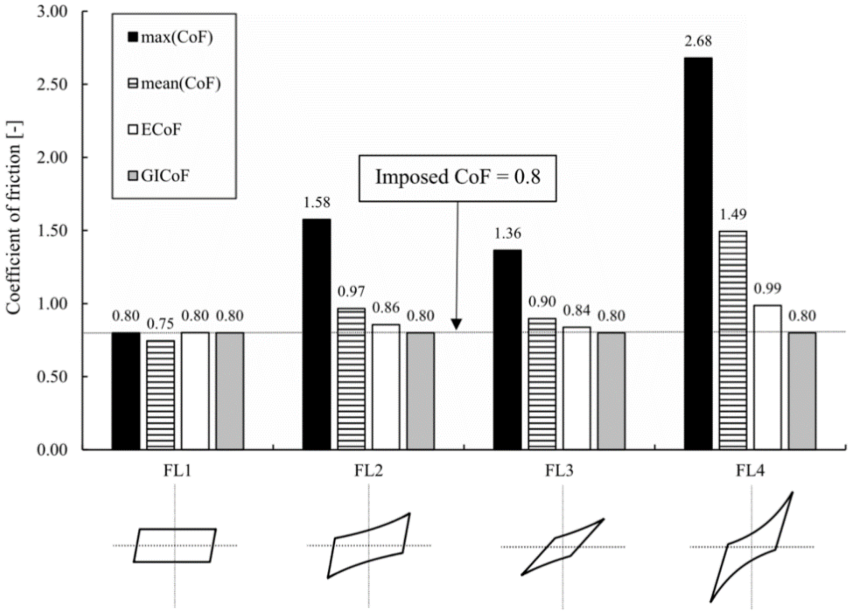

Figure 2.9. Comparison of techniques for calculating coefficient of friction for a range of fretting loop shapes, as presented by Llavori et al. [21].

2.2 Role of displacement amplitude

While displacement amplitude controls the operative sliding regime (detailed in Section 2.1.2) and hence whether degradation occurs primarily via fretting wear or fretting fatigue (at smaller amplitudes), or reciprocating sliding wear (at larger amplitudes), it also has a significant impact on the mechanisms of wear within the fretting wear regime. Processes such as ingress of active species to the contact (e.g. oxygen), the rate at which these are consumed in the formation of debris, and the flow of debris within and out of the contact are all significantly influenced by the sliding amplitude. Fouvry et al. [8] proposed that larger amplitudes may significantly enhance the rates at which oxygen penetrates the interface and oxide debris is ejected from the interface, by further opening the contact to the atmosphere (i.e. increasing the proportion of wear scar area that remains unexposed throughout the fretting cycle), as illustrated in the diagram in Figure 2.10.

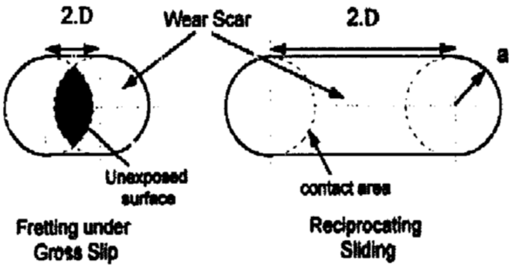

Figure 2.10. Diagram presented by Fouvry et al. [8] illustrating the effect of displacement amplitude on the area of contacts exposed to the atmosphere.

Another important way that displacement amplitude affects the mechanism of fretting wear is its effect on frictional power dissipation in the contact, i.e. the energy that is dissipated over the interface per unit time. Frictional power dissipation has a significant impact on the local temperature increase under a given set of fretting parameters, and is related to the coefficient of friction, slip displacement per cycle (four times the slip amplitude), normal load and fretting frequency, which for the type of contact configuration employed in thesis is described by the relationship described by Equation 2.14.

$$P_{fric} = \frac{dE_d}{dt} = \mu \cdot (4\delta^*) \cdot P \cdot f \qquad \text{Equation 2.14}$$

This section focuses on the impact of displacement amplitude on the rates and mechanisms of fretting wear which, while intrinsically linked, are examined separately for clarity. Reports of the impact of fretting test parameters on wear mechanisms may depend significantly on the experimental configurations employed, experimental design, and the assumptions adopted by individual authors in interpreting results (which may or may not be explicitly stated). Mechanisms of particle detachment and flow within contacts are explored further in Section 2.4.

2.2.1 Dependence of wear rate upon displacement amplitude

Reports regarding the dependence of wear rate (defined in terms of wear volume per unit distance slid or per unit dissipated energy) on displacement vary considerably across the literature, with larger displacement amplitudes being observed to correspond to higher wear rates by Vingsbo and Söderberg [5], Halliday and Hirst [22], Ohmae and Tsukizoe [9], Fouvry et al. [8,16,23], and more recently by Fantetti et al. [24] and Baydoun et al. [10,25]. Such a dependence is typically attributed to larger displacements inhibiting the formation of protective layers of oxide debris, namely by enhancing the rate at which debris particles are ejected from the contact, which is explored in further detail in the following section (Section 2.2.2).

A notable exception to reports of the dependence of wear rate upon displacement amplitude is the 2015 paper by Pearson and Shipway [26], in which it is argued that wear rate is in fact independent of slip amplitude; as part of this it was suggested that reports of a dependence in the literature up to that point may be attributed to two important factors that were overlooked in the original interpretation of experimental data, namely (i) measuring far-field displacement amplitude rather than slip amplitude at the interface; (ii) neglecting to consider a threshold dissipated energy below which wear does not occur. Figure 2.11 shows the original graph of wear volume plotted against dissipated energy presented by Pearson and Shipway [26], with the proposed displacement amplitude-independent wear rate represented by a straight line. It is important to note that for each displacement amplitude (with the exception of $\Delta^* = 100$ μm) the dataset includes wear data for three normal loads (ranging from 250 N to 650 N), which can be inferred from the energy dissipated at each respective displacement amplitude (i.e. higher normal load is associated with higher dissipated energy). However, taking into account the potential impact of normal load on the wear rates observed, it is not clear from this data alone whether wear rate is in fact independent of displacement amplitude over the range of conditions investigated; as such, the linear relationship proposed by Pearson and Shipway [26] must be weighed against evidence to the contrary presented in the aforementioned investigations reporting a dependence of wear rate upon displacement amplitude [5,8–10,22–25], and more information is required to understand the extent to which such a dependence does exist.

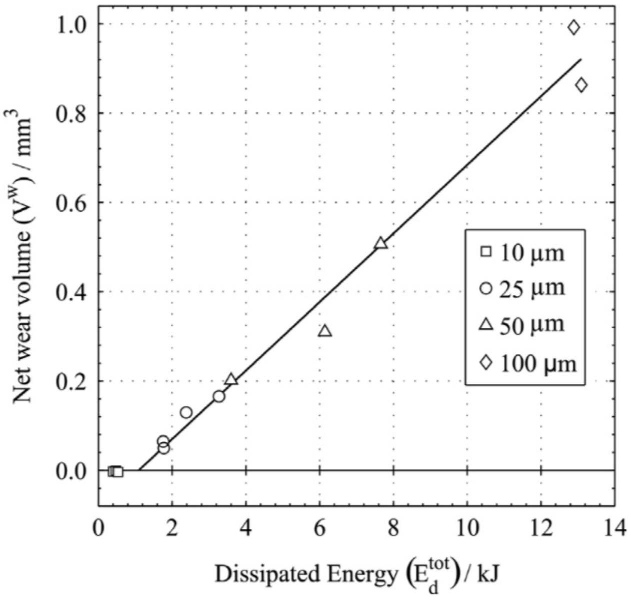

Figure 2.11. Plot of wear volume as a function of dissipated energy originally presented by Pearson and Shipway [26]; it was proposed that a single wear rate (i.e. the gradient of the straight line on this graph) adequately describes wear rate across the studied range of displacement amplitudes (*f* = 20 Hz; 10^5 cycles; *P* = 250 N-650 N).

While the experimental data presented by Pearson and Shipway [26] in support of wear rate being independent of displacement amplitude is limited, the points raised about potential misinterpretation of displacement effects in the literature are nonetheless valid, and highlight that further work is needed to better understand the effect of displacement amplitude on wear rates in fretting.

2.2.2 Impact on the flow of oxide debris particles and the formation of debris beds

In discussions around the dependence of wear rate upon displacement amplitude, the effect is frequently attributed to the impact of displacement amplitude on the formation of oxide debris beds, and the role of wear debris in fretting more broadly. By influencing factors such as the availability of oxygen at the interface to form oxide debris, the rate of asperity interactions and the temperature in the contact, changes in displacement amplitude set up complex interacting effects that are difficult to convolute; this is compounded by the inherent variation in observations reported in fretting literature due to differences in specimen geometry, materials and experimental design, among other things.

Experimental investigations into the role of displacement amplitude in fretting wear indicate that at larger displacement amplitudes, the formation of oxide debris beds is inhibited, with worn surfaces exhibiting a significant degree of adhesive wear at points of metal-to-metal contact [9,27,28]. This was observed by Ohmae and Tsukizoe [9], who also observed larger displacement amplitudes to result in a significant degree of plastic deformation of the substrate, with significant adhesive wear occurring simultaneously with extensive oxidative and abrasive wear.

A similar effect was observed by Warburton et al. [28], who proposed that the higher fretting velocity and rougher surfaces associated with larger displacement amplitudes mean that the oxides produced are swept more efficiently from the asperity sites where wear occurs, which was termed "debris migration".

In order to clarify two "points of general agreement" in the fretting literature, namely (i) that wear rates fall with distance, and (ii) that wear rates can increase dramatically above a critical threshold displacement amplitude, Aldham et al. [27] investigated the role of both displacement amplitude and overall slid distance. They proposed that investigating fretting up to very long test durations (of the order of hundreds of thousands to millions of fretting cycles) is important in quantifying the effects of parameters on the mechanisms of fretting, as the industrial applications in which fretting is observed typically experience a significantly greater number of cycles than are investigated in laboratory conditions, potentially leading to unrepresentative measurements. Moreover, the impact of the overall slip displacement in a fretting contact on the rates and mechanisms of wear are particularly relevant in studies of displacement amplitude where, depending on the design of experiments, larger displacement amplitudes increase the overall distance slid during the course of a fretting test, and as such may result in the misinterpretation of the effects of displacement amplitude on the development of wear.

As displacement amplitude increases frictional power dissipation it is therefore intuitive that larger displacement amplitudes might promote the coalescence of debris particles into compacted beds; however, as outlined above, increasing displacement amplitude is typically observed to have the opposite effect, with oxide debris beds becoming more sparse and the underlying metallic surfaces more exposed. Hayes and Shipway [32] demonstrated that, for the same set of test conditions, higher ambient temperatures were necessary to form stable protective debris beds, with this being attributed to a proposed increase in the rate of debris ejection from the contact at higher displacement amplitudes, requiring stronger cohesive forces between debris particles in the contact to sinter to form a glaze layer.

An enhanced rate of debris ejection was also proposed by Fouvry et al. [16] to cause the dependence of wear rate upon displacement amplitude reported in the same work, outlining a mechanism based on the energy required to generate wear debris and eject it from the interface. In this it was proposed that at larger sliding amplitudes, debris is ejected faster, and less energy is required to eject it, and as such a greater proportion of energy dissipated in fretting contributes to the formation of new wear particles. It is noted that this description requires the assumption that the rate of generation of new fretting debris depends upon the ejection of existing debris from the interface.

Fouvry et al. [8] observed that displacement amplitude has a significant impact on the shape of wear scars, with an enhanced tendency for wear scars to be W-shaped (i.e. with maximum wear near the contact borders and a minimum near the centre) at smaller amplitudes, and to become more U-shaped (i.e. with maximum wear at the centre of the scar) at larger displacements; W-shaped scars were observed in both partial and gross slip regimes (detailed in Section 2.1.2). W-shaped scars have been observed in the literature to consist either of (i) a build-up of primarily oxide debris in the centre of the scar, atop an otherwise U-shaped metal surface [8,23], or; (ii) a predominantly metallic central region of the scar exhibiting significant adhesive wear, with oxide-dominated regions nearer the contact edges (where oxygen availability is greater) exhibiting abrasive wear [10,25,29]. In both scenarios, U-shaped scars are proposed to occur when sufficient oxygen is available throughout the interface to form oxide debris that abrades the surface, resulting in higher wear rates relative to conditions that give rise to W-shaped scars.

In subsequent work by Fouvry et al. [23] investigating the impact of variable gross slip and partial slip conditions on fretting behaviour in Ti-6Al-4V contacts, it was reported that partial slip conditions result in a transition from W-shaped scars to U-shaped scars, due to accelerated fatigue damage of built up oxide layers developed in gross slip conditions, with cracking occurring either between the layer and the substrate or within the layer itself. These damaged oxide layers are not ejected during the fretting process, as there was very little debris ejection observed in the partial slip regime, rather the layers are weakened and subsequently removed by ultrasonic cleaning of specimens upon completion of fretting tests; the mechanism is illustrated in Figure 2.12. This highlights the need to consider the effect of post-test treatment of specimens (e.g. ultrasonic cleaning to remove loose debris) when examining images of worn surfaces, which may significantly affect the extent of wear and the appearance of wear scars.

Furthermore, it should be noted that the mechanism outlined by Fouvry et al. [23] was noted to be dependent upon the substrate material, and so while the effect of sliding amplitude on wear mechanism and wear rate observed for Ti-6Al-4V contacts may be assumed to apply for other adhesive wear materials (i.e. metals with higher surface energy values) such as aluminium alloys, the same cannot be assumed for materials such as steels.

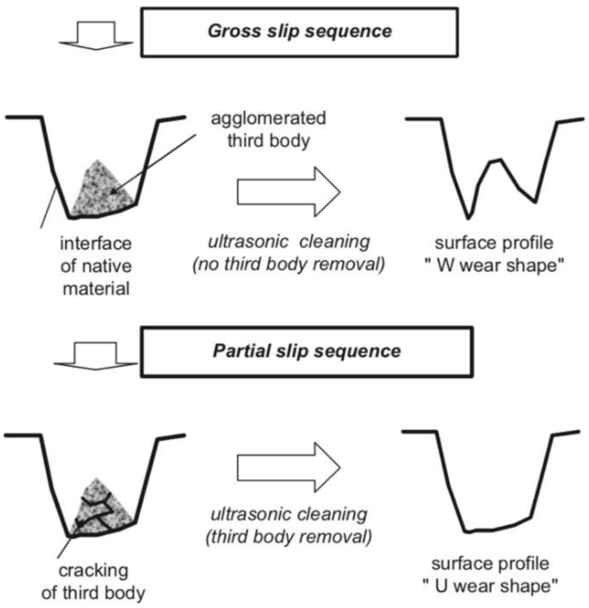

Figure 2.12. Diagram presented by Fouvry et al. [23] to illustrate a proposed mechanism of W- or U-shaped scar formation due to different slip regimes.

2.2.3 Impact on oxygen availability at the interface

Less commonly discussed in investigations of the role of displacement amplitude in fretting is its effect on the ingress of oxygen to the interface, a critical factor in the formation of oxide debris, the importance of which is highlighted in the previous section. As mentioned at the introduction to Section 2.2, a mechanism was proposed by Fouvry et al. [8] by which increasing displacement amplitude, by opening a fretting interface to the atmosphere enhances the rate of flow of oxygen into contacts. A similar concept was proposed in a later paper by Fouvry et al. [29], outlining a "contact oxygenation description of fretting" to describe the effect of parameters such as normal load (both constant and variable) and fretting frequency on fretting, but notably not displacement amplitude. However, exposing a greater area of a wearing surface to the atmosphere is not the only effect of increasing displacement amplitude relevant to contact oxygenation in fretting, as the greater frictional power dissipation at larger displacement amplitudes enhances the rate at which oxygen at the interface is consumed in the formation of oxide debris; as such, larger displacement amplitudes may result in more rapid depletion of interfacial oxygen which is not compensated for by the enhanced rate of oxygen ingress.

Warmuth et al. [30] investigated the exclusion of oxygen from fretting contacts over a range of displacement amplitudes and contact geometries (the latter being the primary focus of the work), observing that fretting contacts with more-conforming geometries (i.e. those with a larger physical width) tended to exclude oxygen from the interface, resulting in the development of metallic wear scars exhibiting significant subsurface damage. Moreover, whether more-conforming contacts developed such metallic wear scars (and the associated layers of damaged metal) was observed to be dependent on displacement amplitude; metallic scars exhibiting significant levels of subsurface damage were observed at larger displacement amplitude ($\Delta^* =$ 100 μm), whereas at smaller displacement amplitude ($\Delta^* = 25$ μm) no such damaged layer was observed, and instead an oxide debris bed was developed. This effect of displacement amplitude, namely that smaller displacement amplitudes promote an oxidative mechanism and larger displacement amplitudes are associated with an apparent restriction in oxygen ingress, contrasts with the mechanism proposed by Fouvry et al. [8] by which increasing displacement amplitude further opens the contact to the atmosphere and therefore results in easier oxygen penetration into a fretting interface. However, the findings of Warmuth et al. [30] do not necessarily indicate that increases in displacement amplitude restrict oxygen ingress, as the large contact sizes employed also act to restrict the flow of oxide debris out of the contact, and the reduced rate of debris ejection may play a significant role in the formation of oxide debris beds at smaller displacement amplitudes which in turn reduce the rate that oxygen is consumed in formation of fresh oxide debris. Furthermore, these contrasting observations highlight the complex nature of the effects of displacement amplitude on fretting mechanisms, and in particular how these may be significantly affected by other contact conditions.

Physical exclusion of oxygen from fretting contacts with more-conforming geometries has also been consistently observed by Baydoun and co-workers [10,25,31] in experimental investigations of the fretting behaviour of large flat-on-flat low alloy strength steel contacts.

However, Baydoun et al. [10] observed that increasing displacement amplitude did not greatly influence the overall mechanism of wear, despite an associated increase in wear rate; in this it was noted that the size of the so-called "adhesive zone" (a central metallic region surrounded by oxide-dominated regions nearer the edges of the wear scar) was independent of displacement amplitude. The authors acknowledged that this was an unexpected result due to the volume of experimental studies showing abrasion to dominate over adhesion as displacement is increased, and employed the aforementioned contact oxygenation concept to describe it; it was proposed that the independence of adhesive zone size on displacement amplitude is a result of two opposing effects balancing out, namely that (i) higher power dissipation increases the rate of oxygen consumption in the contact, and (ii) enhanced debris flow increases exposure of the contact to the atmosphere, and hence increases oxygen ingress.

2.2.4 Summary

In addition to controlling the operative slip regime under a given set of conditions, displacement amplitude has also been noted to affect the overall wear rate in fretting contacts, with this effect typically being attributed to the impact of sliding amplitude on the rate of formation of oxide debris, its flow within the contact and the rate at which it is ejected from the contact. The mechanisms proposed to explain this effect vary considerably across the literature, and there is no broad consensus on which of these is the most broadly applicable.

The uncertainty around the mechanism by which displacement amplitude affects the formation, flow and ejection of oxide debris is compounded by the wide range of specimen geometries and material combinations employed in different investigations of such effects in the literature; there is evidence in the literature that such variation likely has a significant effect on how changes in displacement amplitude affect wear mechanisms in fretting.

In the majority of cases, larger displacement amplitudes have been reported to result in increased wear rates, typically attributed to enhanced flow of oxide debris within and out of the contact.

However, evidence has been presented which suggests that wear rate is not in fact dependent upon displacement amplitude, or at the very least that such a dependence may be less significant than apparent in the literature, although further investigation is needed in this area to better understand this relationship.

Less commonly reported is the impact of displacement amplitude upon the flow of oxygen into fretting contacts, and how this effect relates to the rate of its consumption in the formation of oxide debris. Some workers investigating the role of displacement amplitude in fretting have reported that increasing displacement amplitude facilitates the flow of oxygen into contacts, increasing the availability of oxygen for the formation of oxide wear debris and hence contributing to an increase in the rate of wear; however, it has been commonly reported that wear scars formed at larger displacement amplitudes tend to be more metallic and exhibit significant adhesive wear, indicating that the enhanced rate of oxygen consumption at large displacement amplitudes may offset the easier flow of oxygen into the contact. In any case, there is no broad consensus around the role of displacement amplitude in oxygen ingress and consumption or the flow of oxide debris, and as such further investigation is required to better understand this important factor in the role of oxide debris in fretting contacts.

2.3 Role of fretting frequency

An important aspect of the role of displacement in fretting wear is its impact on the sliding velocity, which is observed to exert a significant influence on wear mechanisms via the associated impact on local temperature. Another factor which controls sliding velocity is fretting frequency, which therefore also acts upon some of the same processes as displacement amplitude, such as the flow of oxygen into the contact, its consumption in the formation of oxide debris, how debris particles behave within the contact and the rate at which they are ejected to play no further role in wear. However, the impact of fretting frequency on wear mechanisms in fretting differs from that of displacement amplitude in a few critical ways, namely (i) the area of the contact exposed to the atmosphere is not directly dependent upon fretting frequency; (ii) the overall slip displacement at a wearing interface is not directly affected by changes in frequency. The effects of frequency and displacement amplitude may therefore be expected to interact to a significant degree, although their respective influences on critical processes of fretting wear may compete as well as work together.

Indeed, the effect of fretting frequency on wear rate is widely observed to differ significantly from that of displacement amplitude, namely that where increases in displacement amplitude are generally observed to result in an increase in wear rate [5,8–10,22–25], increases in fretting frequency are observed to result in significantly reduced wear rates [10,25,29,32–34]. Such a reduction in wear rate with increasing fretting frequency was first noted by Feng and Uhlig [35], who investigated the fretting behaviour of mild steel specimens in atmospheric air and in an inert, nitrogen atmosphere. Conducting fretting tests over a range of frequencies in these different atmospheric conditions highlighted the significant chemical element of the frequency effect, as when fretting tests were conducted in the absence of oxygen, the effect of frequency on wear rate was observed to disappear. A reduction in wear rate with increasing fretting frequency has since been reported in numerous works employing a range of different materials and contact configurations [10,25,29,32–34], and is often attributed to the impact of frequency on the access of oxygen to the contact.

Changes in frequency inherently set up complex interactions between critical processes of fretting wear, as the change in sliding velocity results in an increase in local *temperature* (and hence the rates at which reactions take place), while reducing the *time* between asperity interactions and hence the time over which reactions can take place. Frequency also affects mechanical aspects of fretting contacts such as the imposed strain rate and the mechanical properties of the substrate (due to its impact on local temperature), which may also be in competition with one another; such an effect was noted by Bryggman and Söderberg [36], who observed that increasing frequency acts to soften the underlying bulk material due to the associated increase in local temperature, and that higher frequency also induces higher strain rates, which has the opposite effect. In the same work, however, it was noted that the effect of strain rate on shear flow stress (evaluated using an equation developed by Sundararajan [37]) is small over the range expected in fretting contacts, which exhibit relatively low sliding velocities relative to other forms of sliding wear.

The complex interactions between mechanical and chemical processes inherent to changes in fretting frequency highlight the difficulty associated with deconvoluting these processes in a laboratory environment, in which changes in input parameters may influence several processes simultaneously; however, experimental investigations into the role of fretting frequency, and how this depends upon other fretting parameters, provide valuable insight into the overall impact on the mechanism of fretting.

2.3.1 Impact on oxygen ingress and debris flow

As was highlighted by Feng and Uhlig [35], Van Peteghem et al. [33] observed a significant chemical effect of frequency in fretting of titanium alloy pairs; in this it was observed that, along with a reduction in wear rate, increasing frequency resulted in the formation of titanium nitride in the centre of wear scars, attributed by the authors to depletion of oxygen at the interface associated with the higher frequency. This was further supported by the observation that a greater degree of contact "opening" (i.e. reduction in normal force at the end of each fretting cycle) eliminated the formation of titanium nitride.

Warmuth et al. [34] investigated the fretting behaviour of cylinder-on-flat, high strength steel contacts, using cylinder specimens of various radii with fretting frequencies ranging from 20 Hz to 200 Hz. A reduction in wear rate of over 50% was observed for the less-conforming contact pairs, while a significantly lower reduction was observed in more-conforming pairs; Warmuth et al. [34] attributed this effect to the physically larger contacts excluding oxygen from the interface more effectively than contacts in which oxygen has to penetrate a shorter distance for there to be a sufficient concentration of oxygen present to form oxide debris throughout the interface. Metallic wear scars, i.e. those with sparse coverage by oxide debris and the presence of metallic debris near the centre of the contact, were observed at high frequency (200 Hz) with large physical contact size (i.e. conditions in which oxygen was most effectively excluded), with this contrasting with the predominantly oxide-based wear scars formed at low frequency (20 Hz). Cross-sections of specimens revealed that the oxygen-depleted wear scars formed in the more-conforming contacts at high frequency were associated with significant levels of subsurface damage developing, highlighting the protective role of oxide debris beds in preventing damaging adhesive contact between metallic surfaces. So-called "phenomenological fretting maps" were presented by Warmuth et al. [34] (shown in Figure 2.13) to illustrate how the observed response (namely whether metallic or oxide debris forms, and the extent of debris retention) vary over the examined range of test conditions. It can be seen that at low frequency, wear scars are predominantly oxide-dominated for both high and low contact conformity, as there is more time for oxygen to penetrate the interface, while at higher frequency, metallic debris forms due to a combination of the shorter time and larger distance for oxygen to penetrate the contact. Similarly for debris retention, both high contact conformity and high frequency enhance debris retention, the former due to the physical distance that debris must travel to be ejected from the contact, and the latter due to the greater contact temperature associated with higher frequencies promoting cohesion and sintering of debris particles.

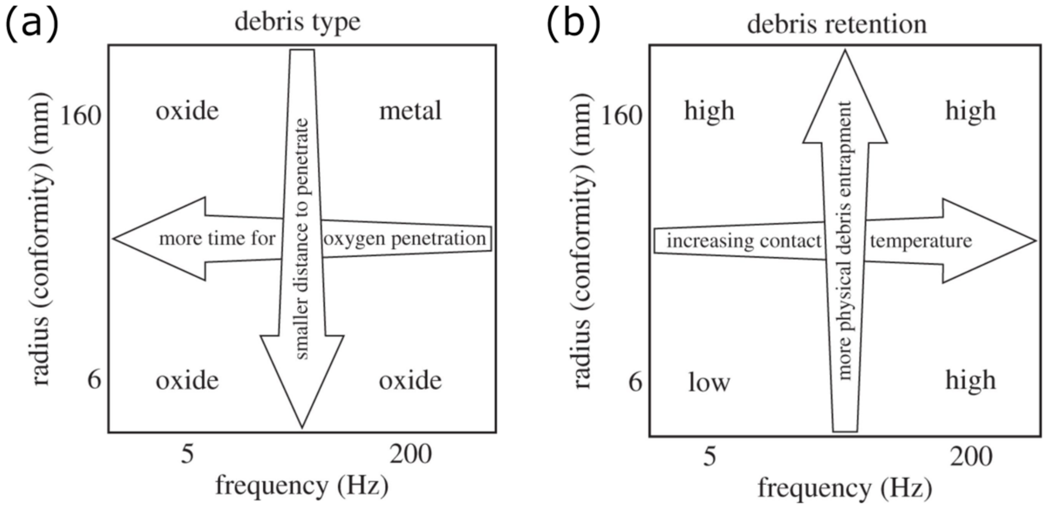

Figure 2.13. Phenomenological fretting maps, originally presented by Warmuth et al. [34], representing the effects of frequency and contact geometry on (a) debris type; (b) debris retention; the arrows superimposed on the map represent associated changes in fundamental processes which control oxygen penetration into the contact and the retention of debris within the contact.

In an investigation of the impact of contact size on fretting wear of steel pairs in a ball-on-flat configuration, Merhej and Fouvry [38] observed large contact widths not to result in oxygen exclusion, but rather to promote the formation of protective oxide beds, attributing this effect to the significantly restricted rate of ejection of oxide debris from the contact at greater contact widths. Physical exclusion of oxygen from cylinder-on-flat contacts with large cylinder radii was observed by Warmuth et al. [30], discussed in Section 2.2.3, which employed the same specimen configuration, material and range of contact geometries, although notably a higher normal load (450 N as opposed to 250 N), a relatively low fretting frequency (20 Hz) and a range of displacement amplitudes (ranging from 25 μm to 100 μm). In this it was observed that more-conforming specimen pairs developed wear scars that were more metallic in nature than those formed in less-conforming pairs, and that these metallic surfaces were associated with significant adhesive wear and hence the formation of a significantly damaged metallic subsurface layer. It is relevant to note that for the same sliding conditions and more-conforming contact configuration, oxygen exclusion *was* observed at low frequency by Warmuth et al. [30] under a normal load of 450 N, although *was not* observed under a normal load of 250 N [34], indicating that the rate of oxygen consumption (related to frictional power dissipation in the contact) is critical in the exclusion of oxygen from fretting contacts.

The important role of frequency in promoting the retention of debris in contacts was observed by Lemm et al. [39], who investigated fretting wear of steel pairs with a significant difference in hardness, and observed the formation of debris beds to be highly dependent on fretting frequency. A higher frequency of 50 Hz was observed to result in a regime in which oxide debris embedded in the softer surface, protecting it significantly from wear while abrading the opposing (harder) surface, which did not develop a coherent oxide debris bed; the preferential wear of the harder specimen of the pair seemingly conflicts with the relationship outlined by Archard [40] in which harder metals are significantly less vulnerable to wear than softer ones. Conversely, when frequency was reduced to 5 Hz (all other factors being equal), a protective debris bed did not form and both hard and soft bodies developed deep wear scars. This was proposed to be a result of the lower contact temperature at lower frequency, meaning that either (i) debris particles could not agglomerate sufficiently to form a bed due to sintering of particles (a temperature-dependent process) occurring at a reduced rate, (ii) reduced degree of thermal softening impedes the mechanical keying of debris into the surface, or a combination of the two.

Regarding the exclusion of oxygen from fretting contacts, a mechanism was proposed by Mary et al. [41], in an experimental study of the effect of contact pressure on fretting of a Ti-17 alloy against Cu-Ni-In interface, in which fretting parameters are noted to affect the rate of consumption of oxygen relative to the rate at which it can be replenished, and hence the dominance of oxygen-deficient "adhesive wear" or oxygen-sufficient "abrasive wear". It was observed that as pressure was increased, a transition in the operative wear mechanism occurred, from a conventional three-body abrasive mechanism at low temperature, marked by low wear rates, to a regime marked by a greater degree of transformation in the subsurface region of the titanium alloy punch and adhesion of this transformed material to the Cu-Ni-In surface, associated with higher wear rates. Previous work on fretting of titanium alloys by Mary et al. [42] found that the adhesive regime was also associated with the formation of titanium nitride (something also observed by Van Peteghem et al. [33]), attributed to a combination of what they termed "oxygen depletion" (alternatively "air distilling"), and severe plastic strains activating the nitriding process.

The oxygen exclusion theory of Mary et al. [41] was referred to in the work of Warmuth et al. [34], forming an important foundation of the oxygen exclusion theory proposed in the latter work. Fouvry and co-workers [10,25,29,31] subsequently combined the mechanisms of oxygen exclusion outlined by Mary et al. [41] and Warmuth et al. [34] in the development of a broader, more quantifiable description of the role of oxygen in fretting wear, found to apply to different materials (Ti-6Al-4V and low alloy steel) and contact geometries (cylinder-on-flat and large flat-on-flat contacts). In this the role of several parameters affecting oxygen flow and consumption were examined, including contact size, fretting frequency, displacement amplitude and normal load (both constant and variable); each of these parameters was observed to contribute to the exclusion of oxygen from the interface, and hence the development of oxygen-depleted "adhesive zones" at the centre of the contact, in which significant adhesive wear occurs. A feature associated with the metallic wear scars formed by the "adhesive" wear mechanism is the transfer of metal between specimens, resulting in the formation of W-shaped scars; as mentioned previously, Ti-6Al-4V is more prone to adhesive wear than steels, although oxygen-depleted, W-shaped wear scars have been observed to occur in both Ti-6Al-4V [29] and low alloy steel pairs [10,25].

This approach accounts for the flow of oxygen both into the contact (fundamental to the oxygen exclusion theory of Warmuth et al. [34]) and the rate at which it is consumed in the contact (based on the concept of "air distilling" outlined by Mary et al. [41,42]) in order to determine whether oxygen concentration in the contact is above the threshold concentration necessary to sustain an oxidative-abrasive wear mechanism; when oxygen concentration is below this threshold value, a transition to a wear mechanism characterised by significant metal-metal contact and adhesive transfer occurs. This interfacial oxygen concentration (IOC) concept – alternatively termed the contact oxygen concept (COC) – outlined by Fouvry et al. [29] was first applied to describe the effect of frequency and variable normal force in cylinder-on-flat Ti-6Al-4V contacts, and has since been expanded to describe similar mechanism changes in flat-on-flat steel pairs over a range of contact sizes, surface textures and test conditions [10,25]. A schematic diagram is presented in Figure 2.14 illustrates the core concept of the model, namely the proposed variation in dioxygen partial pressure (i.e. interfacial oxygen concentration) as a result of oxygen diffusing from the outer environment into the contact, some of which is consumed in the formation of oxide due to the fretting motion; if the dioxygen partial pressure exceeds a threshold value ($P_{O_2,th}$) then wear occurs via an oxidative-abrasive mechanism, while below this threshold wear occurs via an adhesive mechanism, characterised by metal-to-metal contact and transfer of material between surfaces.

The parameter d_O represents the distance from the edges of the contact to the edges of the so-called "adhesion zone" in which oxygen concentration is very limited; this parameter was demonstrated in previous work by Baydoun et al. [10] to be influenced by certain fretting parameters, namely sliding frequency and the contact pressure, while other parameters such as sliding amplitude, contact size and the number of fretting cycles appeared to have no substantial effect. As such, this model predicts that relatively high values of fretting frequency and contact pressure are associated with a tendency towards a greater degree of adhesive wear as opposed to an oxidative-abrasive mechanism, while the other parameters do not significantly affect this transition. These observations highlight the significant effect of frequency on contact oxygenation as part of a broader effect of fretting parameters on the rate of oxygen transport into the interface and its consumption in the formation of oxide, and it may therefore be expected that significant interaction occurs between the effects of parameters, particularly those having a significant effect on oxygen flow into the contact, or debris flow out of the contact.

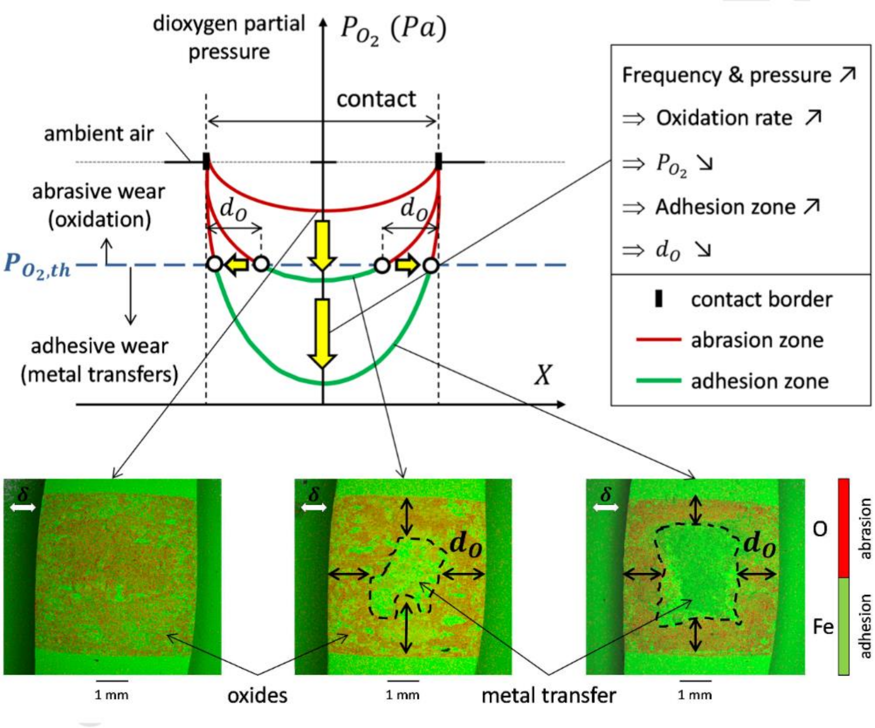

Figure 2.14. Diagram illustrating the core concept of the contact oxygenation description of wear developed by Fouvry and co-workers [29].

2.3.2 Interrelationship with ambient temperature

Besides atmospheric conditions, other parameters have been found to affect how wear rates and mechanisms in fretting respond to changes in frequency. Jin et al. [43] observed the effect of frequency to be affected by temperature, attributed to the combined effects of environmental temperature and local temperature increase due to frictional heating and the corresponding impact on the formation of a stable protective "glaze layer" of sintered wear debris. It was proposed that the greater temperature increase at higher frequencies raised local temperature above a critical point at which a glaze layer could form, at which point wear rate fell significantly. Jin et al. [43] also observed that the temperature at which a protective debris layer forms depends upon the fretting frequency, attributing this effect to the competing effects of rate of oxidation, time between asperity interactions and agglomeration of oxide debris; the diagram shown in

Figure 2.15 is an interaction diagram presented by Jin et al. [43] to clarify the proposed effects of frequency and environmental temperature on the formation of protective debris beds, highlighting the significant degree of interaction between the effects of the two parameters.

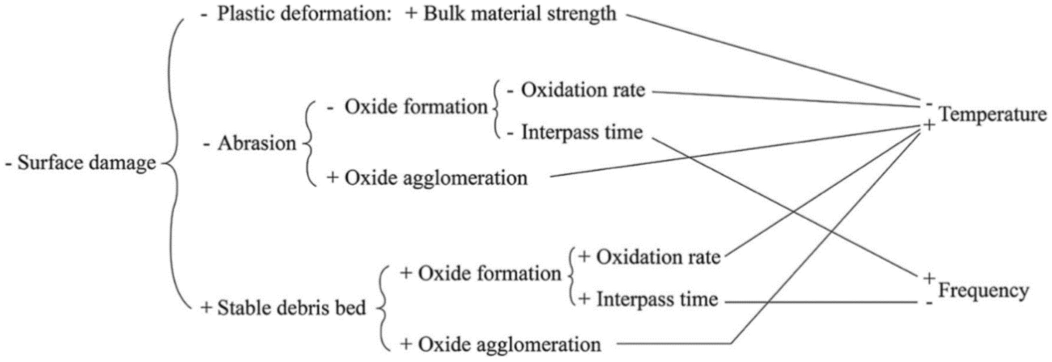

Figure 2.15. Interaction diagram linking experimental parameters with the resulting effects on wear behaviour as presented by Jin et al. [43]

Moreover, it is likely that other fretting test parameters will also exhibit significant interaction with the effect of fretting frequency, as the processes outlined in Figure 2.15 that are acted upon by both temperature and frequency are also affected by other parameters; for example, the “interpass time” is related to the sliding velocity, which is controlled by displacement amplitude as well as frequency. Furthermore, parameters such as displacement amplitude and normal load also influence power dissipation in the contact, and hence the local temperature, which may in turn contribute to interacting effects along the lines of those outlined in Figure 2.15.

2.3.3 Interrelationship with displacement amplitude

Strong evidence has been presented that demonstrates the effect of fretting frequency on wear mechanisms is dependent upon contact conditions affecting the formation and ejection of oxide debris, namely contact geometry and local temperature. As such, it is intuitive to consider whether the effect of frequency is also influenced by other fretting parameters which have a significant effect on debris behaviour, namely displacement amplitude. In light of this, it is surprising that reports in the literature regarding the effect of displacement amplitude on the role of frequency in fretting are relatively sparse; fretting frequency has been observed in some studies to have a greater impact on wear rate at larger displacement amplitudes, although the mechanism behind such an effect has not been clearly outlined.

In their paper clearly demonstrating the significant impact of fretting frequency on wear rates and mechanisms, and the importance of oxygen in this effect, Feng and Uhlig [35] also observed the effect of frequency on wear rate to be greater in fretting at larger displacement amplitudes than at smaller amplitudes; however, this observation was not explored in detail, and no mechanism was proposed to account for the effect. Further observations of a greater impact of fretting frequency on wear rate at larger displacement amplitudes were reported by Toth [32] and Vaessen et al. [44], although similarly to Feng and Uhlig [35] the effect was not explored in depth, and no clear explanation can be found to account for the effect.

One possible explanation is that the change in displacement amplitude is associated with a transition in the operative sliding regime, from partial slip to gross sliding or vice versa; in the partial slip regime, a region in the centre of the contact remains stuck throughout the fretting displacement cycle, and sliding in this regime is in turn associated with significantly lower wear rates in favour of fatigue cracking. Moreover, in the partial slip regime, the roles of oxygen ingress to the contact and that of oxide wear debris (most importantly the formation of debris beds) are diminished relative to fretting in the gross slip regime, and it is these processes which are thought to be critical to how changes in fretting frequency influence wear. As such it can be expected that the operative slip regime may have a significant effect on the role of frequency on wear mechanism. Indeed, Bryggman and Söderberg [36] reported that the critical displacement amplitude between regimes is itself affected by fretting frequency, becoming larger upon increasing frequency from 10 Hz to 100 Hz, and then decreasing as frequency was further increased from 100 Hz to 1000 Hz; the trend as frequency was further increased to 2000 Hz was dependent upon the specimen material, with the critical displacement amplitude continuing to fall for carbon steel pairs, while in stainless steel pairs appeared to increase again.

The observations discussed above indicate that the effect of frequency on the mechanism of fretting may be dependent upon the displacement amplitude, although further work is needed in this area to understand the extent to which displacement amplitude affects the role of frequency in fretting wear in the gross slip regime.

2.3.4 Material dependence

Some works have reported a material dependence of the frequency effect in fretting; Toth [26] observed that softer materials exhibited a greater reduction in wear rate with frequency than harder ones, attributed to a greater tendency for softer materials to exhibit adhesive wear, while Söderberg [29] observed that stainless steel pairs exhibit a more pronounced frequency effect than carbon steel pairs over the same conditions. However, Söderberg [29] observed an *increase* in wear with increasing frequency, contrasting with many other reports of frequency effects in which a reduction in wear rate is often observed, possibly due to the use of wear scar width as the primary metric of wear rate rather than the wear volume.

Both works provide an indication that the frequency effect may be material-dependent, although further work is required in this area to better understand this dependence. Improved understanding of how the frequency effect varies depending on material would be helpful in comparing reports on the frequency effect in the literature, which are often based on different experimental configurations.

2.3.5 Summary

Fretting frequency has been observed in several cases to result in a reduction in wear rate, with this effect being linked to its impact on the flow of oxygen into fretting contacts; the chemical element of the frequency effect is highlighted by evidence that in an inert environment frequency does not have a significant effect on wear rate.

The effect of frequency has been reported to be dependent upon multiple aspects of fretting contacts, such as contact geometry, environmental temperature and displacement amplitude, having potentially significant implications for the development of debris beds and subsurface damage in addition to wear rate. The interaction of fretting frequency with other parameters is typically attributed to the parameters acting upon the availability of oxygen at the fretting interface, as well as retention of oxide debris; however, these processes are not comprehensively understood, and further work is required to understand the ways in which frequency impacts the mechanisms of fretting wear and how this interacts with the effects of other parameters upon the same processes.

2.4 The role of wear debris

The effects of displacement amplitude and frequency on fretting mechanisms are due in significant part to the influence of these parameters on the flow of oxide debris in the contact; the same is true to some extent of all parameters affecting fretting due to the significant entrapment of debris in fretting contacts, which therefore plays a critical role in determining wear mechanisms. In light of this, a greater emphasis has been placed on the role of third bodies in wear over the past few decades; the critical role of debris in tribological interfaces (not limited to fretting contacts) was clearly articulated in 1984 by Maurice Godet [45], who proposed that wear can be considered through the flows of debris in the wear process, separating the processes of particle detachment from wear itself, which was redefined as debris ejected from the contact. In the following decades, Godet and co-workers [45–49] developed the "third body approach" based upon principles of lubrication theory (such as velocity accommodation and load carrying) being applied to the third bodies; third bodies may be either natural (e.g. wear debris) or artificial (e.g. lubricants supplied to the interface).

The flows of debris described by the third body approach were illustrated by Berthier et al. [50,51] via the concept of a "tribological circuit", shown in Figure 2.16; this representation provides a useful summary of the various ways in which debris may be considered to flow in tribological systems, and highlights the concept that material removal from the contact (i.e. wear) is only one of several flows of debris that occur in tribological systems. Third bodies are introduced to the system by (i) detachment of natural third bodies from first body surfaces (i.e. debris formation) and (ii) external supply of artificial third bodies (e.g. lubricants); in this thesis, only dry contacts are investigated, and so only the behaviour of natural third bodies (i.e. wear debris) is considered.

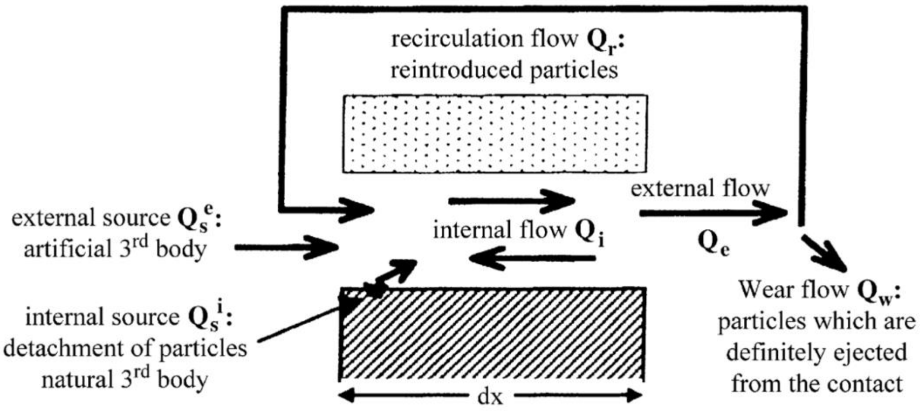

Figure 2.16. Schematic diagram illustrating the concept of the tribological circuit, as presented by Descartes and Berthier [52].

Several attempts have been made to measure the flow of wear debris directly using in-situ visualisation techniques, although due to the considerable technical challenge in observing behaviour in an area that is by definition not exposed to the surrounding environment, conclusions regarding typical metal-against-metal contacts must generally be inferred from a contact that is modified in some way and hence not representative of typical test configurations. A common approach is to conduct wear experiments in which one of the wearing bodies is made of an optically transparent material, such as sapphire or glass, and visually recording how debris flows during the test [52–58]. Such in-situ techniques allow the observer to physically see inside a wearing contact, giving an indication of how flows develop in real time, although a significant drawback is the modification of wear behaviour of the contact by the transparent body, potentially rendering the observations unrepresentative of true behaviour in fretting between two metallic bodies.

Despite not being well suited to direct observation of the flows of debris during fretting tests, more conventional experimental studies of fretting wear employing more representative materials (namely alloys employed in industrial applications in which fretting is typically observed) are therefore critical in improving understanding of the processes by which debris flows within contacts, coalesces to form beds or is expelled from the contact. In order to more effectively deconvolute the complex interacting processes of fretting, careful experimental design is required to interpret the role of specified parameters; examples regarding the effects of displacement amplitude and frequency were presented in the previous sections, in some cases investigated in relation to other relevant factors such as contact geometry and environmental temperature.

In this section, the nature of fretting debris and its role in modifying fretting contacts are explored to clarify the state of knowledge on this critical aspect of the wear process, so as to better understand the ways in which fretting parameters influence these mechanisms and, critically, the interactions between parameters which act upon common processes.

2.4.1 The nature of fretting debris particles

There have been many attempts over the past decades to characterise loose debris generated in fretting tests of steel specimens [3,10], particularly the composition and size of particles and to a lesser extent their morphology. In his book "Fretting Corrosion", published in 1972, Waterhouse [1] reviewed in detail the body of work investigating the nature of fretting debris, and as such only the most relevant aspects to this thesis will be covered in this section, namely dry fretting of steel pairs at room temperature.

While Waterhouse [1] highlighted significant dependence of debris particle composition on atmospheric conditions such as humidity and temperature, debris formed in fretting of steels at room temperature typically consists primarily of the high temperature iron oxide α-Fe_2O_3 (occurring naturally as the mineral haematite) with a proportion of metallic iron also being reported [3,10], although the relative proportions of oxide and metal are not well established. Other iron oxides (namely FeO and Fe_3O_4) have also been reported in fretting of steels at room temperature, albeit much less commonly [3,10,19]; however, it is worth noting that Fe_3O_4 is commonly observed in debris formed in fretting of steel pairs at elevated temperatures [25]. In vacuum or inert gas environments, the quantity of debris produced is much smaller than is formed in air (i.e. wear rate decreases significantly) and is entirely metallic in character [20].

Reports of debris particle size vary to a greater extent than those of composition, with the estimated diameter of fundamental particles ranging from approximately 0.01 μm [21] to several microns [22]. Moreover, general observations regarding the effects of sliding conditions on debris particle size are not readily discerned from these data, which may differ not only due to the different measurement techniques employed, but also the wide range of rigs, materials and conditions employed in the test programmes, and hence the nature of samples.

Of the various mechanisms by which particles can be detached from surfaces in different wear processes, material removal in fretting wear can broadly be described by three dominant mechanisms [22]:

1) Removal of metallic particles by grinding or tearing of welds. Subsequent oxidation does not play an important role in further wear.
2) Removal of metal particles which subsequently oxidise to form an abrasive powder. The abrasive action plays a significant role in further wear.
3) Direct oxidation of surfaces, with the continual removal of the oxide layer by the scraping of asperities from opposing surfaces.

Uhlig [59] proposed that particle detachment in fretting contacts involves both a *mechanical factor* and a *chemical factor*, the former involving the detachment of metallic particles by processes such as abrasion and adhesion which subsequently oxidise, and the latter relating primarily to the scraping off of oxide films formed continually on metallic surfaces exposed by fretting action (termed by Stott et al. [60] as "oxidation-scrape-oxidation"). The role of mechanical and chemical processes in the formation of debris particles is emphasised differently by different authors; for example, a predominantly oxidational (i.e. oxidation-scrape-oxidation) mechanism was favoured by Quinn [61,62], and Stott et al. [60], while others hold that debris is generated in the form of metallic particles which subsequently oxidise in the contact [47,63–68].

Halliday and Hirst [22] concluded that an oxidation-scrape-oxidation a mechanism could not be an controlling factor in fretting wear, with a similar conclusion being reached by Aldham et al. [27], who investigated fretting wear of steel pairs and reported that the softer ferrite phase was detached selectively to form debris rather than pearlite (the harder of the two) taking this as evidence that oxide debris is formed by the detachment and comminution of metallic particles, rather than the scraping off of thin oxide films. Further evidence that metallic particles can oxidise under tribological conditions to form oxide debris was provided by Pendlebury [66], who artificially supplied iron particles to a fretting interface which subsequently oxidised to become iron oxide (Fe_2O_3). In light of this, it appears likely that multiple distinct mechanisms of particle detachment occur concurrently in a fretting contact, as was proposed by Uhlig [59], with the relative roles of mechanical and chemical factors being dependent upon the fretting conditions, including specimen materials [69].

Archard and Hirst [70] identified two distinct wear regimes in unidirectional sliding wear, namely *mild wear*, which gives rise to predominantly oxide wear debris, and *severe wear,* in which large metallic fragments are formed and surfaces become highly damaged; it was noted that debris particle size depends significantly on which of the two regimes dominates, with mild wear producing oxide particles of the order of hundreds of angstroms, and severe wear resulting in metallic particles of the order of 100 μm. The implications of these findings for fretting contacts (as opposed to the unidirectional sliding configuration studied) were explored by Halliday and Hirst [22], who observed that the rates of wear and the appearance of worn surfaces in fretting even at large amplitudes were consistent with the mild wear regime outlined by Archard and Hirst [70]. In the same work, microscopic analysis of ejected debris particles indicated a wear regime closer to that of severe wear at large amplitudes (up to ~400 μm), with some large metallic particles up to 50 μm being observed among smaller oxide particles approximately 0.1 - 1 μm in diameter (potentially becoming as small as 100 Å).

In work on reciprocating sliding wear, Suh proposed the *delamination theory* of wear in which subsurface fatigue cracks grow parallel to the surface, connecting with surface cracks resulting in the removal of plate-like metallic particles. This was supported by Sproles and Duquette [71], who concluded that for the set of conditions studied, the delamination theory is the most suitable model for material removal in fretting. Waterhouse and Taylor [67] also reported that delamination occurs in fretting wear, proposing that fretting debris does not consist solely of surface films that are scraped off, but also contain some larger metallic particles which through comminution in the wear process become increasingly broken down and oxidised. However, Kayaba and Iwabuchi [72] proposed an alternative to the delamination theory to explain the formation of large flake-like particles in fretting, namely that these could be attributed to the stripping of oxide films from metal surfaces in fretting.

2.4.2 The source of fretting debris

In considering the process by which debris particles are formed in fretting, it is naturally relevant to consider the primary source of debris particles, namely the regions of the first body surfaces directly beneath the surface that are transformed by the loads and relative displacements imposed in fretting. Reports of significant transformation of the subsurface are common in fretting literature, with these transformed regions often exhibiting significantly different mechanical properties and chemical composition to that of the bulk material [73–76]; throughout much of the 20th century, such layers have commonly been referred to as “white layers” due to the appearance of steel samples prepared for metallographic observation using chemical etching, although in the 1990s a new term was adopted that more specifically refers to transformed layers formed in tribological systems, namely the tribologically transformed structure (TTS) [74,75,77]. Tribologically transformed structures have been observed in some form in a range of materials including steels [69,73,77–79], titanium alloys [69,73–75,77,80] and nickel-based superalloys [81–84], and exhibits certain common characteristics, namely an ultra-fine grain structure (with grains of the order of tens of nanometres in size), and hence distinct mechanical properties from the bulk material from which it is formed. Another commonly reported characteristic is that the TTS exhibits no significant difference in chemical composition from that of the bulk material [74,75], although some authors have reported TTS layers exhibiting an elevated oxygen concentration relative to the bulk material [84].

A diagram originally presented by Sauger et al. [74] illustrating the location of the TTS in relation to other layers formed in fretting is presented in Figure 2.17, and can be seen to lie between a layer of oxidised debris at the surface, and a region of plastically deformed bulk material between the TTS and the undeformed bulk material. Due to the fine grains developed in the TTS, the region is harder and more brittle than the bulk material, and it was proposed by Sauger et al. [74] that this region acts as the primary source of wear debris in fretting.

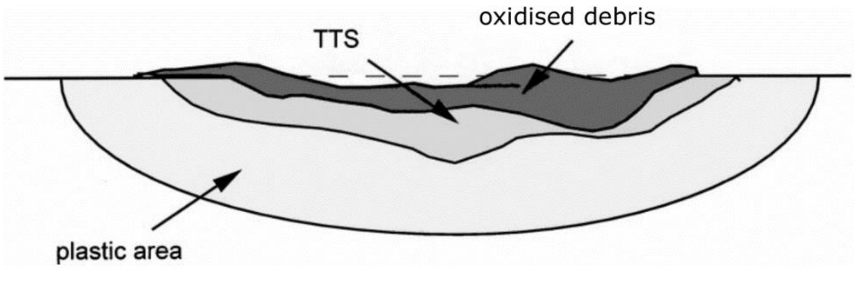

Figure 2.17. Diagram originally presented by Sauger et al. [74] illustrating the location of the TTS relative to other layers formed in fretting.

While the existence and characteristics of TTS are widely reported, the mechanism behind its formation is not well understood, with those proposed in the literature varying considerably. The initial works by Sauger and co-workers [74,75] attributed the formation of TTS to extensive plastic deformation and cyclic work-hardening of the subsurface region, resulting in recrystallization of the microstructure, which eventually becomes too brittle to accommodate the fretting motion and thus fracturing to form metallic wear particles which quickly oxidise in the contact.

Vizintin et al. [85] proposed a mechanism for TTS formation in steel pairs, which was attributed to a martensitic transformation caused by high local "flash" temperatures occurring at asperity tips followed by quenching by the substrate. It was proposed that the large width of the transformed layers relative to their depth was indicative of a temperature-based transformation, as the rapid dissipation of energy into the substrate results in the temperature of the surface being much higher than that found a few microns below the surface, thereby limiting the growth of the layer into substrate. However, this mechanism does not account for the observations of similar TTS layers in a wide range of metals; moreover, temperature rise due to frictional power dissipation in fretting is generally found to be lower than that required to cause the necessary martensitic transformation [86,87], so while rapid temperature cycling may play a role in the process, it appears unlikely that this is the sole mechanism responsible for TTS formation.

Rigney et al. [88] attributed TTS formation to high plastic strains resulting in material transfer, as the deformed structure developed in interfacial sliding is susceptible to shear instabilities, leading to transfer of metallic material between surfaces and mechanical mixing in the near surface region. The mechanical mixing mechanism described by Rigney et al. [88] requires the presence of a second phase, which in the case of homogeneous pairs must be formed through interaction with the environment (i.e. oxidation of metallic material). Sauger et al. [74] investigated the applicability of this mechanism to homogeneous titanium alloy contacts, and found that only traces of oxygen were present in the TTS, and hence proposed that interaction with the atmosphere does not play a primary role in its formation.

Significant material transfer has been observed to occur when surfaces are not separated by a third body layer, resulting in adhesion at metal-metal asperity junctions, with a striking example provided by Nurmi et al. [76], who studied the subsurface damage developed in large annular flat-on-flat contacts of a high strength steel over very large numbers of cycles (up to 3 million) and observed highly damaged and cracked metallic regions extending tens of micrometres into the surface. A subsequent paper by Juoksukangas et al. [89] employing the same contact configuration and test conditions observed similar layers of severely damaged metallic material to develop in different materials, namely structural steel and cast iron. Despite significant variation in the nature of the damaged layers in different regions of the surface and at different test conditions presented by Nurmi et al. [76], these extensively damaged layers were consistently observed to develop at “adhesion spots”, i.e. areas of the fretted surface where there is no oxide layer present to separate metal surfaces, hence resulting in damaging metal-to-metal contact. The damaged layers of metal were observed to exhibit significant porosity, and no significant differences in composition to the bulk material. Moreover, thick layers of oxidised metallic debris were observed atop the TTS layers in some cases, also exhibiting significant porosity, proposed to be formed by adhesive transfer of material between specimens, becoming oxidised in the process. These distinct types of transformed layers are broadly consistent with observations reported by Xin et al. [90] in an investigation of the fretting behaviour of a 304 stainless steel ball against a nickel alloy (690TT) flat. In this, two distinct layers of transformed metallic material were observed, namely (i) regions of near-identical composition to the bulk material, and (ii) regions exhibiting apparent adhesive transfer exhibiting slightly elevated oxygen concentration relative to the bulk material. These two types of transformed layers were classified as Type 1 and Type 2 TTS, the former having an altered composition to the bulk material, and the latter aligning with the more conventional definition (i.e. similar composition to the bulk material). Type 1 TTS was proposed to form through a process involving material transfer and mechanical mixing (resulting in exposure to the atmosphere), while Type 2 TTS was attributed to the more widely favoured mechanism of TTS formation by dynamic recrystallization.

The findings of Xin et al. [90] and Hintikka and co-workers [76,89,91] indicate that oxidation may play a more significant role in the formation of TTS (at least for certain material combinations) than was observed by Sauger et al. [74], which may be due to the investigations examining (i) different material combinations; (ii) different contact geometry; (iii) different sliding conditions, or some combination of the three. Moreover, it is likely that the mechanism of TTS formation varies between different materials and sliding conditions, and hence cannot be described by a single mechanism; such mechanisms therefore remain an important area for further investigation in order to better understand this important aspect of fretting wear.

2.4.3 Tribo-sintering and the formation of glaze layers

While reference is made in several works to the sintering of wear debris to form protective beds [34,39,43,92,93], how such sintering processes occur in tribological conditions remains an area of active investigation. It has been widely reported that at elevated temperatures, in both fretting and sliding wear, a critical temperature is reached at which wear rate falls sharply, remaining very low as temperature is increased further as a result of the formation of a stable, protective layer of sintered oxide debris, termed a "glaze layer" [43,72,92–100]. Glaze layers do not behave in the same way as the compacted oxide debris beds formed at lower temperatures, which are continuously formed and broken down, instead being formed by rapid sintering of debris particles (which occurs much faster at higher temperatures), and as such the layers formed are stable and do not break down. This has a profound impact on the wear mechanism, for when a glaze layer is present at the interface, the underlying metal is largely protected from the atmosphere and asperities of the opposing surface and transfer of species occurs primarily via diffusion through this stable layer [60,95,96,101,102].

The role of sintering in the formation of glaze layers was investigated by Kato and Komai [103], who artificially supplied nanometre-scale particles of oxides of several different metals to rubbing surfaces and observed that a protective bed formed after a shorter slip displacement as the size of supplied particles was reduced, suggesting a strong influence of particle size on debris bed formation. They termed the sintering of oxide particles in tribological conditions "tribo-sintering", highlighting the difference between this process and that of conventional sintering, in which high temperature and pressure are typically sustained for a prolonged period. In tribological interfaces, temperature and pressure are likely to be much more intermittent, as asperities pass over each other throughout the displacement cycle. Conventional sintering typically takes place at temperatures half that of the melting temperature of the material [104], much higher than the temperatures at which tribo-sintering has been observed [105]. It is not possible at present to clarify the reasons for this difference, as the temperatures and pressures may be highly localised and thus vary significantly.

In addition to observing the effect of particle size on tribo-sintering, Kato and Komai [103] also noted that the composition of debris has an impact on sintering, with less diffusive oxides not forming a stable layer under the conditions studied. More recently, Viat et al. [94] observed the formation of a stable debris layer to be dependent upon the auto-diffusion coefficients of the alloying elements present in the first bodies from which the debris is formed.

Glaze layers were observed to form at temperatures as low as 85°C in fretting of steel pairs by Pearson et al. [93], although it was shown by Hayes and Shipway [92] that greater temperatures were required to form a glaze layer when displacement amplitude was increased (all other factors being equal), indicating that for larger displacements a faster rate of sintering is required for particles to remain in the contact.

2.4.4 Summary

It has been clearly demonstrated over the past several decades that retained wear debris plays a critical role in determining the operative physical processes of various forms of sliding wear, with the various aspects of this role being clearly articulated in the "third body approach" outlined by Godet and co-workers in the 1980s and 1990s. The role of debris is particularly significant in fretting contacts, where displacements are small relative to overall contact size, resulting in significant entrapment of debris particles.

The primary source of fretting debris is thought to be the tribologically transformed structure (TTS) developed in the subsurface due to fretting loading; TTS has been widely observed to form in a range of metals, although there is not broad consensus on the mechanism(s) of its formation, or indeed what may be classified as "TTS". Some observers have noted two distinct types of TTS, namely (i) that formed from direct transformation of the bulk material, and (ii) material which has been transferred between specimens, becoming oxidised in the process; however, the latter does not align with the conventional definition of TTS and this remains an area for further investigation. The lack of clarity around the mechanisms of TTS formation necessitate further investigation of the nature of the tribologically transformed structure and the conditions of its formation.

The nature and behaviour of debris particles generated in fretting contacts is complex, and depends upon numerous mechanical and chemical factors that lead to significant variation between different contact configurations, although some key aspects of the role of debris reported in the literature may be summarised as follows:

- For fretting of metallic pairs (the sole consideration of this thesis), wear debris typically consists of oxides of the base metals, while a proportion of debris is metallic [1,106].

- Debris ejected from sliding contacts may be either predominantly oxide-based (indicative of a "mild" wear regime) or consist of larger metallic fragments (indicative of "severe" wear) – whether such regimes exist in fretting wear is not clearly understood.
- Numerous mechanisms of debris formation in fretting have been outlined, although which mechanisms operate under which conditions is not comprehensively understood, with it being likely that multiple mechanisms occur concurrently in a fretting contact under a given set of conditions; in all cases debris particles are subject to extensive deformation and elevated temperatures in the contact.
- Due to the significant degree of debris retention in fretting contacts, retained debris plays a significant role in the wear process; this may be to mitigate wear (acting as a solid lubricant to separate surfaces) or exacerbate it (by acting as abrasives due to the high hardness of oxide relative to that of the metal bodies in contact).
- Whether oxide debris particles coalesce to formation coherent layers (i.e. debris beds) has a significant effect on the extent of damage that occurs due to fretting motion, and high levels of adhesive transfer and damage in the bulk metal can occur if an oxide debris layer is not present to separate metallic surfaces in fretting.
- There are numerous reports in the literature of oxide debris sintering to form stable protective "glaze layers" which accommodate the relative displacements at a fretting interface and result in drastically reduced wear rates; the sintering of debris to form glaze layers has been observed to depend upon fretting parameters and material properties, although further work is needed to better understand the sintering of debris particles and the formation of debris beds.

2.5 Modelling the role of debris in fretting wear

The prevalence of fretting phenomena in numerous industrial applications, along with the severe consequences that may arise from excessive wear to components in-service has naturally led to an in interest in the development of models used to optimise designs to minimise fretting damage, and for accurate lifing of components. However, as has been outlined in this review, fretting wear involves complex interactions between mechanical and chemical processes which depend on numerous factors, and therefore developing generic models capable of accurately modelling fretting wear (as well as other forms of sliding wear) in a wide range of contact configurations is a significant technical challenge. Meng and Ludema [2] reviewed the various wear laws (i.e. empirical models for the prediction of wear in tribological systems) proposed in the literature up to 1995, and found that despite numerous models being proposed, there was generally very little agreement between them. As such, this section does not include a comprehensive review of wear laws proposed in fretting literature, but rather focuses on efforts to develop models based more in the fundamental physical processes of fretting, most notably the role of retained debris, and hence represent steps towards improved generic fretting models.

2.5.1 The Archard wear equation

Arguably the most prevalent model used for prediction of wear in fretting is that proposed by Archard [40], which relates wear rate (wear volume per unit slid distance) to the normal load and indentation hardness of the surface material in a specimen pair. It was Burwell and Strang [107] who first proposed a relationship between wear volume and sliding conditions in which wear volume is directly proportional to sliding distance and normal load, and inversely proportional to the hardness of the softer material; based on the same principles, Archard [40] developed a simple and effective wear law, supposing that wear is dependent on the *real* area of contact, as opposed to the *nominal* area of contact, and in turn that while every asperity contributes to friction, only a proportion give rise to wear particles. By assuming perfect plasticity of asperity contacts, the ratio of normal load to the hardness of the softer material can be used to estimate the real area of contact under a given set of conditions, and hence be used to predict wear volume. Summing over the whole contact area and combining constants gives an expression for wear rate (volume of material removed per unit distance slid) in terms of normal load, hardness of the softer material and a dimensionless wear coefficient. The resulting equation, presented in Equation 2.15, is the only dimensionally correct relationship possible between normal load, hardness and wear rate when the previously outlined assumptions are taken.

$$\frac{Q}{S} = K\frac{W}{H} \qquad \text{Equation 2.15}$$

Where Q is the wear volume, S is distance slid, W is the applied normal load, H is the hardness of the softer material and K is the dimensionless wear coefficient, which is assumed constant throughout the test and which must be determined experimentally.

The Archard wear equation is particularly convenient as a predictive tool due to the ready availability of its inputs and the robustness of its underlying assumptions, although the use of a constant wear coefficient is a significant limitation of the model in situations where friction varies throughout the test. Fouvry et al. [80] proposed an alternative approach in which the wear coefficient is derived using the dissipated energy rather than the slid distance, thereby significantly improving upon one of the major weaknesses of the Archard model.

Both the Archard wear equation and energy wear formulation derived from it are readily modified to be implemented in time-marching numerical models, such as finite element [12,108–113] and boundary element [114] models; in such models, a modified version of the Archard equation is typically used in which wear depth is calculated as opposed to wear volume, allowing for the extent of surface recession (i.e. wear) to be calculated incrementally at each point across the contacting surfaces. These efforts highlight a key advantage of an Archard-type approach to modelling, namely that wear can be predicted reliably and with relatively low computational cost; however, the accuracy of such numerical models is inherently limited by their reliance on the physical accuracy of the underlying model, which involves a wear coefficient that must be derived from experimental data (and is therefore not necessarily representative of wear behaviour in the conditions modelled); moreover, the Archard equation contains no terms relating to the role of retained wear debris in the development of wear, which has been highlighted throughout this review as a critical consideration in fretting wear, further impacting the physical accuracy of wear predictions.

2.5.2 Incorporating the role of retained debris

It is important to note that the wear equation outlined by Archard [40] was originally derived for sliding wear, in which wear debris is more readily ejected and hence plays a diminished role relative to that observed in fretting contacts; consequently, the Archard wear equation (and wear laws derived from it such as the energy wear law developed by Fouvry et al. [80]) are suited to the prediction of the rate of *formation* of debris particles, but contain no terms to account for their *retention* within the contact, and therefore do not model the rate of *ejection* of debris from contacts to be distinct from the rate of its formation.

Quinn [61,62] modified an Archard-type approach assuming a different mechanism of debris particle formation, namely that wear occurs in the "mild" regime outlined by Archard and Hirst [70], using this as the basis of an "oxidational wear" model for sliding wear of alloys. As part of this, the Archard wear coefficient, K was modified to incorporate terms relating to debris formation by oxidation of nascent metal surfaces in addition to the abrasive mechanism assumed in the Archard model, updating its definition in the original Archard equation as the probability that an asperity interaction gives rise to a wear particle; instead, K is related to the thickness of the oxide film formed in a cycle, and assumes that upon reaching a critical thickness the films will detach to form particles. This improves the performance of an Archard-type formulation when the role of oxidation is enhanced, such as under elevated temperature conditions, although is still constrained by some of the same problems as the Archard equation, most notably the assumption that all particles are ejected immediately upon their formation, and hence does not address the gap in modelling the role of debris retained in the contact. Furthermore, the oxidational wear model is constrained by reliance on quantities that are not readily determined experimentally, such as the temperature rise in sliding contact and the activation energy of oxidation, which are likely to differ significantly between static and tribological conditions.

More recently, Dréano et al. [115] outlined a so-called "tribo-oxidation abrasive wear model", extending the Archard equation to incorporate the impact of test conditions on the rate of oxidation of surfaces, and hence predict wear rates more reliably than the Archard equation alone. Similar to the approach taken by Quinn [62], the model of Dréano et al. [115] assumes that particles are formed by an "oxidational" mechanism (i.e. mild wear), and that the Archard wear coefficient is proportional to the oxide thickness. It was noted that the wear behaviour was observed be highly dependent on the environmental temperature, and as such a modified version of the model was developed [116], capable of modelling the impact of the formation of a glaze layer at high temperature; in this updated approach, the oxidational model was combined with the energy wear formulation of Fouvry et al. [80] (as opposed to the Archard equation employed in the previous version of the model intended for use at low to medium temperatures), and a "sintering parameter" was introduced, which when above a critical value results in all further wear ceasing, thereby simulating the role of a glaze layer forming in the contact due to sintering of debris particles. The incorporation of debris sintering into a predictive model by Dréano et al. [116] represents a useful step forward in the modelling the role of *retained* debris in modifying fretting contacts, in addition to updating the wear coefficient to model particle formation.

Numerical models using an Archard-type approach have been developed to account for the presence of a debris layer at the interface having distinct mechanical properties to the first bodies, which serves to modify contact pressure and hence simulate the presence of a third body layer [109,117–120]. However, in these models, wear is still calculated using the Archard equation (or the functionally equivalent energy wear formulation) and are thus still constrained by the accuracy of the Archard wear coefficient. Attempts have also been made to model the role of debris in fretting contacts by directly modelling individual debris particles, specifying material properties and interactions between particles, such as by discrete element modelling [121–124] or a combined finite-discrete element modelling [125–127]; however, the high computational cost associated with modelling particles with realistic sizes and accurately capturing the complex interactions between particles present a significant barrier to the applicability of such models for predictive purposes. Likewise, molecular dynamics models have been developed capable of simulating mechanisms of debris particle detachment such as adhesive wear [128–133], although due to their very high computational cost these models are at present only viable for research into the fundamental mechanisms of wear as opposed to being used for wear prediction in industrial applications.

While modelling the formation, flow and ejection of debris at the particle- or asperity-level via a numerical approach can be seen from the works mentioned above to be a computationally resource-intensive process, the effect of these processes on wear rates may be modelled on the scale of the whole contact using an analytical approach. The value of such an analytical approach was demonstrated by Zhu et al. [134], who applied the principles of the third body approach to develop a model in which it was argued that the expulsion of debris from the contact is dependent upon the physical size of the interface, and this in turn affects the operative mechanism of wear. This was justified by the observation that wear scars formed in fretting of more-conforming contacts (i.e. those with a large cylinder radius and hence large initial contact size) exhibited significant adhesive wear for the first several hundred thousand cycles of a test (a finding also reported by Warmuth et al. [30]), but as tests progressed these contacts wore to become predominantly oxide-based. This was attributed to oxide debris accumulating in the contact, reducing the instantaneous wear rate such that the rate of oxygen flow to the interface (restricted by the large contact size) is sufficient to sustain the formation of oxide debris and thus prevent adhesive wear.

Accordingly, a model was outlined in which the operative wear mechanism and hence the overall wear rate is controlled by either the formation or ejection of oxide debris, whichever of these processes is slowest; due to the proposed dependence of debris ejection upon contact size, which of these processes is rate-determining may change over the course of a test. This relationship is illustrated schematically in Figure 2.18, in which the rates of debris formation and ejection are shown as a function of wear scar width, and the overall wear rate is controlled by the lowest of the two lines (i.e. the slowest of the two rates).

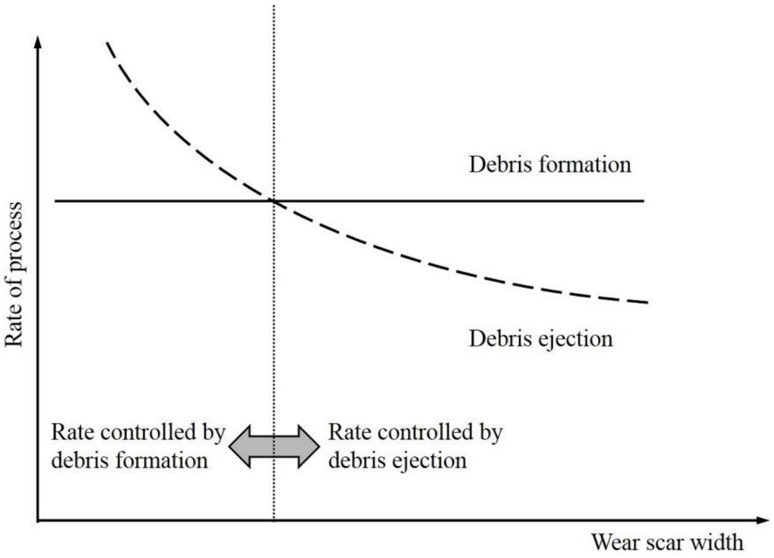

Figure 2.18. Schematic diagram originally presented by Zhu et al. [134] illustrating the proposed dependence of wear rate upon the relative rates of debris formation and ejection with increasing wear scar width; it was proposed that wear rate is controlled by whichever of the two processes is rate-determining (i.e. the lower of the two lines) at a given scar width.

A critical aspect of this model was the observation that the wear volume in a cylinder-on-flat configuration can be accurately predicted using a geometric relationship directly relating the wear volume to the contact width, namely the volume of intersection of the two specimens, as illustrated in Figure 2.19. Using the same constants for both more-conforming and less-conforming geometries, the evolution of wear rate (defined as wear volume per unit energy) predicted using this model was observed to agree well with experimental data for both geometries over a very large range of test durations, from 5000 to 5 million cycles.

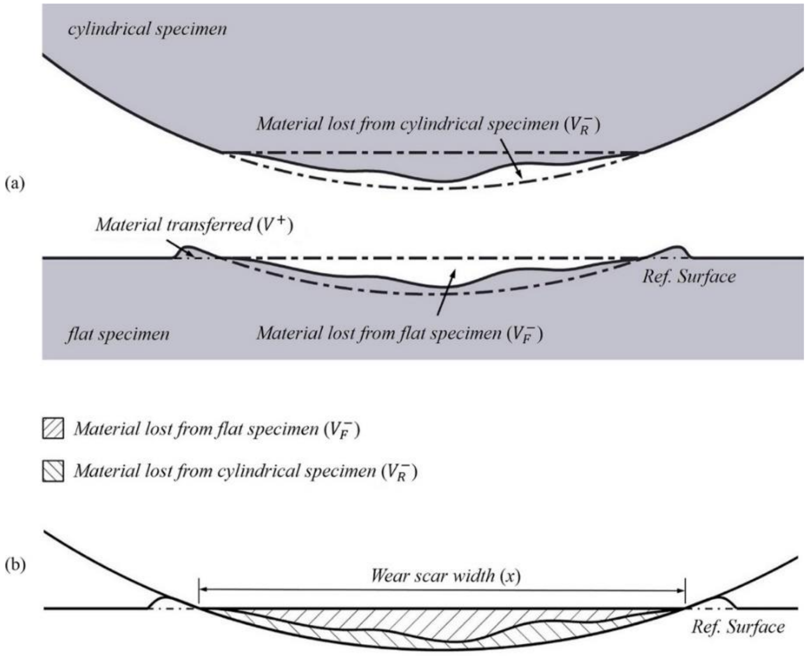

Figure 2.19. Diagram originally presented by Zhu et al. [134] illustrating the proposed relationship between wear scar width and wear volume in a cylinder-on-flat specimen configuration.

The validity of such a model, in which wear rate is determined by the relative rates of internal processes, which in turn are dependent on the physical size of the contact, has significant implications for predictive modelling of fretting wear, particularly in non-conforming contact configurations, in which the size of contacts increases as wear proceeds. The dependence of wear mechanism (and hence wear rate) on contact size suggests that the relative rates of rate-determining processes may vary considerably throughout the duration of a test, which must therefore be taken into account if wear rate is to be predicted accurately.

2.5.3 Modelling oxygen exclusion from the interface

As oxygen plays a critical role in sustaining an abrasive wear mechanism it has been, sliding parameters such as fretting frequency and displacement amplitude can have a significant effect on the availability of oxygen at the fretting interface, and hence the formation of oxide which is critical to the development of wear. In the previous section, attempts to incorporate the role of oxidation in wear of metals were discussed, such as the models of Quinn et al. [61,62] and Dréano et al. [115,116], both of which incorporate the role of oxygenation primarily through the impact of fretting conditions on local temperature, which in turn affects the rate at which oxide films grow on surfaces, which in turn can be used to predict wear volumes. However, neither of these models are able to account for the impact of test conditions of the *depletion* of oxygen at the interface which has been noted experimentally to reduce wear rates.

A model developed by Baydoun et al. [31] has sought to address this, namely by modelling oxygen flow into fretting contacts through debris layers, which are assumed to be porous, powdery structures through which the flow of oxygen can be modelled using an advection-dispersion-reaction (ADR) approach. However, the ADR approach is constrained by the lack of reliable data on the physical characteristics of debris beds, which must therefore be inferred from measurements of oxide layers in static oxidation and bulk quantities of the relevant oxides. Moreover, this modelling approach has not yet been applied to predict the impact of restricted oxygen transport on wear rates. Despite the challenges associated with modelling such complex processes, the modelling efforts of Baydoun and co-workers [10,25,31] serve to highlight the potential benefits to quantitative predictive models to be gained in developing understanding of the role of wear debris in fretting, namely the conditions influencing its formation and flow within contacts, and whether debris is retained in the contact in the form of compacted debris beds or is ultimately ejected from the contact to play no further role in the wear process. Moreover, the development of more physics-based models, that is to say models with reduced reliance on fitting constants used to align empirical models with data from laboratory experiments, is an important step towards modelling the complex interacting processes of fretting wear, and as such remains an important area for future work.

2.6 Summary

Fretting wear is a complex process that is influenced by many factors, with complex interdependencies between both mechanical and chemical processes, and as such much remains to be learned despite the large body of research dedicated to better understanding the processes of fretting since it was first recognised in the early 20th century.

While the effects of many parameters in fretting are well understood individually, how these effects interact with one another can be difficult to deconvolute due to the intricacies of the operative processes such as debris bed formation. The dependence of important processes on factors that vary widely in literature (e.g. contact configuration and specimen material) presents a barrier to a unified understanding of fretting mechanisms and hence widely applicable predictive models. The principles outlined in the "third body approach" of Godet and co-workers provide a useful framework for approaching fretting problems, namely that wear can effectively be considered solely through flows of wear debris.

Displacement amplitude has been noted to have an influence on both oxygen ingress and debris ejection, although some aspects of the role of displacement amplitude remain unclear, with seemingly contradictory results being found in the literature.

Fretting frequency has a significant effect on both mechanical and chemical aspects of fretting wear, having a significant impact on both the temperature generated due to frictional power dissipation and time over which processes such as oxygen ingress and debris sintering can occur.

Both frequency and displacement amplitude have been noted to have a significant impact on the development of debris beds, and there are some limited reports of an interaction between the two parameters, although the mechanism for this has not been explored in detail.

In this thesis, the interacting effects of frequency and displacement amplitude in fretting of a high strength steel are investigated by examining changes in the nature of wear scars and ejected debris resulting from changes in these parameters. The processes involved in the formation of debris beds are explored in detail in order to better understand the complex and competing influences these parameters have on damage and degradation in fretting. It will also be demonstrated that deconvoluting these interactions can aid in the development of phenomenologically consistent predictive models based on fundamental physical principles.

Chapter 3

Experimental methodology

3.1 Specimens

Specimens blanks were machined from a high strength steel (BS S132), and subsequently heat treated using a commercially relevant heat treatment cycle that has been outlined in previous work [135]. The blanks were heated to 940 °C and held for 45 minutes, after which they were oil quenched. Subsequently, they were tempered at 570 °C for 120 minutes and finally air cooled. The composition of the steel, and its mechanical properties after the applied heat treatment are listed in Table 3.1 and Table 3.2, respectively.

Table 3.1. Composition of BS S132 [135]

C	Si	Mn	P	Cr	Mo	Ni	V	Fe
0.35-0.43	0.1-0.35	0.4-0.7	<0.007	<3.0-3.5	0.8-1.1	<0.3	0.15-0.25	Balance

Table 3.2. Mechanical properties of BS S132 [136]

σ_y / MPa	σ_{ut} / MPa	HV30	E / GPa	v
1247	1697	485 ± 10	206.8	0.28

After heat treatment, the blanks were machined to their final dimensions, machining all surfaces to ensure that the outer decarburised layer developed during heat treatment is removed and the properties of the material are consistent with those listed in Table 3.2.

Two specimen geometries were machined, to be arranged in a cylinder-on-flat configuration, shown in Figure 3.1: (i) flat specimens with a width of 10 mm; (ii) cylinder specimens with a radius of 6 mm. Cylinder and flat specimens were machined to a surface roughness (Ra) of 0.4 – 0.7 μm and 0.1 – 0.3 μm respectively, and both geometries have a length of 44 mm and a thickness of 6 mm. The resulting cylinder-on-flat specimen pairs have an initial line contact 10 mm in length, oriented perpendicular to the fretting direction; the width of the line contact is initially determined by the elastic deformation resulting from the applied loading, and due to the non-conforming nature of the contact configuration the width of the contact increases as tests progress and wear develops.

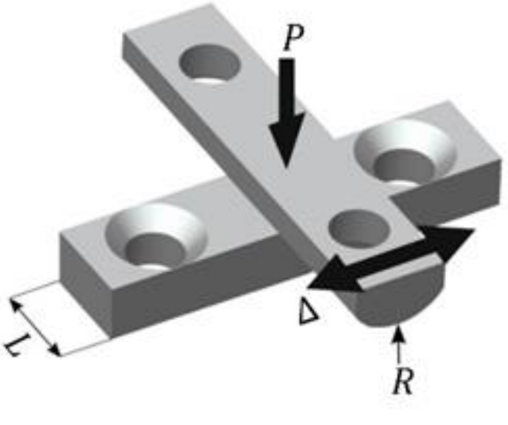

Figure 3.1. Cylinder-on-flat specimen configuration used in fretting tests; L = 10 mm, R = 6 mm.

3.2 Fretting test rig

The test rig used to conduct all of the fretting tests in this thesis was originally developed by Pearson [137], and subsequently modified by Warmuth [138] to expand the range of fretting frequencies that can be tested. A three-dimensional view of relevant parts of the rig is shown in Figure 3.2 (list of components detailed in figure caption), and a simplified schematic diagram of the main components is shown in Figure 3.3.

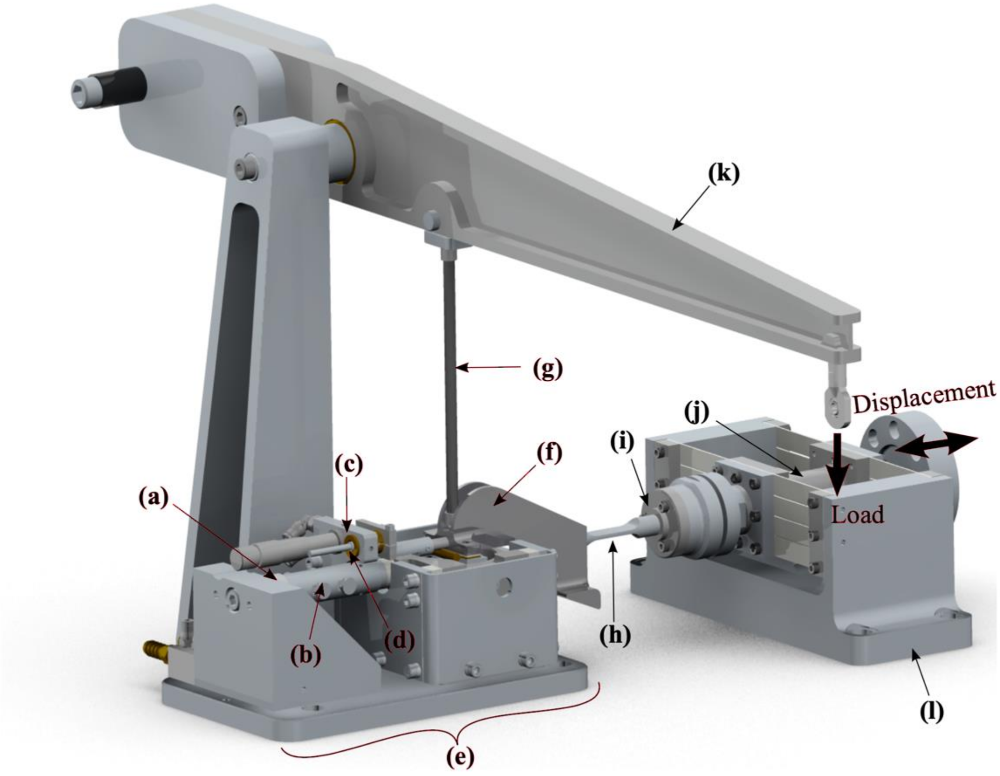

Figure 3.2. CAD model, originally presented by Warmuth [138], showing all the major components of the rig used in the work of this thesis, namely (a) Load cell; (b) Water cooled spacer; (c) Water cooled displacement sensor mount; (d) Capacitance displacement sensor; (e) Heated high frequency module (HFM); (f) Upper specimen mounting block (USMB); (g) Load arm; (h) Drive linkage; (i) Alignment coupling; (j) Stinger housing; (k) Load bar; (l) Linear guide vane assembly.

Relative displacement between specimens is generated at a fixed frequency by an electromagnetic vibrator (EMV) - not shown on the diagrams for clarity – which acts on the upper specimen mounting block (USMB), while the lower specimen mounting block (LSMB) remains fixed. A constant normal load (*P*) is applied to the top of the USMB via a dead weight and a loading arm, with the force applied to the contact being 5 times greater than the load applied to the end of the lever arm.

Displacement is measured by a CS08 Micro-Epsilon capacitance sensor to control the relative displacement between specimens, and tangential force in the contact is measured by a Kistler

9132BA slimline piezoelectric load cell and a Kistler 5073A charge amplifier; tangential force and displacement data are sampled at 200 points per fretting cycle to plot fretting loops and other relevant data for post-test analysis. Fretting loops enable fundamental qualities of the contact to be derived, such as the compliance of the system and the actual slip displacement at the interface; this is fundamental to the analysis of fretting behaviour observed using this rig configuration, as it is the applied displacement (Δ), as opposed to actual slip displacement at the interface (δ), that is controlled and therefore it is important to take into account the compliance of the system when considering the displacement amplitudes occurring during fretting.

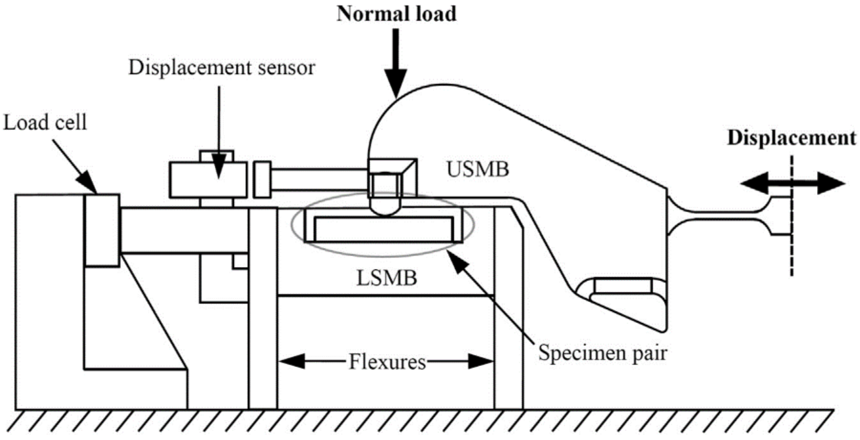

Figure 3.3. Schematic diagram of the main components of the fretting rig used in this study

It has been reported that under some circumstances, the humidity of the air in which fretting tests are conducted can have an impact on both the coefficient of friction and the wear volume [139–142], with behaviour observed at the extremes (i.e. with both fully dry and fully saturated air) differing significantly from that at intermediate humidity. Goto and Buckley [142] investigated the impact of humidity on fretting of pure iron, and observed wear volumes to vary by as much as a factor of three between dry air and 50% relative humidity conditions; however, the greatest variation in both coefficient of friction and wear volume was observed in the 0-20% humidity range, with a much smaller effect as humidity was increased beyond 20%. Between 28% and 50% humidity (the approximate range over which the tests in the present work were conducted) the changes in the coefficient of friction and the wear volume were relatively small (<5% in coefficient of friction and around 10% in wear volume), and as such, humidity control within this range was not deemed necessary.

3.3 Fretting test procedure

Immediately before conducting fretting tests, both specimens are thoroughly cleaned with detergent to remove any grease remaining from the machining process, washed with acetone and industrial methylated spirit (IMS) and then air dried.

Specimens are then mounted in the fretting rig and the desired test parameters are defined using the control software, with the exception of normal load which is determined by physically placing masses on the lever arm. Details of the control system can be found in the thesis of Pearson [137].

Once a test is complete (i.e. run for the specified number of fretting cycles), a sample of loose debris ejected from the contact over the course of the test is retained and stored in an airtight vial for analysis. The worn specimens are then ultrasonically cleaned for 10 minutes in a bath of IMS to remove any loose debris remaining on the worn surfaces, leaving only debris that has been firmly adhered.

All tests were conducted in the gross slip regime, which can be readily established by considering the initial Hertzian contact half-width relative to the slip amplitude; for the contact configuration employed throughout this thesis (namely a 6 mm cylinder-on-flat BS 132 steel contact with a width of 10 mm and a normal load of 450 N) the initial Hertzian contact half-width is 54 μm. However, the scar width increases rapidly as wear occurs (due to the non-conforming nature of the cylinder-on-flat geometry employed), with the relationship between the wear scar semi-width, b, and the wear volume, V_W being well represented by the following relationship [134]:

$$V_W = L\left(R^2 \arcsin\left(\frac{b}{R}\right) - b\sqrt{R^2 - b^2}\right)$$

It can be shown that even in the test which results in the smallest amount of wear (f = 200 Hz and Δ^* = 25 μm) (see Figure 4.1), the scar semi-width (b) has grown to more than 150 μm after only 1% of the total wear in that test, and to more than 320 μm by the time that 10% of the total wear in that test has occurred.

Typical fretting loops at the extremes of displacement amplitude across the range of fretting frequencies tested are presented in Figure 3.4, showing that gross sliding occurs in tests spanning the range of conditions tested in this study, and therefore these tests are in the gross slip regime.

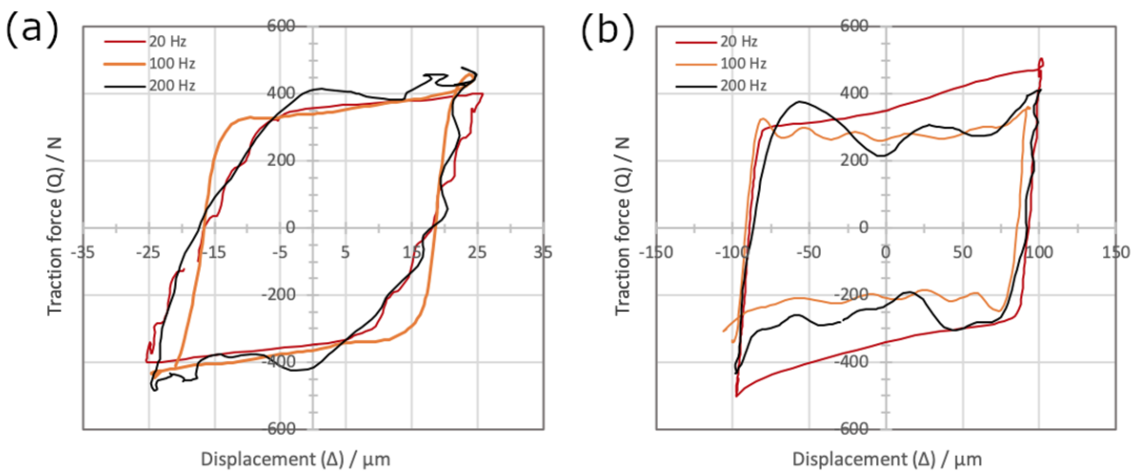

Figure 3.4. Typical fretting loops for tests at each of the fretting frequencies examined in this study, with applied displacement amplitude of (a) 25 μm; (b) 100 μm; despite variations in loop shape with frequency, each of the tests shown can be seen to be in the gross slip regime (P = 450 N; N = 10^5 cycles).

3.4 Characterisation of damage

Using an Alicona G5 profilometer, worn surfaces were scanned to determine the volume of material removed from both specimens due to wear and to assess the profiles of the wear scars. The data processing technique employed is the same as that outlined by Pearson [137].

Worn surfaces were imaged using scanning electron microscopy (SEM) in both plan and sectional view using an FEI Quanta600 MLA SEM. Either a secondary election (SE) or back-scattered election (BSE) detector was used depending on the type of features being images, with SE being best suited to obtaining high-resolution images of topographical features, but gives no indication of the composition of the material being imaged, while BSE provides useful information regarding the composition of surfaces via the contrast between materials of different average atomic number, such as the base metal and oxide debris. Qualitative energy dispersive X-ray spectroscopy (EDX) was used to gain further information regarding the chemical composition of features.

Cross-sections were obtained either by using an abrasive cutting wheel or by electrical discharge machining (EDM), and prepared for metallographic examination by mounting in conductive phenolic resin and grinding with increasingly fine grades of silicon carbide papers, obtaining the final finish by polishing with a 1 μm diamond paste. In cases where a finer finish was required, namely when samples were to be prepared for electron backscatter diffraction (EBSD) observation, this was achieved by an additional polishing stage using 0.06 μm colloidal silica to ensure discernible diffraction patterns could be obtained. EBSD was conducted using a JEOL 7100 F field emission gun SEM to image microstructural features, and to assess the impact of fretting test parameters on changes in grain orientation and phase composition in a more quantitative capacity than the conventional SEM imaging; an acceleration voltage of 15 kV and a step size of 0.1 μm was used to generate such data.

Prior to SEM imaging, ground and polished surfaces were etched with 5% nital in order to reveal features of the microstructure in the SEM images; in the case of specimens prepared for EBSD, the same samples were etched with 5% nital once sufficient EBSD data was deemed to have been generated.

Cross-sections were primarily prepared for cylinder specimens, although were also prepared for flat specimens to enable comparison of the different bodies of the pair, which due to the nature of the contact configuration experience different loading, namely that broadly the same area of the cylinder specimen is always in contact with the flat specimen, while areas of the wear scar on the flat specimen are periodically exposed as the cylinder specimen moves back and forth over the fretting cycle.

Focused ion beam (FIB) milling was used in a limited capacity as a means of exposing the subsurface region of worn specimens for analysis, providing a reference for comparison to cross-sections prepared using the more conventional metallographic preparation technique detailed above.

3.5 Ejected debris characterisation

Ejected debris retained after fretting tests was analysed to assess changes in composition, size and morphology. Composition was measured by X-ray diffraction (XRD), using a Siemens D500 diffractometer with Cu-K$_\alpha$ radiation between 2θ positions of 20° and 120°; to ensure high quality diffraction data, a step size of 0.04° was used with a dwell time of 22 s per step. High quality diffraction data is necessary not only to improve confidence in the measurements of which phases are present in samples, but critically to facilitate the use of Rietveld analysis to assess the relative proportions of each phase in the debris samples.

Rietveld refinements were performed on measured diffraction data using the fundamental-parameters approach to X-ray line profile fitting in Topas V6 software, using a spherical harmonics function to account for discrepancies in the calculated and fitted profiles attributed to complex preferred orientations in the samples.

The size of ejected debris particles was assessed using light diffraction, namely a Coulter LS230, capable of measuring particles ranging from 375 nm to 2 mm in equivalent spherical diameter. Samples of approximately 20 mg of debris powder were dispersed in approximately 3 ml of water, then pipetted into the instrument up to a required obscuration and pumped around the 115 ml cell to obtain size measurements. Repeat measurements were taken for each sample, and different samples measured for the same test conditions to maximise reliability of results.

The morphology of debris particles was observed qualitatively using the same SEM as used for imaging of wear scars (FEI Quanta600 MLA SEM), with samples of loose debris collected after fretting tests being mounted on adhesive carbon tabs and carbon coated for SEM examination; during the process of imaging debris particles, qualitative measurements of particle composition were obtained using energy dispersive X-ray spectroscopy (EDX), allowing for particles to be identified as consisting primarily of metal or oxide.

Chapter 4

Development of debris particles in fretting contacts - effects of displacement amplitude and fretting frequency

4.1 Chapter outline

As discussed in Section 2.2.4, wear debris plays a critical role in determining the mechanisms of fretting wear, which is highly complex due to the large number of variables that may influence both the formation and the flow of debris within contacts; this includes aspects of the nature of the debris particles formed such as the composition and size of particles, which affect their tendency to adhere to one another and to first body surfaces, and ultimately to sinter into protective debris beds. Various experimental studies employing a similar or identical contact configuration to the one employed in this thesis have highlighted the impact of system parameters such as the physical size of contacts [30,34,134], surface hardness [39], fretting frequency [34,39], and displacement amplitude [92] on the flow of debris particles within contacts and hence the formation (or otherwise) of protective debris beds. These parameters vary significantly between experimental configurations employed in the literature, which likely contributes to the variation in reports of fundamental aspects of the nature of debris such as chemical composition. While the nature of fretting debris has been investigated fairly extensively, detailed investigations of the impact of operating conditions on key characteristics, and the development of debris particles in fretting contacts more broadly are relatively scarce.

In the case of displacement amplitude, larger amplitudes are widely reported to enhance the rate of debris ejection in fretting, while there is no broad agreement on the mechanism driving this effect. Conversely, higher fretting frequencies are generally associated with a reduced rate of debris ejection, with this often being attributed to the increase in contact temperature enhancing the adhesive forces between particles and ultimately the sintering of particles to form protective debris beds. Increases in both frequency and displacement amplitude result in increases in contact temperature, although it has been observed that, at larger displacement amplitudes, a higher environmental temperature is required to form a sintered, protective debris bed; this highlights that other factors besides local temperature increase (such as an enhanced rate of debris ejection) are critical in determining the effect of displacement amplitude in fretting.

This research provides an in-depth investigation of the nature of debris generated in fretting wear of high strength steel contacts, and how this varies with changes in both displacement amplitude and fretting frequency for a given set of conditions. The test conditions employed are given in Table 4.1; a range of fretting frequencies and applied displacement amplitudes are tested, with all other conditions being kept equal. The majority of tests are run for a duration of 10^6 cycles in light of findings of Zhu et al. [134] (using the same specimen geometry and material as the present work) indicating that under certain test conditions fretting tests of the order of 10^5 cycles may not reach steady state by the end of the test, and therefore long tests of the order of 10^6 cycles are preferable to ensure that wear mechanisms observed in post-test characterisation are those of the steady state condition. The range of fretting frequencies was chosen based on previous investigations of frequency effects in fretting conducted using the same testing configuration as the present work, namely Warmuth et al. [34] and Jin et al. [43], in which a factor of 10 increase in fretting frequency from 20 Hz to 200 Hz resulted in significant changes in wear rate and the nature of fretting debris; in this work an intermediate condition of 100 Hz is also examined to better understand the nature of wear mechanism changes over the range of frequencies. Values of displacement amplitude were selected such that the behaviour examined is indeed fretting wear (rather than reciprocating sliding wear), and that all tests occur predominantly in the gross slip regime (see Section 3.3); as this has also been a requirement for previous studies using this rig, the values employed in this work align with those employed in previous works using this rig, such as that of Pearson and Shipway [26].

Debris particles ejected over the course of the fretting tests provides useful insight into the effects of frequency and displacement amplitude on the mechanism of fretting. The methodology employed involves the application of techniques which are novel in the context of fretting debris characterisation (most notably quantitative phase characterisation by XRD profile-fitting, i.e. Rietveld analysis); morphology, size and composition of ejected debris particles are investigated and compared to provide a holistic view of the effects of two parameters known to influence debris behaviour in fretting contacts, and how this is reflected in the observed rate of wear. Gaining such understanding of the fundamental processes governing debris behaviour enables a broad mechanism to be outlined for fretting wear in the studied contact configuration, which has implications for understanding the mechanism of fretting more broadly.

Table 4.1. Test conditions used in this study

Frequency, f (Hz)	20, 100, 200
Applied displacement amplitude, Δ^* (μm)	25, 50, 100
Applied normal load, P (N)	450
Hertzian contact pressure, p_0 (MPa)	527
Test duration, N (cycles)	10^6
Temperature, T (°C)	Room temperature

4.2 Results

4.2.1 Wear rate

The extent of wear after the full duration of tests (10^6 fretting cycles) at each of the fretting frequencies and displacement amplitudes tested are shown in Figure 4.1, expressed as total wear volume (net material removed from both specimens) plotted against total energy dissipated over the test; the gradient of a straight line from the origin on these axes represents the average energy wear rate (material loss per unit dissipated energy) at a given set of conditions. Higher dissipated energies reflect higher displacement amplitudes, which slide a greater distance over the same number of cycles. Confidence limits are represented in Figure 4.1 by error bars indicating variation in wear volume and dissipated energy observed in repeat tests; variation in wear volume is within 4% of the average value, while variation in dissipated energy (reflecting variation in distance slid among other things) is slightly greater at approximately 10%. These confidence limits indicate a level of repeatability in experimental measurements in line with that determined in previous work employing the same rig used in this study, in which variation in wear rate of no more than 15% was observed [138].

It can be seen that wear volume is broadly proportional to the energy dissipated at all frequencies examined, with wear rates being broadly independent of displacement amplitude at each frequency. Therefore, wear rate at each fretting frequency can be approximated by a single wear rate, expressed as the gradient of the straight line passing through all three displacement amplitudes, as shown in Figure 4.1. As observed in previous works on the effect of frequency in fretting, increasing frequency results in a significant reduction in wear rate, with an overall reduction of approximately 50% (from 0.0378 $mm^3\ kJ^{-1}$ to 0.0191 $mm^3\ kJ^{-1}$) as frequency is increased from 20 Hz to 200 Hz. It is also noted that the drop in wear rate with frequency is not evenly distributed across this range, with a fivefold increase in frequency from 20 Hz to 100

Hz resulting in a reduction in wear rate of approximately 12%, while a further twofold increase from 100 Hz to 200 Hz results in a much more significant reduction of approximately 43%.

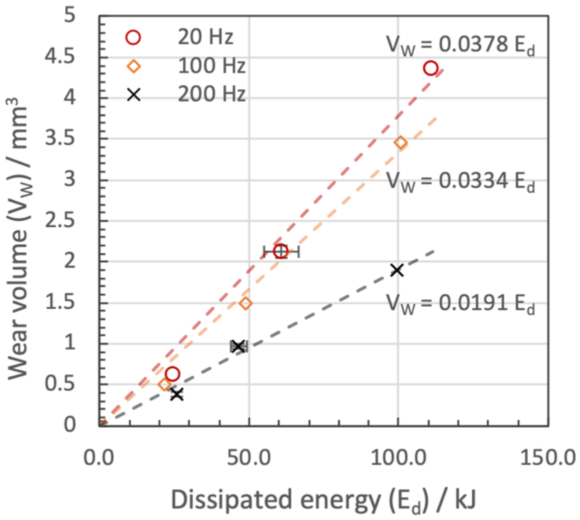

Figure 4.1. Wear volume after 10^6 fretting cycles as a function of dissipated energy for the three fretting frequencies examined in this study; significant differences in dissipated energy reflect the three displacement amplitudes tested.

4.2.2 Coefficient of friction

The relative effects of frequency and displacement amplitude on the coefficient of friction over the range studied are shown in Figure 4.2; in Figure 4.2(a), the energy coefficient of friction (μ_E) is plotted as a function of number of fretting cycles at a fixed frequency (f = 20 Hz) over a range of displacement amplitudes, while Figure 4.2(b) shows μ_E over a range of fretting frequencies at a fixed displacement amplitude ($\Delta^* = 50$ µm). It can be seen that, at a fretting frequency of 20 Hz, displacement amplitude has minimal impact on the coefficient of friction, which after approximately 10,000 cycles lies within the range ~0.75 to ~0.8 at all displacement amplitudes, and remains broadly steady over the remainder of the tests. Fretting frequency, however, has a more significant effect on friction, with μ_E being seen to decrease as frequency is increased; μ_E remains broadly steady over the duration of tests conducted at 20 Hz and 100 Hz, although increases from ~ 0.6 to ~ 0.7 over the duration of the tests at 200 Hz, the highest frequency tested. At all three frequencies, μ_E was in the range ~ 0.7 to ~ 0.8 at the end of the tests.

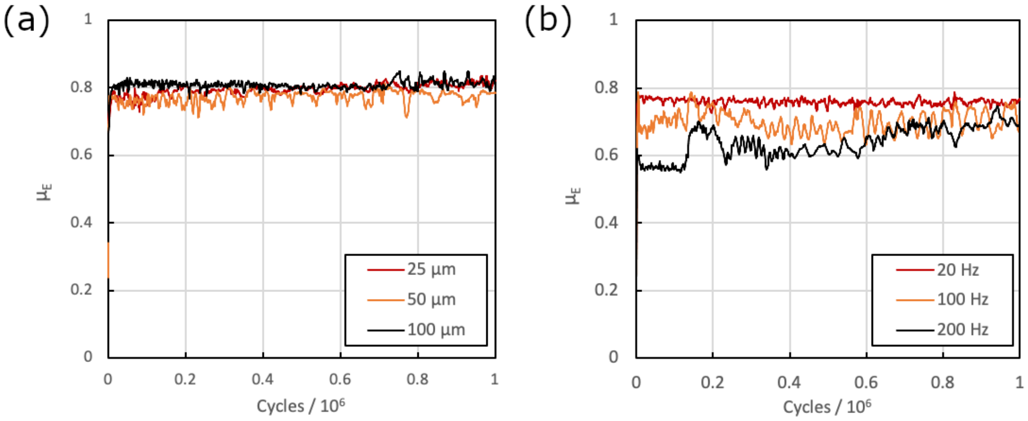

Figure 4.2. Evolution of energy coefficient of friction (μ_E) with number of fretting cycles as a function of (a) applied displacement amplitude (f = 20 Hz); (b) fretting frequency (Δ^* = 50 μm) over the range tested, showing a marked difference in the influence of both frequency and displacement amplitude on friction as both parameters are increased.

Plotting the data as a function of number of fretting cycles has the benefit of being able to show how friction varies over the course of tests, however it is noted that each set of conditions shown in Figure 4.2 is represented by data from a single test, and variation between tests is not captured in this representation. However, repeat tests indicated that, while the value of friction coefficient varies on a cycle-by-cycle basis between tests, the nominal values of the friction coefficient and broad trends regarding the relative magnitude at different test conditions and throughout the duration of tests was consistent between repeats.

4.2.3 Characterisation of ejected debris

4.2.3.1 Compositional analysis

The phases present in samples of fretting debris collected from tests after 10^6 cycles were identified using X-ray diffraction, and profiles calculated to fit the experimental patterns using Rietveld analysis, allowing for the relative proportions of phases to be estimated. These are presented as a function of displacement amplitude in Figure 4.3 and as a function of fretting frequency in Figure 4.4; experimentally measured diffraction patterns are plotted in black, along with the fit with the corresponding fitted profile calculated using Rietveld analysis plotted in red. In all cases, a good fit between experimental measurements and calculated patterns is observed at each test condition. Across the range of frequencies and displacement amplitudes, ejected debris can be seen to consist of two phases: α-Fe_2O_3 (haematite) and α-Fe (ferrite). Distinct peaks at 45 °, 65 ° and 82 ° align with the diffraction pattern of ferrite, while the further expected peaks at 98 ° and 116 ° are less clearly discernible, particularly at the lower displacement amplitude (Δ^* = 25 μm).

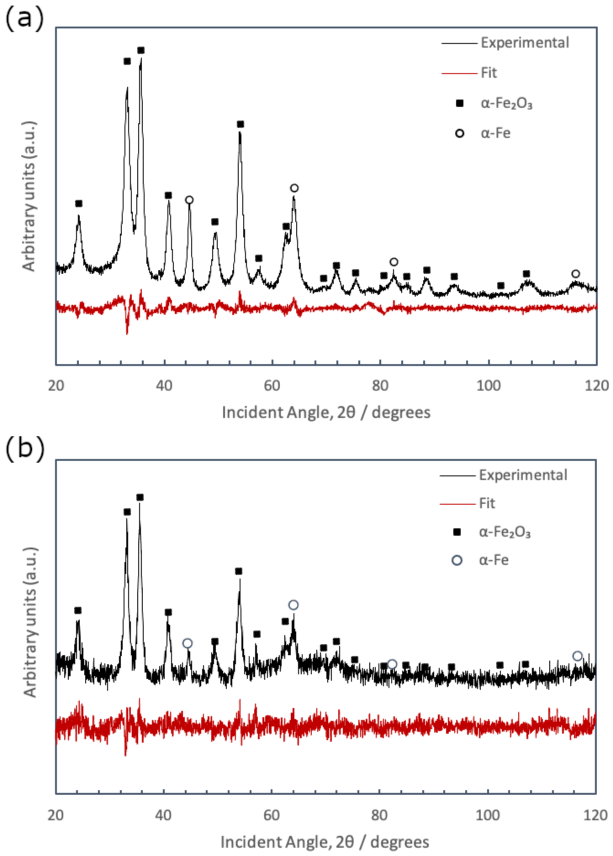

Figure 4.3. Experimental and calculated X-ray ray diffraction patterns of debris collected after 10^6 cycles with an applied displacement amplitude of (a) 100 μm; (b) 25 μm. In each case, the differences between the measured and calculated data are shown.

Using Rietveld analysis to estimate the relative proportions of phase fractions, it is found that at both high and low displacement amplitude debris consists primarily of α-Fe_2O_3 (haematite) with α-Fe (ferrite) making up only a small fraction, with no other phases present. The debris ejected during fretting with a low applied displacement ($\Delta^* = 25$ μm) was found to consist of approximately 2.6 wt.% ferrite, with this fraction increasing to 5.6 wt.% following fretting with a higher applied displacement amplitude ($\Delta^* = 100$ μm); the balance in both cases is made up solely of haematite. These proportions should be approached as approximations, seeing as there are likely to be complex preferred orientations within samples due to the mechanism by which the debris is formed, which although taken into account in the processing of the data cannot be accounted for comprehensively.

As observed over the range of displacement amplitudes, diffraction patterns of ejected debris at all three fretting frequencies (shown in Figure 4.4) can be seen to consist solely of two phases: haematite (α-Fe_2O_3) and ferrite (α-Fe); for clarity, only the peaks corresponding to ferrite have been marked in Figure 4.4, unmarked peaks correspond to haematite.

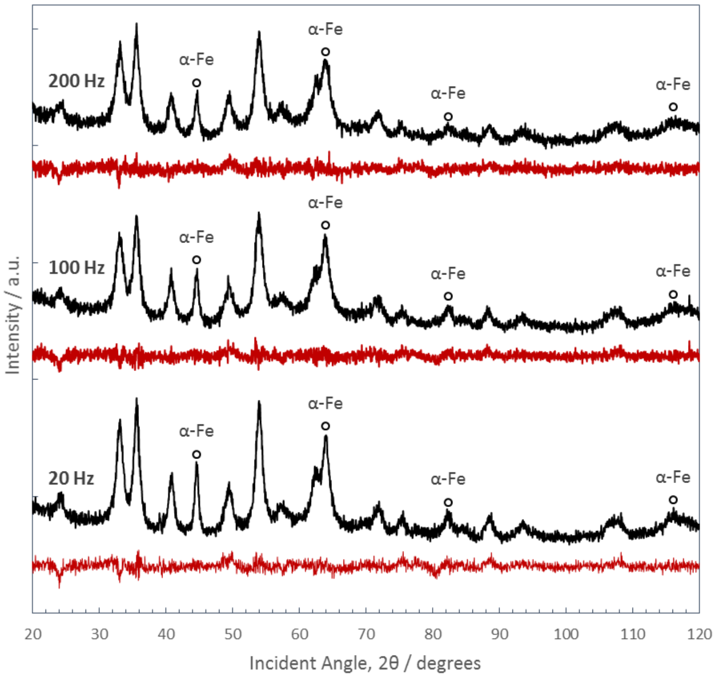

Figure 4.4. X-ray diffraction patterns of debris ejected over the course of fretting tests over the range of frequencies studied; experimental diffraction patterns are plotted along with the fit with patterns calculated using Rietveld analysis.

The relative proportions of the two phases in ejected debris at each of the frequencies and displacement amplitudes examined, calculated using Rietveld analysis, are plotted in Figure 4.5 as a function of fretting frequency; a modest reduction in metallic content with increasing fretting frequency can be seen to occur over the range of frequencies tested, from ~ 5 wt.% to ~ 3.4 wt.%. At all of the displacement amplitudes examined, the metallic content of debris exhibits a modest decrease as frequency is increased from 20 Hz to 200 Hz; conversely, increases in displacement amplitude result in an increase in the mass fraction of metallic iron at every frequency examined, with the extent of this increase being broadly similar at all three frequencies.

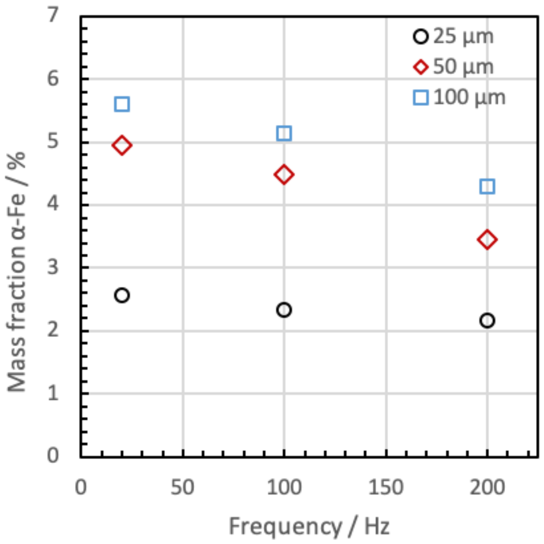

Figure 4.5. Plot of estimated ferrite mass fraction in the loose debris collected following fretting for 10^6 cycles for all combinations of displacement amplitude and fretting frequency examined in this study, showing a decrease in the metallic content of ejected debris as frequency is increased and as the fretting displacement is reduced.

4.2.3.2 Particle size analysis

To assess the size of debris particles and the relative proportions of samples (as a percentage of volume) consisting of particles in a given size range, particle size distributions are presented in the form of histograms over a range of (i) test durations (Figure 4.6); (ii) displacement amplitudes (Figure 4.7); (iii) fretting frequencies (Figure 4.8). Repeat measurements were conducted at select conditions to establish repeatability of the data; where repeat data is available, the range of individual measurements is represented by error bars on the histograms. Repeat measurements were mostly conducted at the extremes of the test matrix, and consequently there are no error bars in Figure 4.8 which contains data at the intermediate displacement amplitude condition (Δ^* = 50 μm).

Debris particles can be seen from Figure 4.6 to cover a wide range of sizes (expressed in terms of equivalent spherical diameter), with diameters ranging from 0.4 μm up to 50 μm; it should be noted that particles as small as 0.0375 μm in diameter are within the measurable range of the equipment used, so the absence of particles below ~ 0.4 μm indicates that this is the minimum size of ejected debris particles, as opposed to smaller particles being outside the observable range. Moreover, Figure 4.6 shows that over the range of test durations examined (all other things being equal) the particle size distribution is broadly unchanged after 10^4 cycles (the shortest duration tested) up to 10^6 cycles (the longest duration tested).

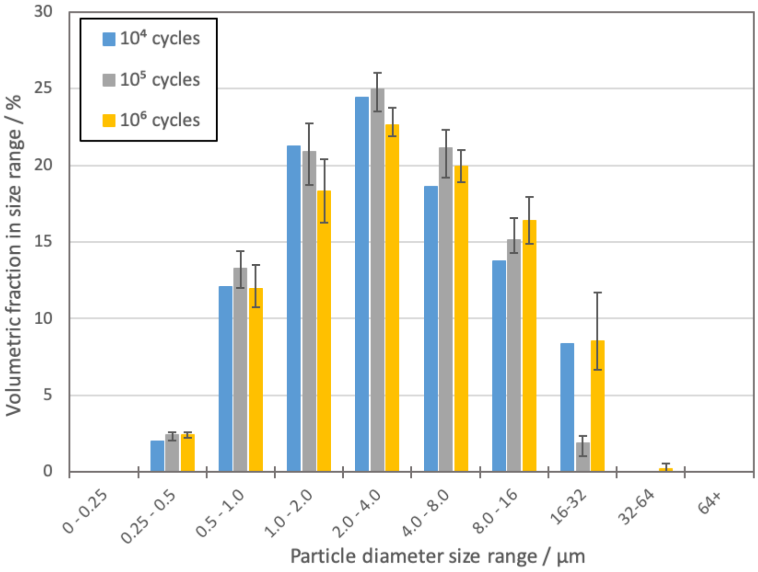

Figure 4.6. Particle size distributions of debris ejected during fretting with a displacement amplitude of 100 μm for a range of test durations, from 10^4 cycles to 10^6 cycles (f = 20 Hz).

Particle size appears to be more sensitive to changes in displacement amplitude, with a considerable change in size distribution as displacement amplitude is increased from 25 μm to

100 μm, shown in Figure 4.7. In all three cases, the greatest proportion of particles have an equivalent spherical diameter within the 1 – 8 μm range, but at the largest of the three amplitudes the distribution is broader than that of the smaller two displacement conditions, with a greater proportion of samples consisting of particles smaller than this range. The overall size range is not significantly affected.

The distributions over the range of fretting frequencies examined (Figure 4.8) show a reduction in the maximum size of ejected particles as frequency is increased, with debris ejected in higher frequency tests (*f* = 100 Hz; *f* = 200 Hz) containing no particles in the 32 – 64 μm range. An overall reduction in ejected particle size with increasing frequency is reflected by the weighting of particle size distributions towards smaller particle diameters at the two higher frequencies, which contain a greater proportion of particles in the range of 0.5 – 4 μm than at 20 Hz.

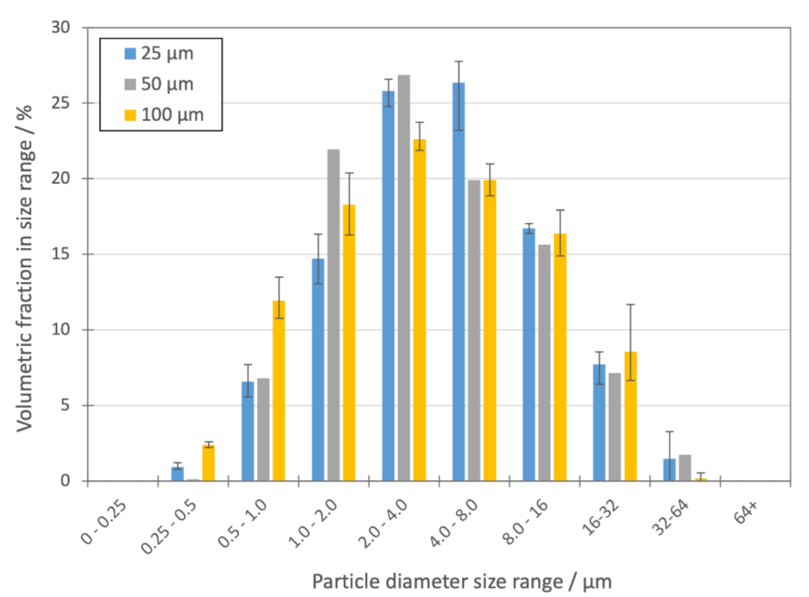

Figure 4.7. Particle size distributions of debris ejected during fretting for 10^6 cycles over the range of displacement amplitudes tested, namely 25 μm, 50 μm and 100 μm (*f* = 20 Hz).

Changes in particle size due to changes in the discussed parameters can be readily compared by representing particle size in terms of the overall average (mean) particle size at a given set of conditions, allowing for a wider range of conditions to be displayed on one graph. This can be calculated from particle size distribution data such as those presented in Figure 4.6 and Figure

4.8 by assuming the size of every particle within a bin to be the central value of that bin, which is multiplied by the corresponding proportion of sample volume that bin represents, divided by the number of observations to yield the mean. The upper and lower limits of estimated mean values are calculated assuming the maximum and minimum value in each bin, respectively.

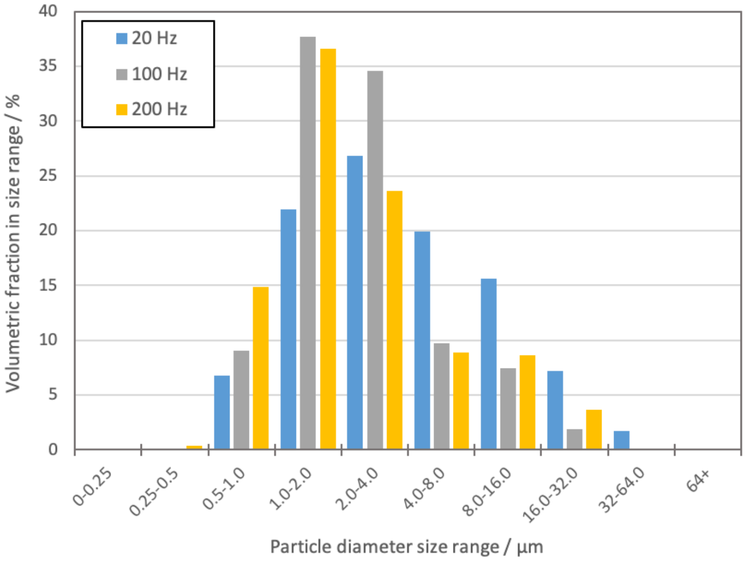

Figure 4.8. Histogram of particle size (expressed as equivalent spherical diameter) distributions of debris ejected after fretting at each of the frequencies tested ($\Delta^* = 50$ µm; $N = 10^6$ cycles).

A plot of the mean size of particles ejected over 10^6 fretting cycles at each frequency and displacement amplitude examined is presented in Figure 4.9, with error bars indicating the maximum range of estimates for mean particle size that can be calculated from the particle size distribution data. As observed for a single displacement amplitude ($\Delta^* = 50$ µm) in Figure 4.8, a reduction in average particle size can be seen to occur as fretting frequency is increased, with such a reduction occurring at all three displacement amplitudes examined. Moreover, the average particle size appears not to depend strongly on displacement amplitude, with no significant difference observed between the average particle size at the two higher displacement amplitudes ($\Delta^* = 50$ µm; $\Delta^* = 100$ µm), and a relatively modest reduction in particle size (no greater than approximately 30%) as displacement amplitude is reduced from 50 µm to 25 µm.

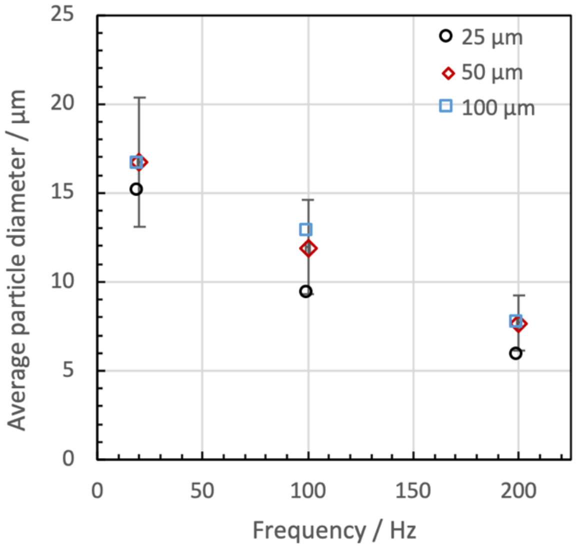

Figure 4.9. Plot of mean diameter of loose debris particles collected following fretting for 10^6 cycles for all combinations of displacement amplitude and fretting frequency examined in this study, showing a decrease in particle size as frequency is increased for all displacement amplitudes tested.

4.2.3.3 Debris particle morphology

To identify and understand the effects of displacement amplitude on the morphology of debris particles ejected from the contact, debris samples were prepared for SEM by applying debris particles (collected after tests as described in Section 3.5) to adhesive carbon tabs, followed by carbon coating; in the SEM images presented in this section, the adhesive carbon tab upon which debris particles are mounted is discernible as the black background of the image. Both secondary electron and backscatter electron imaging techniques were used, with the most appropriate technique being selected based on the information required.

The secondary electron image shown in Figure 4.10(a) highlights the variation in particle size within samples of debris ejected from a high displacement amplitude (Δ^* = 100 µm) test over the course of a test of length 10^6 fretting cycles (debris was collected following completion of the test and following separation of the two first bodies). A large proportion of particles in the sample can be seen to be very small relative to a small number of large particles of the order of tens to hundreds of micrometres in diameter, the same order of magnitude as the displacement amplitude applied at the interface. A higher magnification image of the largest particle in this sample (Figure 4.10(b)) confirms that the particle size is indeed greater than the displacement amplitude employed in the test from which it was generated. While the depth of the particle cannot not be ascertained from the SEM images, it is assumed that the thickness of the particle is small relative to its diameter, that is to say that it is a thin, plate-like piece of debris; qualitative EDX analysis showed the particle to consist solely of iron and oxygen, indicating that it consists (at least in part) of α-Fe_2O_3 as was observed to be the major component of ejected debris samples by XRD and Rietveld analyses (as detailed in Section 4.2.3.1). A striking feature of the large particle is the range of different surface textures that can be observed; Figure 4.10(c) highlights a region exhibiting significant porosity, bearing a resemblance to a vermicular structure observed in sintering processes, in stark contrast to the smooth and glassy surface that can be seen in Figure 4.10(d).

More detailed information regarding the composition of the particle imaged in Figure 4.10 is given in Figure 4.11, in which local EDX data indicate regions where the constituent elements are present, namely iron and oxygen as observed in XRD analysis (Figure 4.3). It appears from the EDX maps presented that while most of the particle consists of oxide, there are regions where oxygen concentration is low and iron is still present, indicating that these are primarily metallic surfaces. However, oxygen concentration appears lower in the EDX measurements due to the low atomic mass of oxygen relative to iron (reducing the strength of the EDX signal), so this does not necessarily indicate that these surfaces are not oxidised, only that the oxygen concentration is lower than in regions where a stronger signal is detected. It should be noted that the regions of the particle imaged in Figure 4.10 correspond to regions consisting primarily of iron oxide (α-Fe_2O_3).

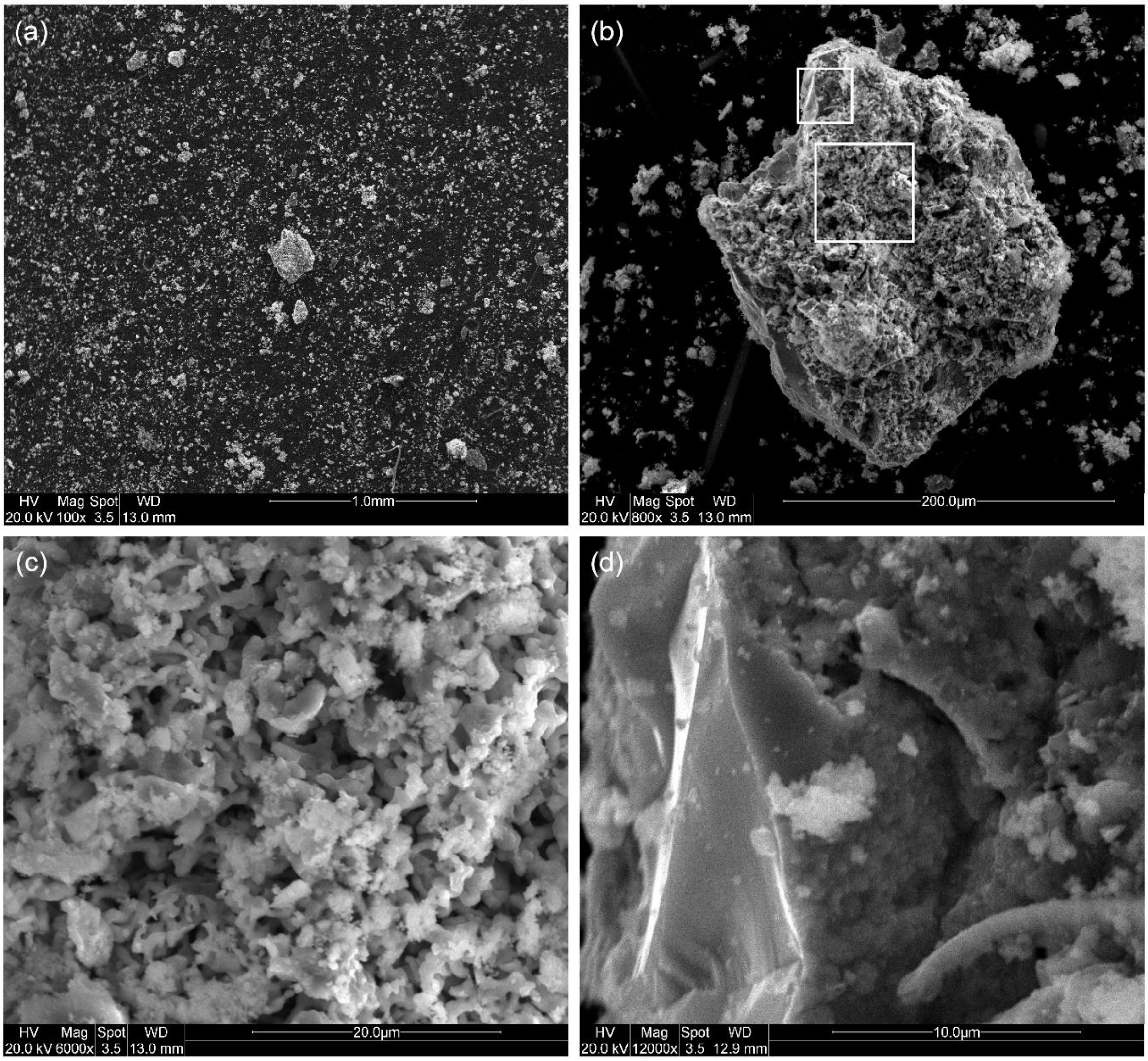

Figure 4.10. SE SEM micrographs of ejected debris collected from a 10^6 cycle test with a displacement amplitude of 100 µm and a frequency of 20 Hz; (a) overview; (b) higher magnification image of large particle seen in the centre of (a); (c) and (d) are higher magnification images of the surface of the particle shown in (b) as highlighted.

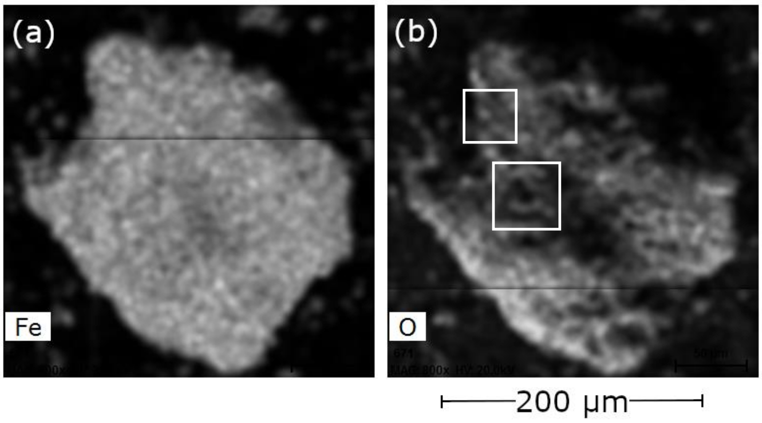

Figure 4.11. EDX maps of the same large debris particle ejected fretting at a high displacement amplitude ($\Delta^* =$ 100 µm) over 10^6 cycles with a frequency of 20 Hz, indicating approximately where the constituent elements are present at the surface, namely: (a) iron; (b) oxygen.

The smaller particles in the same debris sample also exhibited significant variation in their nature, although all appeared to consist of many sub-micron oxide crystallites at varying degrees of sintering, forming larger "particles". This common feature of particles ejected under both high and low displacement conditions is evident in the images presented in Figure 4.12 of two particles of similar size found in the debris ejected during tests with both 100 μm and 25 μm applied displacement amplitudes; at both amplitudes, the smaller individual crystallites that make up the larger particles (Figure 4.12(a) and (c)) can be discerned at higher magnification (Figure 4.12(b) and (d)), and in both cases are of the order of 0.1 μm in diameter. These sub-micron crystallites were not observed in isolation in any of the SEM observations of debris samples over the course of this study, suggesting that such particles have a strong tendency to agglomerate or otherwise bond together (e.g. by sintering) during the fretting process.

Another example of the consolidation of many smaller particles into larger agglomerates is highlighted in Figure 4.13, which appears to be a single flat piece consisting of smaller particles bonded to form a coherent structure in a manner that appears similar to that which occurs in the development of debris beds; similarities in appearance to debris beds that remain adhered within wear scars can be seen from the SEM images shown in Figure 4.14, which show a debris bed formed under the same fretting test conditions as the particle imaged in Figure 4.13. Qualitative EDX analysis confirms that the particle consists largely of oxide, and the appearance of the particle at higher magnification (Figure 4.13(b)) indicates that the particle has been plastically deformed, suggesting that it is indeed a detached piece of debris bed that has been ejected from the contact.

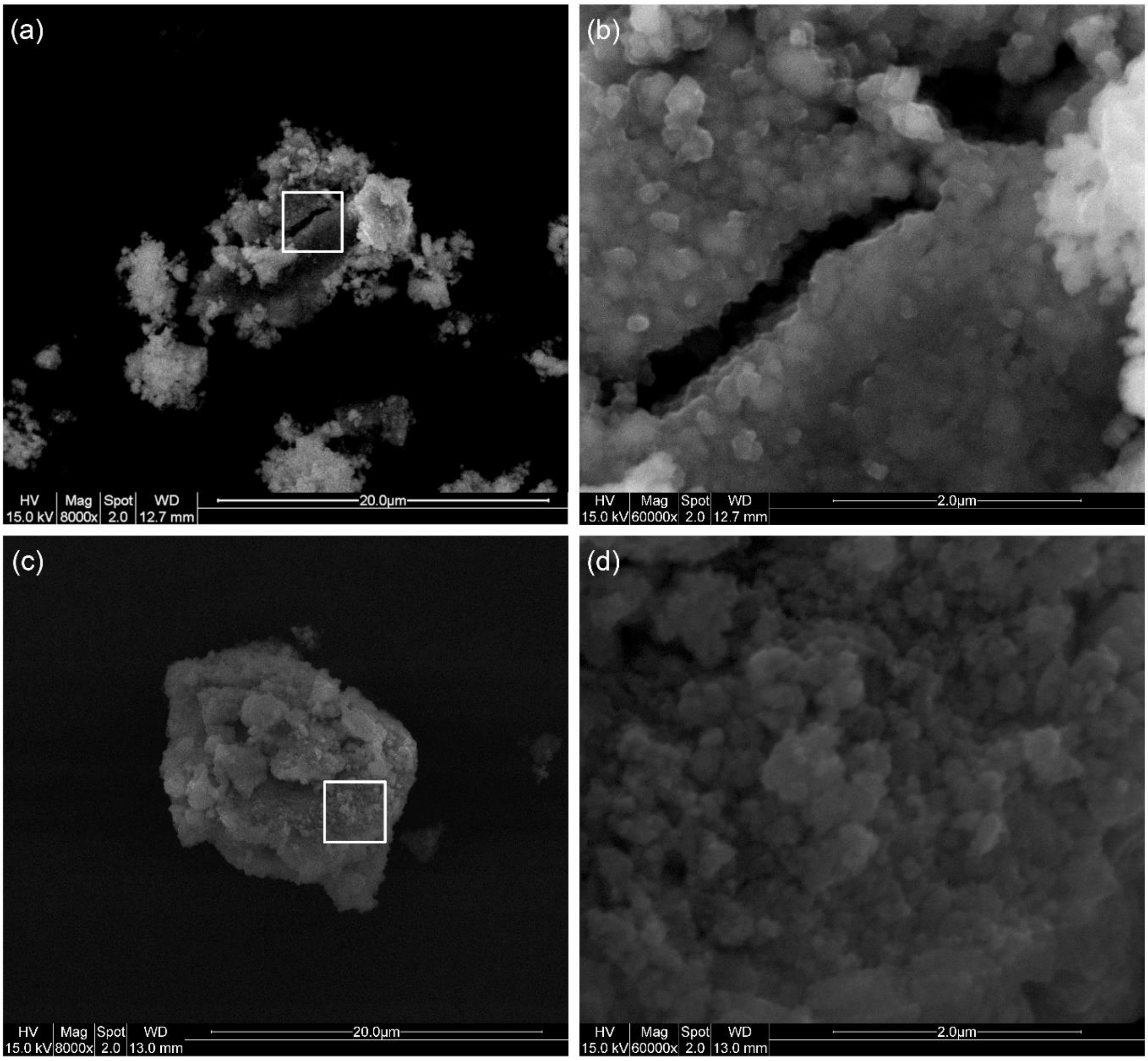

Figure 4.12. High magnification SE SEM micrographs of debris particles ejected during 10^6 cycle test with displacement amplitude of (a)-(b) 100 μm; (c)-(d) 25 μm (f = 20 Hz).

Debris particles similar in appearance (although smaller in size) to that highlighted in Figure 4.13(b) were also observed in ejected debris samples collected after 10^4 cycles, indicating that detachment and ejection of parts of the debris bed occur from an early stage of fretting. It should be noted that it is not possible with the methodology employed in this thesis to determine the stage at which individual particles are ejected from the contact, as the ejected debris samples are collected upon completion of the fretting tests.

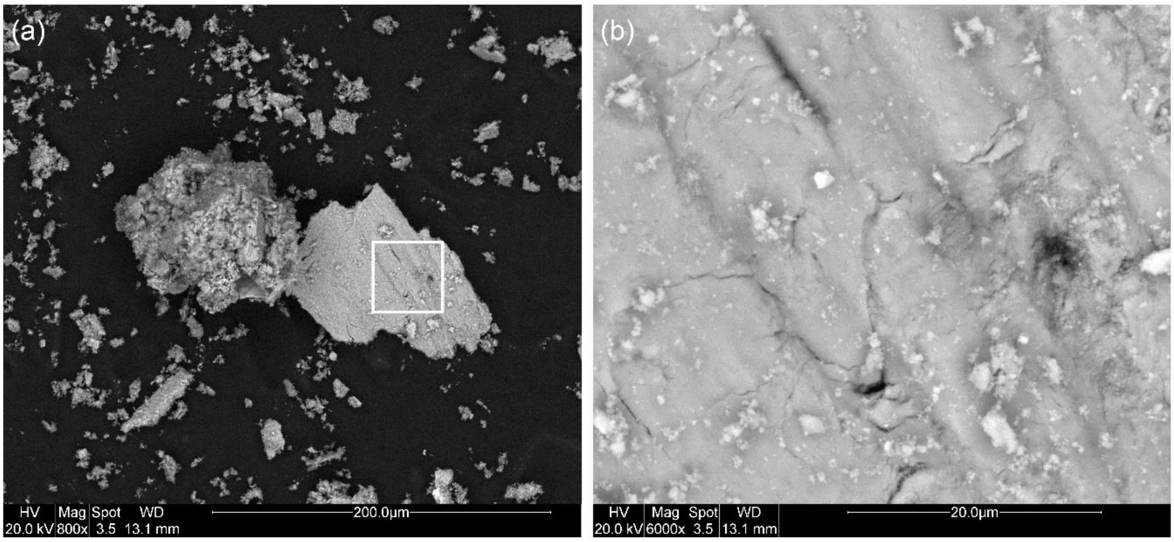

Figure 4.13. BSE SEM micrographs of debris ejected during a 10^6 cycle test with displacement amplitude of 100 µm: (a) low magnification; (b) higher magnification view of the surface of the right-hand larger particle seen in (a) (f = 20 Hz).

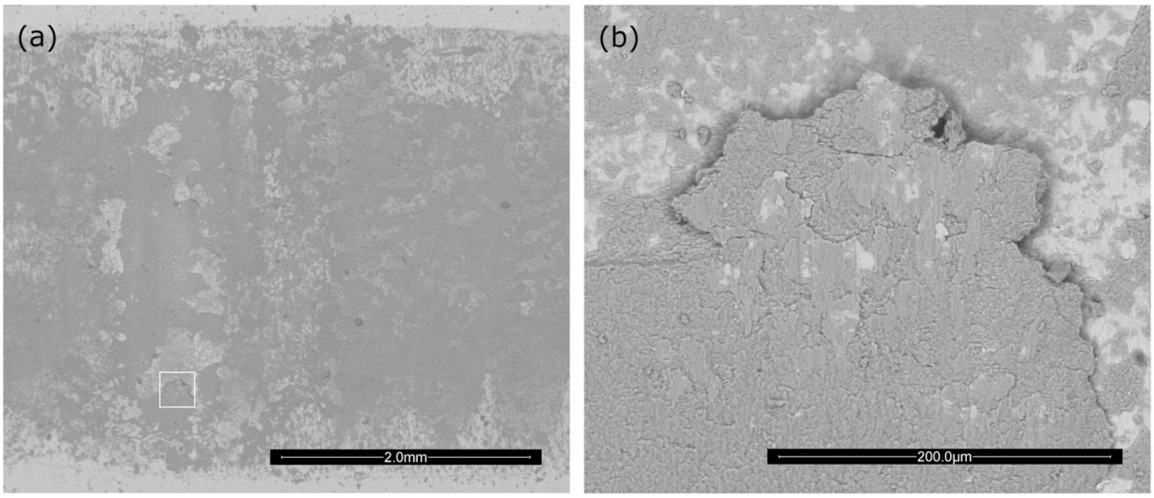

Figure 4.14. BSE SEM micrographs of debris adhered within the wear scar of a flat specimen after fretting for 10^6 cycles with a displacement amplitude of 100 µm and a frequency of 20 Hz at (a) lower magnification; (b) higher magnification.

4.3 Discussion

4.3.1 General characteristics of ejected debris

Wear debris generated and ejected in fretting wear of steel pairs over a range of displacement amplitudes and fretting frequencies is observed to consist almost entirely of the iron oxide haematite, α-Fe_2O_3, with the balance being made up by metallic iron (ferrite), α-Fe. While there is evidence that the proportions of the two phases are influenced by both displacement amplitude and frequency (Figure 4.5), quantitative analysis of XRD data shows that under all conditions examined, the oxide fraction is dominant (>94%). The size of particles ejected over the course of individual fretting tests was observed to range significantly, from approximately 0.4 µm to 50 µm in equivalent spherical diameter (Figure 4.6, Figure 4.8), with the overall size range being broadly similar over the range of displacement amplitudes and frequencies tested.

The observed chemical composition of debris is broadly in line with reports in the literature on the nature of wear debris generated in fretting of steel pairs in air at room temperature (detailed in Section 2.2.4.1), although these vary significantly between experimental studies. Two aspects of debris composition are relevant to consider, these being (i) the phases present; (ii) the relative proportions of these phases. Regarding the former, the two phases observed in this work are consistent with reports in the literature of the composition of debris ejected during fretting of steel pairs at room temperature [1,106]; magnetite (Fe_3O_4) is sometimes observed, particularly in fretting of steels at elevated temperature, while reports of other iron oxides such as FeO are uncommon [1,106]. Quantitative reports of the relative proportions of phases are uncommon in the fretting literature, although Dies [143] reported the proportion of iron in debris produced in fretting of steels to be 3% of sample mass. This is broadly consistent with the metallic content observed in this work (ranging from ~3% to ~6%), although Dies [143] also found 24% of debris mass to consist of FeO, an oxide that is rarely reported to be observed in room temperature fretting, indicating either a very different wear mechanism or a significant difference in the accuracy of the respective measurement techniques. In any case, the phase fractions reported in this chapter provide useful insight into the nature of fretting debris, while the paucity of comparable measurements highlights the need for further work in this area to improve understanding of fretting mechanisms.

The range of particle sizes is broadly consistent with reports in the literature regarding fretting wear of steel pairs in ambient conditions, although such data vary significantly, due to differences in experimental configurations, measurement techniques, and differing definitions of what constitutes a "particle". The wide range of sizes, and the large size of some particles is in agreement with the work of Colombie et al. [47], who investigated the debris generated in fretting of steel pairs and observed ejected particles of Fe_2O_3 ranging in size from ~ 1 μm to ~ 100 μm. However, they also observed a significant proportion of Fe_3O_4 in ejected debris, indicating that quite different fretting behaviour may have been occurring. Halliday and Hirst [22] also observed ejected debris particles ranging from ~ 0.01 μm to 50 μm in diameter, although in this it was observed that larger particles were primarily metallic in nature, while oxide particles were typically of the order of 1 μm in diameter. Reports of significantly smaller debris particles than observed in the present work are fairly common, such as in recent work by Blades et al. [144], in which the debris ejected in fretting of steel contacts in air was found to consist of metal particles of the order of 10 μm in diameter, and oxide particles of the order of 10 nm.

A factor that may contribute significantly to the discrepancy between reports of particles size is the definition of what constitutes a particle; in the present work, the average diameter of ejected debris particles lies in the range of approximately 6 μm – 17 μm (Figure 4.9) which, in addition to the wide range of particle sizes indicates that a significant proportion of ejected debris "particles" are in fact agglomerates of many smaller debris particles, as opposed to individual pieces of wear debris. This is consistent with SEM images that indicate a significant degree of agglomeration and sintering of submicron oxide particles occurs, even under room temperature conditions (Figure 4.10, Figure 4.12, Figure 4.13). Moreover, the overall range and distribution of particle sizes were observed not to change significantly after 10^4 fretting cycles (the shortest test duration examined) up to 10^6 cycles (the longest), indicating that the process of particle detachment, flow within and ejection from the contact has broadly reached steady state even by 10^4 cycles. This is not to say that there is no change in the size of particles formed, as a greater number of larger fragments may be detached as debris beds become more developed over a greater number of cycles; some of these larger pieces are ejected without significant comminution, such as those imaged in Figure 4.10 and Figure 4.13. However, the modest differences in particle size distribution suggest that, in most cases, these large fragments are likely to be broken down into smaller pieces before ejection from the contact.

A variety of surface textures are observed, both in samples (Figure 4.10, Figure 4.12, Figure 4.13) and individual particles (Figure 4.10), although high magnification SEM images indicate that a majority of particles examined exhibit surfaces consisting of many sub-micron crystallites (of the order of 0.1 μm) compacted together to form a coherent whole; XRD and EDX analyses indicate that these crystallites consist of α-Fe_2O_3. There were no cases of individual crystallites being observed in SEM images, indicating that these small particles have a strong tendency to agglomerate and sinter to form the larger particles of several microns in diameter that can be seen in SEM images, and more quantitatively measured via particle size analysis (Figure 4.6).

Evidence of sintering is clearest in the secondary electron micrographs of ejected debris particles presented such as in Figure 4.10, in which the different surface textures observed indicate the different stages of sintering, even within the same particle; a contrast between surface textures is clear from the appearance of the large particle presented at different magnifications, ranging from the smooth, glassy surface visible in Figure 4.10(c), suggesting an advanced degree of sintering, to the more porous surface observed in Figure 4.10(d), similar in appearance to vermicular structures exhibited during conventional sintering processes.

4.3.2 Effects of displacement amplitude and fretting frequency

While ejected debris was observed to be broadly oxide-based under all conditions tested (Figure 4.5), both displacement amplitude and frequency are seen to have an impact on the proportion of debris consisting of metallic iron. At a frequency of 20 Hz, the proportion of sample mass consisting of metallic iron more than doubles from 2.6% to 5.6% with a fourfold increase in applied displacement amplitude, with a similar increase occurring at all other frequencies examined. Conversely, increasing frequency is seen to result in a reduction in the metallic fraction of debris, with this effect being independent of displacement amplitude; at an intermediate displacement amplitude of 50 μm, the metallic fraction of debris falls from 5.0% to 3.4% as frequency is increased from 20 Hz to 200 Hz. As mentioned previously, quantitative analysis of the composition of ejected fretting debris in the literature is limited, and it is therefore difficult to assess how these observations align with reports of similar data by other workers. However, it is notable that there is no transition to a "severe" wear regime, which is widely observed in studies of unidirectional and reciprocating sliding wear [145–147], which in the case of the latter is distinguished from fretting wear primarily by larger displacement amplitudes.

The impact of displacement amplitude and frequency on particle size is more complex, due to the wide range of particle sizes present as evidenced by the distributions presented in Figure 4.6, Figure 4.7 and Figure 4.8. However, both displacement amplitude and fretting frequency can be seen to have an impact on these distributions; in the case of displacement amplitude, increasing displacement amplitude is seen to result in a broader distribution of particle sizes, that is to say that a greater proportion of samples is made up of particles that are both smaller than the average and larger than the average (which is seen in Figure 4.9 not to vary significantly with displacement amplitude). Increasing frequency results in a shift in the size distribution towards smaller particles (Figure 4.8), reflected in the downward trend in average particle size with increasing frequency shown in Figure 4.9. To the author's knowledge, there has been no studies into the effects of sliding conditions such as displacement amplitude and frequency on the size of fretting debris, so the agreement of these results with similar data in the literature cannot be assessed.

In assessing the impact of parameters on particle morphology, the depth of detail in comparisons that can be made between debris formed at different conditions is limited by the significant variation in particle morphology within samples, further limited by the practical constraints of investigating a vast number of particles manually. However, the high magnification images presented in Figure 4.12 indicate that the fundamental structure of particles is broadly similar across the range of displacement amplitudes, namely that particles consist of agglomerates of submicron oxide crystallites of the order of 0.1 μm in diameter, sintered to form larger coherent structures. This in turn suggests that the impact of the studied parameters on the development of debris particles in fretting acts primarily through the formation and breakdown of debris beds (in turn dependent upon agglomeration and sintering of particles), as opposed to the initial detachment of debris particles from the surfaces.

4.3.3 Implications for mechanism of debris development

The observation that over the wide range of fretting frequencies and displacement amplitudes investigated, debris ejected from the contact consists predominantly (>94%) of oxide with only a small fraction of metal, has significant implications for the mechanism by which debris is generated and ejected in fretting. Namely, this indicates that over a range of frequencies and displacement amplitudes, there is no fundamental difference in the mechanism of generation of the expelled debris, that is to say that there is no transition from a "mild" wear regime, in which ejected debris is mostly oxide, to one of "severe" wear, in which large metallic fragments tens of micrometres in diameter are ejected amongst oxide debris. Such a transition has been frequently observed in studies of sliding wear since it was first reported by Archard and Hirst [70] in 1956 [145–147].

The oxide-dominated nature of debris is in line with the oxidative mechanism favoured in works such as those of Quinn [61,62,148] and Stott et al. [60], in which debris particles are proposed to form primarily through the detachment of oxide films formed on nascent metal surfaces by a scraping action of asperities on the opposing body. This was assumed to be the dominant mechanism of debris formation in the work of Warmuth et al. [34], in which the effects of frequency on fretting wear, namely a significant reduction in wear rate and a tendency towards more metallic wear scars at higher fretting frequency, were attributed to the exclusion of oxygen from contacts; however, it should be noted that there is not clear evidence for the extent to which such an oxidational mechanism operates under a given set of conditions, and oxide debris may also form by the oxidation of small metallic particles detached from surfaces [27,28,66].

In the present work, while both fretting frequency and displacement amplitude exert some influence on the metallic proportion of ejected debris in the present work, these changes do not correlate with the effects of the parameters on wear rate (Figure 4.1); accordingly, it is proposed that wear (i.e. material removal) is primarily associated with oxide formation within the contact and its subsequent removal as fine debris particles under all of the conditions examined. However, whether oxide is formed directly on surfaces and detached to form particles, or by the oxidation of metallic particles cannot be confidently stated from the data available; it is assumed, in line with the mechanism proposed by Uhlig [59] (detailed in Section 2.2.4.1) that both may occur simultaneously, depending on local conditions within the contact.

The presence of a substantial metallic content in wear debris formed in sliding contacts has been attributed in some cases to *delamination*, in which subsurface fatigue cracks grow parallel to the surface, which when connected with the surface result in the formation of large, plate-like metallic debris particles. Waterhouse and Taylor [67] proposed that the delamination theory of wear, initially outlined by Suh [149] and further validated by Sproles and Duquette [71], is operative in fretting contacts under certain conditions. Waterhouse and Taylor [67] argued that the plate-like particles observed could not be solely oxide-based due to their thickness, ranging from 1.3 to 3.5 μm, and must therefore have formed by delamination. However, in the decades since Waterhouse and Taylor's paper [67], the significant extent of sintering of oxide particles that occurs in fretting contacts has become better understood, and is reinforced by the findings of the present work; this presents an alternative mechanism by which such particles form, as the plate-like particles attributed to delamination by Waterhouse and Taylor [67] may instead result from detachment of fragments of debris beds, which through compaction and sintering may become significantly larger than oxide films directly formed on surfaces.

Sintering of small oxide particles under tribological conditions to form coherent beds was observed by Kato and Komai [103], who termed the phenomenon "tribo-sintering". Particles of various sizes and forms of oxide were supplied to steel-on-steel interfaces in unidirectional sliding, and observed sintering of particles approximately 300 nm in diameter; this is consistent with the observations of the current work, in which sintering of oxide particles approximately 100 nm in diameter is observed. It is worth noting that in sliding wear, such as the unidirectional sliding configuration employed by Kato and Komai [103], debris is likely to be more readily ejected from the contact than in fretting contacts, and as such it may be expected that sintering of debris particles occurs to a greater extent in fretting contacts due to the longer residence time of particles.

The general expression for the sintering rate of particles (S) presented by Kato and Komai [103] is shown in Equation 1, where D is oxygen diffusion coefficient, d is particle size, and a, m and n are constants:

$$S = a\frac{D^m}{d^n} \qquad \text{Equation 4.1}$$

Kato and Komai proposed that the dependence of sintering rate on particle size (i.e. the value of n) is lower in tribological conditions ($n = 0.6$) than in conventional sintering processes ($n = 3 - 4$) where, despite a lack of clarity surrounding the mechanism of tribo-sintering, it may be expected that high temperatures and pressures can be applied in a more steady and uniform manner over longer periods of time. However, in both cases particle size is evidently an important factor in the development of sintering, with small particles sintering much faster than larger particles.

The significant variation in the nature of surfaces of different debris particles suggests that particles may have very different histories, that is to say that there are several distinct mechanisms by which debris particles form and are ejected from the contact. For example, the debris particle approximately 100 μm in diameter imaged in Figure 4.13 appears consistent with the compacted beds of debris that remain adhered within the contact, such as that shown in Figure 4.14. Such "particles", apparently formed by the fragmenting of debris beds, appear very different to the particles imaged in Figure 4.12, which are not only much smaller in overall size, but do not appear as highly compacted and deformed, indicating that they were ejected before they could be incorporated into debris beds. This is a useful consideration in interpreting the impact of frequency and displacement amplitude on the size of particles ejected from the contact, which relates to the degree of sintering under a given set of conditions. The narrower distribution of particles sizes observed at smaller displacement amplitudes may be due (at least in part) to a reduced rate of debris ejection associated with smaller displacement amplitude, increasing the time that particles reside in the contact and therefore the time over which sintering can occur (reducing the fraction of smaller particles) and over which large fragments of debris beds can be comminuted (reducing the fraction of larger particles). Greater residence time of particles in the contact at smaller displacement amplitudes may also be a factor in the reduced metallic fraction of debris ejected at these conditions, as particles spend longer exposed to the enhanced oxidising conditions inside the contact.

While it is recognised that particles that are eventually ejected from the contact may form by a number of different mechanisms, it is possible to outline a generalised mechanism to describe the observations of this study in the following steps:

1) Oxide (haematite) particles of the order of 0.1 μm in size are formed (either directly from surfaces or by rapid oxidation of small metal particles).
2) These rapidly agglomerate and may even sinter to form particles of a range of sizes up to a few microns in size.
3) Some of these particles are ejected from the contact before they agglomerate / sinter into beds, whilst others are retained in the contact and form part of a debris bed. The surface of the debris bed is more fully compacted / sintered than the underlying regions.
4) After a certain time, parts of the debris bed become detached and are subsequently removed from the contact. Some of these bed fragments are removed with little comminution (yielding debris particles of > 100 μm in size) whilst others are more finely comminuted.

Due to the ejected debris samples being collected upon completion of the fretting tests, it is not possible with the methodology employed in this thesis to determine the stage at which individual particles are ejected from the contact. It is recognised that information regarding how the characteristics of debris evolve over the course of fretting tests would be helpful in developing understanding of the phenomena discussed in this chapter; an approach to generating such data has been demonstrated in recent work by Blades et al. [144], which enables the stage of fretting at which particles are ejected to be identified continuously as a function of cycle number as opposed to the discrete durations observed in this chapter. However, the findings of Blades et al. [144] indicate a high level of dependence of debris characteristics (and the associated impact on mechanisms) upon aspects of the contact configuration such as specimen material and atmosphere; this highlights the practical difficulties associated with comparing observations of debris characteristics in the literature. Moreover, as discussed in Section 4.3.1, it is important to clarify what is meant by terms such as "particle size" in fundamental investigations of fretting debris, which may be interpreted differently due to sintering of debris particles. For example, in the present work, “particle size” is taken to mean the size of individual pieces of debris (typically of the order of ~10 μm to even 100 μm) that have been observed to exhibit a high degree of agglomeration and sintering of smaller “particles” (typically of the order of ~0.1 μm); this stands in stark contrast to the size of debris particles reported by Blades et al. [144], which is observed to lie in the range of <10 nm to approximately 10 μm. Whether this discrepancy is due to differences in operative wear mechanisms, the measurement techniques employed, or the definition of particle size is not immediately clear; mechanisms of debris formation and flow within (and expulsion from) contacts are known to be dependent upon many factors which vary between the two investigations, although a potentially more significant factor may be the different techniques used to measure particle size (transmission electron microscopy in the case of Blades et al. [144], as opposed to the light diffraction technique employed in the present work). The difference in resolvable scale of these measurement techniques, as well as the different requirements involved in processing the data may in turn affect the definition of what constitutes a “particle”, as the boundaries of particles are interpreted differently in these methods. Moreover, the number of particles measured per sample is significantly greater in the light diffraction method employed in the present work than that in TEM, and as such the sizes measured using light diffraction may be more representative of debris ejected during fretting tests.

This speaks to a wider problem in the comparison of fundamental investigations of fretting wear (and particularly those focusing on wear debris), namely that differences in contact configuration, the measurement techniques employed and definitions of debris characteristics may vary significantly between studies, and as such, direct comparisons between studies should be approached carefully. In light of this, it is clear that there remain significant gaps in knowledge in this area, with a clear case to be made for further investigation into the development of debris produced in fretting, and vitally the associated impact on wear rates and mechanisms for the purposes of developing improved predictive models.

4.4 Conclusions

Over the range of conditions studied, the nature of debris appears to be not strongly dependent upon either the fretting frequency or the displacement amplitude, despite significant changes in friction and wear rate over these conditions.

The composition of ejected debris is observed to not be significantly affected by displacement amplitude or fretting frequency over the conditions studied, with the same two phases observed in samples, namely haematite and ferrite, in line with previous work on fretting of steel contacts in air at room temperature. The relative proportions of these phases have been quantitatively assessed and, despite a modest influence of both parameters, in all cases debris was found to consist predominantly of haematite with a small (< 6%) fraction of metallic iron. This indicates that for the test system and operating conditions studied, fretting wear proceeds by a broadly oxidative mechanism (i.e. by the formation and ejection of oxide debris), comparable to the regime of "mild" wear in other types of sliding wear, with no evidence of the associated "severe" wear regime in which a greater proportion of large metallic particles are ejected.

The overall range of particle sizes is broadly constant over the range of conditions examined, ranging from approximately 0.4 μm to 50 μm under all displacement amplitudes, fretting frequencies and test durations tested. However, individual particles with diameters greater than this (of the order of 100 μm) were observed via SEM imaging, thought to be detached pieces of debris beds, and therefore having small thickness relative to observed diameter; this assumption regarding the dimensions of debris beds is based on SEM observations in cross-section (explored in detail in Chapter 5) indicating that debris beds still adhered to surfaces are typically no more than 5 μm in thickness. The average size of particles ranges from 6 μm to 17 μm under all conditions studied, indicating that most debris "particles" are in fact agglomerates formed from many smaller pieces of debris, none of which were observed in isolation. The size of particles is largely independent of number of cycles after 10^4 cycles, indicating that the process is broadly in steady state by this stage. Both displacement amplitude and frequency are seen to affect particle size; a reduction in particle size is observed to occur with increasing frequency, while increasing displacement amplitude does not have a significant impact on the *average* particle size, but results in a greater proportion of both larger and smaller particles being ejected (i.e. a broader size distribution). However, as with the chemical composition of debris, these effects are fairly modest and therefore do not indicate a fundamental change in wear mechanism resulting from changes in these conditions.

The morphology of particles varies significantly within samples, but in all cases observed, particles appear to consist of submicron crystallites of iron oxide, of the order of 0.1 μm in diameter, exhibiting various degrees of sintering. Moreover, the size of crystallites that make up particles appears similar for debris particles ejected under both large and small displacement amplitude conditions, indicating that over the conditions tested, the fundamental mechanism of debris particle formation does not change, and rather the development of debris particles depends on the formation and breakdown of debris beds, and hence the degree of sintering. The different surface textures observed indicate that differing mechanisms by which the particles ejected are formed; some particles are agglomerated into compacted beds that adhere to first body surfaces, which may subsequently become detached to form large particles, while some particles are ejected from the contact before this can occur.

Chapter 5

Interacting effects of displacement amplitude and frequency on debris bed development and subsurface damage

5.1 Chapter Outline

As discussed in Sections 2.2.2 and 2.2.3, both displacement amplitude and fretting frequency have been observed to have a significant impact on both the formation and ejection of oxide debris; both parameters affect some of the same physical processes, such as sliding velocity (and therefore local temperature in the contact), but also have significantly differing effects on other processes such as the rate at which debris is ejected from contacts, which has been reported to increase with increases in displacement amplitude [8,9,22,23,27,28,106], and conversely to fall with increases in frequency [14,34]. It is therefore intuitive that the effects of fretting frequency and displacement amplitude interact to a significant degree, with implications for the dominant mechanisms of wear and the total volume of material loss; such interactions have been noted in fretting literature dating back several decades [32,35,44], although have not been explored in detail, and much remains to be learned about the interaction between these fundamental parameters of fretting wear.

The work presented in this chapter seeks to address this gap in understanding by conducting a thorough investigation of the impact of displacement amplitude and fretting frequency on wear mechanisms in fretting, namely via the impact of these two parameters on the formation of debris beds and the response of the subsurface region; the effects of each parameter are explored individually, as well as the interacting effects with changes in both parameters within the studied range. A mechanism is outlined to explain the observed effects in a phenomenologically consistent framework based on the ingress of environmental species and egress of wear debris.

Where the previous chapter focused on wear debris *ejected* during fretting, this chapter focuses on the formation (or otherwise) of coherent oxide debris beds in contacts, and the impact of changes in frequency and displacement on the development of damage in the subsurface region. The test conditions employed in this study (which cover the same range of conditions examined in the previous chapter) are shown in Table 5.1.

Table 5.1. Test conditions examined in this chapter

Frequency, f (Hz)	20, 100, 200
Applied displacement amplitude, Δ^* (μm)	25, 50, 100
Applied normal load, P (N)	250 N, 450 N
Test duration, N (cycles)	10^4, 10^5, 10^6
Temperature, T (°C)	Room temperature

5.2 Results

5.2.1 Development of wear damage associated with changes in displacement amplitude

The extent of wear over the range of displacement amplitudes and test durations tested is expressed in Figure 5.1(a) in terms of total material removed from both specimens plotted as a function of dissipated energy dissipated over the course of the tests. For each displacement amplitude, higher dissipated energy reflects a greater number of elapsed fretting cycles, and as the number of cycles tested are increased by a factor of 10 with each increment, dissipated energy is plotted on a logarithmic axis. Figure 5.1(b) presents the wear data for 10^6 cycle tests (the longest duration examined) in terms of energy wear rate (volume of material lost per unit dissipated energy) as a function of applied displacement amplitude.

It is evident from Figure 5.1(a) that the amount of material lost due to wear is significantly higher at larger displacement amplitude, with a more than a sixfold increase in wear volume at 10^6 cycles, from approximately 0.6 mm^3 to approximately 4.4 mm^3. However, the increase in wear rate is smaller than the increase in wear volume due to the significantly greater slid distance (and hence dissipated energy) at higher displacement amplitude; the energy wear rate exhibits an increase of almost 50% over the range tested, from 0.0257 mm^3 kJ^{-1} at smaller displacement amplitude ($\Delta^* = 25$ μm) to 0.0392 mm^3 kJ^{-1} at the larger displacement amplitude ($\Delta^* = 100$ μm).

Surface profiles of worn flat specimens fretted for 10^6 cycles at both small and large displacement amplitudes are shown in Figure 5.2; despite significant differences in scar width and depth (reflecting the significant difference in wear volume), there is not a significant difference in the overall wear scar shape, with the greatest wear depth in both wear scars being located broadly along the centreline of the scar.

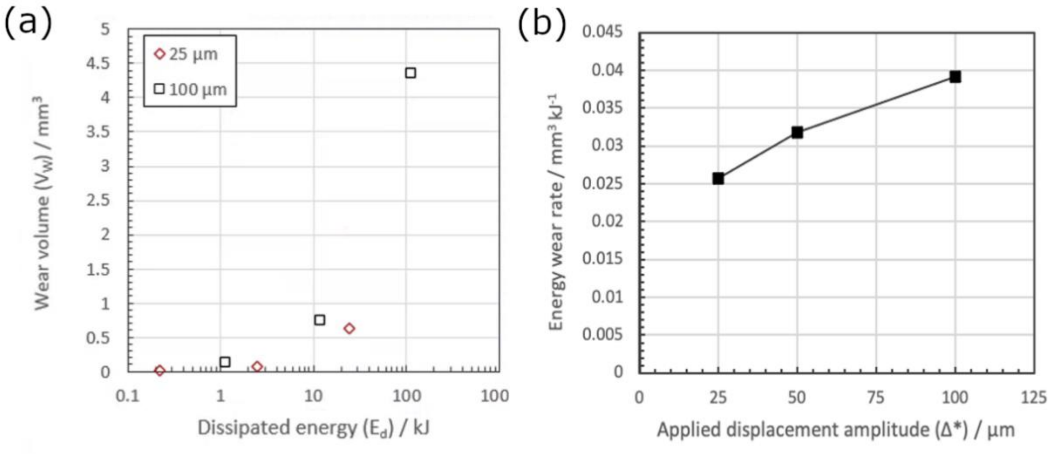

Figure 5.1. Extent of wear over the studied range of displacement amplitudes (a) over the range of test durations as wear volume plotted against dissipated energy; (b) after 10^6 fretting cycles as energy wear rate plotted against displacement amplitude (*f* = 20 Hz; *P* = 450 N).

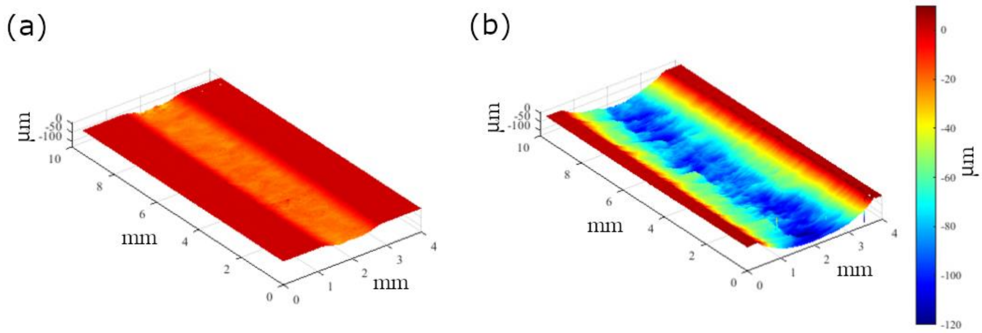

Figure 5.2. Surface profiles of flat specimens fretted for 10^6 cycles at a displacement amplitude of (a) 25 µm; (b) 100 µm (*f* = 20 Hz; *P* = 450 N).

To more effectively compare overall trends in scar shape over the range of conditions tested, averaged 2D profiles were calculated and are presented in Figure 5.3 for flat specimens fretted at both small (Δ^* = 25 µm) and large (Δ^* = 100 µm) displacement amplitudes over the range of durations tested; these can be seen to represent well the overall scar shape as seen in Figure 5.2. Throughout the duration of tests at both small and large displacement amplitudes, wear scars are broadly U-shaped, and that there is no apparent change in scar shape as wear develops. After 10^5 cycles, the depth of the central region of wear scars relative to adjacent regions differs slightly with the change in displacement amplitude; namely, the scars formed at smaller displacement amplitude (Δ^* = 25 µm) exhibit a flatter central region (a region approximately 1 mm in width) than scars formed at larger displacement amplitude ($\Delta^* = 100$ μm), which exhibit more of a V-shape (a region approximately 0.1 mm in width).

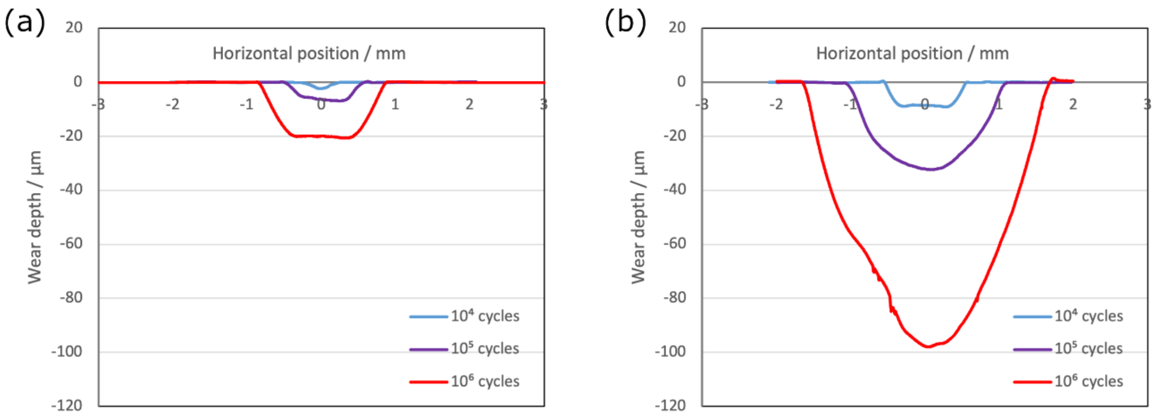

Figure 5.3. Average profiles of the resulting wear scars on the flat specimens from pairs after fretting with an applied displacement amplitude of (a) 25 μm; (b) 100 μm over a range of test durations (f = 20 Hz; P = 450 N; $N = 10^6$ cycles).

The evolution of energy coefficient of friction (as a function of number of cycles) is shown in Figure 5.4, from which it can be seen that over the range studied, coefficient of friction is broadly independent of displacement amplitude, with values at large and small displacement conditions ranging from ~0.75 to ~0.8 and remaining broadly steady over the duration of tests.

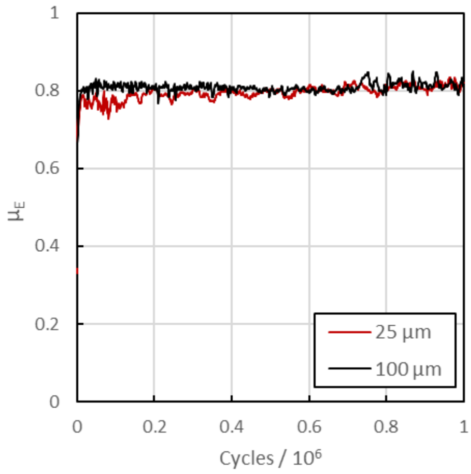

Figure 5.4. Evolution of energy coefficient of friction (μ_E) with number of fretting cycles as a function of applied displacement amplitude over the range tested, showing no significant impact of displacement amplitude on friction (f = 20 Hz; P = 450 N; $N = 10^6$ cycles).

To better understand the effect of displacement amplitude on the development of compacted debris beds, wear scar surfaces were imaged in both plan view and cross-section over the range of displacement amplitudes and test durations examined. BSE SEM is a useful technique in this context due to the ability to clearly contrast oxide debris (darker grey) and exposed metallic surfaces (lighter grey). As highlighted by XRD analysis of ejected debris (Section 4.4.2.3.1), only two phases are present in the ejected debris, and as such it is assumed that debris remaining in wear scars consists solely of these two phases. Accordingly, the contrast between oxide and metal in BSE images provides useful insight into interfacial chemistry, which is reinforced by qualitative EDX measurements.

In examining the images of wear scars, it should be taken into consideration that the ultrasonic cleaning of specimens after tests to remove loose debris may have dislodged pieces of the debris bed, and as such the specimens as imaged may exhibit more exposed metallic regions than were truly exposed during fretting (implications for fretting mechanisms discussed in Section 5.5.3).

Figure 5.5 shows the early stages of debris bed development at both large and small displacement amplitude; it is clear that at both displacement amplitudes an oxide debris bed forms and is adhered to the surface after a relatively short number of cycles, and that at the larger displacement amplitude ($\Delta^* = 100$ μm) the wear scar width is much greater than at the lower displacement amplitude ($\Delta^* = 25$ μm). The wear scar formed at the larger displacement amplitude appears to be more sparsely covered with oxide than that formed at the smaller displacement amplitude; however, higher magnification images indicate that at neither displacement amplitude is the debris bed coverage complete, with exposed metal surfaces visible between patches of oxide even at the lower displacement amplitude.

As test duration is increased, it is clear from the SEM images in Figure 5.6 that even after 10^6 cycles, while debris beds become more developed (i.e. a greater proportion of the surface is covered) at both large and small displacement amplitudes, coverage remains incomplete (i.e. exposed metallic regions remain visible). There is also a significant increase in wear scar width, from approximately 0.4 mm after 10^4 cycles to 1.7 mm after 10^6 cycles for the lower displacement (Δ^* = 25 μm), and from 1 mm to almost 4 mm for the larger displacement (Δ^* = 100 μm) over the same number of cycles (approximately a factor of 4 in both cases).

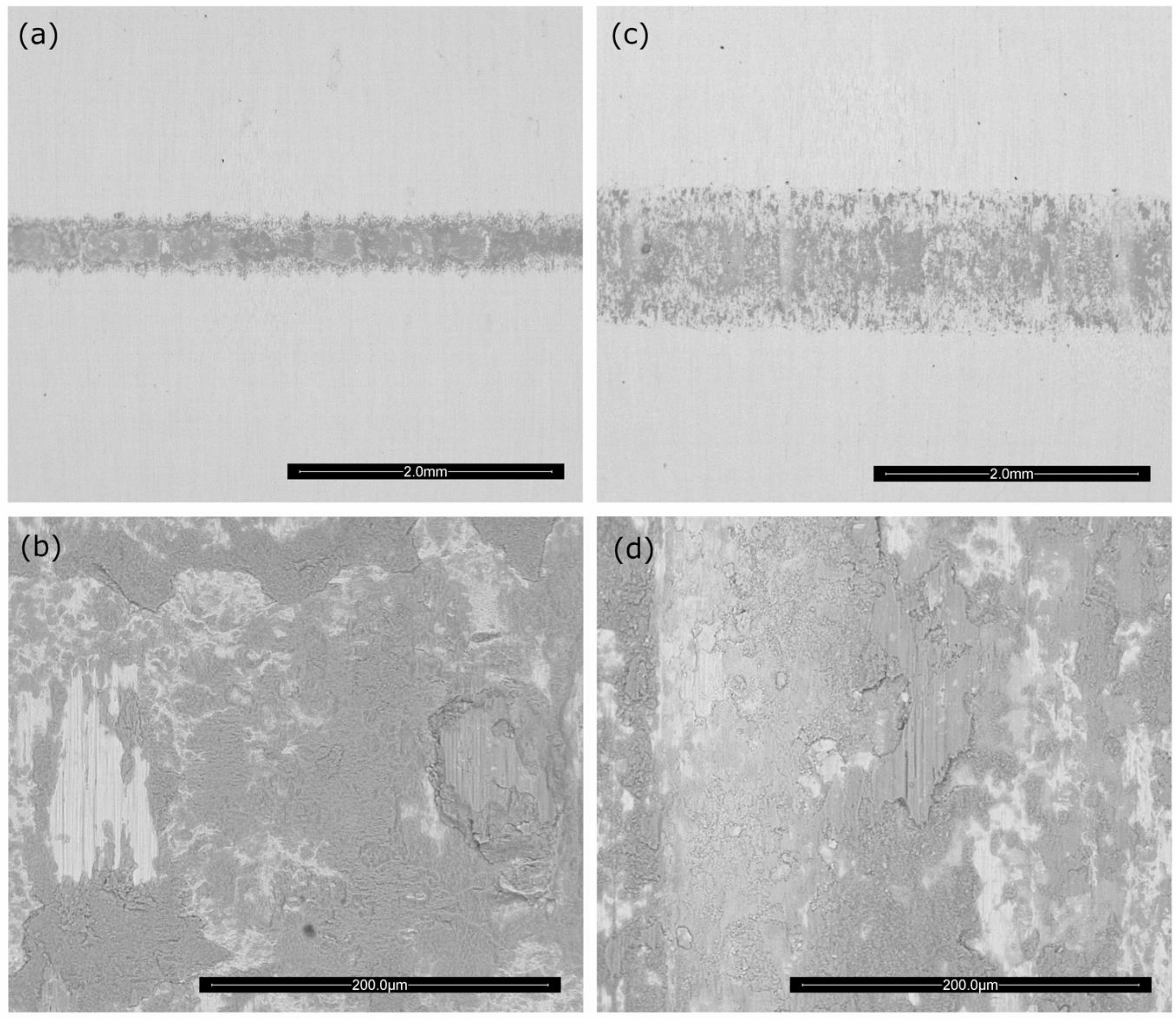

Figure 5.5. BSE SEM micrographs in plan view of flat specimens after fretting for 10^4 fretting cycles with an applied displacement amplitude of: (a)-(b) 25 μm; (c)-(d) 100 μm (f = 20 Hz; P = 450 N).

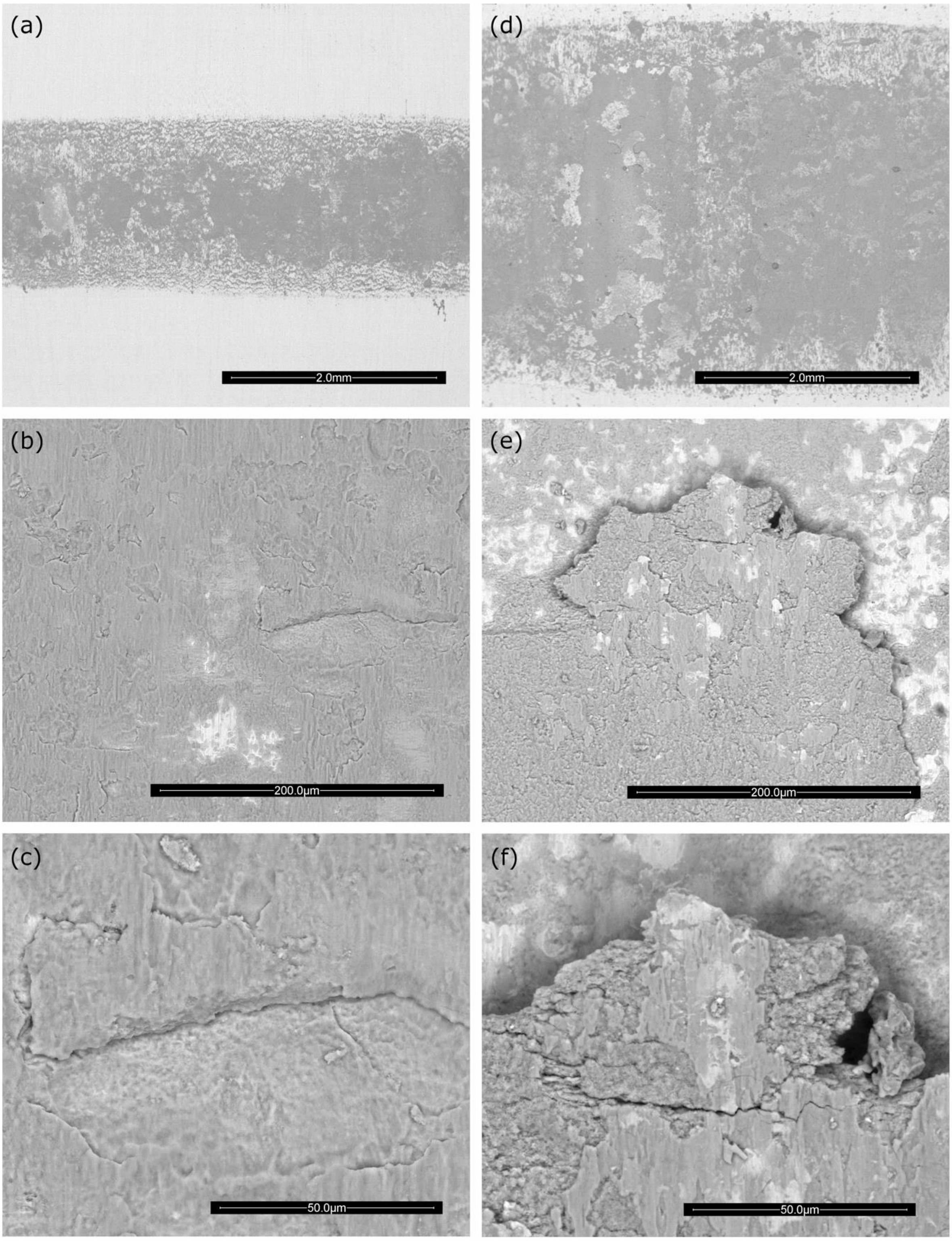

Figure 5.6. BSE SEM micrographs in plan view of flat specimens after fretting for 10^6 fretting cycles with an applied displacement amplitude of: (a) – (c) 25 µm; (d) – (f) 100 µm (f = 20 Hz; P = 450 N).

At higher magnification, it can be seen that the debris bed formed at both large and small displacement amplitudes after 10^6 fretting cycles exhibit cracking at the surface of the bed, suggesting a potential mechanism by which large pieces of compacted debris may become detached from the surface. This is apparent in Figure 5.6(e) and Figure 5.6(f), where a region of developed oxide bed can be seen on top of a more exposed metallic surface (i.e. exhibiting a small degree of oxide coverage), with uneven edges indicating that surrounding pieces have broken away; a crack can be seen to run through a protruding region which, at approximately 50 μm in width, is consistent with the scale of some debris particles observed in the analysis of ejected debris.

Lighter grey regions within the developed oxide debris layers are also visible from the BSE images in Figure 5.6; it is not clear how deep these metallic regions extend beneath the surface of the debris bed (i.e. whether they are caused by a very thin layer of metal smeared across the surface or whether the debris beds contain metal particles several microns in depth), but it is possible that these metallic regions of debris beds may constitute some of the metallic fraction observed in the XRD and Rietveld analyses (Section 4.4.2.3).

The SEM images in Figure 5.7 show the central region of wear scars formed at both displacement amplitudes at a constant magnification, and it can be seen that at both amplitudes there is a coherent bed of oxide debris atop a relatively undeformed and undamaged region of the bulk material. The martensitic structure of the material can clearly be discerned from the images of the etched surfaces, indicating that only minimal grain refinement has occurred; under these conditions, any damaged layer can only extend a very short distance under the surface (no more than a few microns), as no such layer could be identified using the SEM technique employed.

Furthermore, applied displacement amplitude can be seen to have an impact on the thickness of the oxide debris bed formed, with the debris bed formed at the lower of the two displacement amplitudes ($\Delta^* = 25$ μm) being approximately 5 μm in thickness, more than twice the thickness of that formed at the larger amplitude ($\Delta^* = 100$ µm), which is approximately 2 µm. However, considering the variation in debris bed coverage apparent from the plan view images in Figure 5.6, measurements of bed thickness from cross-sections should be approached only as approximations.

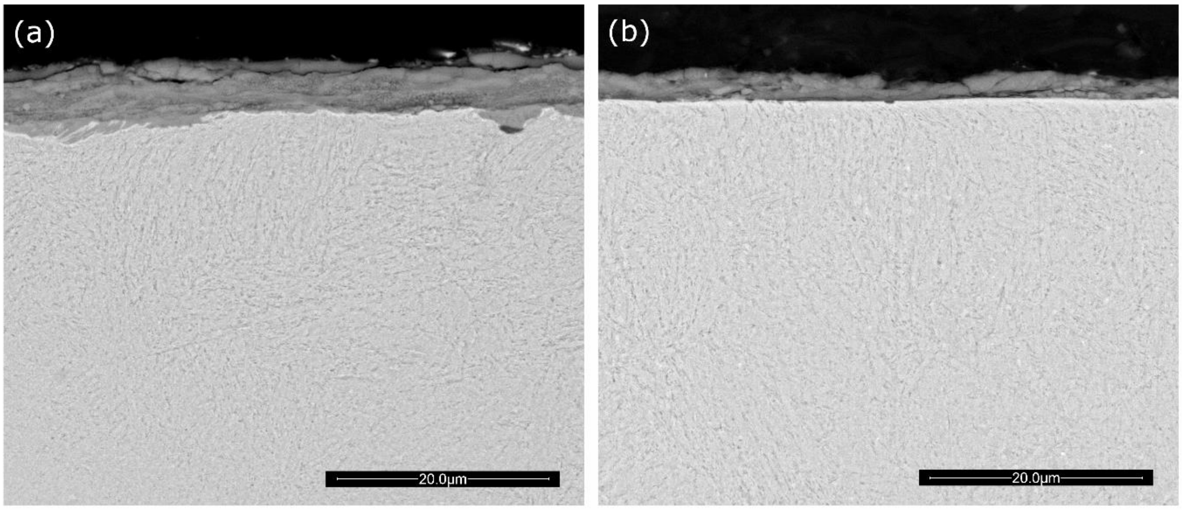

Figure 5.7. BSE SEM micrographs in cross-section of cylinder specimens after fretting for 10^6 fretting cycles with an applied displacement of: (a) 25 µm; (b) 100 µm ($f = 20$ Hz; $P = 450$ N).

The coverage of the surfaces by oxide debris is consistent with the SEM images of the debris beds developed within the wear scars at these conditions in Figure 5.6; this suggests that while areas of metallic surfaces may be exposed by the breakdown of debris beds during fretting tests, these regions do not remain exposed long enough for significant adhesion or subsurface damage to occur.

5.2.2 Development of wear damage associated with changes in fretting frequency

The extent of wear as a function of fretting frequency at the set of test conditions examined ($\Delta^* = 50$ µm; $P = 450$ N; $N = 10^6$ cycles) is expressed in Figure 5.8 in the form of (a) wear volume; (b) energy wear rate. In line with other works investigating the effect of frequency in fretting wear [10,25,29,33,34,115] (detailed in Section 4.2.3), increasing fretting frequency is seen to result in the amount of wear being significantly reduced; the wear volume at 200 Hz is approximately 53% smaller than that formed at 20 Hz (with all other input parameters being equal), with a reduction in wear rate of approximately 40%.

The reduction in the extent of wear is reflected in the shape of the wear scars, which can be seen in the surface profiles of flat specimens presented in Figure 5.9 for each of the frequencies tested, and the associated average profiles in Figure 5.10. As well as a general reduction in wear scar width and depth, the wear scars developed at the two higher frequencies exhibit central regions that are raised relative to the surrounding material, located along or close to the centreline of the scar.

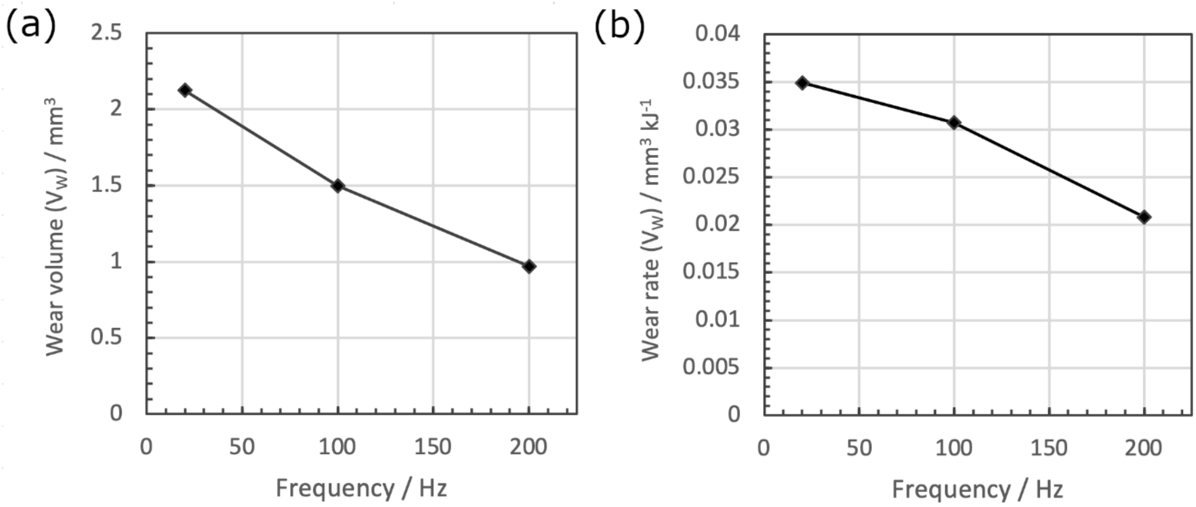

Figure 5.8. Extent of wear at the three frequencies tested, expressed as: (a) net total wear volume; (b) energy wear rate (Δ^* = 50 μm; P = 450 N; N = 10^6 cycles).

The evolution of energy coefficient of friction (as a function of number of cycles) is shown in Figure 5.11, from which it can be seen that over the range of frequencies tested, while the values at all three frequencies at the end of the tests range from ~0.7 to ~0.8, coefficient of friction decreases as frequency is increased. The coefficient of friction remains broadly steady over the duration for tests conducted at 20 Hz and 100 Hz, and at the highest fretting frequency (200 Hz) increases from ~0.6 to ~0.7 over the duration of the test.

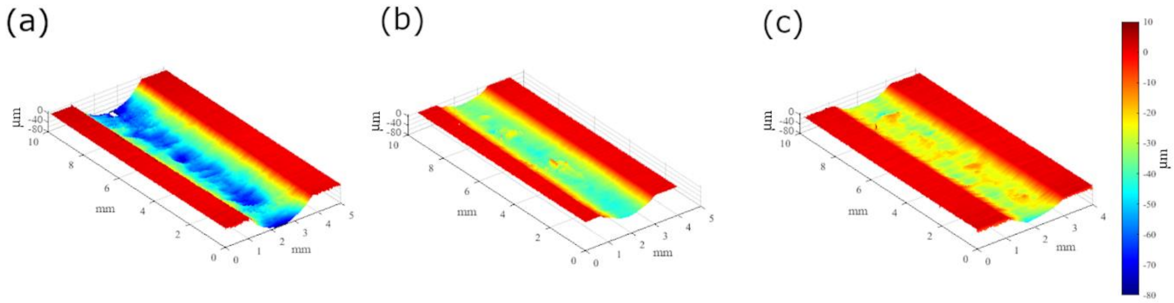

Figure 5.9. 3D surface profiles of wear scars on the flat specimens after fretting for 10^6 cycles with an applied displacement amplitude of 50 μm with frequencies of (a) 20 Hz; (b) 100 Hz; (c) 200 Hz ($\Delta^* = 50$ μm; $P = 450$ N).

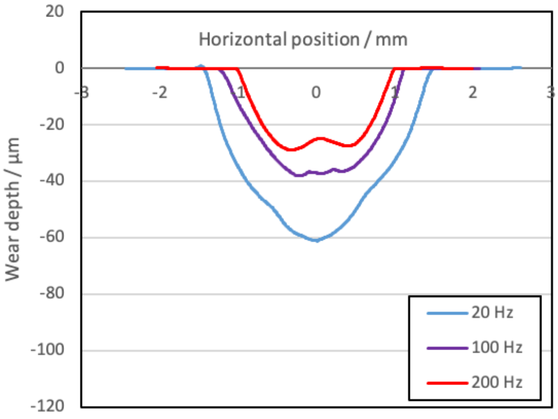

Figure 5.10. Average profiles of the wear scars on the flat specimens over the range of frequencies tested ($\Delta^* = 50$ μm; $P = 450$ N; $N = 10^6$ cycles).

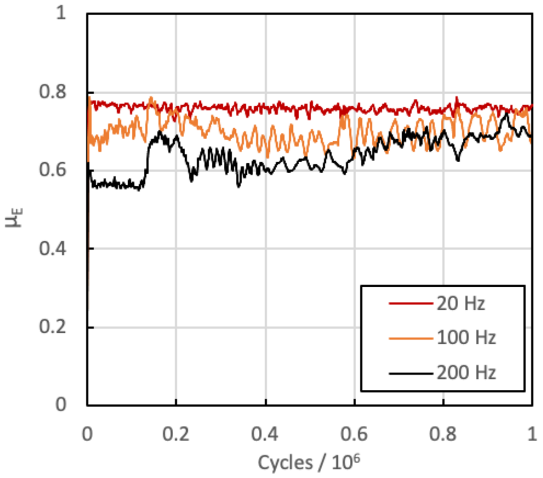

Figure 5.11. Evolution of energy coefficient of friction (μ_E) with number of fretting cycles as a function of fretting frequency over the range tested; friction can be seen to be lower at higher fretting frequencies, with this effect diminishing as tests progress ($\Delta^* = 50$ μm; $P = 450$ N; $N = 10^6$ cycles).

The nature of worn surfaces developed over the range of frequencies tested, particularly the coverage by compacted beds of mostly oxide debris, is shown in BSE SEM images of wear scars in Figure 5.12. As with the average worn profiles presented in Figure 5.10(b), it is clear from the SEM images in Figure 5.12 that increasing fretting frequency has a significant effect on the development of the wear scar, with scars becoming narrower and the surfaces more metallic as frequency is increased from 20 Hz to 200 Hz. At the lowest frequency (f = 20 Hz), coverage by a developed oxide debris bed extends throughout the wear scar, as observed in Section 5.5.2.1, while wear scars developed at higher frequencies appear very different in both the extent of debris coverage and the composition of the debris retained within the scar. At both 100 Hz and 200 Hz, large patches of metallic material of the order of 1 mm in width are visible in central regions of the wear scars (identifiable as such by the lighter contrast of the BSE image relative to the darker oxide regions), which correspond to the regions that are raised relative to surrounding material observed from profilometry data in Figure 5.9 and Figure 5.10.

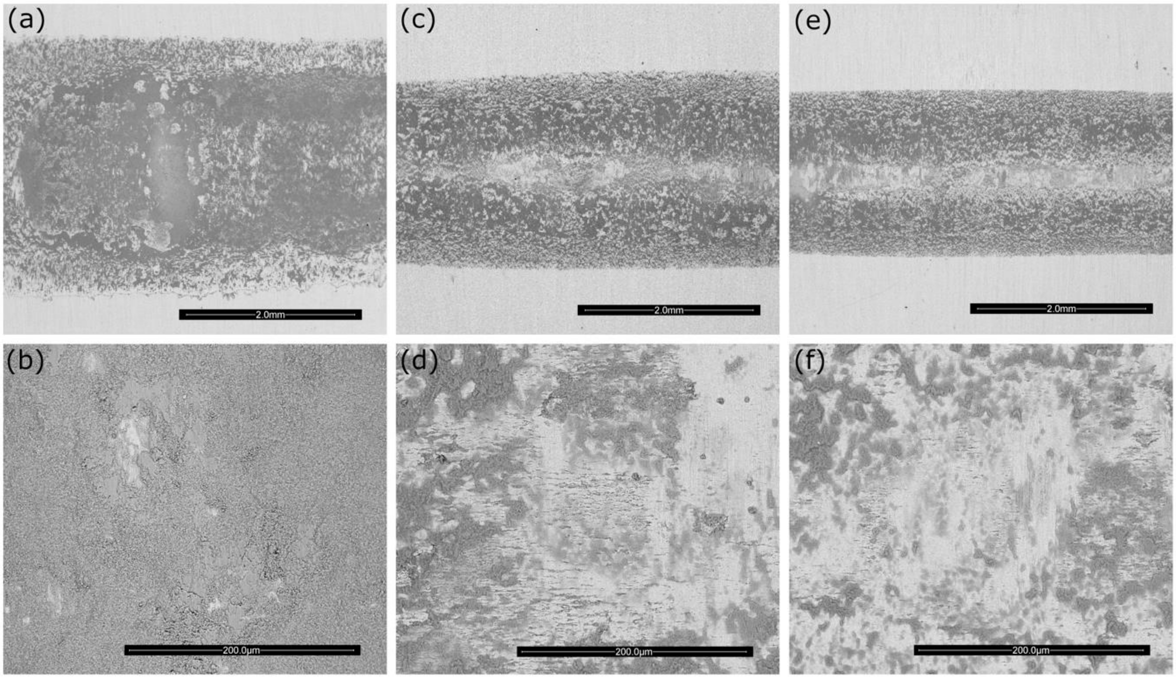

Figure 5.12. BSE micrographs of flat specimens in plan view at high and low magnification after fretting tests at a frequency of (a)-(b) 20 Hz; (c)-(d) 100 Hz; (e)-(f) 200 Hz (Δ^* = 50 μm; P = 450 N; $N = 10^6$ cycles).

Examining specimens in cross-section, it can be seen that the tendency towards the development of more metallic surfaces at higher fretting frequencies is associated with a significant difference in the nature of the subsurface region, which at the two higher frequencies exhibits significant subsurface damage. Figure 5.13 shows a BSE SEM image in cross-section of the cylinder specimen of a pair fretted at low frequency (*f* = 20 Hz), in which the wear scar surface is covered by a coherent bed of oxide debris approximately 5 μm in thickness, identified as iron oxide by its dark contrast relative to the bulk metal and confirmed by qualitative EDX analysis. While the image in Figure 5.13(a) shows only a small region of the scar (approximately 70 μm in width), this debris bed was observed to span most of the width of the wear scar and to be broadly consistently in thickness. This behaviour is consistent with cross-sections of cylinder specimens after fretting at both smaller and larger amplitudes (at the same frequency) presented in Figure 5.7 (Section 2.1).

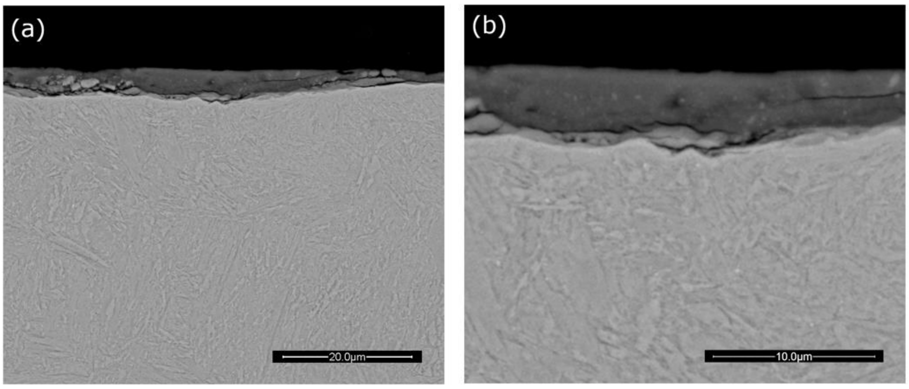

Figure 5.13. BSE SEM micrograph in cross-section of an etched cylindrical specimen after fretting at 20 Hz ($\Delta^* = 50$ μm; $P = 450$ N; $N = 10^6$ cycles).

When fretting frequency is increased to 100 Hz, the nature of the subsurface changes significantly; Figure 5.14 shows a cylinder specimen fretted at 100 Hz exhibiting significant levels of subsurface damage, with a region of severely damaged, predominantly metallic material (identifiable as such by its similar contrast to the bulk metal in the BSE image) extending approximately 30 μm into the surface.

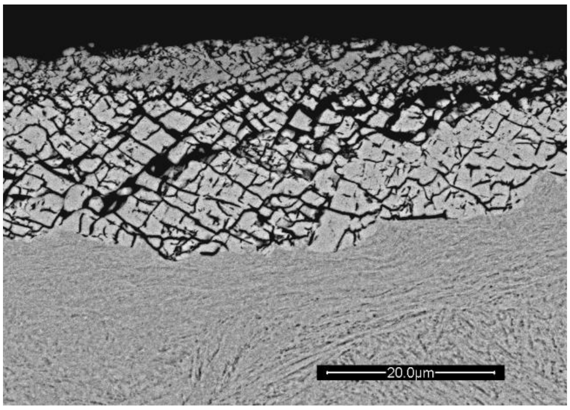

Figure 5.14. BSE SEM micrograph in cross-section of an etched cylindrical specimen after fretting at 100 Hz, showing a region of severely cracked metallic material in the near-surface region (Δ^{*} = 50 µm; P = 450 N; N = 10^6 cycles).

A secondary electron (SE) micrograph of the same specimen at higher magnification is presented in Figure 5.15, providing greater detail of the appearance of the damaged region; from this it can be seen that the fragments of metal in this region are of the order of 2-3 µm in width (and broadly equal height), and exhibit a significant degree of porosity.

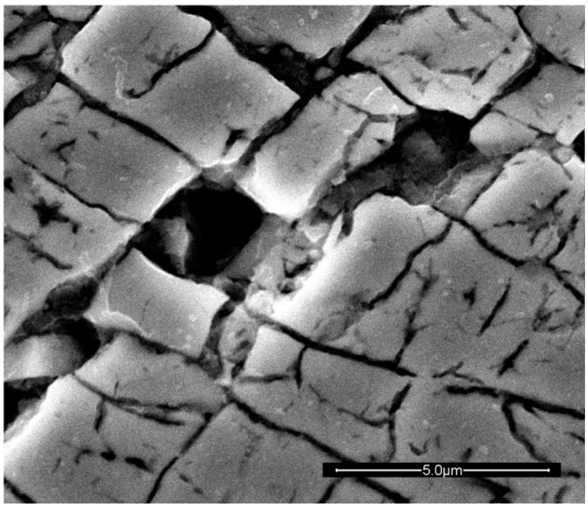

Figure 5.15. SE SEM micrograph at high magnification the damaged region developed in a cylinder specimen after fretting at a frequency of 100 Hz; the metallic structure can be seen to exhibit significant porosity and an even cracking pattern (Δ^{*} = 50 µm; P = 450 N; N = 10^6 cycles).

In examining cross-sections of repeat tests at the same set of test conditions, as well as multiple cross-sections from specimens, such a severely cracked metallic region was observed to be consistently formed at this set of conditions. However, the nature of subsurface damage developed was also observed to vary significantly, as can be seen in the BSE images shown in

Figure 5.16; as images are presented at various magnifications, it should be noted that the lowest magnification (Figure 5.16(a)) is the same as that used in Figure 5.13(a) and Figure 5.14. In this case, a region of highly porous and severely cracked metallic material develops in the near-surface region, although BSE contrast indicates an elevated oxygen concentration in the layer relative to the bulk material, or the cracked metal layer in Figure 5.14; a debris bed approximately 2 μm in thickness lies atop the surface, with this being thinner and sparser than the debris bed observed at 20 Hz (Figure 5.13).

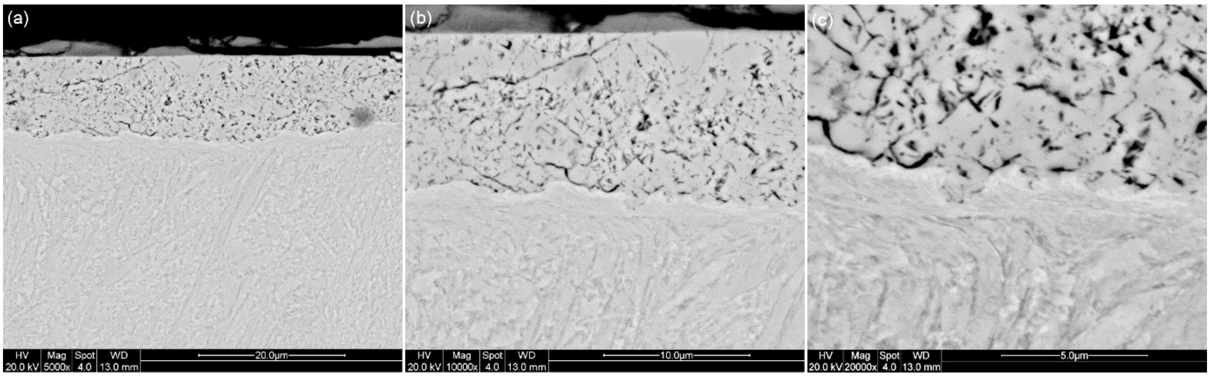

Figure 5.16. BSE SEM micrographs in cross-section at increasing magnifications of an etched cylindrical specimen after fretting at 100 Hz, showing a region of highly damaged, partially oxidised metal ($\Delta^* = 50$ μm; $P = 450$ N; $N = 10^6$ cycles).

While the damaged layer in Figure 5.16 is a darker shade of grey than the bulk material in the BSE image, the difference in contrast between it and the oxide layer at the surface indicates that the porous layer is not a layer of oxide debris, rather it appears to be largely metallic in nature. Qualitative EDX analysis showed the oxygen concentration in this layer to be only slightly higher than that in the bulk metal, and to be much lower than that of the oxide debris bed; the damaged metallic layer is therefore confirmed not to consist of oxide debris, and instead consists of metallic material that may have been transferred between opposing first bodies (as opposed to a transformation of the microstructure progressively extending into the subsurface region). As both types of damage have been confirmed to consist primarily of transformed metallic material, these damaged regions will heretofore be referred to as the tribologically transformed structure (TTS). It is worth noting that the distinct types of damaged metallic layers developed, namely (i) largely unoxidised layers of damaged metal, and; (ii) porous metallic regions that exhibit a slightly elevated oxygen concentration, indicating some degree of transfer between specimens, are broadly consistent with observations reported by Xin et al. [84] of TTS development in fretting of nickel alloy 690TT against a stainless steel counterbody, with these being termed Type I and Type II TTS, respectively (discussed in Section 2.2.4.2).

The higher magnification images of the specimen in Figure 5.16(b) and (c) provide a more detailed view of how this type of damage develops; similar to the "Type I" form of TTS, the layer can be seen to consist of a severely fragmented structure, with fragments on the order of 0.5 – 1 μm in size, but with some that are much larger. A highly sheared layer approximately 1 – 2 μm in thickness formed by plastic deformation of the underlying material can be seen clearly in Figure 5.16(c), separating the transformed material and the undeformed bulk material. Moreover, a distinct boundary can be seen between the transformed material and the thin layer of deformed bulk material, supporting the observation that the transformed layer has at least in part formed through material transfer as opposed to transformation of the underlying surface material.

A wider view of the same specimen, shown in Figure 5.17, shows the layer to span a width of approximately 300 μm in a central region of the wear scar, broadly consistent with the central metallic region visible at the surface of the corresponding flat specimen shown in Figure 5.12(c); this region is significantly smaller than the total width of the wear scar, which is greater than 2 mm.

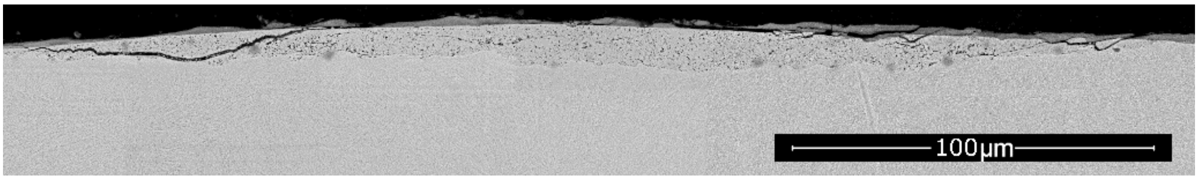

Figure 5.17. BSE SEM image of the central region of the wear scar in cross-section after fretting at 100 Hz; the porous and cracked TTS region can be seen to extend a width of approximately 300 μm across the wear scar (Δ^* = 50 μm; P = 450 N; N = 10^6 cycles).

Due to the technique used to prepare cross-sections for metallographic observation, namely cutting with an abrasive wheel and polishing with increasingly fine grades of silicon carbide papers, it is important to clarify whether the extensive cracking observed is caused (at least in part) by the preparation technique employed. A BSE SEM image of a cross-section prepared using focused ion beam (FIB) milling of a flat specimen fretted at 100 Hz is presented in Figure 5.18; it can be seen that the subsurface region exhibits extensive cracking, very similar in appearance to that observed in the corresponding cylinder specimen (Figure 5.14(b), Figure 5.16), confirming that the cracking pattern observed in cross-sections is developed during the fretting process as opposed to being caused by damage sustained in preparation of samples.

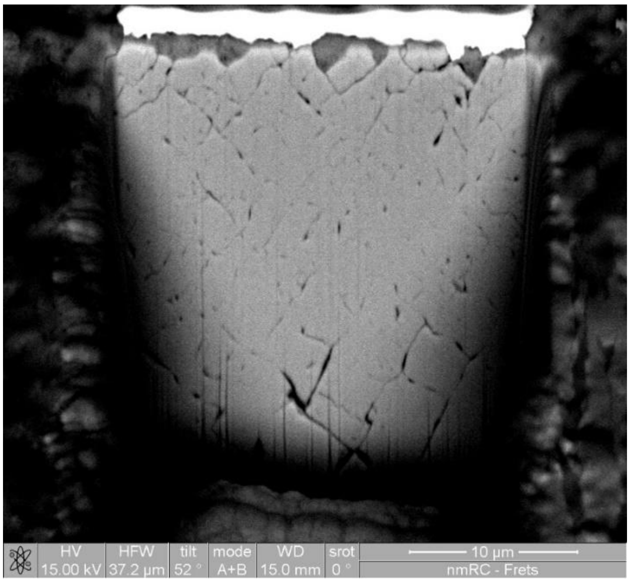

Figure 5.18. BSE SEM micrograph of a flat specimen machined using focused ion beam milling in cross-section (f = 100 Hz; Δ^* = 50 μm; P = 450 N; N = 10^6 cycles).

Fretting at high frequency (f = 200 Hz) can be seen from the images in Figure 5.19 (with magnifications consistent with those used in Figure 5.16) to also result in the development of significant subsurface damage, bearing similarities to the Type I TTS layer formed at 100 Hz. Figure 5.19(a) shows a highly deformed layer of metallic material extending approximately 20 µm below the surface, with no discernible oxide debris bed at the surface; the deformed region is similar in composition to the bulk material and contains several large cracks. While several cracks can be seen to run through the damaged layer (confirmed by qualitative EDX to exhibit no significant difference in composition to the bulk material), no cracks can be seen to extend from the TTS layer into the bulk material.

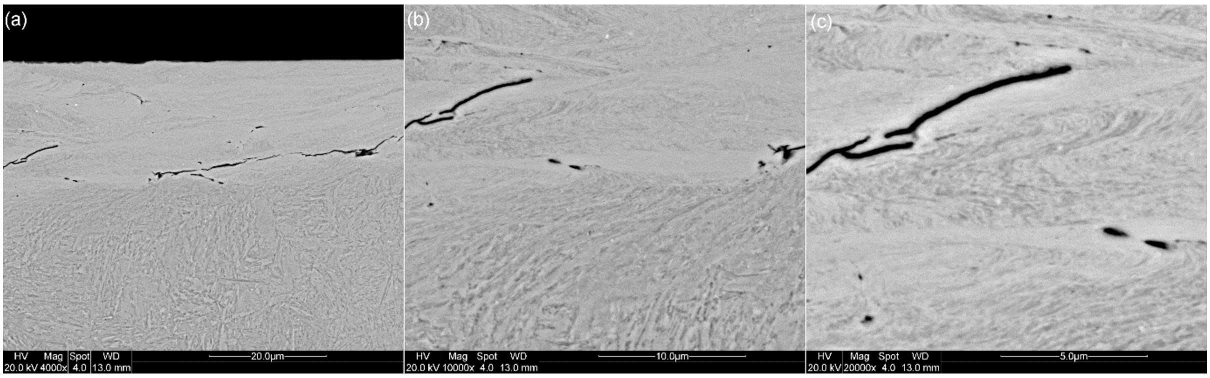

Figure 5.19. BSE SEM micrographs at increasing magnifications in cross-section of an etched cylindrical specimen after fretting at 200 Hz, showing severe deformation and cracking of the TTS layer (Δ^* = 50 µm; P = 450 N; N = 10^6 cycles).

At higher magnifications (Figure 5.19(b) and (c)), severe plastic deformation of the microstructure in the TTS layer relative to the bulk material can be identified clearly from the etched surface of the cross-sectioned specimen, although to varying extents across the layer; in some regions martensitic laths are still discernible in the deformed microstructure, whilst other regions appear to be more severely deformed (identifiable as such by the lighter etching in these highly deformed regions). Cracks and small pores are found spanning the damaged layer, with this being generally confined to the most highly deformed regions.

The transformed region developed at 200 Hz can be seen in Figure 5.20 to extend approximately 250 µm across the central region of the wear scar (similar to the TTS layer developed at 100

Hz), with a long crack broadly marking the boundary between the damaged layer and the bulk material.

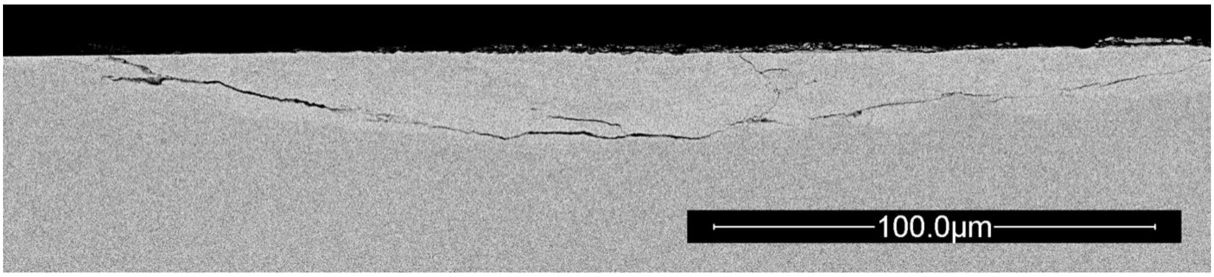

Figure 5.20. BSE SEM image of the central region of the wear scar in cross-section after fretting at 200 Hz; the damaged TTS region can be seen to extend a width of approximately 250 µm across the wear scar ($\Delta^* = 50$ µm; $P = 450$ N; $N = 10^6$ cycles).

As was observed at the 100 Hz condition, the nature of the subsurface damage developed at higher fretting frequency was also found to vary considerably; an example of this variation is presented in Figure 5.21, showing a region of severely cracked metallic material developed in the wear scar of a cylinder specimen after fretting with a frequency of 200 Hz.

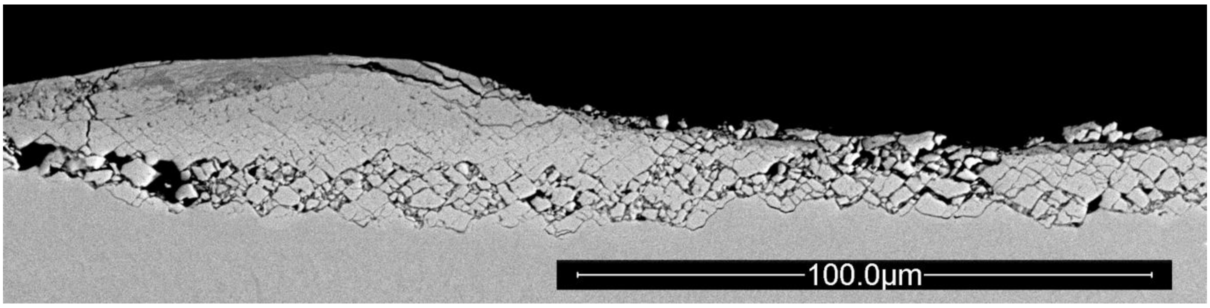

Figure 5.21. BSE SEM image in cross-section of the central region of a wear scar developed in fretting at 200 Hz; a severely damaged region can be seen to extend a width of approximately 200 µm across the wear scar ($\Delta^* = 50$ µm; $P = 450$ N; $N = 10^6$ cycles).

Another image of the same wear scar shown in Figure 5.21 is presented in Figure 5.22, showing a region of partially oxidised metallic material (consistent with "Type II" TTS), similar in appearance to that formed at a frequency of 100 Hz, thereby confirming that both of the higher frequencies ($f = 100$ Hz; $f = 200$ Hz) can result in the formation of both types of subsurface damage.

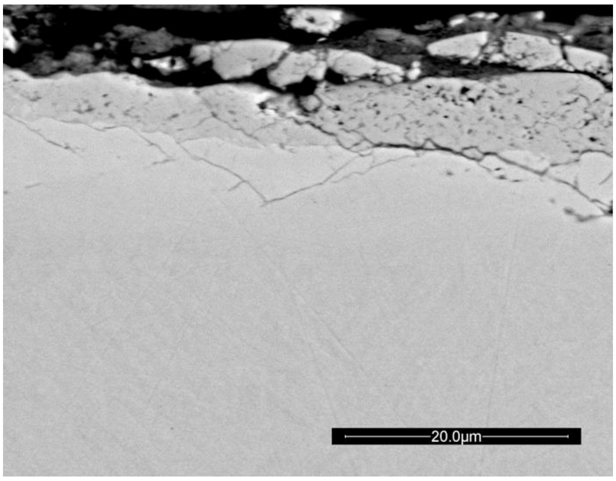

Figure 5.22. BSE SEM image of the central region of the wear scar in cross-section after fretting at 200 Hz; the damaged TTS region can be seen to extend a width of approximately 300 μm across the wear scar (Δ^* = 50 μm; P = 450 N; N = 10^6 cycles).

Changes in the microstructure of the near-surface region developed at each of the three frequencies was assessed using electron backscatter diffraction (EBSD), namely variations in grain size and orientation, that cannot be readily identified from BSE images. Inverse pole figure images (hereby referred to as EBSD maps) were generated for the same cross-sections of cylinder specimens shown in Figure 5.13, Figure 5.16 and Figure 5.19, and are presented in Figure 5.23. The EBSD maps each cover an area of 15 μm × 30 μm, which where possible is highlighted in white on corresponding BSE images; this is only included for the two higher frequencies, where distinctive features of the damaged subsurface enabled the exact regions to be located. At low frequency (f = 20 Hz) the EBSD mapped region includes the oxide debris layer across the surface. Black regions of the maps represent unindexed areas, that is to say areas for which diffraction patterns could not be resolved, which inherently occurs at grain boundaries but may occur as a result of high levels of deformation and damage to the microstructure.

The EBSD images show significant differences in the microstructure of the subsurface region developed at each of the three fretting frequencies; at 20 Hz, there is little evidence of significant deformation or refinement of grains, and the typical martensitic lath structure is visible across the whole surface. As frequency is increased to 100 Hz, there is evidence of a much more significant degree of deformation and grain refinement near the surface, with significant shearing of the bulk material to a depth of approximately 5 μm beneath the boundary with the TTS layer. The TTS layer itself is so severely deformed and damaged that very little of the region could be indexed, as evidenced by the black region immediately beneath the surface.

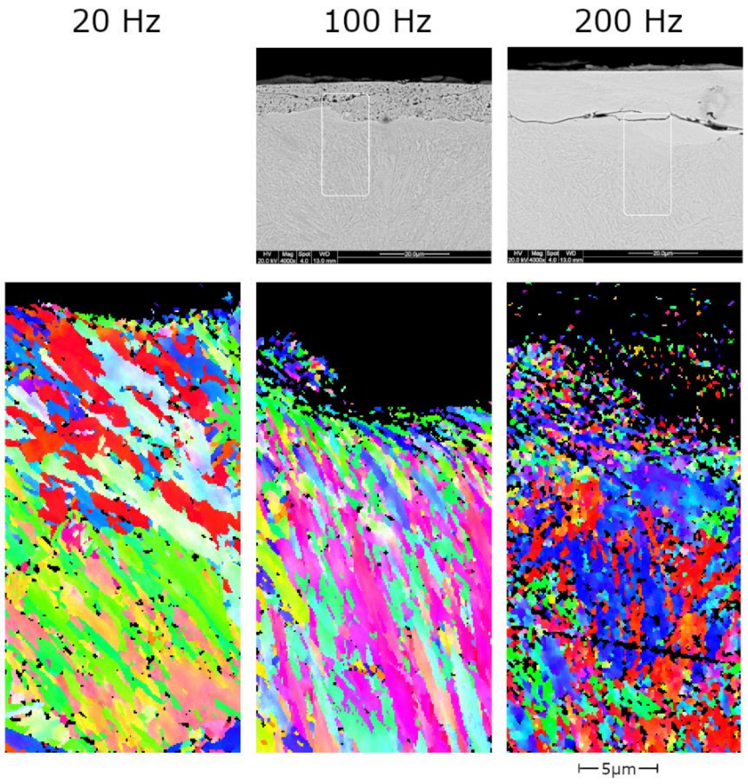

Figure 5.23. Inverse pole figure images obtained using EBSD in central regions of the wear scars of cylindrical specimen for all frequencies tested; where possible, the exact location of the EBSD image is highlighted in corresponding BSE SEM images. It should be noted that the different image types have different scale bars ($\Delta^* = 50$ μm; $P = 450$ N; $N = 10^6$ cycles).

At the highest frequency ($f = 200$ Hz), the TTS region appears to be less severely damaged than that developed in fretting at half the frequency ($f = 100$ Hz), with a greater proportion of the layer being indexable. However, the layer remains mostly unindexable, indicating significant damage to the microstructure. Significant grain refinement is apparent in the region of the TTS closest to the bulk material, although the bulk material itself is not significantly deformed to a depth greater than a few micrometres.

5.2.3 Interaction of displacement amplitude and frequency effects

In the previous two sections, the effects of displacement amplitude and frequency are examined individually, with one of the two parameters being held constant while the other is varied. In the present section, emphasis is placed on the interaction of the two parameters, investigating the development of debris beds and subsurface damage at each of the three displacement amplitudes and fretting frequencies tested in the previous sections of this chapter, i.e. the same range investigated in the previous chapter.

The extent of wear at each of the fretting frequencies and applied displacement amplitudes examined are presented in Figure 5.24, in the same form as presented in Chapter 4 (Section 4.2.1, Figure 4.1), in which the nature of wear debris ejected during fretting at these conditions was investigated. The wear volume after the full duration of tests (10^6 fretting cycles) is plotted against total energy dissipated over the test, with the energy wear rate (material loss per unit dissipated energy) represented by the gradient of a straight line from the origin. Higher dissipated energies reflect higher displacement amplitudes, which slide a greater distance over the same number of cycles.

As shown for a single displacement amplitude in Section 5.5.2.2, increasing frequency results in a significant reduction in wear rate at all three of the displacement amplitudes tested; from Figure 5.24 it can be seen that over the conditions examined wear rate is broadly independent of displacement amplitude at each frequency, and can therefore be approximated by a single straight line through all three displacement amplitudes, with this wear rate seen to decrease by approximately 50% as frequency is increased from 20 Hz to 200 Hz, from 0.0378 $mm^3\ kJ^{-1}$ to 0.0191 $mm^3\ kJ^{-1}$. It is notable that the drop in wear rate with frequency is not evenly distributed across the range of frequencies, with a fivefold increase in frequency from 20 Hz to 100 Hz resulting in a reduction in wear rate of approximately 12%, while a further twofold increase from 100 Hz to 200 Hz results in a much more significant reduction of approximately 43%.

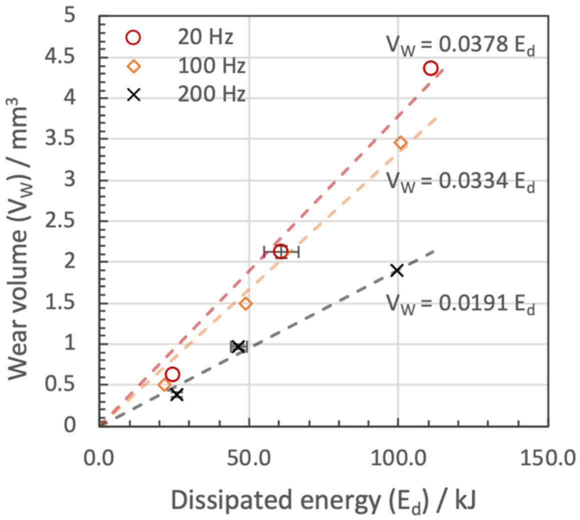

Figure 5.24. Wear volume after 10^6 fretting cycles as a function of dissipated energy for the three fretting frequencies examined in this study; significant differences in dissipated energy reflect the three displacement amplitudes tested (P = 450 N; N = 10^6 cycles).

The energy coefficient of friction (μ_E) over the full duration of tests at these conditions are plotted against number of cycles in Figure 5.25. At small displacement amplitude (Δ^* = 25 μm, Figure 5.25(a)), μ_E is seen to increase from ~ 0.6 to ~ 0.8 over the first ~10 000 fretting cycles, and then remain broadly steady over the remainder of the test; this is largely independent of fretting frequency, with similar observed behaviour at small displacement amplitude across the range of frequencies. The dependence of μ_E upon fretting frequency is seen to be greater when displacement amplitude is larger, with a reduction in μ_E observed at the two higher applied displacement amplitudes (50 μm and 100 μm). It is also notable that at low frequency (f = 20 Hz), μ_E is broadly independent of displacement amplitude, with values lying in the range of ~0.77 to 0.8 over the range of displacement amplitudes. Moreover, the lowest values of μ_E are observed at the highest displacement amplitude (Δ^* = 100 μm) and the two higher frequencies, falling within the range of ~0.45 to 0.65; at the highest frequency (200 Hz), μ_E is observed to be highly unstable, exhibiting significant repeated fluctuations (> 0.1) over periods of ~ 30 000 cycles for the majority of the test.

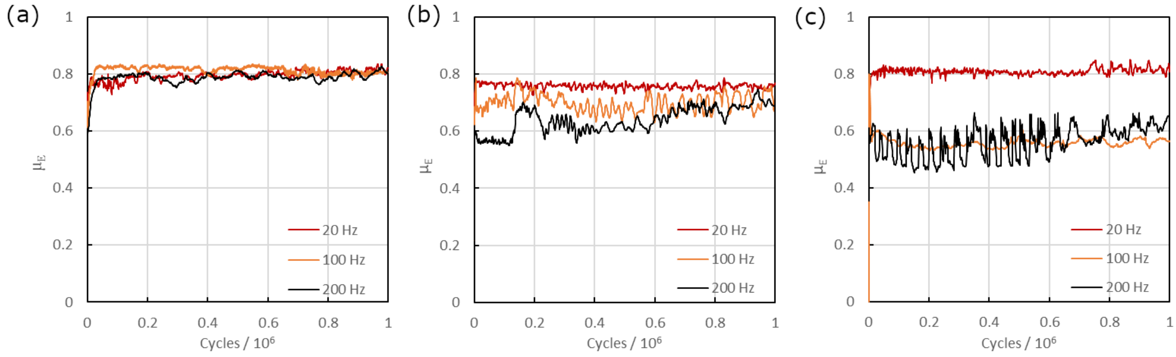

Figure 5.25. Evolution of energy coefficient of friction (μ_E) with number of fretting cycles at displacement amplitude (a) 25 µm; (b) 50 µm; (c) 100 µm over the range of frequencies tested, showing an increasingly significant influence of both frequency and displacement amplitude on friction as both parameters are increased (P = 450 N; $N = 10^6$ cycles).

As observed in Section 5.5.2.2, increases in frequency result in changes in wear scar shape (Figure 5.9 and Figure 5.10) that can be well represented and readily compared by using averaged profiles, as well as identifying whether scars are broadly U-shaped or W-shaped. The impact of displacement amplitude on these changes in scar shape with increasing frequency is highlighted by the surface profiles of flat specimens fretted at high frequency (f = 200 Hz) at each of the three displacement amplitudes tested, presented in Figure 5.26. At all three displacement amplitudes, the wear scars exhibit significant variations in surface height, but at higher displacement amplitudes there is a marked difference in the nature of these variations; at small displacement amplitude (Δ^* = 25 µm), as shown in Figure 5.26(a), the central region of the scar is significantly raised relative to the maximum wear depth, while as displacement amplitude is increased to 50 µm (Figure 5.26(b)) the raised central region becomes less coherent and more dispersed. Figure 5.26(c) shows that at the highest displacement amplitude (Δ^* = 100 µm) there is no raised region at the centre of the scar, with the greatest wear depth occurring at the centre.

Average profiles developed over the range of displacement amplitudes at each of the three frequencies are shown in Figure 5.27. From these it can be seen that, at small displacement amplitude (Δ^* = 25 μm), scars become increasingly W-shaped as frequency is increased, while at higher displacement amplitudes this effect is less pronounced, with wear scars formed at the highest displacement amplitude (Δ^* = 100 μm) remaining U-shaped across the range of frequencies tested.

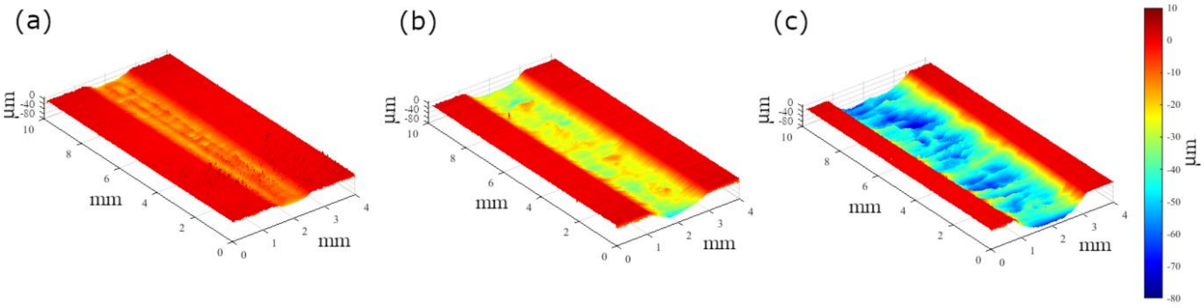

Figure 5.26. 3D surface profiles of wear scars on flat specimens after fretting at the highest frequency tested (f = 200 Hz) for 10^6 cycles with applied displacement amplitudes of (a) 25 μm; (b) 50 μm; (c) 100 μm (P = 450 N; N = 10^6 cycles).

A change in scar shape from U-shaped to W-shaped as frequency is increased has been reported in the literature, such as by Fouvry et al. [29] with this being associated with restricted oxygen access inhibiting the formation of an accommodating oxide debris layer between first body surfaces and thereby promoting adhesive transfer of material between specimens. U-shaped scars are formed when sufficient oxygen is present at the interface to continually form oxide, separating surfaces and reducing adhesive contact (the primary mode of damage instead being abrasion by hard oxide particles), while W-shaped scars are formed when oxygen concentration is insufficient to form such an oxide layer throughout the contact, leading to metal-to-metal contact and adhesive transfer.

The BSE SEM images of the wear scars in plan view in Figure 5.28 show that oxygen starvation is not necessarily the cause of W-shaped scars under all conditions; at small displacement amplitude (Δ^* = 25 μm) it can be seen that wear scars are covered by a coherent bed of oxide debris at each of the frequencies tested. Similarly, scars developed at low frequency (f = 20 Hz) are also covered by primarily oxide debris beds, although there appear to be more areas where the beds have broken down (identifiable from exposed regions of the underlying metallic surface that appear brighter). As mentioned in Section 5.5.2.1, it should be noted that the ultrasonic cleaning of specimens after tests to remove non-adhered debris may have dislodged parts of the compacted debris bed, and as such the extent to which such areas were exposed during fretting is not clear.

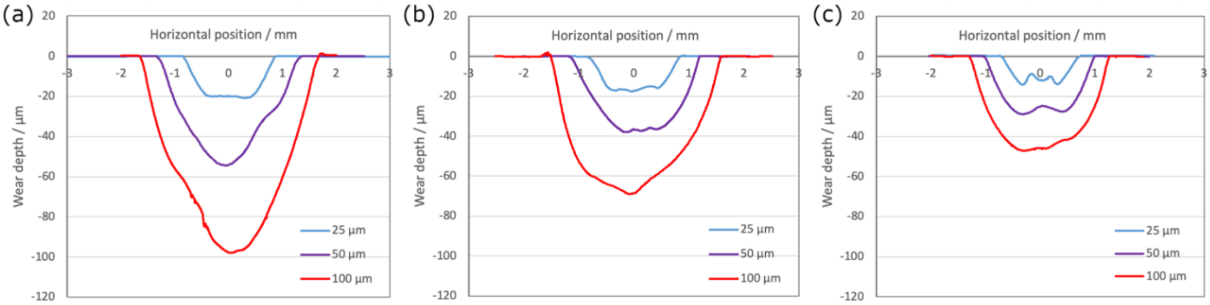

Figure 5.27. Average wear scar profiles of flat specimens after fretting for 10^6 cycles at three different applied displacement amplitudes with frequencies of (a) 20 Hz; (b) 100 Hz; and (c) 200 Hz. Scars can be seen to become more W-shaped as displacement amplitude decreases and frequency increases (P = 450 N).

Despite the presence of exposed metallic regions at both low frequency (f = 20 Hz) and small displacement amplitude (Δ^* = 25 µm) conditions, oxide coverage is fairly uniform, spanning the width of the scar. Moreover, at small displacement amplitude (Δ^* = 25 µm), debris beds appear to become more coherent as frequency is increased; comparing the images in Figure 5.28 to the wear scar profiles in Figure 5.27, the increasingly coherent oxide debris beds with increasing frequency (Figure 5.28) can be seen to correspond to more W-shaped scars (Figure 5.27), indicating that under these conditions, the raised central region consists (at least in part) of retained oxide debris.

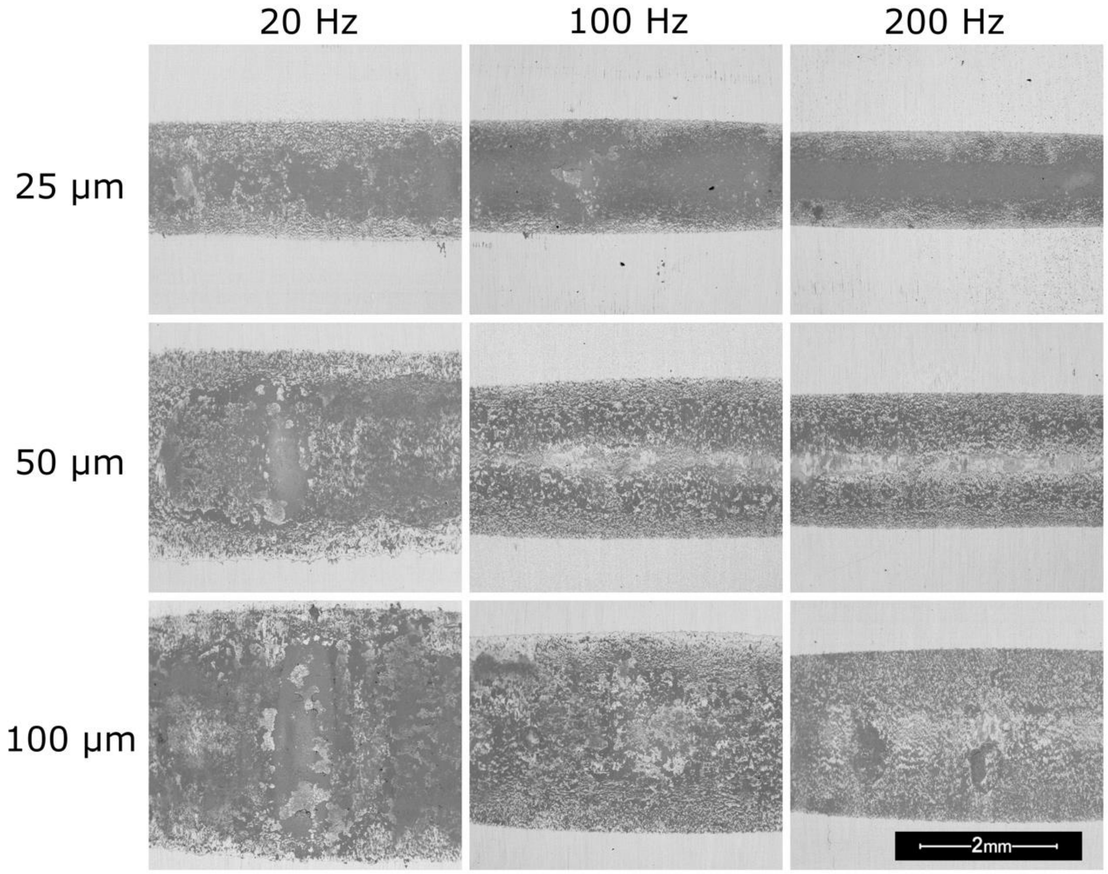

Figure 5.28. BSE SEM micrographs in plan view of the wear scars developed on flat specimens after fretting for 10^6 cycles over the range of frequencies and displacement amplitudes tested, showing a marked difference in the nature of the debris beds, with reduced oxide coverage observed at larger displacement amplitudes and higher frequencies (P = 450 N).

Oxide coverage becomes less uniform with increases in both frequency and displacement amplitude, with wear scar surfaces becoming increasingly metallic; this is particularly pronounced in the central regions of scars where it is expected that oxygen access is most restricted. At the intermediate displacement amplitude (Δ^* = 50 μm), wear scars at the two higher frequencies (f = 100 Hz; f = 200 Hz) can be seen to be W-shaped (Figure 5.27), but unlike the oxide-dominated central region observed at the smaller displacement, the raised regions at the centre of wear scars can be seen to be primarily metallic in nature, identifiable as such by the bright contrast in the BSE image relative to the darker oxide regions nearer the edges, suggesting that the raised regions consist at least in part of transferred metal. As displacement amplitude is further increased to 100 μm, the central regions of the scars formed at the two higher frequencies are still metallic, although the regions are not as defined from the bordering oxide regions as at the smaller displacement (Δ^* = 50 μm), and can be seen from average profiles to not be significantly raised relative to the surrounding material, as wear scars are U-shaped.

The difference in the nature of worn surfaces developed at the highest frequency (f = 200 Hz) over the range of displacement amplitudes can be seen in greater detail in Figure 5.29, which show central regions of wear scars at higher magnification. It is evident that displacement amplitude has a significant impact on the damage sustained by the surface material remaining in the centre of wear scars after fretting at this frequency; at small displacement amplitude (Δ^* = 25 μm), a coherent oxide debris bed covers the surface, while at the two higher displacement amplitudes, oxide coverage is much more sparse and the exposed metallic surfaces exhibit severe cracking.

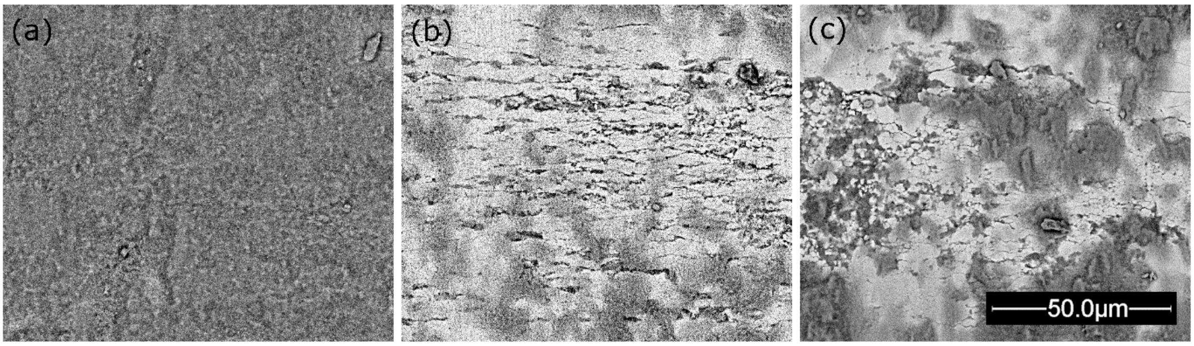

Figure 5.29. High magnification BSE SEM micrographs of flat specimens in plan view after fretting at high frequency (f = 200 Hz) for 10^6 cycles with an applied displacement amplitude of: (a) 25 μm; (b) 50 μm; (c) 100 μm (P = 450 N).

In order to better understand the nature of the damage developed in worn specimens over the range of fretting frequencies and applied displacement amplitudes, BSE SEM images of the wear scars of cylindrical specimens in cross-section are presented in Figure 5.30 in the same format as the plan view images in Figure 5.28. Across the range of frequencies, all wear scars formed at small displacement amplitude ($\Delta^* = 25$ μm) exhibit minimal deformation of the microstructure, and coherent beds of oxide debris are adhered to the surface; likewise, coherent oxide coverage and minimal deformation of the microstructure are observed at low frequency ($f = 20$ Hz) across the range of displacement amplitudes. However, at higher frequencies and larger displacement amplitudes, the nature of the subsurface region differs significantly, with inconsistent oxide coverage and a layer of severely damaged metallic material extending tens of micrometres into the surface.

Comparison with cross-sections of flat specimens indicate that the severely damaged layer of metallic material occurs in both the flat and cylinder specimens of the pair.

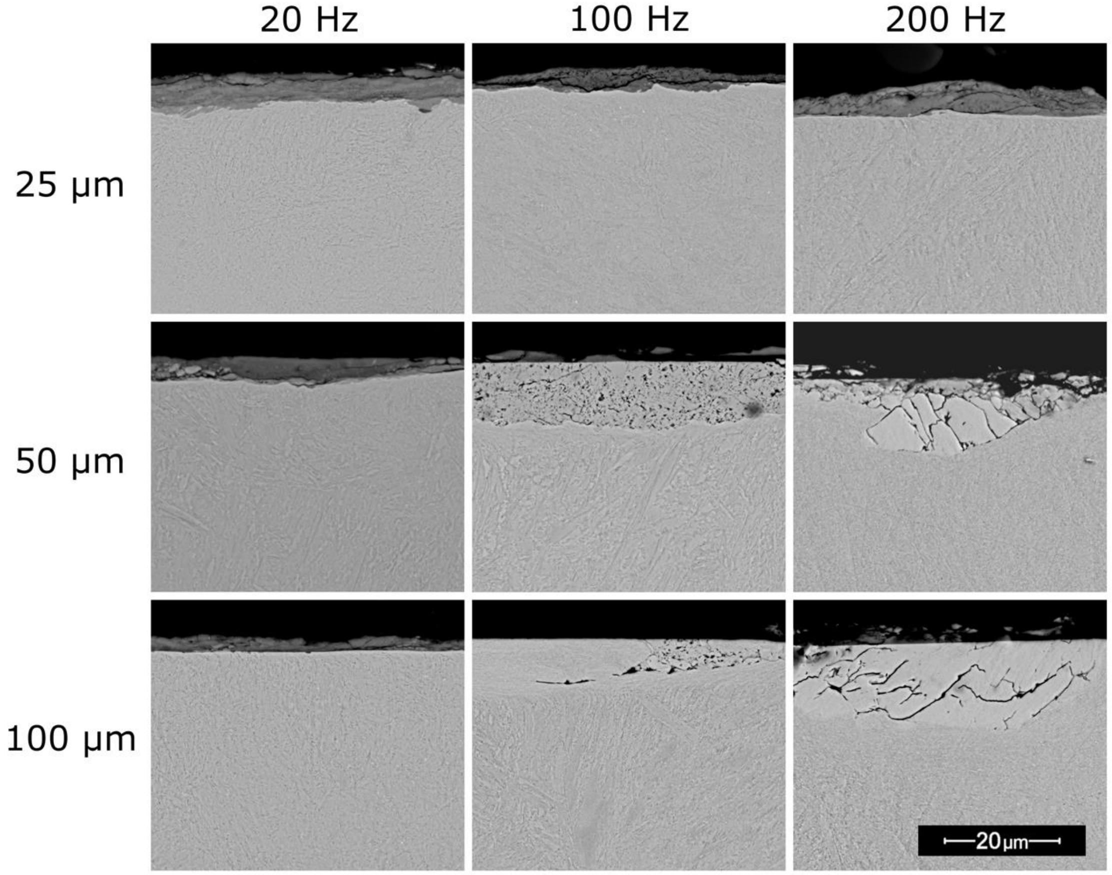

Figure 5.30. BSE SEM micrographs in cross-section of cylinder specimens after fretting for 10^6 cycles over the range of frequencies and applied displacement amplitudes examined, showing the development of significant levels of subsurface damage associated with increases in both parameters ($P = 450$ N).

In order to show all combinations of the three frequencies and displacement amplitudes tested, the images in Figure 5.30 show only a small region of the wear scars, approximately 50 μm in width and 40 μm in height, while the scars can be seen from the profiles in Figure 5.27 and the plan-view SEM images in Figure 5.28 to range from ~1.5 mm to ~4 mm in total width. Images showing a greater area of the wear scars were presented in Section 5.2.2 for the scars formed in fretting with an intermediate displacement amplitude of 50 μm and fretting frequencies of 100 Hz (Figure 5.17) and 200 Hz (Figure 5.20); from these it was observed that the most severely damaged region is approximately 300 μm in width in both cases. At larger displacement, the size of the affected zone can be seen to be much larger, as can be seen from the SEM images of the highest displacement amplitude, highest frequency condition presented in Figure 5.31; due to the large width of the zone relative to its depth, the surface was imaged in four immediately adjacent sections, with an arrow on the image indicating their position. The damaged region can be seen to span a width of approximately 800 μm within the wear scar, and to extend approximately 20-30 μm below the surface.

The transformed microstructure and cracking in this region can be seen in greater detail in Figure 5.32, which shows a smaller region of the same wear scar, approximately 100 μm in width, near the right edge of the region imaged in Figure 5.31. The microstructure in this region appears heavily modified, exhibiting little evidence of the original martensitic lath structure of the bulk material and instead appearing highly smooth, indicating that the region is highly damaged as it has only been lightly etched relative to the bulk material. A distinct boundary can be seen to separate the bulk material and the damaged metallic region, which exhibit significant differences in both the basic microstructure and the presence of cracks, with extensive cracking in the damaged region that does extend into the bulk material. This sharp boundary suggests that the layer has been formed at least in part by adhesive transfer, but due to the like-on-like nature of the contact configuration employed in this study, this cannot be conclusively determined. An oxide debris bed several microns in thickness can be seen atop the damaged metal, although it appears to be severely fragmented, in contrast to the coherent oxide layers developed at conditions exhibiting minimal subsurface damage (i.e. low frequency and small displacement amplitude).

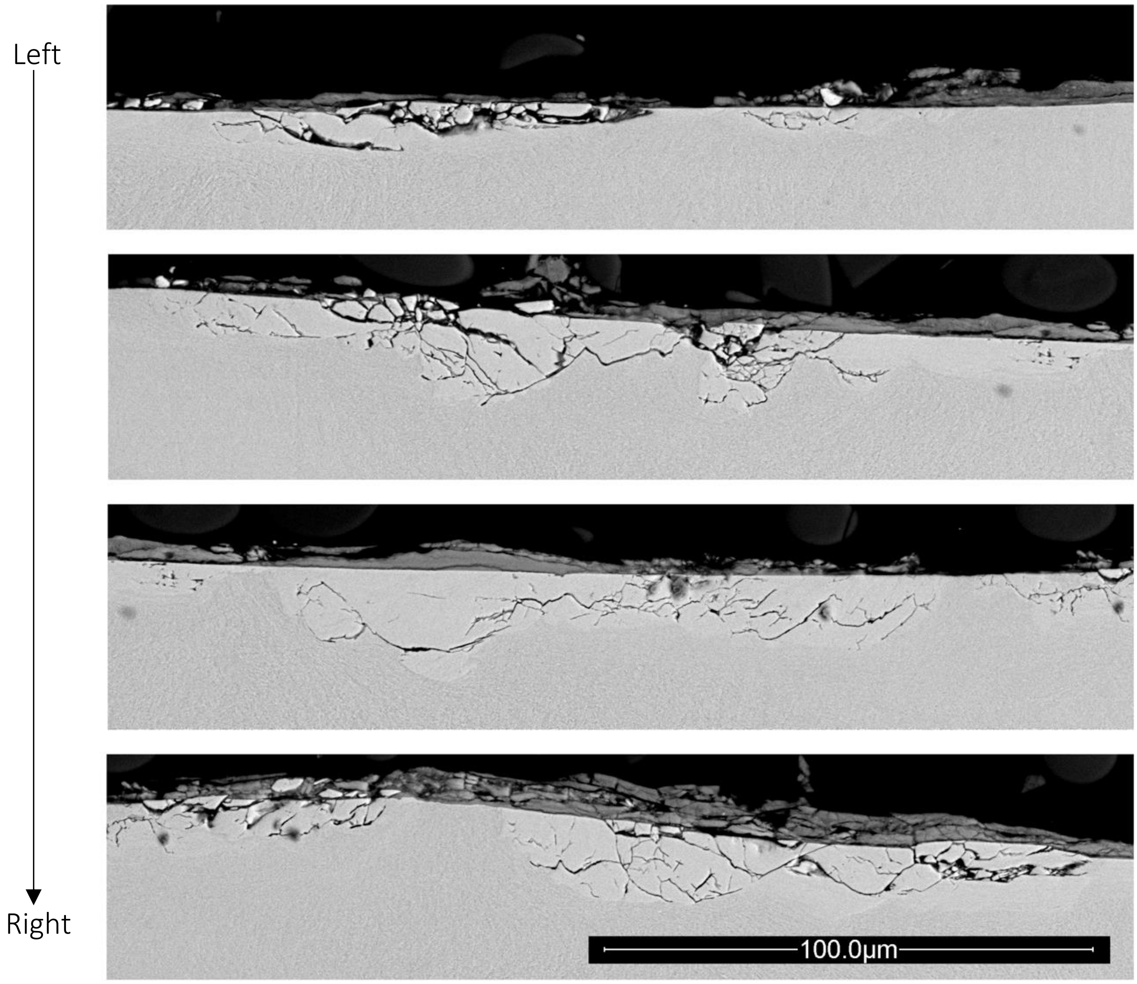

Figure 5.31. BSE SEM micrographs at immediately adjacent locations in the same wear scar, formed during fretting at the highest frequency and largest displacement amplitude tested, showing the significant proportion of wear scar width exhibiting extensive cracking in the near surface region (f = 200 Hz; Δ^* = 100 µm; P = 450 N; N = 10^6 cycles).

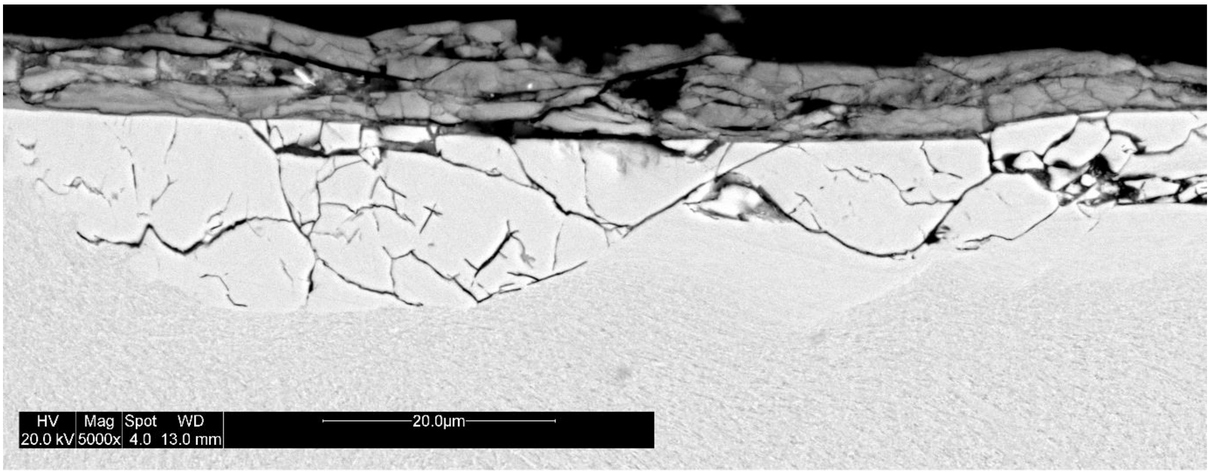

Figure 5.32. BSE SEM micrograph in cross-section of a cylinder specimen fretted at high frequency (f = 200 Hz) with a large displacement amplitude (Δ^* = 100 μm), showing extensive cracking in the near surface region in which there is little evidence of the original martensitic microstructure (P = 450 N; $N = 10^6$ cycles).

5.3 Discussion

5.3.1 Summary of observed behaviour

Two broad classes of behaviour have been observed to occur over the range of test conditions examined, related to the nature of the wear scar surface, the development of sub-surface damage below the wear scar and the energy coefficient of friction, μ_E; clear correlation exists between these three features, with the key similarities and differences across the tested range of displacement amplitudes and fretting frequencies summarised in Table 5.2.

From the features outlined in Table 5.2 it can be seen that under conditions exhibiting the type of fretting behaviour termed "Regime I" is associated with a high coefficient of friction (relative to other conditions tested in this work), wear scars develop oxide debris beds across the majority of the wear scar surface, and there is no significant damage to the microstructure discernible beneath the underlying metal surface. While two types of extensive sub-surface damage are observed to occur (namely one involving direct transformation of the bulk material and another involving adhesive transfer), both are only observed in cases where the wear scar surface is predominantly metallic (i.e. where a protective oxide debris bed fails to develop); as such it is proposed that the failure to form a protective debris bed results in the development of extensive sub-surface damage. Moreover, the failure to develop a protective oxide layer at the surface (resulting in surfaces being predominantly metallic) is associated with a lower coefficient of friction than conditions in which an oxide layer does form; this contrasts with numerous reports in the fretting literature (as well as other forms of sliding wear) that the presence of an oxide debris layer at a wearing interface acts to reduce the coefficient of friction.

Table 5.2 Summary of the features observed in fretting over the range of frequencies and displacement amplitudes examined. Two broad regimes are identified; Regime I (light grey) is characterised by an oxide dominated scar surface, limited sub-surface damage and a high value of μ_E; in Regime II (dark grey), the scar surface is dominated by metal, there is extensive sub-surface damage and a reduced value of μ_E is observed.

		Fretting frequency		
		20 Hz	100 Hz	200 Hz
Applied displacement amplitude	25 µm	• Oxide scar surface • Limited sub-surface damage • High value of μ_E	• Oxide scar surface • Limited sub-surface damage • High value of μ_E	• Oxide scar surface • Limited sub-surface damage • High value of μ_E
	50 µm	• Oxide scar surface • Limited sub-surface damage • High value of μ_E	• Metallic scar surface • Extensive sub-surface damage • Reduced value of μ_E	• Metallic scar surface • Extensive sub-surface damage • Reduced value of μ_E
	100 µm	• Oxide scar surface • Limited sub-surface damage • High value of μ_E	• Metallic scar surface • Extensive sub-surface damage • Reduced value of μ_E	• Metallic scar surface • Extensive sub-surface damage • Reduced value of μ_E

It is clear that the behaviour observed depends upon both the fretting frequency and upon the displacement amplitude, with a Regime I response being observed across the tested range of displacement amplitudes at the lowest frequency, and vice versa at the smallest displacement amplitude. As such, this discussion will explore the impact of these parameters on the tendency for protective, oxide-based debris beds to form during fretting, taking into account their associated impact upon ejected debris investigated in the previous chapter (Chapter 4).

5.3.2 Role of frictional power dissipation

Before considering the effects of the fretting frequency and the applied displacement amplitude separately, it is noted that which of the two regimes occurs is dependent upon displacement amplitude and fretting frequency, which also affect frictional power dissipation in the contact (discussed in Section 2.2.2); it must therefore be considered whether it is the combination of high displacement amplitude and high frequency which induces a change in behaviour from Regime I to Regime II, or whether it is in fact a result of high frictional power dissipation in the contact (generated by that combination of high displacement amplitude and high frequency) which actually results in the transition.

A reasonable starting point is to examine the conditions within the test matrix, highlighting cases in which different combinations of fretting frequency and applied displacement amplitude result in broadly similar frictional power dissipation, but that do not exhibit the same wear regime. This assumes that some aspects of fretting behaviour remain constant over these conditions, such as the coefficient of friction and the slip ratio, which can be seen not to truly be constant, although these differences may be considered to be sufficiently small for this approximate comparison to remain valid. One such example of comparable power dissipation at different fretting frequencies and applied displacement amplitudes occurs where $\Delta^* = 25\ \mu\text{m}$ and $f = 200$ Hz (in Regime I) has broadly the same power dissipation as that occurring where $\Delta^* = 50\ \mu\text{m}$ and $f = 100$ Hz (in Regime II). The fact that the behaviour observed at the former is in Regime I, while at the latter is in Regime II indicates that frictional power dissipation alone does not determine the observed wear regime.

To further investigate the role of frictional power dissipation in the observed change in wear regime, additional tests were conducted in which frequency and applied displacement amplitude were maintained at $\Delta^* = 50$ μm and $f = 100$ Hz, but where the frictional power dissipation was varied by changing the applied load from the standard value of 450 N to 250 N. This comparison has the advantage of being able to explore the role of power dissipation without significant changes in other key factors affected by frequency and displacement, such as the sliding velocity (and hence the time between asperity interactions).

As with comparisons within the test matrix, comparing tests conducted at different normal loads requires the assumption that some aspects of fretting behaviour remain constant, which in reality may be seen to vary, namely the coefficient of friction and slip ratio, although examination of these effects indicates that they do not change significantly over the range examined. In light of this, it may be assumed that the power dissipated under conditions where $\Delta^* = 50$ μm, $f = 100$ Hz and $P = 250$ N is similar to that where $\Delta^* = 25$ μm, $f = 100$ Hz and $P = 450$ N.

Cross-sections of specimens worn under three sets of conditions are presented in Figure 5.33, with Table 5.3 suggesting appropriate comparisons which can be made between the test conditions and sub-surface damage observed in the tests presented in Figure 5.33.

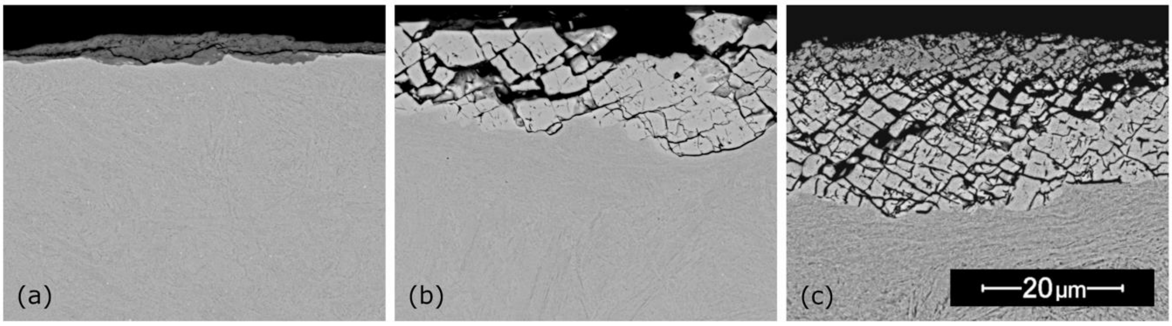

Figure 5.33. BSE SEM images in cross-section of cylinder specimens after fretting under different combinations of displacement amplitude and normal load: (a) $\Delta^* = 25$ μm, $P = 450$ N; (b) $\Delta^* = 50$ μm, $P = 250$ N; (c) $\Delta^* = 50$ μm, $P = 450$ N; showing significant variation in the extent of subsurface damage that develops ($f = 100$ Hz; $N = 10^6$ cycles).

Table 5.3 Comparisons which can be made within Figure 5.33

Comparisons available in Figure 13	Applied displacement amplitude	Fretting frequency	Frictional power dissipation	Sub-surface damage
(a) and (b)	Different	Same	Similar	Different
(b) and (c)	Same	Same	Different	Similar

A comparison of Figure 5.33 (a) and (b) where the frictional power dissipation is similar reveals very different sub-surface damage (associated with the difference in applied displacement amplitude); moreover, comparison of Figure 5.33 (b) and (c) where the frictional power dissipation is different reveals very similar sub-surface damage (associated with the fact that the applied displacement amplitude is the same in both cases). As such, it is argued that the transitions between Regime I and Regime II are associated with changes in fretting frequency and with changes in displacement amplitude, and not with changes in frictional power dissipation.

5.3.3 The combined role of frequency and displacement amplitude on development of a protective oxide-based debris bed

In previous work investigating the role of frequency in fretting wear, using the same material and specimen configuration used in this thesis, Warmuth et al. [34,138], noted that increasing frequency was associated with debris retained in wear scars becoming increasingly metallic, attributed to restricted oxygen access to the interface due to the higher sliding velocity. Warmuth et al. presented cross-sections of specimens fretted at the highest frequency tested (f = 200 Hz), and observed that there was no significant level of material transfer of deformation of the microstructure, although a highly damaged metallic region was observed to occur at the same imposed conditions the cylinder specimen of the pair had a greater radius (160 mm as opposed to 6 mm); such a region was proposed to form due to adhesive wear occurring in regions where oxygen was most effectively excluded from the interface, namely the centre of more-conforming contacts. Moreover, that the damaged metallic region was not observed at the smaller radius (R = 6 mm) was interpreted as an indication that oxygen was less effectively excluded by less-conforming contacts, and hence that the physical width of the contact was a critical factor in the effect of frequency on fretting wear, and of oxygen ingress to fretting contacts more broadly. It should be noted that the work of Warmuth et al. [34] focused on tests run for significantly fewer cycles than in the present work (10^5 cycles as opposed to 10^6 cycles in the present work) and employed a lower applied normal load (250 N as opposed to 450 N in the present work).

The results presented in this chapter (namely Sections 5.2.2 and 5.2.3) indicate that the significant adhesive wear and subsurface damage observed by Warmuth et al. [34] for more-conforming contacts (albeit developed under lower normal load and over fewer cycles) occurs to a similar extent in fretting of less-conforming contacts, which suggests that the conditions employed in the present work have a significant impact on the access of oxygen to the interface. This is further highlighted by the observed impact of displacement on how changes in frequency affect the development of debris beds and subsurface damage in fretting contacts.

While an increase in wear rate with increasing displacement amplitude is observed at a single frequency (Figure 5.1), this difference appears less significant when viewed in the context of wear rates observed across the range of frequencies tested; taken together, the wear rates observed across the range of displacement amplitudes and frequencies examined indicate that, over the studied range, wear rate is largely independent of displacement amplitude. A possible reason for this is that proposed by Pearson and Shipway [26], namely the existence of a threshold energy before which no wear takes place, which when calculating wear rate as a function of dissipated energy, may exaggerate differences between wear rates measured in tests with significantly different dissipated energies (such as those conducted at different displacement amplitudes). In light of this, a single wear rate may be considered representative of all of the displacement amplitudes tested at a given frequency; moreover, a significant reduction in wear rate was observed with increasing frequency for all three displacement amplitudes examined

(Figure 5.24), with an increase in frequency from 20 Hz to 200 Hz resulting in a reduction in wear rate of approximately 50%. However, the reduction in wear rate with frequency is observed to be nonlinear, with a much greater reduction as frequency is increased from 100 Hz to 200 Hz than between 20 Hz and 100 Hz. These changes in wear rate can be seen not to correlate strongly with the observed damage mechanism (Figure 5.30). Moreover, the different damage mechanisms observed are not reflected in the composition of ejected debris, investigated in detail in Chapter 4 over the same test conditions examined in this chapter; while the composition and size of debris are affected by both frequency and displacement amplitude, ejected debris particles consist mostly of oxide (>94%) under all conditions tested, indicating that the onset of metal-to-metal contact and adhesive wear is not accompanied by a transition to a severe wear regime in which large metallic debris particles are ejected. The implications of this discrepancy between the observed wear regime and the nature of debris ejected from the contact addressed directly in Section 5.3.4.

The impact of frequency on debris bed coverage (and in turn wear scar shape) is markedly different at large and small displacements; at small displacement amplitude (Δ^* = 25 μm), wear scars are oxide-dominated and can be seen to become more coherent (i.e. exhibiting fewer exposed metallic regions) as frequency is increased (Figure 5.28, Figure 5.29) corresponding to increasingly W-shaped wear scars (Figure 5.27). Conversely, at high displacement amplitude (Δ^* = 100 μm), while scars remain U-shaped across the range of frequencies, increasing frequency results in debris beds becoming sparser, with a significant proportion of the surface of the wear scar exhibiting exposed metal surfaces.

W-shaped wear scars formed in fretting of metals have been reported in several experimental investigations [8,10,25,29], and are typically associated with a change in wear mechanism from a predominantly abrasive mechanism in which oxide forms throughout the scar, resulting in large wear volumes and U-shaped wear scars, to one in which inhibited oxygenation at the centre of the contact results in adhesive metal transfers, resulting in smaller wear volumes and W-shaped wear scars, The formation of such W-shaped scars is influenced by a number of fretting parameters, including fretting frequency, displacement amplitude, normal load and material combination [23,25]. Fouvry et al. [23] observed W-shaped scars have been observed to develop in fretting of Ti-6Al-4V, with the raised central region of the scar being observed to consist of an oxide layer atop an otherwise U-shaped scar, and in a separate work to consist of TTS-metal transfers occurring due to adhesive wear [25,29]. It has also been reported that W-shaped scars are more typical of fretting of light alloys such as Ti-6Al-4V than steels [23] due to the higher surface energies of the former enhancing their tendency to exhibit adhesive wear.

Both types of W-shaped scars are observed in the present work, each occurring upon increases in fretting frequency, with the nature of the wear mechanism transition dependent on the applied displacement amplitude. At an intermediate displacement amplitude (Δ^* = 50 μm), W-shaped scars Figure 5.10, Figure 5.27 can be seen to be associated with metallic wear scar surfaces (i.e. sparse oxide coverage near the centre of the wear scar), while at lower displacement amplitude (Δ^* = 25 μm) W-shaped scars are associated with the development of a coherent oxide bed, exhibiting no evidence of significant adhesive wear. This indicates that the combination of high fretting frequency and low displacement amplitude are conducive to the retention of oxide debris within the contact, forming a coherent layer that is adhered within the central region of the contact. Moreover, as displacement amplitude is increased, the enhanced rate of debris ejection associated with the larger amplitude inhibits the formation of such an oxide layer, resulting in significant adhesive wear at the centre of the scar.

A significant impact of both frequency and displacement amplitude upon debris retention is consistent with observed effects of both parameters individually reported in the literature [8,9,23,34,92]. The primary effect of increasing frequency is to enhance debris *retention*, with this mostly being attributed to the associated increase in contact temperature (affecting factors such as the rate of debris sintering and the mechanical strength of the bulk material), while increasing displacement amplitude is typically observed to have the opposite effect, promoting the *ejection* of debris particles from the contact.

The interacting effects of frequency and displacement amplitude observed in this chapter arise not only from the impact of both parameters on the rate of debris expulsion, but rather on three key processes that determine the dominant wear mechanism, of which debris expulsion is one, namely:

1) Ingress of oxygen to the contact.
2) Formation of oxide debris.
3) Expulsion of oxide debris from the contact.

It is proposed that whichever of these rates is lowest controls the overall wear mechanism, with this depending on both displacement amplitude and frequency; for example, in the case of small displacement amplitude ($\Delta^* = 25$ μm) and low frequency ($f = 20$ Hz), the rate of oxygen ingress to the contact is sufficient to generate oxide debris due to the low sliding velocity (increasing the time for oxygen to penetrate the contact and reducing the rate of oxygen consumption in forming oxide), while the increase in local temperature due to frictional power dissipation is relatively small and hence results in the oxide being readily ejected. Together, this results in a predominantly oxidative-abrasive wear regime and hence the development of an oxide-dominated, U-shaped wear scar. As frequency is increased, oxygen is more effectively excluded, resulting in an overall reduction in wear rate relative to the same conditions at a lower frequency, while the higher local temperature results in oxide debris being more effectively retained, promoting the sintering of debris particles to form a protective debris bed; the rate of debris expulsion from the contact is thereby sufficiently low that enough oxygen is present to form oxide throughout the contact, preventing significant metal-to-metal contact and resulting in an oxide-dominated, W-shaped wear scar.

In the case of larger displacement amplitudes, the balance is different; at large displacement amplitude (Δ^* = 100 μm) and high frequency (f = 200 Hz), a metallic, U-shaped scar (Figure 5.27(c)) develops, indicating that the enhanced rate of debris ejection is dominant over any increase in the rate of debris sintering resulting from the increased local temperature associated with higher frictional power dissipation. Rather than a localised metallic region at the centre of the scar, an oxide bed can be seen to partially cover the whole surface (Figure 5.28); however, much of the underlying metallic surface remains exposed, and the significant subsurface damage observed at these conditions (Figure 5.30) indicates that while temperature and oxygen access are sufficient to form oxide throughout the contact, the rate of oxide formation and its expulsion from the contact together mean that conditions are not conducive to the formation of a protective debris bed.

The interacting effects of frequency and displacement amplitude on rate-determining processes are illustrated in Figure 5.34 via a series of phenomenological fretting maps, in a format similar to that used by Warmuth et al. [34], with arrows representing changes in key physical processes superimposed over the relative rates over the range of conditions tested in this study. Together with the experimental observations presented in this chapter, these maps highlight the competition between key processes in determining the operative wear mechanisms at different frequencies and displacement amplitudes. For example, in Figure 5.34(a) small displacement amplitude and high frequency can be seen to severely restrict oxygen ingress, due to the relatively short time that the contact is exposed to the atmosphere (due to the high frequency) and the small proportion of the contact that is exposed to the atmosphere (due to the small displacement amplitude). However, Figure 5.34(c) indicates that the rate of expulsion of debris from the contact at this conditions is also severely restricted, due to the relatively high local temperature (due to the high frequency) and large proportion of the contact that remains covered (due to the small displacement amplitude). Experimental data for this condition shows that a coherent debris bed forms (Figure 5.28), resulting in an oxide-dominated W-shaped scar (Figure 5.27) and no significant subsurface damage (Figure 5.30), indicating that it is the rate of debris expulsion from the contact that is the lower of the two rates, and hence debris expulsion is the rate-determining process.

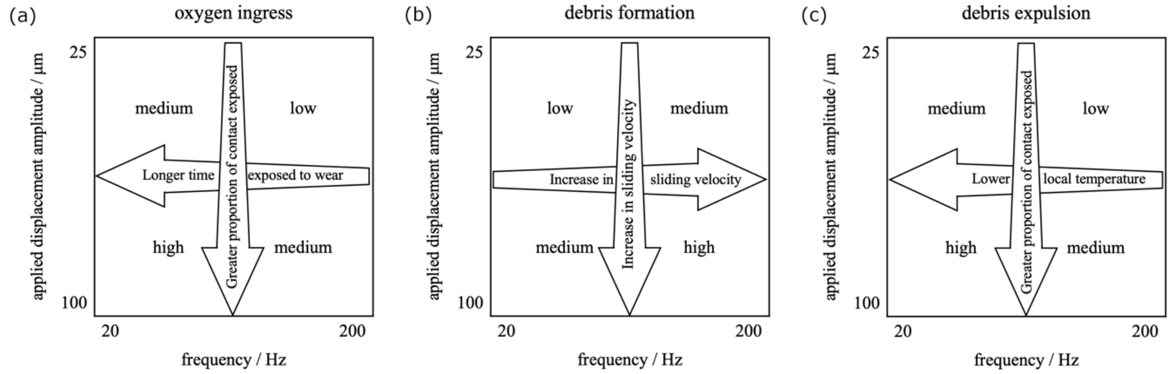

Figure 5.34. Phenomenological fretting maps illustrating how changes in displacement amplitude and frequency affect rate-determining processes (a) oxygen ingress; (b) debris formation; (c) debris expulsion; arrows superimposed on the maps indicate changes in important physical processes affecting debris bed formation over these conditions.

5.3.4 Difference between retained and ejected debris

The changes in composition of retained debris due to changes frequency and displacement amplitude are not reflected in debris actually ejected from the contact, which was observed in the previous chapter not to exhibit significant changes in size and composition over the same range of conditions. While displacement amplitude has a fairly significant effect on the metallic fraction of ejected debris (which, despite always being a small proportion, increases by over a factor of 2 as displacement amplitude is increased from 25 µm to 100 µm), these changes are similar regardless of whether or not a coherent debris bed forms. Likewise, the modest reduction in metallic content with increasing frequency is seen not to correlate with the tendency towards more metallic wear scars under the same conditions. This may be attributed to high local temperatures associated with the high frequency and displacement amplitude conditions that result in the development of more metallic wear scars, increasing the cohesive forces between metallic particles and hence promoting their retention near the centre of the contact, while particles that are eventually ejected must travel to the edges of the contact where the availability of oxygen is greater, and the rate of oxidation is enhanced due to increased local temperature. The composition of ejected debris is therefore not fully representative of all debris formed during fretting, but serves to highlight the localised nature of changes in debris formation in areas where oxygen access is restricted.

While the results presented in this chapter reveal a significant impact of displacement amplitude and frequency upon the mechanism of fretting, namely via their impact on the flow of wear debris and the formation (or otherwise) of protective debris beds, the limited impact of these parameters on the size and composition of debris particles ejected from the contact detailed in the previous chapter suggests that, despite the observed change in damage mechanism, wear (i.e. material removal) always occurs via a predominantly oxidative mechanism, and at no point is there a transition to a severe wear regime in which larger, more metallic debris particles are ejected.

5.4 Conclusions

The effects of displacement amplitude and frequency in fretting wear were investigated, both together and separately, and are shown to exhibit a significant degree of interdependence, with the impact of each of the two parameters on the wear rate and damage mechanism varying based on the magnitude of the other. Two distinct wear regimes were identified, namely (i) at low frequencies and displacement amplitudes, an oxide debris bed forms that covers most of the worn surface, preventing the development of subsurface damage and adhesive transfer but resulting in relatively high wear rates, and (ii) at high frequencies and displacement amplitudes, oxide coverage of worn surfaces is relatively sparse and significant metal-to-metal contact occurs, resulting in the development of significant subsurface damage and adhesive transfer. It is argued that the transitions between the two regimes are associated with changes in fretting frequency and displacement amplitude and are not solely a result of the impact of these parameters on frictional power dissipation. It is noted that while both fretting frequency and displacement amplitude both influence frictional power dissipation, they also affect a number of other processes that are critical to fretting wear; it is proposed that the interacting effects of frequency and displacement amplitude arise from the impact of both parameters on three key processes, namely (i) ingress of oxygen to the contact; (ii) formation of oxide debris; (iii) expulsion of oxide debris from the contact.

As has been observed previously in fretting experiments utilising the same specimen configuration [34], increasing fretting frequency results in a significant reduction in wear rate and to result in wear scars becoming more metallic (i.e. reduced coverage by oxide debris beds). However, this effect is observed in the present work to be dependent upon the displacement amplitude; at smaller displacement amplitude, increasing frequency does not result in scars becoming more metallic, but rather results in the formation of a more coherent debris bed, attributed to these conditions promoting the retention of debris in the contact and hence its tendency to sinter to form a bed.

Two distinct types of damaged metallic layers were observed to develop, one characterised by a porous region of transformed metal, having broadly the same composition as the bulk material; the second is characterised by a slightly elevated oxygen concentration relative to the bulk material, indicating that material in the layer may have been transferred between opposing specimens. Due to the like-on-like nature of the contact configuration employed, it is not possible to assess the extent to which such layers may have been formed by adhesive transfer; this may be resolved by conducting further work using dissimilar pairs, for example steels with similar mechanical properties but different chemical composition, allowing for the origin of damaged material to be readily identified. Both types of damaged layers are observed under conditions in which a debris bed does not form, namely at elevated fretting frequency when displacement amplitude is sufficiently large, reinforcing the observation that it is the inability to form a coherent oxide debris bed that results in the development of these transformed sub-surface layers.

Furthermore, the increasingly metallic nature of wear scars formed at high displacement amplitudes and fretting frequencies contrasts with the comparatively negligible change in the composition of ejected debris over the range of conditions outlined in Chapter 4, in which it was observed that the composition and size of particles ejected from the contact does not exhibit a significant change over the same range of conditions. This indicates that the metallic debris formed under high frequency and displacement conditions is largely retained within contacts. The difference between retained and ejected debris indicates that despite the onset of significant subsurface damage, including adhesive transfer of metallic particles between first bodies, this is not associated with a fundamental change in the mechanism of material removal from the contact (i.e. wear) over the range of conditions examined.

It is noted that the interaction between the effects of frequency and displacement amplitude on fretting wear (via interacting effects on oxygen ingress, debris formation and debris ejection) has implications regarding the development of predictive models of fretting wear, which are explored in the following chapter.

Chapter 6

Modelling wear rates and mechanisms in fretting using a rate-determining process approach

6.1 Chapter outline

The previous chapters have highlighted the critical role of the transport of oxygen and wear debris in determining the operative mechanisms of wear, although accounting for the role of debris has been a key challenge in the development of accurate predictive models for fretting wear [109,117,119,120,122]. In the previous two chapters it has been observed that wear debris consists almost entirely of oxide across the range of displacement amplitudes and fretting frequencies examined, despite significant changes to the nature of wear scars over these conditions; it is therefore proposed that over these conditions wear proceeds by the ejection of oxide debris from the contact, that is to say that if oxide is unable to form then wear cannot proceed, as metallic debris (formed when oxygen concentration at the interface is too low to form a separating layer of oxide debris) is retained within the contact rather than ejected. It therefore follows that transport of oxygen into the contact is also a necessary condition for wear to proceed, as this is necessary for the formation of the oxide-based debris. In this chapter, these hypotheses based on the experimental observations from the previous chapters are used to outline a new model for the prediction of wear rates in fretting wear incorporating the role of transport of oxygen and wear debris in determining wear mechanisms.

When discussing models used for the prediction of wear rates in fretting, a useful reference point is that outlined by Archard [40], which is widely used in numerical models of fretting [12,86,108–110,150], as discussed in detail in Section 2.2.5. Originally derived for sliding wear, the Archard wear equation relates the wear rate (defined as volume of material loss per unit distance slid) to parameters that are mostly readily determined, namely the applied normal load and indentation hardness of the softer of the two bodies; however, the model also requires a wear coefficient, which must be determined experimentally, to account for various complex interacting processes that vary between different wearing systems. Moreover, the sliding wear configuration for which the Archard equation was originally derived differs from fretting wear in several ways, which must be considered and justified if an Archard-type formulation is to accurately predict wear rates in fretting; in addition to the formation of debris particles, two key processes are restricted in fretting contacts relative to sliding contacts due to the fact that the contact remains largely closed (i.e. the amplitude of motion is normally much less than the size of the contact), namely:

(i) Transport into the contact of any environmental species involved in debris formation (e.g. oxygen).

(ii) Transport of the debris out of the contact so that wear can continue.

Both of the above processes are more restricted in fretting contacts than in sliding contacts (i.e. those with significantly larger displacement amplitudes) and therefore have a significant impact on wear rate. The Archard equation in its original form does not contain any terms relating to either of these two processes; consequently, whilst the Archard wear equation and the energy wear approach derived from it [80] are suited to the prediction of the rate of *formation* of debris particles, they cannot account for the role of oxygen availability in the formation of oxide debris or for the role played by debris particles once detached from surfaces and their subsequent *ejection* from the contact. It is therefore important to consider the distinction between particle detachment and debris ejection (i.e. wear) when looking to develop improved models for the prediction of fretting wear.

A model developed by Zhu et al. [134] demonstrated the potential value of this concept in wear modelling, applying the core principles of the third body approach to derive an analytical model for wear rate in fretting contacts based upon a simple hypothesis. In this model, the overall wear rate is assumed to be controlled by the slowest of two critical "rate-determining" processes, these being: (i) debris formation within the contact; (ii) flow of debris out of the contact (debris ejection). It was postulated that the rate of ejection of debris from the contact is inversely proportional to the size of the contact (specifically, its dimension parallel to the direction of fretting), and as such (with a non-conforming contact geometry) the relative rates of the rate-determining processes may change over the course of a test as the contact size increases. This relationship is illustrated in Figure 6.1, in which the overall wear rate is controlled by the slowest of the two rates (i.e. the lowest of the two lines). The wear volumes calculated using the model exhibited good fit with experimental data over a range of contact geometries and test durations (number of fretting cycles).

The apparent validity of such a model, in which wear rate is determined by the relative rates of internal processes, which in turn are dependent on the physical size of the contact, has significant implications for predictive modelling of fretting wear; as fretting tests are conducted with non-conforming contact configurations (that is to say contacts for which size increases as wear proceeds), the relative rates of rate-determining processes may vary considerably, which must therefore be taken into account if wear rate is to be predicted accurately.

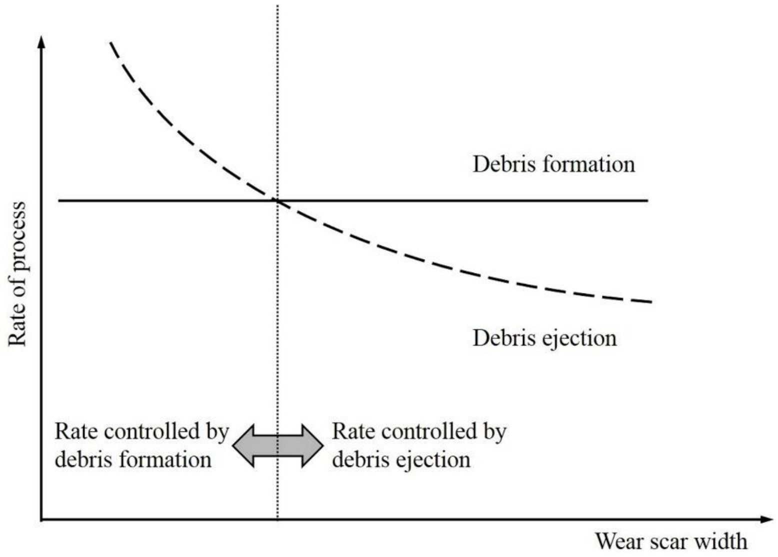

Figure 6.1. Schematic diagram illustrating the proposed dependence of wear rate upon the relative rates of debris formation and ejection with increasing wear scar width presented by Zhu et al. [134]; it was proposed that wear rate is controlled by whichever of the two processes is rate-determining (i.e. the lower of the two lines) at a given scar width.

In the previous chapter of this thesis, it has been demonstrated that the rate of oxygen flow into the contact may restrict the rate at which oxide debris may be formed under certain conditions, namely at high fretting frequencies and large displacement amplitudes. However, the model of Zhu et al. [134] does not address the role played by flow of oxygen into the contact (a necessary precursor to the formation of oxide debris) and the potential for this to be the rate-determining process. As such, the model of Zhu et al. [134] cannot accurately model effects such as that of fretting frequency on wear rate, which has been attributed by several authors to the exclusion of oxygen from the fretting interface [10,25,29,31,33–35].

A model developed by Baydoun et al. [32] simulates the flow of oxygen into fretting contacts, using this to predict the concentration of oxygen across the wear scar and hence determine whether oxygen-deprived “adhesive zones” develop under a given set of conditions, and the size of such zones. This model represents a significant step forward in the quantitative modelling of oxygen transport in fretting contacts, although does not model the associated impact of restricted oxygen transport on wear rates.

In this chapter, a novel formulation for prediction of wear rates and mechanisms in fretting is outlined, building upon the rate-determining process concept proposed by Zhu et al. [134] incorporating the flows of both wear debris and oxygen in fretting contacts in a comprehensive framework for modelling the rates and mechanisms of fretting wear. The applicability of the formulation to predicting wear rates and mechanisms is demonstrated using a time-marching approach, with results being compared to experimental data over a broad range of parameters, including the range of fretting frequencies and displacement amplitudes examined in the previous two chapters.

6.2 The basis for a new model for fretting wear

6.2.1 Predicting wear volume as a function of wear scar width

In developing the model, reference is made to the recent paper of Zhu et al. [134], where fretting of a cylinder-on-flat, high strength steel specimen arrangement was investigated and modelled, the same geometry and material combination as that used in this thesis (detailed in Section 3.1). In this, it was demonstrated that the total wear volume, V of the specimen pair is very well described by a simple geometrical relationship, namely the volume of intersection of the plane and cylinder, as illustrated in Figure 6.2. As such, the width and volume of wear scars developed in this specimen configuration were determined to be related to each other by the relationship described by Equation 6.1:

$$V = L\left(R^2 \arcsin\left(\frac{b}{R}\right) - b\sqrt{R^2 - b^2}\right) \qquad \text{Equation 6.1}$$

where L is the length of the line contact, R is the radius of the cylindrical specimen and b is the contact semi-width. It is argued that in order to preserve this geometrical relationship, the instantaneous rate of wear (in terms of recession of the surface) must be the same at all positions within the wear scar. Moreover, this geometrical relationship between the scar semi-width and the scar volume was shown to be valid over a wide range of scar widths, and for cylinders of two very different radii , as can be seen from the alignment between model predictions of wear volume and dissipated energy with experimental data shown in Figure 6.3

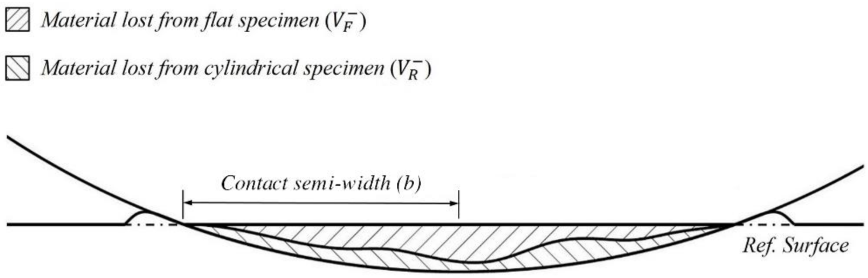

Figure 6.2. Schematic diagram illustrating material removal between the two specimens of the pair where the combined wear on the two specimens results in a total worn volume equivalent to the minor cylindrical segment of intersection.

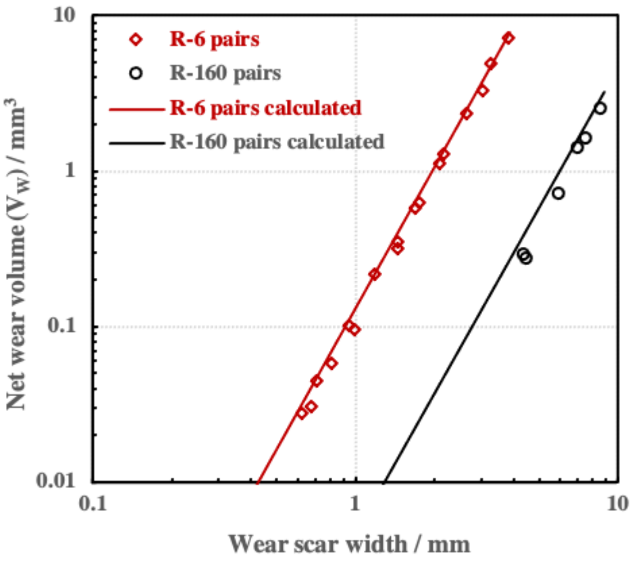

Figure 6.3. Measured wear volume plotted against wear scar width for a cylinder-on-flat fretting pair with cylinders of two radii (R = 6 mm and R = 160 mm), originally presented by Zhu et al. [134]; lines plotted alongside the measured values represent the predicted relationships based upon Equation 6.1.

6.2.2 The rate-determining process

In the previous chapter (Section 5.3), three processes were proposed to govern the overall process of wear, restated here as follows:

1. Wear debris consisting primarily of oxide is generated as a result of the relative motion between the bodies in the contact under load; the rate at which material is detached from the surfaces is governed by the Archard wear rate.
2. Oxygen flows into the contact so that the newly exposed metal surfaces can be oxidised (which then allows for the oxide removal to form debris to occur as described in stage 1); this rate of oxide formation is governed by oxygen transport.
3. The oxide debris formed flows out of the contact, allowing the two first bodies to come into contact (i.e. they are no longer separated by an accommodating bed of debris), thus allowing the wear process to continue.

The overall process of wear depends on the relative rates of these three processes (oxygen ingress, debris formation and debris egress); indeed, the observed rate of wear will be that controlled by the *smallest* of the three rates described, with that process being termed the *rate-determining process*. Later in the chapter, it will be argued that the rates of oxygen ingress and debris egress are dependent upon the contact width, illustrated schematically in Figure 6.4, with the rate-determining process being identifiable as the one with the smallest rate (i.e. the lowest of the three lines). In this illustration, the rate determining process can be seen to change as scar width increases, from an Archard-wear rate to a debris-egress controlled wear rate and finally to an oxygen access-limited wear rate.

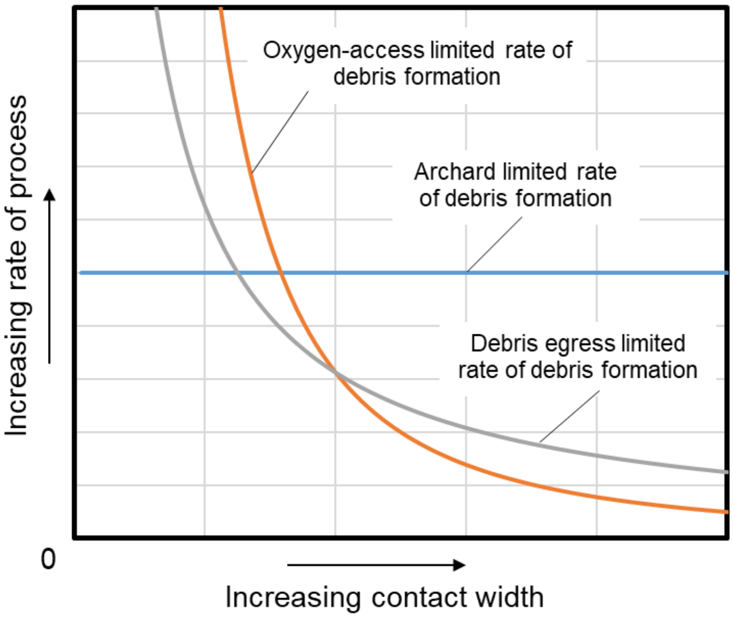

Figure 6.4. Schematic diagram illustrating the variations in the three rate-determining processes that control the overall rate of wear as a function of contact width; the observed rate of wear at a given contact width is equal to that of the operative process, namely that with the lowest of the three rates.

6.3 Derivation of rate equations

6.3.1 Rate of debris formation as described by the Archard wear equation (or similar)

As discussed previously, the Archard wear equation [40] is a widely used model for the prediction of wear rate (i.e. rate of change of wear volume with the distance slid at the interface) in sliding contacts, which is based on the supposition that the rate of wear depends upon the properties of the materials which make up the couple, which in turn influence the real area of contact under a given set of conditions. In the present work, wear rates are expressed as energy-based wear rates (i.e. change in wear volume per unit energy) as per the formulation proposed by Fouvry and co-workers [80] that is functionally equivalent to that proposed by Archard [40]. This wear rate will be termed $\left(\frac{dV}{dE}\right)_{Arch}^{max}$ with the subscript "*Arch*" referring to "Archard", and the superscript "*max*" indicating that this is the maximum rate of Archard wear assuming that no other constraints operate. It is proposed that this rate $\left(\frac{dV}{dE}\right)_{Arch}^{max}$ is a constant in accord with the original proposal of Archard and subsequent researchers.

6.3.2 Rate of debris formation controlled by oxygen transport into the contact

As mentioned previously, in order for oxide to form, oxygen must first penetrate the contact from the surrounding environment, and hence the maximum wear rate that can be sustained at a given set of conditions may be derived, based on the process of transport of atmospheric oxygen from the edge of the contact to the centre (i.e. the entire width of the contact). The concentration of oxygen at the edge of the contact will be that of the environment (and therefore can be directly measured), while the concentration within the contact itself becomes depleted as oxygen is consumed in the formation of oxide debris; as such, there will be a concentration gradient in oxygen across the contact, resulting in flux of oxygen into the contact from the surrounding environment. In order for oxide-based debris to form, there must be sufficient concentration of oxygen present to facilitate this process; given that the rate of wear is assumed to be constant at all points across the contact (originally proposed by Zhu et al. [134] and restated in Section 6.2.1), it follows that the rate at which oxygen is consumed in the formation of oxide must also be the same at all points across the contact. Consequently, the point within the contact with the lowest oxygen concentration will be along the centreline of the contact; a schematic diagram illustrating the proposed variation in oxygen concentration along the width of the contact is presented in Figure 6.5.

In cases where the rate of oxygen transport exceeds the rate of oxygen consumption (in the formation of oxide), the oxygen concentration remains positive across the whole scar, as represented by the blue line in Figure 6.5, whereas if a high rate of debris formation results in the rate of oxygen consumption exceeding the rate at which oxygen can be transported through the interface, then oxygen concentration at some points in the scar may fall to zero, preventing the formation of oxide debris (and thus the progress of wear); a case in which the rate of debris formation is limited by oxygen starvation is illustrated by the grey line in Figure 6.5. The orange line in Figure 6.5 represents the critical rate of oxygen transport, at which oxygen concentration reaches zero at the centreline but remains positive at all other points in the contact; if the rate of oxygen transport is lower than this critical rate, wear ceases to occur, and this condition is associated with the maximum wear rate limited by oxygen transport, termed $\left(\frac{dV}{dE}\right)_{ot}^{max}$ with the subscript "*ot*" referring to "oxygen transport".

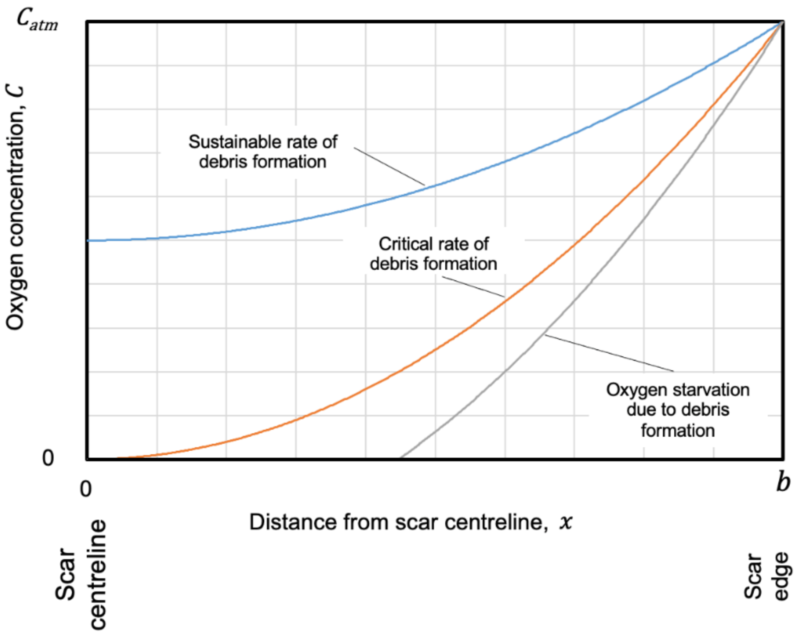

Figure 6.5. Diagram illustrating the proposed variation of oxygen concentration across the contact for three different rates of debris formation; C_{atm} is the atmospheric oxygen concentration.

The equation describing this rate (used in the rest of this work) is derived as follows.

As mentioned previously, the consumption of oxygen within the contact gives rise to a concentration gradient in oxygen across the interface, and at steady state, there is no change in concentration of oxygen with time at a given point in the contact. This approach to modelling the flow and consumption of oxygen is illustrated in Figure 6.6 for a given element within the interface between two fretting bodies; from this it is clear that there is balance between the oxygen flux in to the element, the rate of oxygen consumption in the debris formation process, and the oxygen flux out of the element (towards the contact centreline).

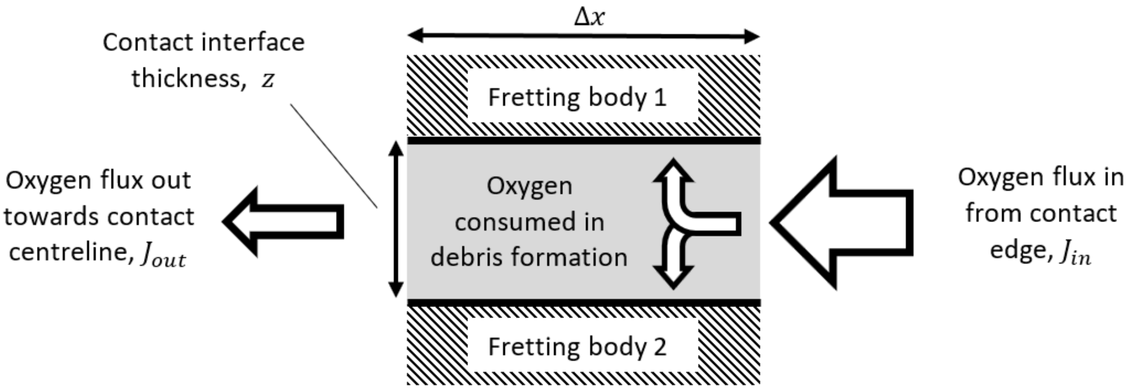

Figure 6.6. Illustration of oxygen flow and consumption in an element of the fretting contact interface; the interface is of length, L (in the direction into/out of the page), thickness, z, and the element under consideration has a width Δx.

An equation describing this can be written as follows:

$$z\,L\,J_{in} = z\,L\,J_{out} + \dot{m}\,L\,\Delta x \qquad \text{Equation 6.2}$$

where L is the length of the fretting contact and z is the thickness of the interface, J_{in} and J_{out} are the oxygen fluxes (kg m^{-2} s^{-1}) in and out of the element, respectively, and $\dot{m}$ is the consumption rate of oxygen (kg m^{-2} s^{-1}) by reaction with the surface to make oxide at the rate required by the wear process, which must be the same across the whole contact (as argued in Section 6.2.1).

Equation 6.2 can be rewritten as follows:

$$J_{in} = J_{out} + \frac{\dot{m}}{z}\,\Delta x \qquad \text{Equation 6.3}$$

As the width of the element, Δx, tends towards zero, this can be rewritten as follows:

$$\frac{dJ}{dx} = -\frac{\dot{m}}{z} \qquad \text{Equation 6.4}$$

Assuming that Fick's first law of general diffusion applies to oxygen transport through the contact interface, we can write:

$$J = -D\frac{dC}{dx} \qquad \text{Equation 6.5}$$

where C is the oxygen concentration (kg m^{-3}) and D (m^{2} s^{-1}) is the appropriate diffusion coefficient for transport of oxygen through the interface. The derivative of this yields:

$$\frac{dJ}{dx} = -D\frac{d^2C}{dx^2} \qquad \text{Equation 6.6}$$

Combining Equation 6.4 and Equation 6.6 yields:

$$\frac{\dot{m}}{z} = D\frac{d^2C}{dx^2} \qquad \text{Equation 6.7}$$

Taking into account the geometry of the specific specimen configuration to be modelled (namely a cylinder-on-flat fretting contact as has been used in the experimental work presented in the previous two chapters), we are able to define boundary conditions; in this case, the contact is symmetrical about the contact centreline (see Figure 6.2), and oxygen transport into the contact occurs from both contact edges. There can thus be no net flux of oxygen across the centreline of the contact, and therefore no gradient in oxygen concentration at this point. With reference to Figure 6.5, we can therefore define boundary conditions as follows:

1. when $x = b$ (i.e. at the scar edge), $C = C_{atm}$ where C_{atm} is the atmospheric concentration of oxygen;
2. when $x = 0$ (i.e. on the scar centreline), $\frac{dC}{dx} = 0$

Integrating Equation 6.7 with these boundary conditions yields:

$$C = C_{atm} - \left(\frac{\dot{m}}{2\,z\,D}\right)(b^2 - x^2) \qquad \text{Equation 6.8}$$

Oxygen starvation in the contact is defined as being when the oxygen concentration falls to zero at any point within the fretting contact (which means that the oxygen supply for oxide debris formation cannot be sustained); the lowest oxygen concentration anywhere in the system will be when $x = 0$, and therefore to avoid oxygen starvation the oxygen concentration on the centreline must be greater than or equal to zero. This constraint can be combined with Equation 6.8 to yield the following requirement for avoiding oxygen starvation:

$$C_{atm} > \left(\frac{\dot{m}}{2\,z\,D}\right) b^2 \qquad \text{Equation 6.9}$$

Now, the consumption rate of oxygen required for debris formation, $\dot{m}$, will be proportional to the observed time-based rate of wear in the contact as follows:

$$\dot{m} = A\,\frac{dV}{dt} \qquad \text{Equation 6.10}$$

where A is a constant (kg m^{-5}).

The rate at which energy is dissipated in the contact per unit time can be described as follows:

$$\frac{dE}{dt} = 4\,\delta\,\mu\,P\,f \qquad \text{Equation 6.11}$$

where δ is the displacement amplitude, P is the applied load, f is the fretting frequency, and μ is the coefficient of friction.

Equation 6.11 can be rewritten in the form of a time-based wear rate as follows:

$$\frac{dV}{dt} = \frac{dE}{dt}\,\frac{dV}{dE} = 4\,\delta\,f\,P\,\frac{dV}{dE} \qquad \text{Equation 6.12}$$

Combining Equation 6.9, Equation 6.10 Equation 6.12 yields an inequality that defines when wear can proceed without oxygen starvation as follows:

$$C_{atm} > \left(\frac{2\,A\,\delta\,\mu\,P\,f\,b^2}{z\,D}\right)\left(\frac{dV}{dE}\right)_{ot} \qquad \text{Equation 6.13}$$

where $\left(\frac{dV}{dE}\right)_{ot}$ is the rate of wear controlled by oxygen transport. Assuming that the interface thickness, z, is constant, Equation 6.13 can be rewritten in terms of a maximum wear rate controlled by the oxygen transport, $\left(\frac{dV}{dE}\right)_{ot}^{max}$.

$$\left(\frac{dV}{dE}\right)_{ot}^{max} = B\frac{C_{atm}\, D}{\delta\, \mu\, P\, f\, b^2} \qquad \text{Equation 6.14}$$

where C_{atm} is the oxygen concentration in the atmosphere, D is the appropriate diffusion coefficient for transport of oxygen through the interface, and B is a constant (with units of kg m^{-6}) in which other constants are subsumed. As mentioned previously, the subscript "*ot*" refers to "oxygen transport" and the superscript "*max*" indicates that this is the maximum rate of at which oxide can be formed without oxygen starvation assuming that no other constraints operate. It can be seen from Equation 6.14 that if wear is controlled by oxygen starvation, then the maximum rate of wear that can be sustained is proportional to both C_{atm} and D, and is inversely proportional to δ, μ, P, f and b^2.

6.3.3 Rate of wear controlled by debris egress from the contact

Once formed, oxide-debris must leave the contact in order for wear to take place. It is proposed that in each cycle, debris particles move towards the edge of the contact with a net displacement proportional to the slip amplitude. The flow of particles within the contact will also be influenced by the tendency of the debris particles to sinter into debris beds, which will tend to significantly restrict the flow of debris out of the contact; the sintering of debris will be strongly affected by temperature, which will in turn be controlled by several factors, with the most significant factors being those of the temperature of the environment and the local temperature increase due to frictional power dissipation (controlled by fretting conditions). However, the present work focuses on fretting behaviour at room temperature, and it is therefore assumed that glaze layers do not form over the range of conditions examined and that the role of debris sintering may be neglected.

The rate of wear controlled by the rate at which debris can be lost from the contact (i.e. the rate of wear per unit energy dissipated in the contact) $\left(\frac{dV}{dE}\right)_{de}^{max}$ where the subscript "*de*" refers to "debris egress" and (as with the rate equations already outlined) the superscript "*max*" indicates that this is the maximum rate of wear associated with debris egress assuming that no other constraints operate.

As argued previously, the rate at which wear proceeds at any time within a test must be the same at any point within the fretting scar. Due to the non-conforming nature of the cylinder-on-flat specimen configuration employed, wear scar width increases as wear proceeds, continually bringing new surface into the wear scar in the process; newly exposed surfaces will experience an initial transient as they are brought into the scar, but then will continue to wear in steady state. The thickness of the debris bed also experiences a transient stage in which thickness increases in the early stages of a test, but it too reaches a steady state condition; in steady state, the rate at which wear debris is created is equal to the rate at which it is expelled from the contact, and there is therefore a steady flow of debris out of the contact from the position at which it was formed.

The nature of debris flow out of the contact is a complex process which is not comprehensively understood, in particular its dependence upon parameters such as displacement amplitude [26]; as such, in order to derive an equation to describe this process, some aspects of the dependence of debris egress on fretting parameters must be assumed; an advantage of the modelling approach presented in this thesis (namely that the overall rate of wear is determined by competition between rate-determining processes) is the ability to readily revise the exact derivations of the individual rate equations as knowledge around these fundamental processes develops over time. A reasonable starting point for the flow of debris out of a fretting contact might be that of rheology, which is consistent with assumptions made in works in the area of third body flows [122,151]. It is therefore assumed that the debris flow rate will be proportional to the slip amplitude, δ and the length L of the line contact (since the volume flow rate will simply scale with the length of the contact) and the applied pressure (which in the case of the cylinder-on-flat contact is simply $(P/2bL)$; these assumptions align with previous work where the flow rate of debris in a cylinder-on-flat contact was shown to be proportional to the wear scar width [134]. It may also be assumed that the rate of debris volume loss is proportional to the rate of wear (loss of metal from the first bodies) with a constant of proportionality given by the Pilling-Bedworth ratio, R_{PB}. These assumptions can be combined to yield an expression for the maximum wear rate per cycle that can be sustained under a given set of conditions as limited by debris egress as follows:

$$\left(\frac{dV}{d\mathrm{N}}\right)_{de} = \frac{F\,L\,\beta\,\delta}{R_{PB}}\,\frac{P}{2\,b\,L} \qquad \text{Equation 6.15}$$

where F is a constant, and β is the ratio of the net displacement of a debris particle per cycle and the slip amplitude; it is noted that β will depend upon the cohesive forces between particles within the debris bed.

In a similar fashion to Equation 6.11, the frictional energy dissipated per cycle can be derived as follows:

$$\frac{dE}{dN} = 4\,\delta\,\mu\,P \qquad \text{Equation 6.16}$$

Equation 6.15 and Equation 6.16 can then be combined to derive the limiting wear rate in terms of volume of material loss per unit energy, given by Equation 6.17:

$$\left(\frac{d\mathrm{V}}{d\mathrm{E}}\right)_{de} = \frac{G\,\beta}{\mu\,b} \qquad \text{Equation 6.17}$$

where G is a constant in which the other constants are subsumed and having units of $\mathrm{m}^4\,\mathrm{J}^{-1}$.

6.3.4 The observed wear rate

It is argued that the observed rate of wear is controlled by whichever of the three key processes outlined above is slowest at a given point in a test; as such, the wear rate observed in the system is given by the following:

$$\left(\frac{dV}{dE}\right)_{obs} = \min\left[\left(\frac{dV}{dE}\right)_{Arch}^{max}, \left(\frac{dV}{dE}\right)_{ot}^{max}, \left(\frac{dV}{dE}\right)_{de}^{max}\right] \qquad \text{Equation 6.18}$$

where the subscript "obs" indicates "observed" and "$\min\,[x, y, z]$" indicates that the smallest of the three values is selected.

It is noted that whilst $\left(\frac{dV}{dE}\right)_{Arch}^{max}$ is a constant for a given system, both $\left(\frac{dV}{dE}\right)_{ot}^{max}$ and $\left(\frac{dV}{dE}\right)_{de}^{max}$ are functions of the wear scar width, b; the significance of this dependence for fretting wear testing is described as follows:

1. If the wear rate is controlled by the Archard wear equation throughout a test, the observed wear rate will be a constant. However, if the observed wear rate is controlled at any point during the test by either oxygen transport into the contact or by debris egress from the contact, the wear rate will not be a constant and will fall as the test proceeds (i.e. as the wear scar width, b increases).
2. Since the wear scar width, b, increases throughout a test for the cylinder-on-flat geometry considered in this study, and $\left(\frac{dV}{dE}\right)_{ot}^{max}$ and $\left(\frac{dV}{dE}\right)_{de}^{max}$ are both functions of b, then the rate determining process may change throughout a test.
3. The evolution of the wear volume with energy dissipated is therefore dependent upon the history of the process, and can only be determined by a time-marching method.

6.3.5 Structure of a suitable time-marching model

As the overall rate of wear is dependent upon the history of wear throughout the test up to a given point (resulting from the dependence of rate-determining processes on wear scar width), a time-marching method is necessary to implement the model to calculate wear rates. The structure of a suitable simple time-marching method is illustrated in Figure 6.7

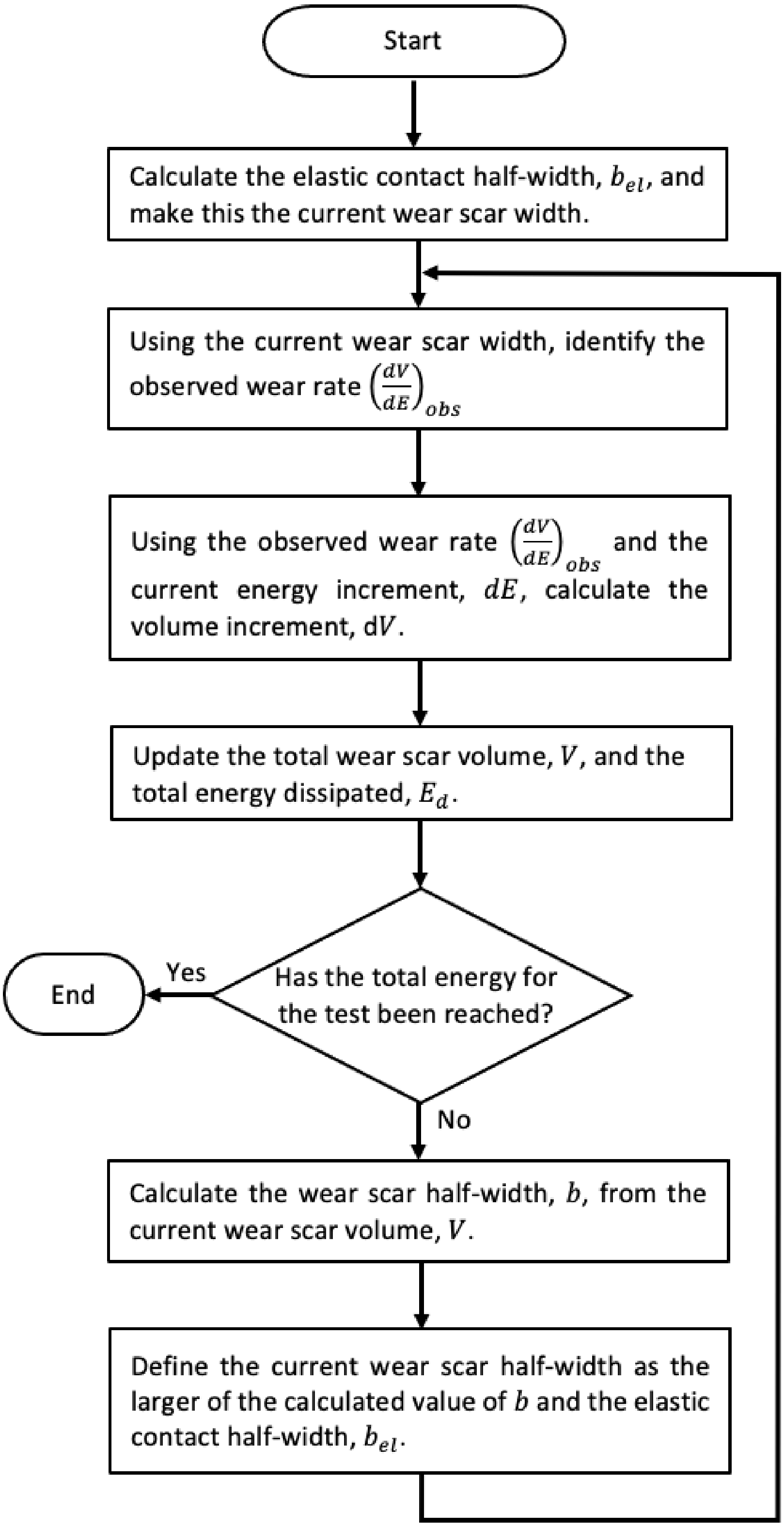

Figure 6.7. Basic process flow chart for the evolution of the wear scale volume as a function of energy dissipated in the contact.

An appropriate energy increment, dE, must be selected to step through the model, with this having an impact both on the computational cost of the model and the observed wear rate (as this is dependent upon the wear scar width. This increment does not need to be constant throughout the test, allowing for a smaller increment to be used in the early stages of the test (when the contact grows rapidly relative to the initial contact size) and for larger increments to be used in later stages of the test (when changes in contact size represent a much smaller proportion of the contact size at a given instant). For the work of this chapter, the increment is defined as a proportion of the overall energy dissipated, E_d, (calculated as a function of slip amplitude, normal load and coefficient of friction, shown in Equation 6.16, summed over the total number of cycles), with the energy increment, dE, initially being defined as $10^{-7}E_d$, later being stepped up to $10^{-6}E_d$ and then to $10^{-4}E_d$ over the course of the test.

6.4 Tuning the model against experimental data

The model is based upon three equations which describe the various competing rates; whilst each of these equations indicates the dependence of the particular process upon the fretting test parameters and conditions (including the instantaneous contact width, b), each equation also depends upon constants, the definitions of which are outlined in this section.

In defining the constants, it is noted at this stage that this model is not currently in a form where it can be fully predictive. Instead, the model seeks to identify how the fretting test parameters and conditions (including the instantaneous scar size, b) influence the relative rates of the key physical processes, and thus influence which of these processes is rate-determining in a given situation. The constants will therefore also influence the prediction of the wear volume under a given set of conditions, shifting the rates of the three processes relative to each other in a way that will critically influence which of the processes is the controlling (operative) process at any time.

In this chapter, the constants are tuned against experimental data related to the fretting wear of a high strength steel in a cylinder-on-flat specimen geometry conducted at the University of Nottingham, including the experiments presented in the previous two chapters of this thesis. It is important to note that in this test facility, it is the applied far-field displacement amplitude (Δ^*) as opposed to the slip amplitude in the contact itself (δ^*) which is controlled, with the latter being derived from fretting loops. Consequently, the stiffness of the system (S), which incorporates the contact stiffness as well as compliance in the testing rig, is critical in determining the actual slip amplitude, which must be incorporated into the model. The relationship between the slip amplitude and displacement amplitude is given in Equation 6.19:

$$\delta^* = \Delta^* - \frac{\mu P}{S} \qquad \text{Equation 6.19}$$

Based on an analysis of fretting loops, namely analysing the gradient of the regions at the ends of the displacement cycle over which no slip occurs (see Section 2.1.3, Figure 2.3), a stiffness value of 40 N μm^{-1} was determined to be the most representative of tests over the range of conditions employed, and is henceforth used in tuning the model.

It is recognised that the coefficient of friction, μ, is dependent upon the conditions of the test, and in some cases, varies within a test. However, the range over which μ varies is relatively small over a wide range of conditions. Given that there is currently no physical basis for the prediction of μ dependent upon the test conditions, a constant value of 0.7 has been selected for the model predictions which is applied for all the test conditions.

The three key equations and the values of the associated constants are presented in Table 6.1; the details of how the constants were derived are outlined in the following sections (Sections 6.4.1 to 6.4.3).

Table 6.1 Summary of the competing rate equations and the evaluated and defined constants.

Physical process	**Equation**	**Constants to be defined or requiring evaluation**	**Value employed in the model**
Debris egress	$\left(\frac{dV}{dE}\right)_{de}^{max} = \frac{G\,\beta}{\mu\,b}$	$(G \times \beta)$	$23.6 \times 10^{-18}\, m^4\, J^{-1}$
Archard wear	$\left(\frac{dV}{dE}\right)_{Arch}^{max} = A$	A	$90 \times 10^{-15}\, m^3\, J^{-1}$
Oxygen transport	$\left(\frac{dV}{dE}\right)_{ot}^{max} = B\,\frac{C_{atm}\,D}{\delta\,\mu\,P\,f\,b^2}$	$(B \times D)$	$186 \times 10^{-21}\, m^8\, kg_{O_2}^{-1}\, s^{-1}$
		C_{atm}	$0.3\, kg_{O_2}\, m^{-3}$

6.4.1 The debris egress constant $(G \times \beta)$

Previous work from the University of Nottingham, namely that of Zhu et al. [134] has addressed the dependence of the instantaneous wear rate on the width of the fretting scar for fretting in a cylinder-on-flat specimen pair arrangement. In that work, fretting tests with two different cylinder-on-flat geometries were employed (cylinders with radii of both 6 mm and 160 mm) over a range of test durations. Wear volumes and associated dissipated energy values from the fretting tests in that work are shown in Figure 6.8.

All fretting tests in the work of Zhu et al. [134] were conducted at 20 Hz, and as such it can be assumed that under these conditions the oxygen-access limited rate of debris formation, $\left(\frac{dV}{dE}\right)_{ot}^{max}$, was never rate limiting (i.e. was never the smallest of the three rates); this was never considered or addressed in the paper of Zhu et al. [134], although the formation of oxide-dominated wear scars at the longer test durations was interpreted as being indicative of a debris-egress controlled wear mechanism (as opposed to one of oxygen exclusion resulting in metallic wear scars). A schematic diagram is presented in Figure 6.9 to describe the assumptions made in that work, showing the rates of the three key processes as a function of energy dissipated in a test; the limiting rate of oxygen ingress is the highest of the three lines over the range shown, and therefore does not affect the operative wear mechanism.

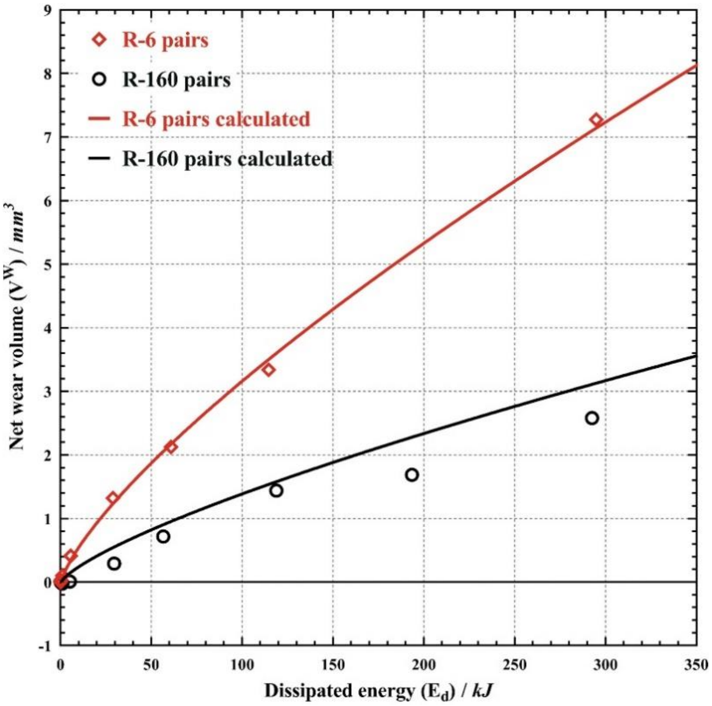

Figure 6.8. Experimental data from fretting tests with cylinder-on-flat geometry with cylinders of 6 mm (R-6) and 160 mm (R-160). Alongside the data are calculated rates of wear for the two geometries based upon the assumption that the wear rate is directly proportional to the inverse of the wear scar width with the same constant of proportionality being employed for the two cases [134].

In that previous work, the total test duration was large (5×10^6 cycles) and therefore, the authors assumed that the initial period where the Archard limited rate of debris formation would be operative (i.e. was the lowest of the three rates) was negligible. Moreover, at the start of the test, the scar semi-width, b, is the elastic contact width, b_{el} (i.e. b is never zero) and so the debris egress limited rate of debris formation, $\left(\frac{dV}{dE}\right)_{de}^{max}$, is never infinite. As such, it was assumed that the behaviour over the whole test was debris egress limited and therefore the behaviour could be described by:

$$\left(\frac{dV}{dE}\right)_{de}^{max} = \frac{\alpha}{b} \qquad \text{Equation 6.20}$$

with the same value of α describing the behaviour for the two different test geometries.

The success of this approach (and therefore the validity of the assumptions made) is illustrated in Figure 6.8 where a value of α of 3.4 × 10^{-17} m^4 J^{-1}, (i.e. 3.4 × 10^{-2} mm^4 kJ^{-1}) results in a very satisfactory fit to the experimental data for the two different geometries.

The relationship described by Equation 6.20 is effectively a simplified form of the equivalent rate of debris egress derived in the present work (Equation 6.17), although in the former the test parameters and constants indicated in Equation 6.17 were subsumed into a single constant, α; knowing the test conditions under which the previous work was conducted allowed the debris egress constant $(G \times \beta)$ to be evaluated as 23.6 × 10^{-18} m^4 J^{-1} (23.6 × 10^{-3} mm^4 kJ^{-1}).

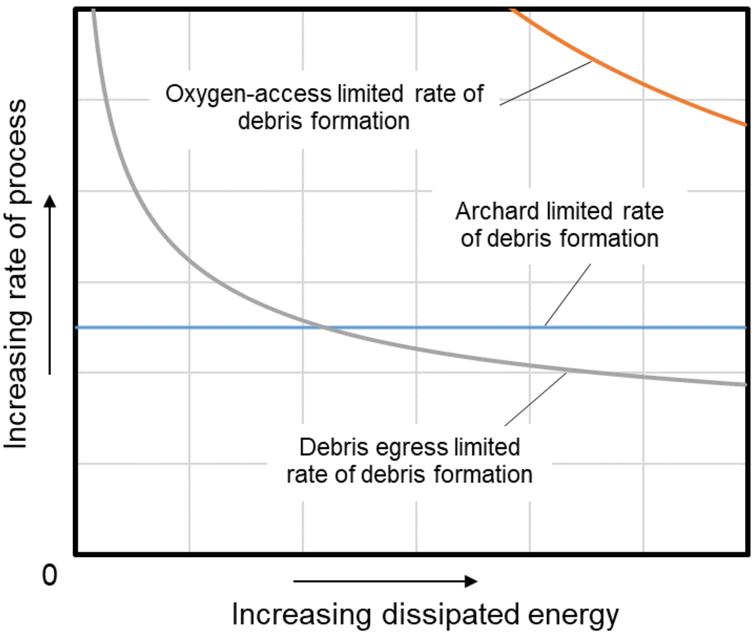

Figure 6.9. Schematic diagram illustrating the evolution of the rates of the three governing processes with energy dissipated in a test.

6.4.2 The Archard wear constant (A)

As discussed in Section 6.4.1, in the work presented in Figure 6.8, the assumption was made that the initial period where the Archard limited rate of debris formation was operative (i.e. was the lowest of the three rates) was negligible. This assumption becomes less valid for tests of smaller duration (i.e. where smaller values of energy are dissipated over the course of the test). In the test programme reported in Figure 6.8, tests had been conducted over a very wide range of durations; however, the quality of the fit between the experimental data and the predictions is difficult to gauge at the smallest test durations, which is precisely the region where any influence of the Archard limited rate of debris formation would be most pronounced. As such, the data for the fretting tests with the 6 mm radius cylinder presented in Figure 6.8 are re-presented in Figure 6.10 on a log-log scale (with test durations spanning the range 2000 cycles to 5×10^{6} cycles), enabling the quality of the fit at the small test durations to be better discerned.

As can be inferred from Figure 6.10, the effect of the Archard wear constant will be more significant at smaller values of energy dissipated (indeed, for tests of short enough duration, the rate-determining process throughout the whole test could be that of Archard wear). However, in all tests, if the Archard limited rate of debris formation is ever operative, this will only be the case at smaller values of energy dissipated. Using the time-marching methodology presented in this chapter, the evolution of the wear volume with energy dissipated has been evaluated for various values of the Archard wear constant; five examples are presented in Figure 6.10 where comparisons can readily be made with the experimental data across the range. It can be seen that the fit with experimental data is good at the higher values of energy dissipated, irrespective of the value of the Archard wear constant selected; however, at the smaller values of energy dissipated (where the effect of the Archard wear constant is most significant), the data fit best with values of the Archard wear constant of between 0.08 $\text{mm}^{3}\ \text{kJ}^{-1}$ and 0.1 $\text{mm}^{3}\ \text{kJ}^{-1}$. Values of 0.04 $\text{mm}^{3}\ \text{kJ}^{-1}$ and 0.06 $\text{mm}^{3}\ \text{kJ}^{-1}$ result in under-predictions of the wear volume at lower values of dissipated energy, whilst a value of 0.15 $\text{mm}^{3}\ \text{kJ}^{-1}$ results in an over-prediction. As such, it is proposed that a value of the Archard wear constant of 0.09 $\text{mm}^{3}\ \text{kJ}^{-1}$ ($90 \times 10^{-15}\ \text{m}^{3}\ \text{J}^{-1}$) will provide an appropriate fit to the data, and this value will be employed for the remainder of the analysis as a constant for this material system.

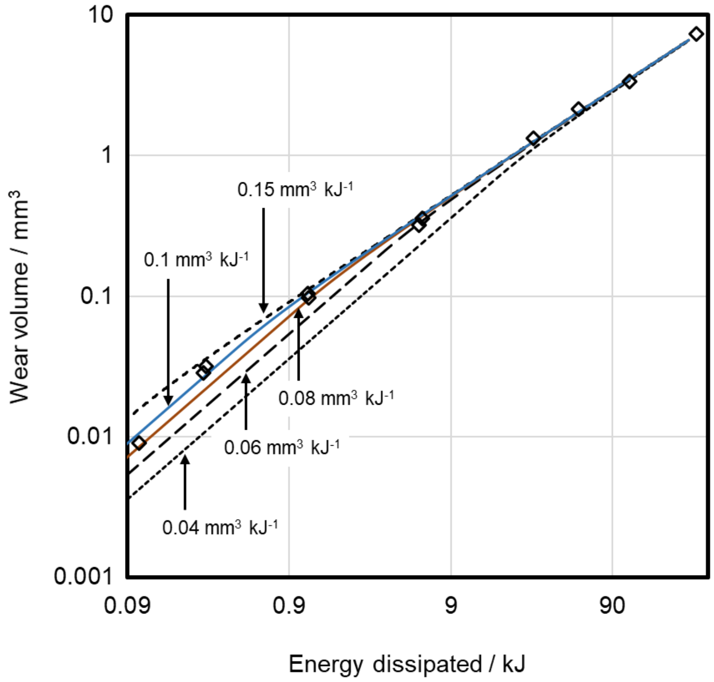

Figure 6.10. The data from Figure 6.8 for the R-6 pair presented on a log-log scale along with the predicted relationship between wear volume and energy dissipated using the time-marching technique with a range of values of the Archard wear constant as indicated.

6.4.3 The oxygen transport constant $(\boldsymbol{B} \times \boldsymbol{D})$

Oxygen transport into the contact will become the rate determining process when the rate becomes the lowest of the three rates (i.e. the orange line becomes the lowest line in a representation such as that in Figure 6.9). The form of the equation for $\left(\frac{dV}{dE}\right)_{ot}^{max}$ (Equation 6.14) indicates that low values are promoted by high frequencies, applied loads and slip amplitudes in the fretting test.

In the previous two chapters, fretting tests were conducted using the same material combination as employed by Zhu et al. [134] over a range of fretting frequencies and displacement amplitudes for tests of 1 x 10^6 cycles in duration, and it was observed that increases in both of these parameters over the range examined inhibits the formation of oxide debris beds, resulting in metallic wear scars; significant subsurface damage was observed under these conditions where an oxide debris bed did not form, and it was proposed that this was due to changes in the relative rates of oxygen ingress to the contact and the egress of oxide, resulting in oxygen exclusion from the centre of the interface.

The wear volumes measured over this range of frequencies and displacement amplitudes are shown as a function of energy dissipated in Figure 6.11 (presented earlier in this thesis, namely Figure 4.1 and Figure 5.24 in Sections 4.2.1 and 5.2.3, respectively), where it is seen that (i) the wear volumes as a function of energy dissipated are very similar for tests conducted at 20 Hz and 100 Hz; (ii) the wear volumes as a function of energy dissipated are significantly different for tests conducted at 100 Hz and 200 Hz. The fact that at 20 Hz and 100 Hz the behaviour is very similar (despite the changes in $\left(\frac{dV}{dE}\right)_{ot}^{max}$ associated with differences in the displacement amplitude and fretting frequency) indicates that under these conditions, $\left(\frac{dV}{dE}\right)_{ot}^{max}$ is not strongly rate determining (i.e. the rate of wear controlled by debris egress is either lower or very similar in magnitude).

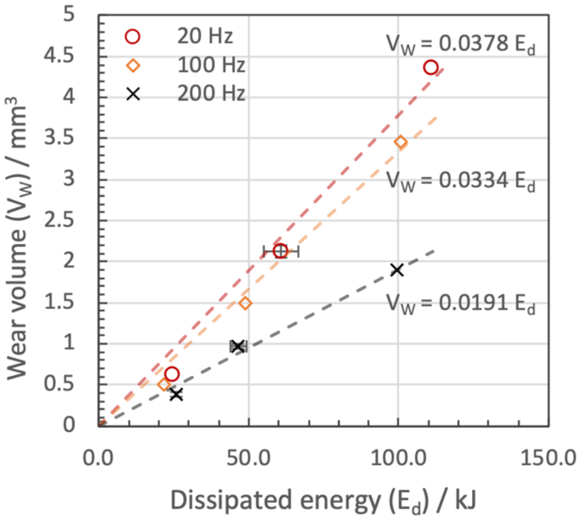

Figure 6.11. Wear volume after 10^6 fretting cycles as a function of dissipated energy for the three fretting frequencies examined as indicated; the three values of dissipated energy for each fretting frequency relate to the three displacement amplitudes employed in the tests (namely 25 μm, 50 μm and 100 μm).

It is proposed (with reference to the schematic diagram in Figure 6.4) that when the rate associated with oxygen transport is not rate-limiting (i.e. the orange line is not the lowest of the three lines at any point), then there is sufficient oxygen at the interface to sustain the formation of oxide debris, and metal-metal contact (which results in the development of significant subsurface damage) will not occur. Conversely, it is proposed that when oxygen transport is the rate-determining process, the formation of oxide debris is inhibited, and thus a protective debris layer does not form, resulting in the subsurface deformation associated with metal-metal contact and the formation of a metallic transfer layer. The oxygen transport constant $(B \times D)$ can therefore be tuned based on these observations of oxygen exclusion.

Using a volume fraction of oxygen in air of 21% and a molar volume of 22.4 × 10^{-3} m^3 at standard temperature and pressure, the oxygen content in the atmosphere (C_{atm}) can be calculated to be ~ 0.3 kg m^{-3}. To ensure that all of the four cases identified in which subsurface damage develops have (at least) the final stages of the test being oxygen-transport limited (i.e. the lowest of the three rates) results in a requirement that $(B \times D) \leq 186 \times 10^{-21}\, m^8\, kg_{O_2}^{-1}\, s^{-1}$. Higher values of $(B \times D)$ up to about $300 \times 10^{-21}\, m^8\, kg_{O_2}^{-1}\, s^{-1}$ do lead to some improvements in the accord between the experimentally measured wear volumes and the predicted wear volumes but above this value, the predicted behaviour begin to deviate more markedly from the experimental data (see Figure 6.12); moreover, using a higher value of $(B \times D)$ means that oxygen transport is never rate-determining for the case with Δ^* = 50 μm and f = 100 Hz, meaning that sub-surface damage observed following testing under these conditions cannot be readily rationalised. As such, it is proposed that a value of $(B \times D)$ of $186 \times 10^{-21}\, m^8\, kg_{O_2}^{-1}\, s^{-1}$ will provide an appropriate fit to the data and other experimental observations, and this value will be employed for the remainder of the analysis as a constant for this system.

To more clearly compare the accord between the wear rates predicted by the model and those generated experimentally three graphs are presented in Figure 6.13, one for each fretting frequency, in which the experimental data are plotted alongside values predicted with a value of $(B \times D)$ of $186 \times 10^{-21}\, m^{8}\, kg_{O_2}^{-1}\, s^{-1}$ over the range of displacement amplitudes. The predicted values can be seen to be in relatively good agreement with corresponding experimental data across the range of frequencies and displacement amplitudes, broadly capturing the trends associated with changes in the parameters at all conditions; however, the differences between the experimental and predicted values are significant at many of the conditions examined, indicating that there are some issues with the model that must be examined in order to improve its alignment with experimental observations.

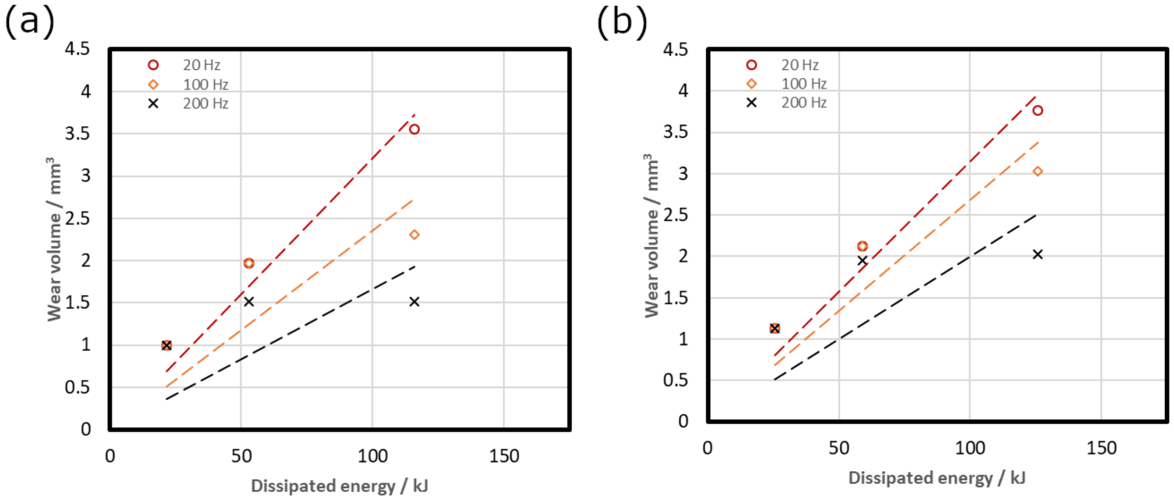

Figure 6.12. Wear volume expressed as a function of dissipated energy as predicted by the model using the same test conditions as the experimental data in Figure 6.11 and a value of the debris egress constant $\boldsymbol{(B \times D)}$ of (a) $\boldsymbol{1.86 \times 10^{-19}\, m^{8}\, kg_{O_2}^{-1}\, s^{-1}}$; (b) $\boldsymbol{3.0 \times 10^{-19}\, m^{8}\, kg_{O_2}^{-1}\, s^{-1}}$.

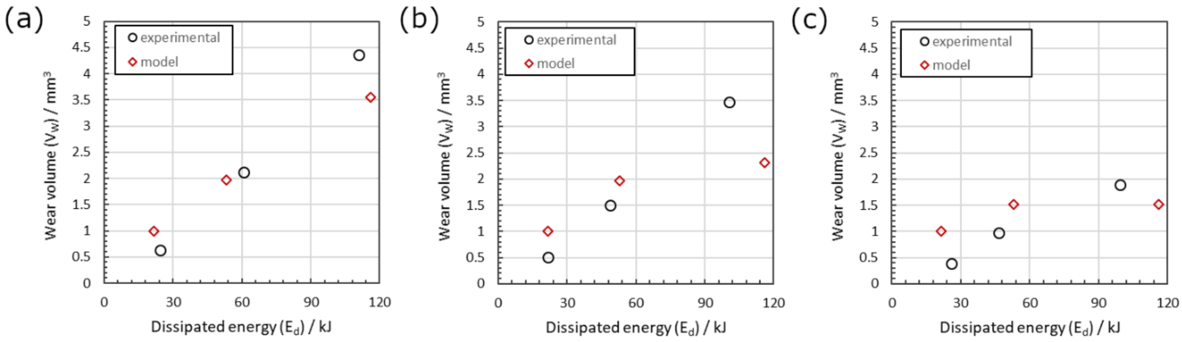

Figure 6.13. Comparison of predicted values and experimental measurements for the extent of wear as a function of dissipated energy in fretting with applied displacement amplitudes of 25 μm, 50 μm and 100 μm with a fretting frequency of (a) 20 Hz; (b) 100 Hz; (c) 200 Hz (P = 450 N; N = 10^6 cycles; L = 10 mm).

6.5 Employing the model to analyse the effects of frequency and displacement amplitude on rate-determining processes

In addition to the alignment of the model with experimentally measured wear rates, the dependence of the relative magnitudes of the three key processes upon fretting parameters can provide useful insight into the operative mechanisms of wear that result in the overall wear rate observed. As such, the model can be used to analyse the wear mechanism transition investigated in Chapter 5, namely a transition from a regime associated with oxide-dominated wear scars and limited subsurface damage (despite significant levels of wear), termed "Regime I", to one associated with predominantly metallic wear scars and the development of significant subsurface damage, termed Regime II. Regime I was observed at low displacement amplitudes and fretting frequencies, while Regime II behaviour is associated with increases in both parameters; the role of fretting frequency and displacement amplitude in this transition is difficult to deconvolute in a purely qualitative manner due to both parameters acting upon many of the same processes, and as such, in this section the effects of these parameters on the operative mechanism of wear is examined using the more quantitative framework outlined already in this chapter. The rates of processes predicted by the model and the associated overall wear rates are discussed in light of the experimental results presented in the previous chapters over the same conditions, namely those shown in Table 6.2.

The evolution of rate-determining processes predicted by the model over the range of frequencies and displacement amplitudes investigated in Chapters 4 and 5 are presented in Figure 6.14, in the same format as top surface and cross-section SEM presented in Figure 5.28 and Figure 5.30. It should be noted that the total energy dissipated is dependent upon displacement amplitude, although not upon fretting frequency, and as such the horizontal axis of the graphs presented in Figure 6.14 is constant across each row, and increases down each column. The difference in overall dissipated energy between the different displacement amplitude conditions is reflected in the spacing between the vertical gridlines, which in all cases is fixed at 10 kJ, with closer spacing therefore representing larger overall dissipated energy. In all of the graphs presented, the range of dissipated energy on the horizontal axis is greater than the total energy dissipated at each condition, which is identifiable as the dissipated energy at the point where each of the three rate lines end.

Table 6.2. Test conditions for which experimental and predicted values are compared in this section, namely the range of displacement amplitudes and fretting frequencies investigated in the previous chapters of this thesis.

Frequency, f (Hz)	20, 100, 200
Applied displacement amplitude, Δ^* (μm)	25, 50, 100
Applied normal load, P (N)	450
Test duration, N (cycles)	10^6
Temperature, T (°C)	Room temperature

It should be noted that, due to the rates of both oxygen ingress and debris egress being dependent upon the contact width, *b*, the rates of both processes are influenced by the overall wear rate as an indirect effect of the overall wear rate on wear scar width; as such, small variations in the rate of debris egress can be seen across the range of frequencies and displacement amplitudes arising as a result of the indirect effect of overall wear rate on scar width as opposed to a direct effect of the parameters upon the rate itself.

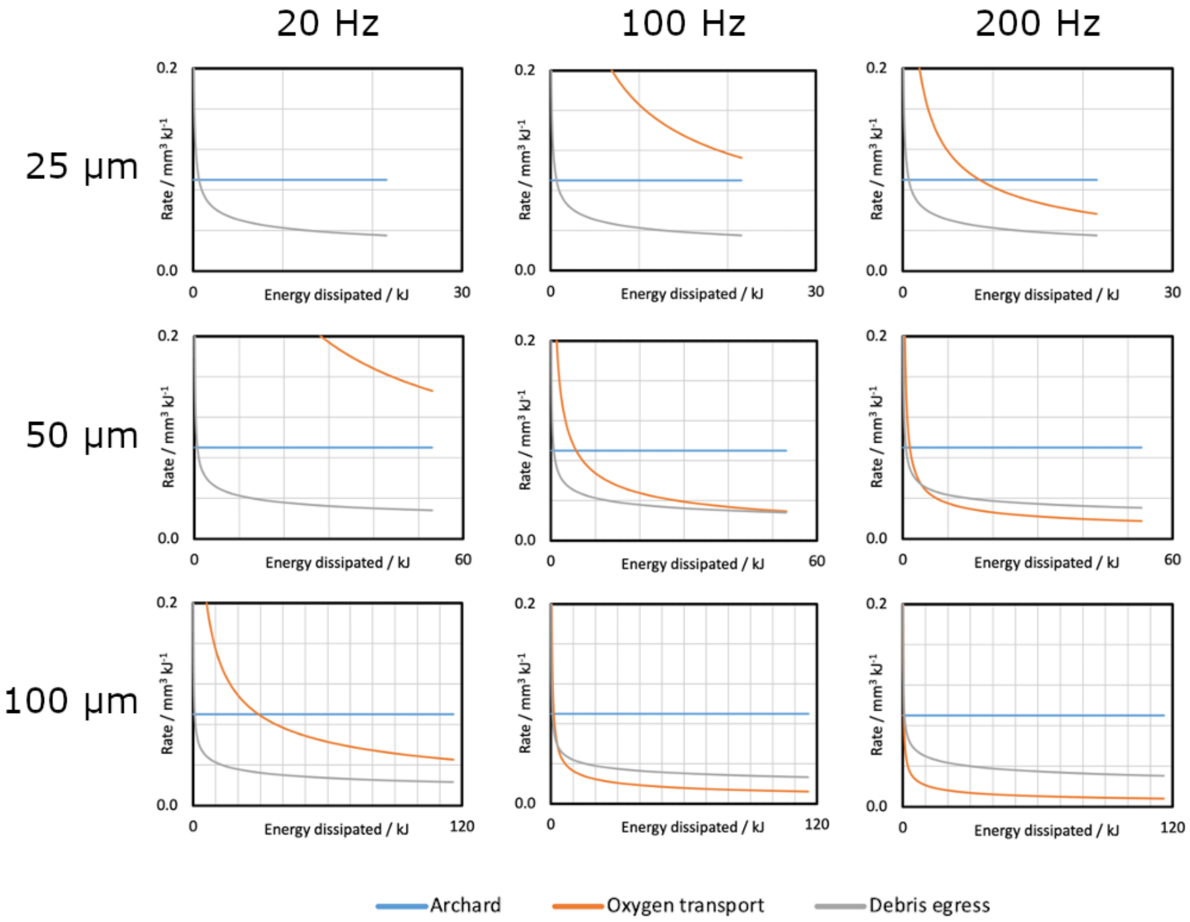

Figure 6.14. Evolution of rate-determining processes over the range of displacement amplitudes and frequencies studied experimentally in this thesis; gridlines are spaced by 10 kJ in each of the graphs, highlighting the difference in total dissipated energy associated with changes in displacement amplitude (P = 450 N; $N = 10^6$ cycles; L = 10 mm).

At low displacement amplitude (Δ^* = 25 µm) and low frequency (f = 20 Hz), wear is predicted by the model to be limited by the rate of debris egress from an early stage and to remain so throughout the duration of the test; the rate of debris egress remains constant across all three frequencies, and as such the wear rate is predicted to be equal between all three of these conditions. Increasing frequency can be seen to result in the limiting rate of oxygen ingress falling significantly, although never becoming rate-determining at any point in the test, and as such the model predicts that in all of these cases there is sufficient oxygen ingress to the contact to form oxide throughout the full width of the interface. Likewise, at low frequency (f = 20 Hz) wear is predicted to be controlled by debris egress from the contact across the range of displacement amplitudes examined; again, the rate of debris egress is consistent across the range of conditions (up to the respective dissipated energy at each condition). The limiting rate of oxygen ingress can be seen to fall significantly as displacement amplitude is increased, although it does not become rate-determining in any of the tests over this range of displacement amplitudes at this frequency. This response aligns with the experimental observations reported in the previous chapter for the same range of conditions, namely that wear occurs in Regime I across the examined range of either frequencies or displacement amplitudes when the other parameter is held at a low value.

With increases in both frequency and displacement amplitude, the rate of debris egress remains broadly constant across the range of conditions, while the rate of oxygen ingress can be seen to fall significantly, so much so as to become the rate-determining process; this is predicted to occur in tests with the two largest displacement amplitudes ($\Delta^* = 50$ μm ; $\Delta^* = 100$ μm) at the two higher frequencies ($f = 100$ Hz; $f = 200$ Hz), although the stage of the test at which oxygen ingress becomes rate-determining varies. These conditions were all observed in Chapter 5 to exhibit Regime II behaviour, in which a coherent oxide debris bed does not form across the entire wear scar surface, which instead is largely metallic in character with this being associated with the development of significant subsurface damage. It is noted that at the intermediate displacement amplitude and frequency condition ($\Delta^* = 50$ μm; $f = 100$ Hz), the rate of oxygen ingress only becomes rate-determining towards the very end of the test, with debris egress being rate-determining for the majority of the test duration; as such this is predicted to be a borderline case in which oxygen access is severely restricted, although not so much as to limit the overall rate of wear.

To clarify the impact of displacement amplitude on the relative rates of processes, the observed wear rate at any given point in a test (i.e. the lowest of the three rate lines shown in Figure 6.14) is plotted on the same scale for all three displacement amplitudes at each frequency in Figure

6.15. It can be seen that at low frequency, the rate-determining processes at each displacement amplitude overlay one another directly up to the respective dissipated energy of each condition. At higher fretting frequency, the effect of displacement amplitude on observed wear rate becomes more pronounced; at a frequency of 100 Hz, a reduction in observed wear rate (over the shared range of dissipated energy) is only observed as displacement amplitude is increased above 50 μm, while at the highest fretting frequency (f = 200 Hz) a reduction in observed wear rate occurs with each increase in displacement amplitude above 25 μm.

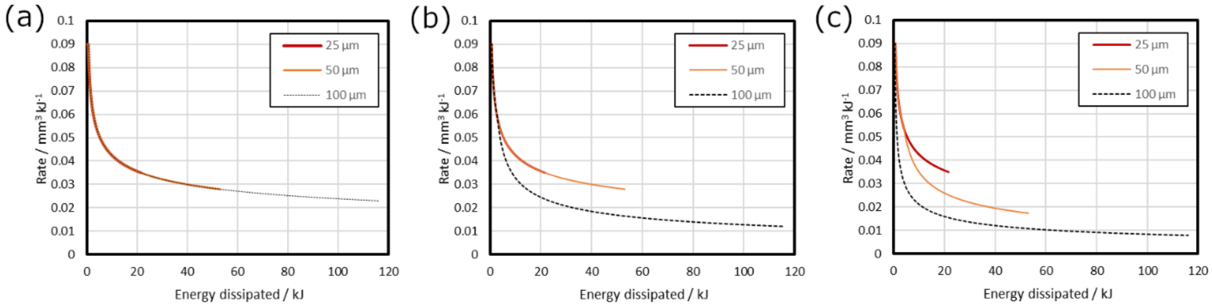

Figure 6.15. Observed wear rate (i.e. the rate of the rate-determining process at a given dissipated energy) across the range of displacement amplitudes examined at a fretting frequency of (a) 20 Hz; (b) 100 Hz; (c) 200 Hz (P = 450 N; $N = 10^6$ cycles; R = 6 mm; L = 10 mm).

6.6 Modelling the effects of parameters not examined in the experimental programme of this thesis

The ability of the model to accurately represent physical behaviours of fretting contacts is further investigated in this section by comparing the behaviour predicted by the model to observations reported in the literature. The values of proportionality constants used are the same as those outlined in Section 6.4 and employed in Section 6.5.

6.6.1 Contact geometry and frequency

Using the same material combination and specimen configuration as the present work, Warmuth et al. [34] investigated the effects of fretting frequency and contact geometry (by varying the radius of the cylinder specimen), observing significant interaction between the two parameters resulting from changes in the rates of oxygen ingress to and debris expulsion from the interface. It was observed that the effect of increasing fretting frequency on wear mechanism is dependent upon contact conformity; less-conforming (i.e. smaller cylinder radius) contacts were observed to develop oxide-dominated wear scars at both low (f = 20 Hz) and high frequency (f = 200 Hz), while more-conforming (i.e. larger cylinder radius) contacts developed oxide-dominated scars at low frequency (f = 20 Hz) and more metallic wear scars at high frequency (f = 200 Hz). This was attributed to oxygen being more effectively excluded from the interface by large physical contact sizes (due primarily to the greater distance required for oxygen penetration into the interface) and high fretting frequency (due primarily to the reduced time for oxygen penetration); as such, at the conditions examined, *either* high frequency or large contact size was not in itself sufficient to result in oxygen starvation, with increases in *both* parameters being required to induce an oxygen-deficient wear mechanism. This observation may be restated within the physical framework outlined in this chapter, namely that high frequency and large contact width both act to reduce the limiting rate of oxygen transport into the contact such that it may become the rate-determining process, resulting in insufficient oxygen at the interface to form an oxide debris bed and hence the development of more metallic wear scars; understanding of this can be gained by examination of Figure 6.16, which shows the evolution of rate-determining processes predicted by the model over the same conditions as tested by Warmuth et al. [34].

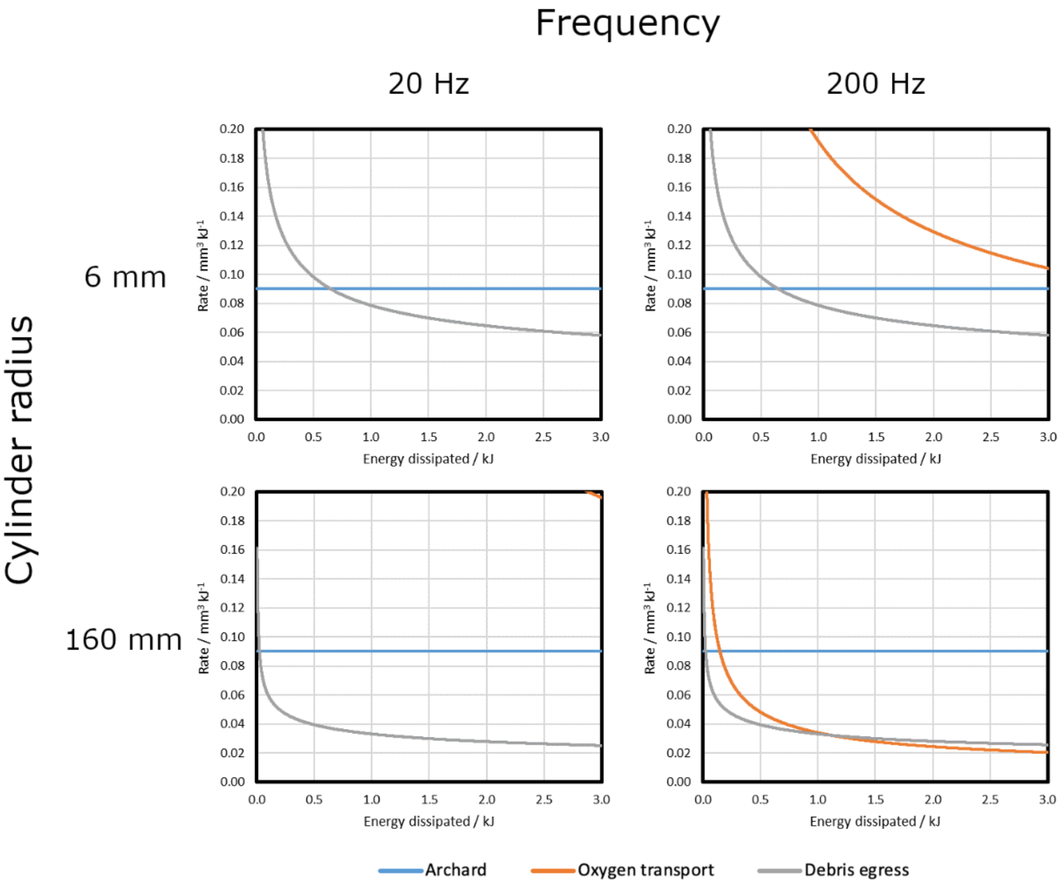

Figure 6.16. Evolution of rate-determining processes (as a function of dissipated energy) in fretting with different combinations of cylinder radius and fretting frequency, indicating a change in wear mechanism consistent with that reported by Warmuth et al. [34] ($\Delta^* = 50$ μm; $P = 250$ N; $N = 10^5$ cycles; $L = 10$ mm; $\mu = 0.7$).

It can be seen that for the less-conforming specimen geometry (R = 6 mm) and low frequency (f = 20 Hz), wear is controlled by either Archard wear or debris egress throughout the duration of the tests examined. It should be noted that in both cases the rate of oxygen ingress is too high to be represented on the same scale as the other conditions while still being able to see with sufficient detail which processes control the overall wear rate. At the high frequency condition, the maximum rate of oxygen ingress comes down significantly, although never so much as to become rate-determining and thus has no effect on overall wear rate. Conversely, at high frequency the more-conforming pair (R = 160 mm) is initially controlled by debris egress but becomes limited by the rate of oxygen ingress after approximately 1 kJ has been dissipated in the contact. The degradation behaviour predicted by the model is therefore in agreement with the observations of Warmuth et al. [34] that at this set of conditions it is only when oxygen ingress is restricted by both high frequency and more conforming contact geometry that wear mechanism changes to one in which oxygen starvation occurs and an oxide debris bed does not form.

6.6.2 Normal load

Previous work by Pearson and Shipway [26] investigated the fretting behaviour of the same specimen configuration and material combination as the present work over a range of normal loads, providing useful reference data for the alignment of the model with the effect of normal load. Tests were conducted at a fretting frequency of 20 Hz, an applied displacement amplitude of 50 μm and normal loads of 250 N, 450 N and 650 N. Experimental data are plotted alongside the corresponding model predictions in Figure 6.17 with higher dissipated energy reflecting a higher normal load. The average wear rates of both the model predictions and experimental values can be seen to be in relatively good agreement, exhibiting broadly the same trend as the experimental data, although wear volumes are slightly overestimated at the lower two normal loads and slightly underestimated at the highest load (650 N). Dissipated energy is slightly underestimated in all cases, likely to be due at least in part to a discrepancy in the rig stiffness, which was reported in the work of Pearson and Shipway [26] to be 57 MN m^{-1}, significantly higher than the 40 MN m^{-1} used in the present work.

The associated rates of key processes are shown in Figure 6.18, from which it can be seen that in all cases wear is controlled by Archard wear for a brief initial period (approximately the first 0.6 kJ), and then by debris egress for the remainder of the tests. The rate of oxygen ingress falls significantly as normal load is increased from 250 N to 650 N but does not become rate-determining in any of the test conditions examined.

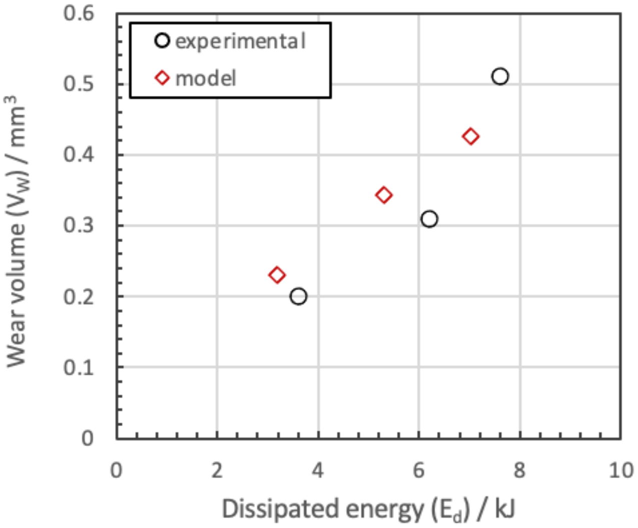

Figure 6.17. Plot of experimentally measured wear volumes (originally presented by Pearson and Shipway [26]) as a function of dissipated energy for fretting with applied normal loads of 250 N, 450 N and 650 N, and the corresponding predicted values; higher normal loads are reflected by higher dissipated energy (f = 20 Hz; Δ^* = 50 µm; N = 10^5 cycles; R = 6 mm; L = 10 mm).

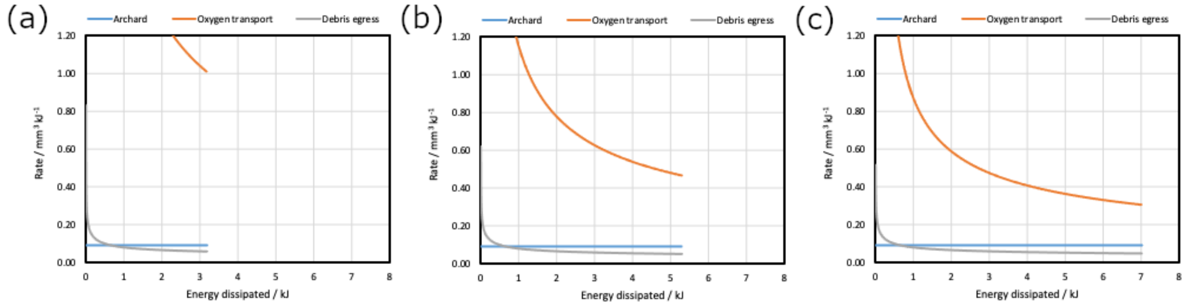

Figure 6.18. Evolution of rate-determining processes (as a function of dissipated energy) in fretting over the range of normal loads examined by Pearson and Shipway [26], namely (a) 250 N; (b) 450 N; (c) 650 N (R = 6 mm; f = 20 Hz; Δ^* = 50 µm; N = 10^5 cycles; L = 10 mm; μ = 0.7).

The observed wear rate at any given point is shown in Figure 6.19 for all three normal loads, and it can be seen that each of the cases overlays directly up to the respective dissipated energy at each normal load, and as such the increases in wear rate observed as normal load is increased are a result of the greater amount of energy dissipated, as opposed to changing the operative mechanism of wear.

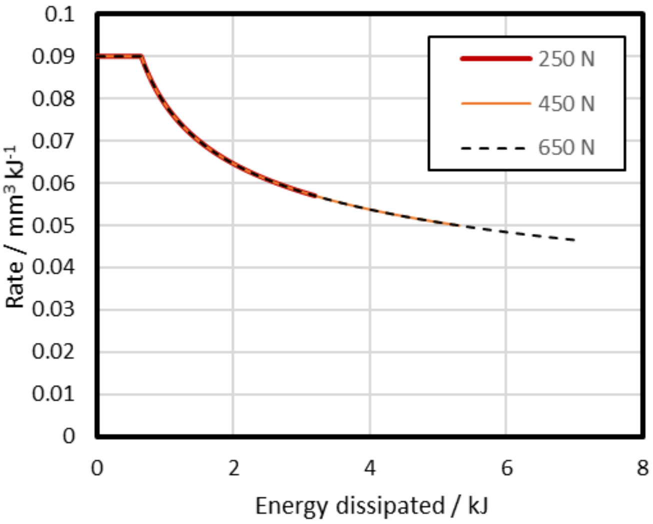

Figure 6.19. Observed wear rate (i.e. the rate of the rate-determining process at a given dissipated energy) across the range of normal loads examined, namely (a) 250 N; (b) 450 N; (c) 650 N (Δ^* = 50 μm; f = 20 Hz; N = 10^5 cycles; R = 6 mm; L = 10 mm).

6.6.3 Atmospheric oxygen concentration

It has been reported in several experimental investigations [1,35,106,152,153] that when oxygen pressure in the atmosphere is significantly reduced, such as in vacuum or an inert atmosphere such as argon or nitrogen, an oxidative wear mechanism cannot be sustained throughout the interface and wear occurs predominantly via an adhesive mechanism, and as such the overall wear rate falls significantly. Such a response can be rationalised within the physical framework outlined in the present work, as the maximum wear rate that can be sustained by oxygen ingress will fall along with the reduced atmospheric oxygen concentration. To the author's knowledge, there is no published data relating to fretting wear of a comparable contact configuration and material combination to the present work, and accordingly a direct comparison of model predictions and experimental data is not possible. However, the response of the model to reduced atmospheric oxygen concentration more broadly can be examined in order to evaluate the alignment with that which has been widely reported in the literature for various specimen geometries and material combinations.

The evolution of rate-determining processes in standard temperature and pressure air and an atmosphere in which the oxygen pressure is reduced by a factor of 1000 (simulating vacuum conditions) are shown in Figure 6.20. Reducing the atmospheric pressure (and hence the oxygen partial pressure) can be seen to result in the limiting rate of oxygen ingress falling sharply, becoming the rate-determining process from the beginning of the test and remaining so throughout the duration of the test. This is associated with a near total cessation of material removal (wear), although in reality significant subsurface damage and adhesive transfer would likely occur in the oxygen-limited regime.

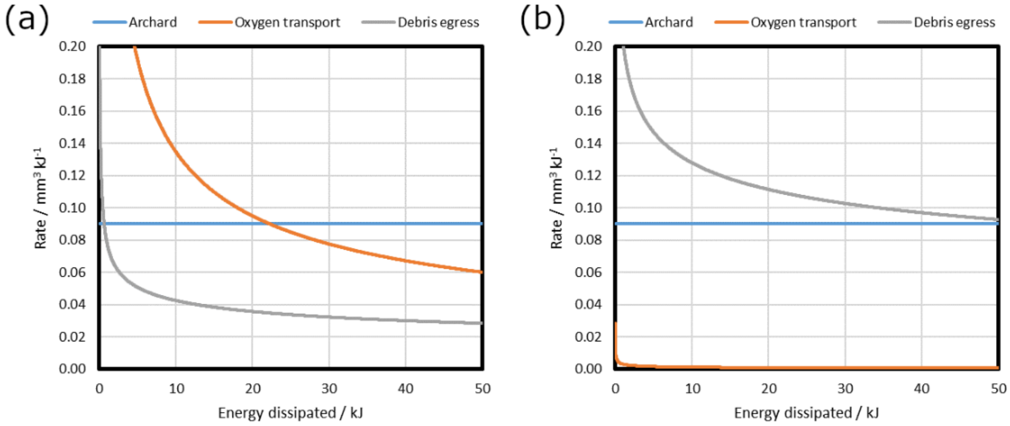

Figure 6.20. Evolution of rate-determining processes (as a function of dissipated energy) in fretting in air with a pressure of (a) 1 atm; (b) 0.001 atm; (R = 6 mm; f = 50 Hz; Δ^* = 50 μm; P = 450 N; N = 10^6 cycles; L = 10 mm; μ = 0.7)

6.6.4 Length of line contact

The length of the line contact is another parameter which would be expected to affect the rate-determining processes and hence the overall rate of wear in fretting, but for which there is not comparable experimental data that the model predictions can benchmarked against. It would be expected that increasing the length of the line contact whilst maintaining a constant normal load (thereby reducing the load per unit length) would result in a wear scar of smaller width for the same total wear volume, and that this in turn would affect the rates of key processes.

How this change in line contact length affects rate-determining processes can be seen in Figure 6.21, showing one case in which the length is equal to that of the experimental configuration employed in this work (L = 10 mm), and another under the same conditions except but with a line length of 1 m. In the shorter line case (L = 10 mm), the observed wear rate is determined by Archard wear for a brief initial period and then by debris egress for the remainder of the test, while increasing line contact length to 1 m increases the maximum rates of oxygen ingress and debris egress such that the observed wear rate is determined by Archard wear for the duration of the test. It can be seen that the same change in contact length raises the oxygen ingress line substantially more than the debris egress line, with this being due to oxygen ingress being dependent upon b^2, while debris egress is only dependent upon b. This is in part due to the same normal load being distributed over a longer length, and the commensurately narrower wear scar that forms; this increases the rate at which oxygen can penetrate the contact and that debris can be ejected.

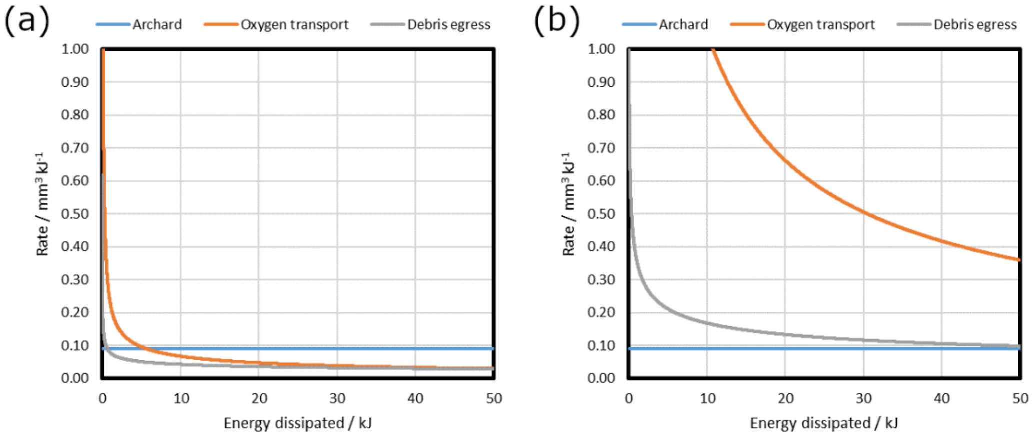

Figure 6.21. Evolution of rate-determining processes (as a function of dissipated energy) over the first 50 kJ dissipated in fretting in which the line contact has length (a) 10 mm; (b) 1000 mm; (R = 6 mm; f = 100 Hz; Δ^* = 50 μm; P = 450 N; N = 10^6 cycles; μ = 0.7)

6.7 Discussion

The previous sections demonstrate the alignment of the model with experimental data over a broad range of parameters, including parameters outside the set of frequencies and displacement amplitudes against which the values of proportionality constants are tuned. In assessing the capability of the model to predict fretting behaviour there are two aspects to consider, namely

(i) the total wear volume and dissipated energy (i.e. the wear rate) and (ii) the relative rates of key processes and which processes are rate-determining over a given set of conditions (i.e. the wear mechanism); it is noted that the accuracy of the model with regard to these two critical aspects of fretting behaviour does not necessarily align for a given set of conditions, with the values of constants being selected to provide optimum alignment with both the rates of processes relative to one another and the overall wear rate (as discussed in Section 6.4).

The relative rates of key processes (and hence wear mechanisms) predicted by the model exhibit good agreement with experimental observations over most of the conditions examined, although the difference between experimental and predicted wear rates is generally not insignificant, with differences in predicted and experimental wear volumes ranging from approximately 3% to as large as 90%; the values of dissipated energy predicted are generally in better alignment with experimental measurements, with differences ranging from 0.7% to 23%. The accuracy of predicted wear mechanisms and the ability of the model to capture broad trends in wear rate over a broad range of parameters provide a promising indication of the predictive capability of the proposed framework, although the significant differences in wear rates highlight that some of the assumptions involved in the model need to be fully evaluated and tested to identify the source of the discrepancies and hence improve the overall framework. As such, this discussion will address areas in which the model in its current form predicts changes in key processes, and identify areas where further work is needed to refine the approach to improve the accuracy of predictions and broaden the range of parameters over which it can be employed.

6.7.1 Reasons for error in prediction of fretting behaviour

While the model broadly captures the reduction in wear rate with frequency over the range of displacement amplitudes examined observed in the experiments (Figure 6.13), wear rates can be seen to be overestimated at the two lower displacement amplitudes (25 μm and 50 μm) and to be underestimated at the highest displacement amplitude ($\Delta^* = 100$ μm) at each frequency. Two factors that are likely to contribute to this effect are (i) the dependence of the rates of oxygen transport and debris egress upon the width of the contact, which is in turn dependent upon dissipated energy and hence displacement amplitude, and (ii) the assumed relationship between displacement amplitude and debris egress. Regarding the former, the narrower wear scars associated with smaller displacement amplitudes result in the operative wear rate being higher for a greater proportion of the test, as the rate of debris egress being proportional to $\frac{1}{b}$ and the rate of oxygen transport is proportional to $\frac{1}{b^2}$. Conversely, when wider scars form at larger displacement amplitudes, the rate of oxygen ingress falls at a faster rate than the rate of debris egress resulting in smaller wear volumes, particularly in conditions in which the rate of oxygen transport is reduced by other factors such as high fretting frequency. Furthermore, the overestimation of wear rates at small displacement amplitudes (for which debris egress is the rate-determining process) may be exacerbated by the relationship between displacement amplitude and debris egress; in the present work a simple relationship is assumed by which the displacement of a debris particle towards the edge of the contact is directly proportional to the applied displacement amplitude, although the nature of this relationship is not well understood and further work into the effect of displacement amplitude on debris egress may allow for an experimentally-derived relationship between the displacement of a debris particle towards the edge of the contact and the applied displacement amplitude to be implemented in the model.

Another possible reason for discrepancies in wear rates relates to the mechanism by which oxygen transport into the contact affects the formation of oxide debris; in the present work, restriction of oxygen transport to the interface only brings about changes in wear rate when oxygen becomes rate-determining; as such, this mechanism does not account for any effects on contact oxygenation relating to the impact of fretting parameters on the thickness of oxide films formed between asperity interactions (as per the "oxidational wear" model of Quinn [62]). The implications for wear prediction are apparent in the comparison to the work of Warmuth et al.

[34] regarding the effect of frequency and contact geometry on oxygen exclusion in Figure 6.16. Over the range of conditions employed in that work, without changing the values of proportionality constants the model accurately predicts that high frequency and large contact conformity result in oxygen exclusion from the interface and hence restricts the formation of oxide debris beds. However, in the same work of Warmuth et al. [34] where such a wear mechanism transition was reported, it was also reported that increasing frequency resulted in a reduction in wear rate that was significantly greater in less-conforming pairs than non-conforming pairs (i.e. increasing frequency was associated with a reduction in wear rate even when an oxide debris bed was observed to form). This was attributed to the effect of frequency on the time between asperity interactions and hence the thickness of oxide films before being scraped off to form a wear particle, an effect which is not accounted for in the rate-determining process model. The rate-determining process model is nonetheless well suited to predicting the effect of full oxygen exclusion from the interface, further demonstrated by the response to fretting in atmospheric conditions other than standard laboratory air, such as vacuum as demonstrated in Section 6.6.3, although it is noted that the mechanism of oxygen transport implemented in the model may be refined in future work.

6.7.2 Modelling approach: whole contact or local condition

As mentioned previously, the modelling framework outlined is closely related to that proposed by Zhu et al. [134], in which wear rate is modelled in terms of competing processes, with the observed wear rate being limited by whichever process occurs at the slowest rate (i.e. the rate-determining process). In this previous work, two processes were proposed to control wear rate, namely (i) debris formation as described by the Archard wear law (or equivalent), or (ii) debris expulsion from the interface. The wear volumes predicted using this approach were observed to exhibit good agreement with experimental data over a wide range of test durations, although other fretting parameters such as frequency, displacement amplitude and normal load were not examined. In this chapter a similar framework has been proposed, adopting some of the same underlying principles of the model of Zhu et al. [134] such as the dependence of the rates of key processes (and hence the observed wear rate) upon the physical size of the contact (namely the width of the contact formed between a cylinder and a flat), and the geometric relationship used to calculate wear volume as a function of wear scar width. The model outlined in the present work incorporates oxygen transport into the contact as a potentially rate-determining process, and directly relates the rates of key processes to fretting parameters, allowing for the effects of a wide range of fretting parameters on wear rates and mechanisms to be predicted, including the test-controlled parameters of frequency, displacement and normal load, along with other aspects of the contact configuration (such as the dimensions of the cylinder-on-flat contact patch and the concentration of the atmosphere). That the same set of constants can describe the effects of such a wide range of parameters with reasonable accuracy is very promising, highlighting the potential of the proposed modelling framework to predict fretting behaviour over a broad range of conditions based on the underlying physical principles of the model. It is relevant to note, however, that due to the assumed geometric relationship used to calculate wear volume as a function of wear scar width (and hence the assumption that wear proceeds equally at all points in the scar), the model is best suited to modelling of behaviour of the whole contact, such as the operative wear mechanism and the overall wear volume, as opposed to modelling the evolution of wear scar profiles based on local contact conditions at multiple points across the scar. Changes in wear scar shape were noted in the previous chapter to occur due to a wear mechanism transition relating to the formation and retention of oxide debris; however, it is not expected that these changes in wear scar shape have a significant impact on the overall wear volume, and as such the assumption that wear proceeds at the same rate across the contact is not expected to negatively impact the accuracy of wear volume predictions.

The "whole contact" nature of the model also influences the mechanism by which oxygen transport limits wear rates (i.e. oxygen exclusion), as it is assumed that wear proceeds at the same rate across the interface, with the rate of wear across the scar falling such that oxygen concentration remains above a threshold value (assumed to be zero). This contrasts with the contact oxygenation concept of Fouvry and co-workers [10,25,29,31], in which wear rate is considered to vary locally within the scar based on oxygen concentration, which may see a transition from oxidative-abrasive wear to adhesive wear as oxygen concentration drops below a threshold value, with wear rate being lower near the centre of the wear scar and faster in the regions of the scar close to the edge of the contact patch where oxygen concentration is higher. Such an approach to modelling oxygen transport has the advantage of potentially being able to simulate the formation of W-shaped scars in which oxide-dominated lateral regions border a central metallic region, which have been associated with oxygen exclusion in experimental investigations [10,25,29], including the previous chapter of this thesis. The approach to oxygen transport taken in the present work is a relatively simple model suited to predicting the effect of oxygen transport upon overall wear volume, and whether oxygen-deprived regions will form anywhere at the interface. As such, the oxygen concentration in the contact is not related to the local evolution of the wear scar surface, and the location or dimensions of any adhesive transfer or transformed metallic regions that form, although as mentioned previously this is not expected to have a significant effect on the accuracy of wear volume predictions.

6.8 Conclusions

- Wear rates can be modelled via the competition between three key processes of fretting wear; it is the slowest of these which becomes the "rate-determining process" which governs the overall rate of wear.

- Equations are derived for rates of oxygen ingress and debris egress (identified in Chapter 5 as being critical to the operative mechanism) which compete with the abrasive wear behaviour described by Archard to control overall wear rate.
- These equations are derived based on current understanding of the physics of fretting wear (notably including the observations outlined in the previous two chapters) but may be modified in future without disrupting the structure of this modelling approach.
- The competitive rate-determining method provides a method for modelling the role of debris in fretting wear, incorporating the role of oxygen ingress to the interface in debris formation, and the rate at which oxide is ejected from the contact, which are both critical in enabling wear to proceed.
- Moreover, the model may be implemented using a simple time-marching method.
- Due to the assumed geometric relationship used to calculate wear volume as a function of wear scar width (and hence the assumption that wear proceeds equally at all points in the scar), the model is arguably best suited to modelling the behaviour over the whole contact, such as the operative wear mechanism and the associated wear volume under a given set of conditions, as opposed to precise evolution of wear scar profiles; this is not expected to have a significant impact on the accuracy of predictions of overall contact behaviour, although there may be benefit in investigating this in future work in this area.
- Future developments may include the modification of the model to incorporate the effects of temperature (both environmental and local increase due to frictional power dissipation) on debris sintering, and hence the formation of glaze layers that have been reported to significantly reduce wear rates at high temperatures.

Conclusions

The fretting wear response of a high strength steel has been examined over a range of fretting frequencies and displacement amplitudes, with emphasis placed on characterisation of wear debris, both in the form of compacted beds retained in the contact and particles ejected during the wear process. Two distinct wear regimes were identified, namely (i) at low frequencies and displacement amplitudes, an oxide debris bed covers most of the worn surface, preventing the development of subsurface damage and adhesive transfer but resulting in relatively high wear rates, and (ii) at high frequencies and displacement amplitudes oxide coverage of worn surfaces is relatively sparse, resulting in metal-to-metal contact and the development of significant subsurface damage and adhesive transfer. In either regime, the nature of debris ejected during fretting appears to be not strongly dependent upon either the fretting frequency or the displacement amplitude, indicating that there is no change in the fundamental mechanism by which debris is expelled from the contact, despite significant changes in friction and wear rate over these conditions. As such, it is proposed that over the range of frequencies and displacement amplitudes examined wear proceeds by a broadly oxidative mechanism (i.e. by the formation and ejection of oxide debris), comparable to the regime of "mild" wear in other types of sliding wear, with no evidence of a transition to a "severe" wear regime in which a greater proportion of large metallic particles are ejected.

The composition of ejected debris is in line with previous work on fretting of steel contacts in air at room temperature with two phases observed in samples, namely haemetite and ferrite, the relative proportions of which were quantitatively assessed and, despite a modest influence of both parameters, in all cases debris was found to consist predominantly of haemetite with a small (< 6%) fraction of metallic iron.

Likewise, the overall range of particle sizes is largely independent of frequency and displacement amplitude, ranging from approximately 0.4 μm to 50 μm under all conditions tested, and is observed to reach a broadly steady state condition at an early stage of fretting tests. The relative size of debris particles within samples is found to be somewhat affected by both frequency and displacement amplitude, with increasing frequency resulting in a greater proportion of smaller particles being ejected from the contact (reducing the average size), while increasing displacement amplitude results in a greater proportion of both larger and smaller particles being ejected (i.e. a broader size distribution), without having a significant impact on the average size.

The morphology of particles indicated a significant degree of sintering of submicron oxide crystallites, none of which were observed in isolation; the size of the crystallites appears similar for debris particles ejected under both large and small displacement amplitude conditions, indicating that over the conditions tested, the fundamental mechanism of debris particle formation does not change, and rather the development of debris particles depends on the formation and breakdown of debris beds, and hence the degree of sintering. Further evidence of significant debris sintering is found in the large size of ejected debris particles provides occurring within the fretting contact, with the average size of ejected particles ranging from 6 μm to 17 μm under all conditions studied, and individual particles with diameters of the order of 100 μm being observed via SEM imaging, thought to be detached pieces of debris beds (i.e. small thickness relative to observed diameter).

Regarding the two distinct wear regimes observed, it is noted that the effects of displacement amplitude and frequency in fretting wear are interdependent, with the impact of either parameter on the wear rate and damage mechanism depending upon the magnitude of the other. At low frequency, increasing displacement amplitude does not significantly affect the development of oxide debris beds, while at high frequency, increasing displacement amplitude results in a transition from an oxidation-dominated wear mechanism to one in which a protective oxide debris bed cannot form, resulting in an increase in metal-metal contact and the development of severe subsurface damage.

Displacement amplitude is observed to not significantly impact wear rate over the range of conditions examined, while increasing fretting frequency is found to result in a significant reduction in wear rate at each of the displacement amplitudes examined. However, displacement amplitude has a significant impact on the effect of frequency on damage mechanism which at larger displacement amplitudes results in wear scars becoming more metallic (i.e. reduced coverage by oxide debris beds), and at smaller amplitudes to result in a more coherent oxide debris bed being formed.

It is argued that whether wear occurs in Regime I or Regime II is a result of the magnitudes of the fretting frequency and displacement amplitude, and not solely due to the effects of these parameters on frictional power dissipation; while both fretting frequency and displacement amplitude influence frictional power dissipation in the contact, they also affect a number of other processes that are critical to fretting wear of which power dissipation is only one. It is proposed that the interacting effects of frequency and displacement amplitude arise from the impact of both parameters on three key processes, namely (i) ingress of oxygen to the contact; (ii) formation of oxide debris; (iii) expulsion of oxide debris from the contact.

On this basis, a model is proposed in which wear rates can be modelled via the competition between these three processes, with the observed wear rate being governed by whichever of these rates is the smallest, accordingly termed the "rate-determining process". Equations for the rates of the three key processes are derived based on current understanding of the physics of fretting wear, enabling the model to be implemented using a simple time-marching method. Wear rates and mechanisms (i.e. which processes are operative at a given set of conditions) predicted using this model show relatively good agreement with experimental data over a diverse range of fretting parameters, including the effects of frequency and displacement amplitude investigated in this thesis as well as reports in the literature employing the same specimen configuration and material combination. It is noted that the rate equations in the model are based on a number of assumptions, the validity of which must be assessed in future work, although these may be readily modified within the proposed model framework as understanding of the physical behaviours develops.

Future work

Investigating model assumptions

The model outlined in Chapter 6 represents a useful step forward in the development of physics-based predictive models incorporating the role of debris in the mechanisms of wear; however, the model is based on several assumptions, all clearly outlined in the model's construction, which must be investigated in detail in order to improve the accuracy of predictions going forward. Evidence for some of these assumptions, such as wear being controlled by the ejection of oxide debris has been presented in this thesis, while some, such as the relationship between displacement amplitude and the ejection of oxide debris are based on broader trends reported in literature, which vary between authors and the details of which are still not well understood. The impact of displacement amplitude on wear rate and on processes highlighted in this thesis as having a significant impact on wear mechanisms, namely oxygen transport and debris expulsion, should therefore be targeted in future work. Improving understanding of the effects of displacement amplitude on these processes will be critical in refining the modelling approach outlined in this thesis, and it therefore an important area for future work; this may be simplified by careful selection of fretting parameters to eliminate the influence of selected processes, for example by running tests at low frequency so that oxygen transport is not a limiting factor in any of the experiments. Fretting response should be investigated over a wider range of displacement amplitudes in this thesis (e.g. up to several hundred micrometres) and over a wide range of test durations, providing greater insight into the effects of displacement amplitude on debris expulsion and oxygen transport in fretting. For the same number of cycles, larger displacement amplitudes result in a greater overall slip displacement, and so examining a range of test durations may enable the impact of the amplitude of displacement to be more clearly discerned.

Using the rate-determining process model in conjunction with experimental testing

The rate-determining process model outlined in Chapter 6 states that the rates of key processes are dependent upon the wear scar width, and as such the magnitude of rates relative to one another varies throughout the duration of a test. The model therefore predicts the evolution of these processes over the full duration of the test, allowing for the operative mechanism at any stage of the test to be identified. The accuracy of the model may therefore be assessed by conducting laboratory experiments of various durations, enabling the operative wear mechanisms and overall wear rates predicted by the model to be compared to experimental data.

Incorporating the effects of temperature

The robustness of the model may also be improved by incorporating the effects of temperature on key processes, most notably the sintering of debris to form protective glaze layers, which have been found to significantly reduce wear rates. This could be achieved using a method similar to that developed by Dréano et al. [116], in which a "sintering parameter" is introduced to incorporate the effects of fretting parameters on local temperature, and thus adjust wear rate based on whether the sintering parameter is above or below a threshold value representing the critical temperature for glaze layer formation at a given set of conditions, the value of which may be based on experimental observations. Moreover, it is acknowledged that the values of proportionality constants employed in the present work (particularly the diffusion coefficient in the equation for oxygen transport) are expected to be temperature-dependent; in the present work, only fretting at room temperature is examined, and as such it is assumed that over the range of conditions examined, the effect of temperature on overall wear behaviour is small and therefore adequately represented in the tuning of the model to experimental data (Section 6.4), although such an assumption may not be made when considering fretting at elevated temperatures.

Contact geometry

All of the experimental work presented in this thesis was generated using a cylinder-on-flat specimen configuration with a 6 mm radius. Specimen geometry can be modified to increase the radius of the cylinder specimen (and hence the conformity of the contact) and potentially other dimensions of the specimens such as the width of the flat specimen (and hence the length of the line contact). Moreover, the geometric relationship between wear volume and the width of the wear scar assumed in the modelling framework outlined in Chapter 6 has so far only been developed and validated for a cylinder-on-flat configuration; developing corresponding relationships for other common specimen geometries such as sphere-on-flat and cross cylinders and applying these in a similar modelling framework would be of great value in enhancing the applicability of the model in engineering applications.

Material combination

The work of this thesis examines only one material combination, namely self-mating high strength steel contacts, which is used as the basis for a new model for fretting wear; however, it is clear from the body of fretting research that different materials may exhibit significantly different wear behaviour under the same conditions, and as such there would be significant benefit to investigating the applicability of the model to other material combinations. These may include dissimilar pairs, enabling insight to be gained into the impact on wear mechanisms of opposing specimens having either different mechanical properties, chemical compositions or both; for example, investigating fretting behaviour of specimens with differing chemical composition would be useful in assessing the extent to which the damaged layers observed in the present work at high frequencies and displacement amplitudes are formed due to transfer of material between specimens. Furthermore, materials such as titanium alloys and nickel- and cobalt-based superalloys are particularly relevant to engineering applications in which fretting is observed, and so understanding how the behaviour of these materials differs from that observed in this thesis for steel pairs is paramount to improving the applicability of models such as that outlined in Chapter 6 in industrial applications.

References

[1] R.B. Waterhouse, Fretting corrosion, Pergamon Press, 1972.

[2] H.C. Meng, K.C. Ludema, Wear models and predictive equations: their form and content, Wear. 181–183 (1995) 443–457. https://doi.org/10.1016/0043-1648(95)90158-2.

[3] E.M. Eden, W.N. Rose, F.L. Cunningham, The endurance of metals: experiments on rotating beams at University College, London, Proc. Inst. Mech. Eng. 81 (1911) 829–880.

[4] G.A. Tomlinson, The rusting of steel surfaces in contact, Proc. R. Soc. A. 115 (1927) 472–483.

[5] O. Vingsbo, S. Söderberg, On fretting maps, Wear. 126 (1988) 131–147. https://doi.org/10.1016/0043-1648(88)90134-2.

[6] R.D. Mindlin, Compliance of elastic bodies in contact, J. Appl. Mech. Trans. ASME. 16 (1949) 259–268.

[7] C. Cattaneo, Sul contatto de due corpi elastici: Distribuzione locale deglisforzi, Rend. Dell'Accademia Naz. Dei Lincei. 6 (1996) 342–349.

[8] S. Fouvry, P. Kapsa, L. Vincent, Quantification of fretting damage, Wear. 200 (1996) 186–205. https://doi.org/https://doi.org/10.1016/S0043-1648(96)07306-1.

[9] N. Ohmae, T. Tsukizoe, The effect of slip amplitude on fretting, Wear. 27 (1974) 281–294. https://doi.org/https://doi.org/10.1016/0043-1648(74)90114-8.

[10] S. Baydoun, S. Fouvry, An experimental investigation of adhesive wear extension in fretting interface: Application of the contact oxygenation concept, Tribol. Int. 147 (2020) 106266. https://doi.org/10.1016/J.TRIBOINT.2020.106266.

[11] K.L. Johnson, Contact mechanics, Cambridge university press, 1987.

[12] I.R. McColl, J. Ding, S.B. Leen, Finite element simulation and experimental validation of fretting wear, Wear. 256 (2004) 1114–1127. https://doi.org/https://doi.org/10.1016/j.wear.2003.07.001.

[13] R.D. Mindlin, H. Deresiewicz, Elastic spheres in contact under varying oblique forces, Trans. ASME. 20 (1953) 327–344.

[14] X. Jin, Investigation of the interrelated effects of temperature and frequency on fretting wear, University of Nottingham, 2017.

[15] X. Jin, W. Sun, P.H. Shipway, Derivation of a wear scar geometry-independent

coefficient of friction from fretting loops exhibiting non-Coulomb frictional behaviour, Tribol. Int. 102 (2016) 561–568. https://doi.org/10.1016/j.triboint.2016.06.012.

[16] S. Fouvry, P. Duó, P. Perruchaut, A quantitative approach of Ti–6Al–4V fretting damage: friction, wear and crack nucleation, Wear. 257 (2004) 916–929. https://doi.org/https://doi.org/10.1016/j.wear.2004.05.011.

[17] D.M. Mulvihill, M.E. Kartal, A. V Olver, D. Nowell, D.A. Hills, Investigation of non-Coulomb friction behaviour in reciprocating sliding, Wear. 271 (2011) 802–816. https://doi.org/10.1016/j.wear.2011.03.014.

[18] Z.R. Zhou, L. Vincent, Mixed fretting regime, Wear. 181–183 (1995) 531–536. https://doi.org/10.1016/0043-1648(95)90168-X.

[19] M.H. Zhu, Z.R. Zhou, On the mechanisms of various fretting wear modes, Tribol. Int. 44 (2011) 1378–1388.

[20] J. Hintikka, A. Lehtovaara, A. Mäntylä, Normal displacements in non-Coulomb friction conditions during fretting, Tribol. Int. 94 (2016) 633–639. https://doi.org/10.1016/j.triboint.2015.10.029.

[21] I. Llavori, A. Zabala, A. Aginagalde, W. Tato, J.J. Ayerdi, X. Gómez, Critical Analysis of Coefficient of Friction Derivation Methods for Fretting under Gross Slip Regime, Tribol. Int. 143 (2020). https://doi.org/10.1016/j.triboint.2019.105988.

[22] J. Halliday, W. Hirst, The fretting corrosion of mild steel, Proc. R. Soc. A Math. Phys. Eng. Sci. 236 (1956) 411–425.

[23] S. Fouvry, C. Paulin, S. Deyber, Impact of contact size and complex gross–partial slip conditions on Ti–6Al–4V/Ti–6Al–4V fretting wear, Tribol. Int. 42 (2009) 461–474. https://doi.org/https://doi.org/10.1016/j.triboint.2008.08.005.

[24] A. Fantetti, L.R. Tamatam, M. Volvert, I. Lawal, L. Liu, L. Salles, M.R.W. Brake, C.W. Schwingshackl, D. Nowell, The impact of fretting wear on structural dynamics: Experiment and Simulation, Tribol. Int. (2019). https://doi.org/10.1016/j.triboint.2019.05.023.

[25] S. Baydoun, S. Fouvry, S. Descartes, P. Arnaud, Fretting wear rate evolution of a flat-on-flat low alloyed steel contact: A weighted friction energy formulation, Wear. 426–427 (2019) 676–693. https://doi.org/https://doi.org/10.1016/j.wear.2018.12.022.

[26] S.R. Pearson, P.H. Shipway, Is the wear coefficient dependent upon slip amplitude in fretting? Vingsbo and Söderberg revisited, Wear. 330–331 (2015) 93–102. https://doi.org/10.1016/j.wear.2014.11.005.

[27] D. Aldham, J. Warburton, R.E. Pendlebury, The unlubricated fretting wear of mild steel in air, Wear. 106 (1985) 177–201. https://doi.org/https://doi.org/10.1016/0043-1648(85)90109-7.

[28] J. Warburton, The fretting of mild steel in air, Wear. 131 (1989) 365–386. https://doi.org/https://doi.org/10.1016/0043-1648(89)90176-2.

[29] S. Fouvry, P. Arnaud, A. Mignot, P. Neubauer, Contact size, frequency and cyclic normal force effects on Ti–6Al–4V fretting wear processes: An approach combining friction power and contact oxygenation, Tribol. Int. 113 (2017) 460–473.

[30] A.R. Warmuth, S.R. Pearson, P.H. Shipway, W. Sun, The effect of contact geometry on fretting wear rates and mechanisms for a high strengthsteel, Wear. 301 (2013) 491–

500. https://doi.org/10.1016/j.wear.2013.01.018.

[31] S. Baydoun, P. Arnaud, S. Fouvry, Modelling adhesive wear extension in fretting interfaces: An advection-dispersion-reaction contact oxygenation approach, Tribol. Int. (2020) 106490. https://doi.org/https://doi.org/10.1016/j.triboint.2020.106490.

[32] L. Toth, The investigation of the steady stage of steel fretting, Wear. 20 (1972) 277–286. https://doi.org/https://doi.org/10.1016/0043-1648(72)90409-7.

[33] B. van Peteghem, S. Fouvry, J. Petit, Effect of variable normal force and frequency on fretting wear response of Ti–6Al–4V contact, Wear. 271 (2011) 1535–1542. https://doi.org/https://doi.org/10.1016/j.wear.2011.01.060.

[34] A.R. Warmuth, P.H. Shipway, W. Sun, Fretting wear mapping: The influence of contact geometry and frequency on debris formation and ejection for a steel-on-steel pair, Proc. R. Soc. A Math. Phys. Eng. Sci. 471 (2015). https://doi.org/10.1098/rspa.2014.0291.

[35] I.M. Feng, H.H. Uhlig, Fretting corrosion of mild steel in air and in nitrogen, J. Appl. Mech. 21 (1954) 395–400.

[36] U. Bryggman, S. Söderberg, Contact conditions in fretting, Wear. 110 (1986) 1–17. https://doi.org/https://doi.org/10.1016/0043-1648(86)90148-1.

[37] G. Sundararajan, An analysis of the localization of deformation and weight loss during single-particle normal impact, Wear. 84 (1983) 217–235.

[38] R. Merhej, S. Fouvry, Contact size effect on fretting wear behaviour: Application to an AISI 52100/AISI 52100 interface, Lubr. Sci. 21 (2009) 83–102. https://doi.org/10.1002/ls.74.

[39] J.D. Lemm, A.R. Warmuth, S.R. Pearson, P.H. Shipway, The influence of surface hardness on the fretting wear of steel pairs—Its role in debris retention in the contact, Tribol. Int. 81 (2015) 258–266. https://doi.org/https://doi.org/10.1016/j.triboint.2014.09.003.

[40] J.F. Archard, Contact and rubbing of flat surfaces, J. Appl. Phys. 24 (1953) 981–988. https://doi.org/10.1063/1.1721448.

[41] C. Mary, S. Fouvry, J.M. Martin, B. Bonnet, Pressure and temperature effects on Fretting Wear damage of a Cu–Ni–In plasma coating versus Ti17 titanium alloy contact, Wear. 272 (2011) 18–37.

[42] C. Mary, T. Le Mogne, B. Beaugiraud, B. Vacher, J.M. Martin, S. Fouvry, Tribochemistry of a Ti alloy under fretting in air: Evidence of titanium nitride formation, Tribol. Lett. 34 (2009) 211–222. https://doi.org/10.1007/s11249-009-9426-6.

[43] X. Jin, P.H. Shipway, W. Sun, The Role of Temperature and Frequency on Fretting Wear of a Like-on-Like Stainless Steel Contact, Tribol. Lett. 65 (2017) 77. https://doi.org/10.1007/s11249-017-0858-0.

[44] G.H.G. Vaessen, C.P.L. Commissaris, A.W.J. De Gee, Fretting Corrosion of Cu-Ni–Al against Plain Carbon Steel, in: Proc. Inst. Mech. Eng. Conf. Proc., SAGE Publications Sage UK: London, England, 1968: pp. 125–128.

[45] M. Godet, The third-body approach: A mechanical view of wear, Wear. 100 (1984) 437–452. https://doi.org/10.1016/0043-1648(84)90025-5.

[46] M. Godet, Third-bodies in tribology, Wear. 136 (1990) 29–45. https://doi.org/10.1016/0043-1648(90)90070-Q.

[47] C. Colombié, Y. Berthier, A. Floquet, M. Godet, Fretting: Load carrying capacity of wear debris, J. Tribol. 106 (1984) 192–200. https://doi.org/10.1115/1.3260881.

[48] Y. Berthier, L. Vincent, M. Godet, Velocity accommodation in fretting, Wear. 125 (1988) 25–38. https://doi.org/10.1016/0043-1648(88)90191-3.

[49] Y. Berthier, L. Vincent, M. Godet, Velocity accommodation sites and modes in tribology, Eur. J. Mech. A/Solids. 11 (1992) 35–47.

[50] Y. Berthier, Maurice Godet's third body, in: D. Dowson (Ed.), Proc. 22nd Leeds-Lyon Symp. Tribol. Third Body Concept, Tribology Series (31), 1996: pp. 21–30.

[51] N. Fillot, I. Iordanoff, Y. Berthier, Wear modeling and the third body concept, Wear. 262 (2007) 949–957. https://doi.org/10.1016/j.wear.2006.10.011.

[52] S. Descartes, Y. Berthier, Rheology and flows of solid third bodies: Background and application to an MoS1.6 coating, Wear. 252 (2002) 546–556. https://doi.org/10.1016/S0043-1648(02)00008-X.

[53] D. Play, Visualization of chalk wear, in: Proc. 3rd Leed-Lyon Symp. Wear Non-Metallic Mater. 1978, Mechanical Engineering Publications, 1978.

[54] Y. Berthier, D. Play, Wear mechanisms in oscillating bearings, Wear. 75 (1982) 369–387.

[55] H.E. Sliney, Dynamics of Solid Lubrication as Observed by Optical Microscopy, A S L E Trans. 21 (1978) 109–117. https://doi.org/10.1080/05698197808982866.

[56] M. Belin, J.M. Martin, Triboscopy, a new approach to surface degradations of thin films, Wear. 156 (1992) 151–160.

[57] A. Jullien, M.H. Meurisse, Y. Berthier, Determination of tribological history and wear through visualisation in lubricated contacts using a carbon-based composite, Wear. 194 (1996) 116–125. https://doi.org/https://doi.org/10.1016/0043-1648(95)06813-9.

[58] S.D. Dvorak, K.J. Wahl, I.L. Singer, In Situ Analysis of Third Body Contributions to Sliding Friction of a Pb–Mo–S Coating in Dry and Humid Air, Tribol. Lett. 28 (2007) 263–274. https://doi.org/10.1007/s11249-007-9270-5.

[59] H. Uhlig, Mechanism of fretting corrosion, J. Appl. Mech. 21 (1954) 401–407.

[60] F.H. Stott, J. Glascott, G.C. Wood, Factors affecting the progressive development of wear-protective oxides on iron-base alloys during sliding at elevated temperatures, Wear. 97 (1984) 93–106. https://doi.org/https://doi.org/10.1016/0043-1648(84)90084-X.

[61] T.F.J. Quinn, Oxidational wear, Wear. 18 (1971) 413–419. https://doi.org/10.1016/0043-1648(71)90005-6.

[62] T.F.J. Quinn, Role of oxidation in the mild wear of steel, Br. J. Appl. Phys. 13 (1962) 33.

[63] I.M. Feng, B.G. Rightmire, An Experimental Study of Fretting, Proc. Inst. Mech. Eng. 170 (1956) 1055–1064. https://doi.org/10.1243/PIME_PROC_1956_170_089_02.

[64] J.M. Bailey, D. Godfrey, Coefficient of friction and damage to contact area during the early stages of fretting II: steel, iron, iron oxide, and glass combinations, 1954.

[65] D. Godfrey, J.M. Bailey, Coefficient of Friction and Damage to Contact Area During the Early Stages of Fretting I: Glass, Copper, or Steel Against Copper, 1953.

[66] R.E. Pendlebury, Paper IV(iii) Unlubricated fretting wear of mild steel surfaces in air at room temperature. Part III. The conversion of (artificial) metallic wear particles to oxide, Tribol. Ser. 12 (1987) 99–103. https://doi.org/https://doi.org/10.1016/S0167-8922(08)71053-8.

[67] R.B. Waterhouse, D.E. Taylor, Fretting debris and the delamination theory of wear, Wear. 29 (1974) 337–344. https://doi.org/10.1016/0043-1648(74)90019-2.

[68] D. Godfrey, Investigation of fretting by microscope obervation, 1950.

[69] P. Blanchard, C. Colombie, V. Pellerin, S. Fayeulle, L. Vincent, Material effects in fretting wear: application to iron, titanium, and aluminum alloys, Metall. Trans. A. 22 (1991) 1535–1544. https://doi.org/10.1007/BF02667367.

[70] J.F. Archard, W. Hirst, The wear of metals under unlubricated conditions, Proc. R. Soc. London. Ser. A. Math. Phys. Sci. 236 (1956) 397–410. https://doi.org/10.1098/rspa.1956.0144.

[71] E.S. Sproles Jr, D.J. Duquette, The mechanism of material removal in fretting, Wear. 49 (1978) 339–352.

[72] T. Kayaba, A. Iwabuchi, The fretting wear of 0.45% C steel and austenitic stainless steel from 20 to 650 °C in air, Wear. 74 (1981) 229–245. https://doi.org/https://doi.org/10.1016/0043-1648(81)90165-4.

[73] T. Liskiewicz, K. Kubiak, T. Comyn, Nano-indentation mapping of fretting-induced surface layers, Tribol. Int. 108 (2017) 186–193. https://doi.org/10.1016/j.triboint.2016.10.018.

[74] E. Sauger, S. Fouvry, L. Ponsonnet, P. Kapsa, J.M. Martin, L. Vincent, Tribologically transformed structure in fretting, Wear. 245 (2000) 39–52. https://doi.org/10.1016/S0043-1648(00)00464-6.

[75] E. Sauger, L. Ponsonnet, J.M. Martin, L. Vincent, Study of the tribologically transformed structure created during fretting tests, Tribol. Int. 33 (2000) 743–750. https://doi.org/10.1016/S0301-679X(00)00088-8.

[76] V. Nurmi, J. Hintikka, J. Juoksukangas, M. Honkanen, M. Vippola, A. Lehtovaara, A. Mäntylä, J. Vaara, T. Frondelius, The formation and characterization of fretting-induced degradation layers using quenched and tempered steel, Tribol. Int. 131 (2019) 258–267. https://doi.org/https://doi.org/10.1016/j.triboint.2018.09.012.

[77] Z.R. Zhou, E. Sauger, J.J. Liu, L. Vincent, Nucleation and early growth of tribologically transformed structure (TTS) induced by fretting, Wear. 212 (1997) 50–58. https://doi.org/10.1016/S0043-1648(97)00141-5.

[78] M. Busquet, S. Descartes, Y. Berthier, Formation conditions of mechanically modified superficial structures for two steels, Tribol. Int. 42 (2009) 1730–1743. https://doi.org/10.1016/j.triboint.2009.04.045.

[79] J. Vizintin, B. Podgornik, M. Kalin, J. Pezdirnik, F. Vodopivec, Three-body contact temperature in fretting conditions, in: Proc. Twenty-Second Leeds–Lyon Symp. Tribol. Lyon, Fr., Elsevier Amsterdam, 1995.

[80] S. Fouvry, T. Liskiewicz, P. Kapsa, S. Hannel, E. Sauger, An energy description of wear mechanisms and its applications to oscillating sliding contacts, Wear. 255 (2003) 287–298. https://doi.org/https://doi.org/10.1016/S0043-1648(03)00117-0.

[81] L. Xin, Y. Lu, T. Shoji, The comparative study on nanostructured tribolayers of Alloy 690TT subjected to fretting wear under different oxygen contents, Mater. Charact. 131 (2017) 157–167. https://doi.org/10.1016/j.matchar.2017.04.034.

[82] J. Li, M. Ma, Y.H. Lu, L. Xin, Evolution of wear damage in Inconel 600 alloy due to fretting against type 304 stainless steel, Wear. 346–347 (2016) 15–21. https://doi.org/10.1016/j.wear.2015.10.011.

[83] L. Xin, H. Luo, J. Han, Y. Lu, T. Shoji, Damage mechanism of Alloy 690TT mated with Type 304 stainless steel during fretting wear in partial slip regime, Mater. Charact. 132 (2017) 284–292. https://doi.org/10.1016/j.matchar.2017.08.024.

[84] L. Xin, Z. Wang, J. Li, Y. Lu, T. Shoji, Microstructural characterization of subsurface caused by fretting wear of Inconel 690TT alloy, Mater. Charact. 115 (2016) 32–38. https://doi.org/10.1016/j.matchar.2016.03.010.

[85] J. Vižintin, M. Kalin, B. Podgornik, F. Vodopivec, The effect of slip amplitude and test time on fretting wear in metal-metal contact, Tribotest. 3 (1996) 149–165. https://doi.org/https://doi.org/10.1002/tt.3020030204.

[86] X. Jin, P.H. Shipway, W. Sun, The role of frictional power dissipation (as a function of frequency) and test temperature on contact temperature and the subsequent wear behaviour in a stainless steel contact in fretting, Wear. 330–331 (2015) 103–111. https://doi.org/10.1016/j.wear.2015.02.022.

[87] M.F. Ashby, J. Abulawi, H.S. Kong, Temperature Maps for Frictional Heating in Dry Sliding, Tribol. Trans. 34 (1991) 577–587. https://doi.org/10.1080/10402009108982074.

[88] D.A. Rigney, Transfer, mixing and associated chemical and mechanical processes during the sliding of ductile materials, Wear. 245 (2000) 1–9.

[89] J. Juoksukangas, V. Nurmi, J. Hintikka, M. Honkanen, M. Vippola, A. Lehtovaara, A. Mäntylä, J. Vaara, T. Frondelius, Cracks and degradation layers in large flat-on-flat fretting contact with steels and cast iron, Tribol. Int. 145 (2020) 106102. https://doi.org/https://doi.org/10.1016/j.triboint.2019.106102.

[90] L. Xin, Y. Lu, T. Shoji, The role of material transfer in fretting wear behavior and mechanism of Alloy 690TT mated with Type 304 stainless steel, Mater. Charact. 130 (2017) 250–259.

[91] J. Juoksukangas, V. Nurmi, J. Hintikka, M. Vippola, A. Lehtovaara, A. Mäntylä, J. Vaara, T. Frondelius, Characterization of cracks formed in large flat-on-flat fretting contact, Int. J. Fatigue. 124 (2019) 361–370. https://doi.org/10.1016/j.ijfatigue.2019.03.004.

[92] E.K. Hayes, P.H. Shipway, Effect of test conditions on the temperature at which a protective debris bed is formed in fretting of a high strength steel, Wear. 376–377 (2017) 1460–1466. https://doi.org/10.1016/j.wear.2017.01.057.

[93] S.R. Pearson, P.H. Shipway, J.O. Abere, R.A.A. Hewitt, The effect of temperature on wear and friction of a high strength steel in fretting, Wear. 303 (2013) 622–631. https://doi.org/10.1016/j.wear.2013.03.048.

[94] A. Viat, A. Dreano, S. Fouvry, M.I. De Barros Bouchet, J.F. Henne, Fretting wear of pure cobalt chromium and nickel to identify the distinct roles of HS25 alloying elements in high temperature glaze layer formation, Wear. 376–377 (2017) 1043–1054. https://doi.org/10.1016/j.wear.2017.01.049.

[95] F.H. Stott, The role of oxidation in the wear of alloys, Tribol. Int. 31 (1998) 61–71. https://doi.org/10.1016/S0301-679X(98)00008-5.

[96] F.H. Stott, High-temperature sliding wear of metals, Tribol. Int. 35 (2002) 489–495.

[97] P.L. Hurricks, The fretting wear of mild steel from room temperature to 200°C, Wear. 19 (1972) 207–229. https://doi.org/https://doi.org/10.1016/0043-1648(72)90304-3.

[98] P.L. Hurricks, The fretting wear of mild steel from 200 to 500 C, Wear. 30 (1974) 189–212.

[99] R. Rybiak, S. Fouvry, B. Bonnet, Fretting wear of stainless steels under variable temperature conditions: Introduction of a "composite" wear law, Wear. 268 (2010) 413–423. https://doi.org/10.1016/j.wear.2009.08.029.

[100] F. Alkelae, S. Fouvry, Identification of parameters influencing the glaze layer formation and stability at high temperature for a Waspaloy/René125 contact under fretting wear conditions, Wear. 390–391 (2017) 41–48. https://doi.org/10.1016/j.wear.2017.07.008.

[101] J.E. Wilson, F.H. Stott, G.C. Wood, Development of wear-protective oxides and their influence on sliding friction, Proc. R. Soc. London, Ser. A Math. Phys. Sci. 369 (1980) 557–574.

[102] J. Jiang, F.H. Stott, M.M. Stack, The role of triboparticulates in dry sliding wear, Tribol. Int. 31 (1998) 245–256. https://doi.org/10.1016/S0301-679X(98)00027-9.

[103] H. Kato, K. Komai, Tribofilm formation and mild wear by tribo-sintering of nanometer-sized oxide particles on rubbing steel surfaces, Wear. 262 (2007) 36–41. https://doi.org/10.1016/j.wear.2006.03.046.

[104] R.M. German, Sintering theory and practice, Solar-Terrestrial Phys. (Solnechno-Zemnaya Fiz. (1996) 568.

[105] K. Adachi, K. Kato, Formation of smooth wear surfaces on alumina ceramics by embedding and tribo-sintering of fine wear particles, Wear. 245 (2000) 84–91. https://doi.org/10.1016/S0043-1648(00)00468-3.

[106] P.L. Hurricks, The mechanism of fretting - A review, Wear. 15 (1970) 389–409. https://doi.org/10.1016/0043-1648(70)90235-8.

[107] J.T. Burwell, C.D. Strang, Metallic wear, Proc. R. Soc. London. Ser. A. Math. Phys. Sci. 212 (1952) 470–477. https://doi.org/10.1098/rspa.1952.0239.

[108] J. Ding, S.B. Leen, I.R. McColl, The effect of slip regime on fretting wear-induced stress evolution, Int. J. Fatigue. 26 (2004) 521–531. https://doi.org/https://doi.org/10.1016/j.ijfatigue.2003.09.001.

[109] J. Ding, I.R. McColl, S.B. Leen, P.H. Shipway, A finite element based approach to simulating the effects of debris on fretting wear, Wear. 263 (2007) 481–491. https://doi.org/https://doi.org/10.1016/j.wear.2006.12.056.

[110] J. Ding, I.R. McColl, S.B. Leen, The application of fretting wear modelling to a spline coupling, Wear. 262 (2007) 1205–1216. https://doi.org/https://doi.org/10.1016/j.wear.2006.11.017.

[111] C. Paulin, S. Fouvry, C. Meunier, Finite element modelling of fretting wear surface evolution: Application to a Ti-6A1-4V contact, Wear. 264 (2008) 26–36. https://doi.org/10.1016/j.wear.2007.01.037.

[112] C. Mary, S. Fouvry, Numerical prediction of fretting contact durability using energy wear approach: Optimisation of finite-element model, Wear. 263 (2007) 444–450. https://doi.org/10.1016/j.wear.2007.01.116.

[113] T. Liskiewicz, S. Fouvry, Development of a friction energy capacity approach to predict the surface coating endurance under complex oscillating sliding conditions, Tribol. Int. 38 (2005) 69–79.

[114] L. Rodríguez-Tembleque, R. Abascal, M.H. Aliabadi, A boundary elements formulation for 3D fretting-wear problems, Eng. Anal. Bound. Elem. 35 (2011) 935–943. https://doi.org/10.1016/j.enganabound.2011.03.002.

[115] A. Dréano, S. Fouvry, G. Guillonneau, A tribo-oxidation abrasive wear model to quantify the wear rate of a cobalt-based alloy subjected to fretting in low-to-medium temperature conditions, Tribol. Int. 125 (2018) 128–140. https://doi.org/10.1016/j.triboint.2018.04.032.

[116] A. Dreano, S. Fouvry, G. Guillonneau, A combined friction energy and tribo-oxidation formulation to describe the high temperature fretting wear response of a cobalt-based alloy, Wear. 426–427 (2019) 712–724. https://doi.org/https://doi.org/10.1016/j.wear.2019.01.023.

[117] S. Basseville, E. Héripré, G. Cailletaud, Numerical simulation of the third body in fretting problems, Wear. 270 (2011) 876–887. https://doi.org/10.1016/j.wear.2011.02.016.

[118] V. Done, D. Kesavan, M. Krishna R, T. Chaise, D. Nelias, Semi analytical fretting wear simulation including wear debris, Tribol. Int. 109 (2017) 1–9. https://doi.org/10.1016/j.triboint.2016.12.012.

[119] P. Arnaud, S. Fouvry, S. Garcin, A numerical simulation of fretting wear profile taking account of the evolution of third body layer, Wear. 376–377 (2017) 1475–1488. https://doi.org/https://doi.org/10.1016/j.wear.2017.01.063.

[120] P. Arnaud, S. Fouvry, A dynamical FEA fretting wear modeling taking into account the evolution of debris layer, Wear. 412–413 (2018) 92–108. https://doi.org/10.1016/j.wear.2018.07.018.

[121] B. Sève, I. Iordanoff, Y. Berthier, A discrete solid third body model: Influence of the intergranular forces on the macroscopic behaviour, Tribol. Ser. 39 (2001) 361–368. https://www.scopus.com/inward/record.uri?eid=2-s2.0-0035785421&partnerID=40&md5=31a9bcfc066a1a88ca17ee418ee99e0b.

[122] I. Iordanoff, Y. Berthier, S. Descartes, H. Heshmat, A review of recent approaches for modeling solid third bodies, J. Tribol. 124 (2002) 725–735. https://doi.org/10.1115/1.1467632.

[123] N. Fillot, I. Iordanoff, Y. Berthier, Modelling third body flows with a discrete element method-a tool for understanding wear with adhesive particles, Tribol. Int. 40 (2007) 973–981. https://doi.org/10.1016/j.triboint.2006.02.056.

[124] I. Iordanoff, B. Seve, Y. Berthier, Solid third body analysis using a discrete approach: Influence of adhesion and particle size on macroscopic properties, J. Tribol. 124 (2002) 530–538. https://doi.org/10.1115/1.1456089.

[125] B.D. Leonard, A. Ghosh, F. Sadeghi, S. Shinde, M. Mittelbach, Third body modeling in fretting using the combined finite-discrete element method, Int. J. Solids Struct. 51 (2014) 1375–1389. https://doi.org/10.1016/j.ijsolstr.2013.12.036.

[126] B.D. Leonard, P. Patil, T.S. Slack, F. Sadeghi, S. Shinde, M. Mittelbach, Fretting wear modeling of coated and uncoated surfaces using the combined finite-discrete element method, J. Tribol. 133 (2011). https://doi.org/10.1115/1.4003482.

[127] B.D. Leonard, F. Sadeghi, S. Shinde, M. Mittelbach, Rough surface and damage mechanics wear modeling using the combined finite-discrete element method, Wear. 305 (2013) 312–321. https://doi.org/10.1016/j.wear.2012.12.034.

[128] A.I. Vakis, V.A. Yastrebov, J. Scheibert, L. Nicola, D. Dini, C. Minfray, A. Almqvist, M. Paggi, S. Lee, G. Limbert, J.F. Molinari, G. Anciaux, R. Aghababaei, S. Echeverri Restrepo, A. Papangelo, A. Cammarata, P. Nicolini, C. Putignano, G. Carbone, S. Stupkiewicz, J. Lengiewicz, G. Costagliola, F. Bosia, R. Guarino, N.M. Pugno, M.H. Müser, M. Ciavarella, Modeling and simulation in tribology across scales: An overview, Tribol. Int. (2018). https://doi.org/10.1016/j.triboint.2018.02.005.

[129] J.F. Molinari, R. Aghababaei, T. Brink, L. Frérot, E. Milanese, Adhesive wear mechanisms uncovered by atomistic simulations, Friction. 6 (2018) 245–259.

[130] R. Aghababaei, D.H. Warner, J.-F. Molinari, Critical length scale controls adhesive wear mechanisms, Nat. Commun. 7 (2016) 1–8.

[131] R. Aghababaei, D.H. Warner, J.-F. Molinari, On the debris-level origins of adhesive wear, Proc. Natl. Acad. Sci. 114 (2017) 7935–7940.

[132] R. Aghababaei, On the origins of third-body particle formation during adhesive wear, Wear. 426 (2019) 1076–1081.

[133] R. Aghababaei, T. Brink, J.-F. Molinari, Asperity-level origins of transition from mild to severe wear, Phys. Rev. Lett. 120 (2018) 186105.

[134] T. Zhu, P.H. Shipway, W. Sun, The dependence of wear rate on wear scar size in fretting; the role of debris (third body) expulsion from the contact, Wear. 440–441 (2019). https://doi.org/10.1016/j.wear.2019.203081.

[135] A.L. Mohd Tobi, J. Ding, S. Pearson, S.B. Leen, P.H. Shipway, The effect of gross sliding fretting wear on stress distributions in thin W-DLC coating systems, Tribol. Int. 43 (2010) 1917–1932. https://doi.org/10.1016/j.triboint.2010.01.018.

[136] S.B. Leen, I.J. Richardson, I.R. McColl, E.J. Williams, T.R. Hyde, Macroscopic fretting variables in a splined coupling under combined torque and axial load, J. Strain Anal. Eng. Des. 36 (2001) 481–497. https://doi.org/10.1243/0309324011514647.

[137] S.R. Pearson, The effect of nitriding on the fretting wear of a high strength steel at ambient and elevated temperatures, University of Nottingham, 2013.

[138] A.R. Warmuth, The effect of contact geometry and frequency on dry and lubricated fretting wear, University of Nottingham, 2014.

[139] K.H.R. Wright, An investigation of fretting corrosion, Proc. Inst. Mech. Eng. 167 (1953) 556–574.

[140] R.C. Bill, Review of factors that influence fretting wear, Mater. Eval. Under Frett. Cond. (1982).

[141] P. de Baets, G. Kalacska, K. Strijckmans, F. Van de Velde, A.P. Van Peteghem, Experimental study by means of thin layer activation of the humidity influence on the fretting wear of steel surfaces, Wear. 216 (1998) 131–137. https://doi.org/https://doi.org/10.1016/S0043-1648(97)00189-0.

[142] H. Goto, D.H. Buckley, The influence of water vapour in air on the friction behaviour of pure metals during fretting, Tribol. Int. 18 (1985) 237–245. https://doi.org/10.1016/0301-679X(85)90069-6.

[143] K. Dies, Friction Oxidation as a Chemico-Mechanical Process, Arch. Fur Das Eisenhullenwes. 10 (1943) 399.

[144] L. Blades, D. Hills, D. Nowell, K.E. Evans, C. Smith, An exploration of debris types and their influence on wear rates in fretting, Wear. 450–451 (2020) 203252. https://doi.org/https://doi.org/10.1016/j.wear.2020.203252.

[145] A. Iwabuchi, K. Hori, H. Kubosawa, The effect of oxide particles supplied at the interface before sliding on the severe-mild wear transition, Wear. 128 (1988) 123–137. https://doi.org/10.1016/0043-1648(88)90179-2.

[146] H. Kato, Effects of supply of fine oxide particles onto rubbing steel surfaces on severe-mild wear transition and oxide film formation, Tribol. Int. 41 (2008) 735–742. https://doi.org/10.1016/j.triboint.2008.01.001.

[147] K. Hiratsuka, K. Muramoto, Role of wear particles in severe–mild wear transition, Wear. 259 (2005) 467–476. https://doi.org/https://doi.org/10.1016/j.wear.2005.02.102.

[148] T.F.J. Quinn, The oxidational wear of low alloy steels, Tribol. Int. 35 (2002) 691–715. https://doi.org/10.1016/S0301-679X(02)00039-7.

[149] N.P. Suh, An overview of the delamination theory of wear, Wear. 44 (1977) 1–16. https://doi.org/10.1016/0043-1648(77)90081-3.

[150] X. Jin, W. Sun, P.H. Shipway, The role of geometry changes and debris formation associated with wear on the temperature field in fretting contacts, Tribol. Int. 102 (2016) 392–406. https://doi.org/10.1016/j.triboint.2016.05.043.

[151] N. Fillot, I. Iordanoff, Y. Berthier, Simulation of wear through mass balance in a dry contact, J. Trib. 127 (2005) 230–237.

[152] A. Iwabuchi, T. Kayaba, K. Kato, Effect of atmospheric pressure on friction and wear of 0.45% C steel in fretting, Wear. 91 (1983) 289–305. https://doi.org/https://doi.org/10.1016/0043-1648(83)90074-1.

[153] A. Iwabuchi, K. Kato, T. Kayaba, Fretting properties of SUS304 stainless steel in a vacuum environment, Wear. 110 (1986) 205–216. https://doi.org/https://doi.org/10.1016/0043-1648(86)90098-0.